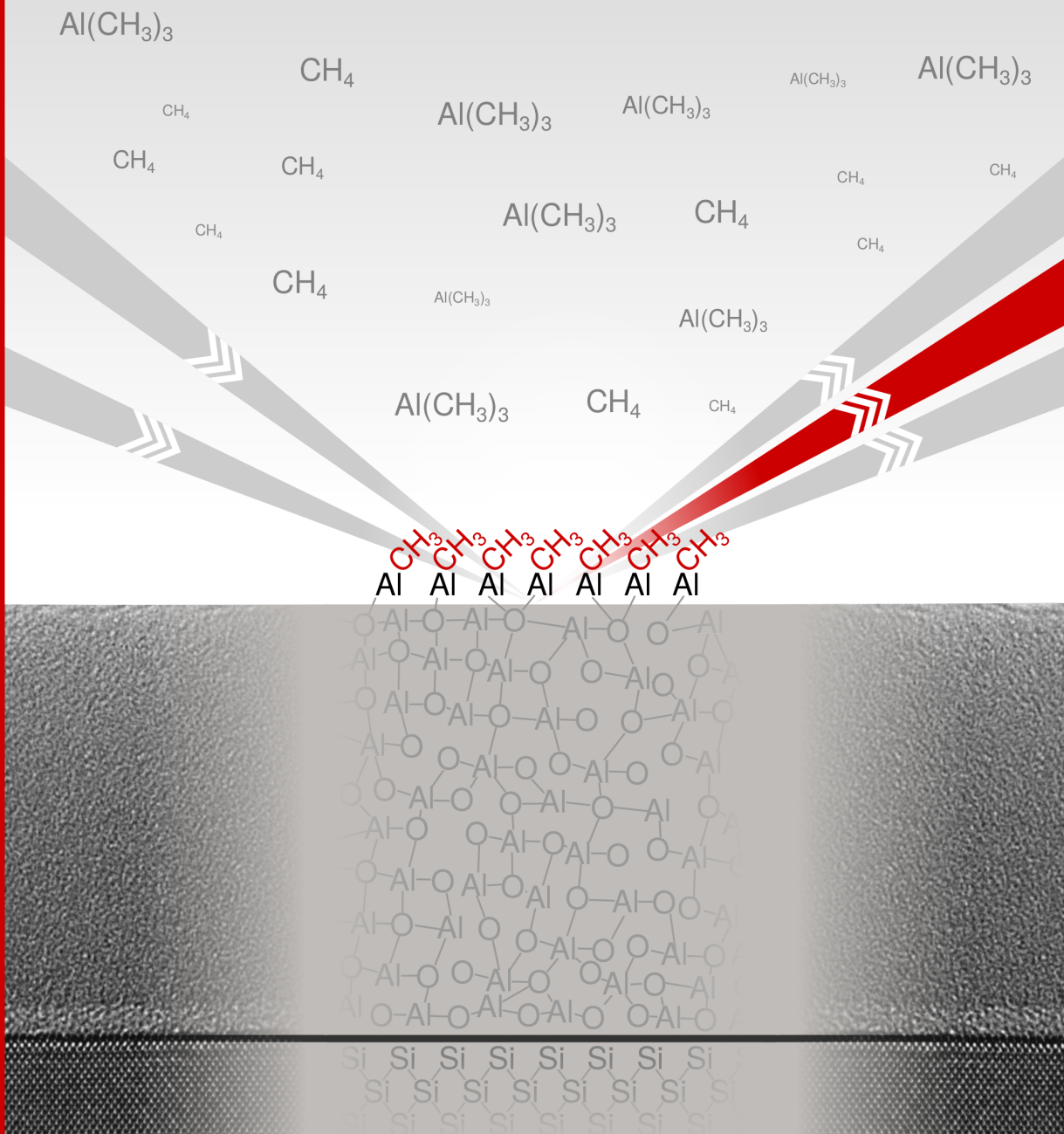


# Sum-Frequency Generation Study of the Surface Chemistry During Atomic Layer Deposition

Vincent Vandalon



# Sum-Frequency Generation Study of the Surface Chemistry During Atomic Layer Deposition

PROEFSCHRIFT

ter verkrijging van de graad van doctor aan de Technische Universiteit  
Eindhoven, op gezag van de rector magnificus prof.dr.ir. F.P.T. Baaijens,  
voor een commissie aangewezen door het College voor Promoties, in het  
openbaar te verdedigen op dinsdag 20 juni 2017 om 16:00 uur

door

Vincent Vandalon

geboren te Geleen

Dit proefschrift is goedgekeurd door de promotoren en de samenstelling van de promotiecommissie is als volgt:


voorzitter: prof.dr.ir. G.M.W. Kroesen  
1e promotor: prof.dr.ir. W.M.M. Kessels  
2e promotor: prof.dr.ir. M.C.M. van de Sanden  
leden: prof.dr. E.P.A.M Bakkers  
prof.dr. M. Bonn (UvA)  
prof.dr. M.A. Stöhr (RUG)  
dr. S.D. Elliott (Tyndall National Institute)  
adviseur: dr. P. Poodt (TNO)

*Het onderzoek dat in dit proefschrift wordt beschreven is uitgevoerd in overeenstemming met de TU/e Gedragscode Wetenschapsbeoefening.*

«Cela est bien dit, répondit Candide, mais il faut cultiver notre jardin.»  
from *Candide, ou l'Optimisme* by Voltaire

This research is supported by the Dutch Technology Foundation STW, which is part of the Netherlands Organisation for Scientific Research (NWO).



This dissertation was typeset in  $\text{\LaTeX}$  and written using the  editor making use of open-source software such as Inkscape and Python.

Cover art & dissertation layout by Vincent Vandalon

Printed and bound by Gildeprint Drukkerijen, Enschede

A catalogue record is available from the Eindhoven University of Technology Library

ISBN: 978-90-386-4283-3

# Contents

<b>1</b>	<b>Introduction</b>	<b>7</b>
1.1	Nano-electronics and the need for ultrathin films . . . . .	7
1.2	Ultrathin films grown by atomic-layer deposition . . . . .	9
1.3	Studying surface chemistry with BB-SFG . . . . .	11
1.4	Goals, context, and outline . . . . .	13
<b>2</b>	<b>Principles of optical sum-frequency generation to study surface chemistry</b>	<b>19</b>
2.1	Introduction . . . . .	19
2.2	Phenomenological description of SFG . . . . .	20
2.3	Macroscopic model of SFG . . . . .	27
2.4	Spectral shape of a SFG signal . . . . .	29
2.5	Microscopic description and modeling BB-SFG spectra . . . . .	37
<b>3</b>	<b>BB-SFG setup for ALD growth mechanism studies</b>	<b>45</b>
3.1	Introduction . . . . .	45
3.2	General considerations for vibrational BB-SFG . . . . .	46
3.3	The femtosecond laser system: a tunable mid-IR & visible light source . . . . .	49
3.4	Beam tailoring to achieve temporal and spatial overlap . . . . .	54
3.5	ALD reaction chamber . . . . .	56
3.6	Detection of the BB-SFG signal . . . . .	58
3.7	Recommendations for improvements . . . . .	60
<b>4</b>	<b>Practical considerations for BB-SFG spectroscopy studying ALD growth on <i>c</i>-Si</b>	<b>65</b>
4.1	Introduction . . . . .	65
4.2	Suitable benchmarks for the BB-SFG setup . . . . .	66
4.3	Study case: UV exposure of the H/Si(111) surface . . . . .	73
4.4	Exploiting linear optics for increased sensitivity . . . . .	76
4.5	Suppression of non-resonant signal . . . . .	82
4.6	Summary . . . . .	86

<b>5</b>	<b>Initial growth of Al<sub>2</sub>O<sub>3</sub> by atomic layer deposition studied with vibrational sum-frequency generation</b>	<b>91</b>
5.1	Introduction . . . . .	92
5.2	Vibrational broadband sum-frequency generation . . . . .	94
5.3	Experimental details . . . . .	95
5.4	Results . . . . .	99
5.5	Concluding remarks . . . . .	104
5.A	Appendix . . . . .	108
<b>6</b>	<b>What is limiting low-temperature atomic layer deposition of Al<sub>2</sub>O<sub>3</sub>? A vibrational sum-frequency generation study</b>	<b>113</b>
6.1	Introduction . . . . .	114
6.2	Experimental details . . . . .	115
6.3	Results . . . . .	116
6.4	Conclusion . . . . .	121
6.A	Appendix . . . . .	122
<b>7</b>	<b>Revisiting the growth mechanism of atomic layer deposition of Al<sub>2</sub>O<sub>3</sub>: a vibrational sum-frequency generation study</b>	<b>129</b>
7.1	Introduction . . . . .	130
7.2	Growth mechanism of ALD of Al <sub>2</sub> O <sub>3</sub> . . . . .	132
7.3	Experimental details . . . . .	139
7.4	Results and Discussion . . . . .	141
7.5	Conclusion . . . . .	157
7.A	Appendix . . . . .	159
<b>8</b>	<b>Surface chemistry during atomic-layer deposition of Pt studied with vibrational sum-frequency generation</b>	<b>169</b>
8.1	Introduction . . . . .	170
8.2	Sum-frequency generation . . . . .	172
8.3	Experimental details . . . . .	176
8.4	Results and discussion . . . . .	177
8.5	Discussion of the reaction mechanism . . . . .	188
8.6	Conclusion . . . . .	189
8.A	Appendix . . . . .	189
<b>9</b>	<b>Conclusion and Outlook</b>	<b>195</b>
9.1	Conclusion . . . . .	195
9.2	Outlook . . . . .	196
<b>10</b>	<b>Summary</b>	<b>199</b>
	<b>Contributions of the author</b>	<b>201</b>
	<b>Acknowledgments</b>	<b>203</b>
	<b>Curriculum vitae</b>	<b>205</b>

## 1.1 Nano-electronics and the need for ultrathin films

Nano-electronic components in devices such as central-processing units (CPU), graphics-processing units (GPU), and memory chips rely on ultrathin films to fulfill key aspects in their design.<sup>1,2</sup> With dimensions of some of the individual components smaller than 100 nanometers, the thickness of these ultrathin films is often in the range of nanometers.<sup>1-3</sup> Some examples of these nano-electronic devices and their components are shown in Fig. 1.1. The figure also illustrates the ubiquitous use of ultrathin films in these components. With the drive towards reduced power consumption, increased miniaturization, and improved efficiency of these devices, the requirements on these ultrathin films are becoming ever more demanding.<sup>2</sup> At the same time, the yield of the production processes has to be maintained or improved. These trends result in the demand for:

- Better thickness control, requiring a sub-nanometer accuracy and precision.
- Higher-quality material or more complex materials, such as doped materials or ternary compounds.
- Less variation in the film thickness over a large area, e.g. below 2.5 % of the film thickness over a 200 mm wafer.
- Less variation in the film thickness on complex 3D structures, e.g. below 5 % of the film thickness in, for example, a trench structure.

The latter criteria are often referred to as the uniformity and conformality of the deposited film, respectively.<sup>4</sup> Furthermore, the operating conditions for the deposition of the thin films are becoming more demanding. For example, low temperatures are required for deposition on e.g. temperature sensitive structures. All this leads to a driving force for research and innovation in the field of ultrathin-film deposition.

A large part of the research effort in this field is focused on characterizing the properties of the ultrathin films as well as on characterizing the deposition process.<sup>5</sup> This empirical approach has led to valuable innovation and new applications. However, it is also important to strive towards a detailed and fundamental understanding of the deposition processes. Mechanistic studies



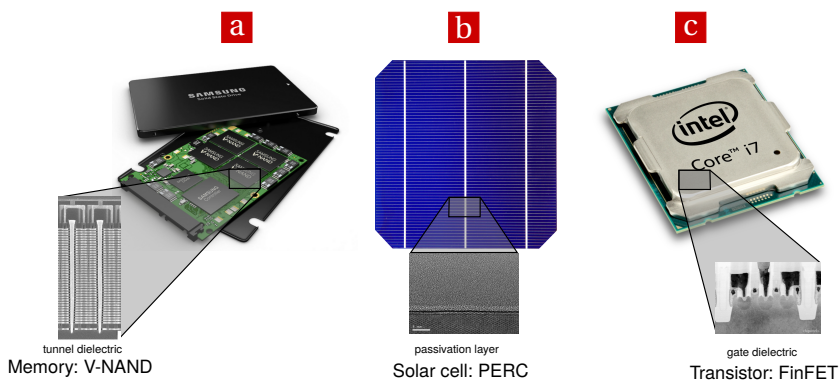


**Figure 1.1:** Three examples of state-of-the-art devices with nano-electronic components relying on ultrathin-films. In all of these examples, atomic-layer deposition (ALD) is a key step in fabrication process: **(a)** A solid-state drive (SSD) used for data storage based upon vertical negative-AND (V-NAND) flash memory. ALD is used for the deposition of the tunnel dielectric which is a key component in the V-NAND memory. ([www.samsung.com](http://www.samsung.com) and [www.chipworks.com](http://www.chipworks.com)) **(b)** A *c*-Si solar cell used for generation of electricity with a Passivated Emitter Rear Cell (PERC) type architecture. ALD can be used to deposit a  $\text{Al}_2\text{O}_3$  films which act as a passivation layer at the rear side, enhancing the performance of the device. **(c)** A central processing unit (CPU) used in high performance computing based upon a fin field-effect transistors (FinFET) architecture. The gate dielectric it is prepared by ALD and this dielectric layer is key in the performance of the FinFET transistor. ([www.intel.com](http://www.intel.com) and [www.chipworks.com](http://www.chipworks.com))

can reveal underlying principles of the growth mechanism which might be exploited to improve or extend the capabilities of a deposition process. Moreover, these fundamental studies can guide the more empirical research by highlighting which parameters are important. A good example of how mechanistic studies can lead to new and better control over material processing can be found in the work of **Coburn and Winters**. They investigated plasma assisted etching of Si and  $\text{SiO}_2$  by methodically studying the etch mechanism under realistic conditions. This allowed them to identify the key processes at play during the etch process.<sup>6</sup> For example, the fluorine to carbon ratio was found to be the dominant parameter controlling the directionality of the etch process of  $\text{SiO}_2$ . This insight explained a whole range of empirical findings, but more importantly, they were able to tune the etch process from isotropic to anisotropic by simply changing the plasma chemistry.<sup>6</sup> This success is one of the many examples that illustrate the need for fundamental mechanistic studies. Furthermore, it underscores the need to perform these studies under realistic operating conditions by analysis techniques capable of monitoring the etch and deposition mechanisms *in-situ*.

## 1.2 Ultrathin films grown by atomic-layer deposition

Atomic-layer deposition (ALD) is an enabling technique for the deposition of ultrathin films in nano-electronic components. The ALD process can meet the aforementioned requirements of sub-nanometer thickness control, conformality, and uniformity.<sup>2,5</sup> Furthermore, a wide variety of materials such as metal oxides, metal nitrides, and metals can be deposited by ALD at relatively low temperatures (typically between room temperature and 400°C).<sup>5</sup> In fact, all of the devices shown in Fig. 1.1 are currently in production and use ALD for the deposition of 1 or more key functional layers.

To understand why ALD is able to meet these requirements, it is insightful to elucidate the (generalized) growth mechanism of most ALD processes. A single “atomic layer” of material is deposited during ALD by sequentially exposing a surface to two or more gas/vapor phase reactants, as is illustrated in Fig. 1.2. This sequence of steps is called an ALD cycle which consists of two “half-cycle” or multiple “sub-cycles”. In each half-cycle, the reactants chemisorb onto, or react with, the surface in a *self-limiting fashion*.<sup>4,5</sup> The self-limiting nature of the surface reactions is the defining feature of ALD which is the result of a carefully chosen chemistry. At the end of each half-cycle, the surface sites available for the ALD reaction have been depleted and the half-cycle is said to be “saturated”. Exposing the surface to more reactant no longer affects the amount of chemisorbed reactants. This basically makes the amount of the material deposited in an ALD cycle *flux independent* once the saturated condition is reached. The highly repeatable and well defined amount of material deposited by this sequence of steps is referred to as the growth-per-cycle (GPC). By repeating the ALD cycle, a film can be deposited with sub-nanometer thickness control and the *self-limiting* reactions make the ALD film *inherently* uniform and conformal.<sup>5</sup> The cyclical nature of the ALD process, allowing it to be repeated, requires that the surface at the end of the ALD cycle is identical to the surface at the beginning of the ALD cycle. As mentioned before, the ALD process is *flux independent* because the reaction of a reactant with the surface typically terminates due to the depletion of certain surface groups. This behavior is lost if these surface groups would be re-generated by the simultaneous presence of other gas-phase reactants. Moreover, in some cases the reactants can undergo mutual gas-phase reactions resulting in undesirable reaction products. Therefore, it is essential to separate the reactant steps either temporally or spatially. The reactant species are often referred to as either a precursor or a co-reactant depending on their role in the ALD process. Reactants that deposit metal atoms (e.g. Pt,Al,Ti) or metalloid (e.g. Si,Ge,B) atoms are often referred to as precursors. Reactants that either deposit nonmetal atoms (e.g. N,O,S,P) or are not incorporated into the film are often referred to as co-reactants. However, deviations from this nomenclature exist.

Practically speaking, most of the ALD processes take place in a reactor chamber operating at medium vacuum with pressures ranging from ~ 25

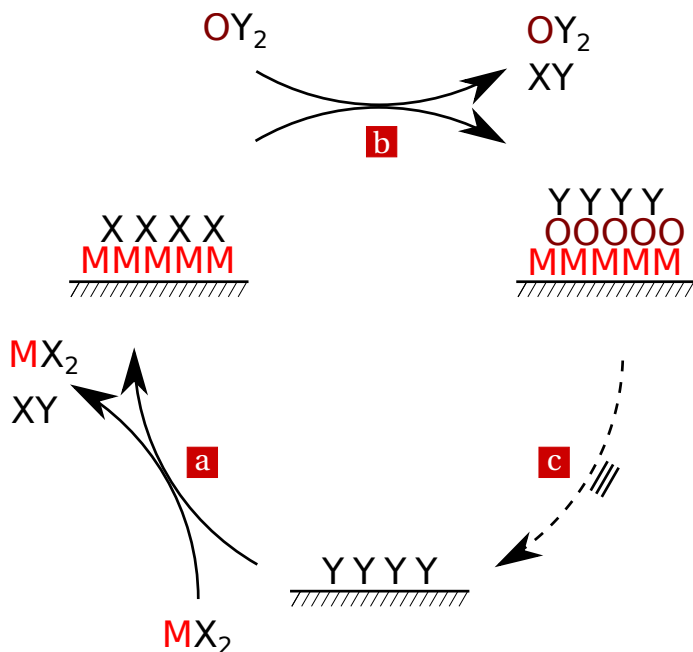


**Figure 1.2:** Schematic of the growth mechanism of a generic and idealized ALD process forming a metal-oxide (MO) with  $MX_2$  as precursor and  $OY_2$  as co-reactant. **(a)** The  $-Y$  functionalized surface is exposed to the metal precursor which chemisorbs onto this surface releasing  $XY$  as a gas-phase reaction product. This reaction is *self-limiting* which can be caused by, for example, the depletion of the  $-Y$  surface groups. At the end of the half-cycle, the surface is  $-X$  functionalized and a layer of  $M$  atoms has been deposited. **(b)** The  $-X$  functionalized surface is exposed to the co-reactant. The co-reactant chemisorbs onto the surface releasing  $XY$  as a gas-phase reaction product. This reaction is also *self-limiting*, making the ALD process *flux independent*. At the end of the half-cycle, the surface is  $-Y$  functionalized and an “atomic layer” of MO has been deposited. **(c)** The surface at the end of the co-reactant half-cycle is identical to the starting surface of the precursor half-cycle. This is essential because it allows the ALD process to be repeated. Note that the gas-phase reaction products and the unconsumed precursor or co-reactant molecules are removed at the end of both half-cycles. In this case, the gas-phase reaction product for both half-cycles (**(a)** and **(b)**) are the same, but in general different reaction products might be formed.

Torr down to  $1 \cdot 10^{-3}$  Torr. The reactants often emanate from chemicals in the liquid or solid state and are dosed into the reactor in the vapor phase. The reactant steps are separated temporally and the gas-phase species are removed after saturation by either pumping or purging the gas-phase species from the reactor. On the other hand, ALD processes at atmospheric pressure as well as processes which rely on spatial separation of the reactants are currently emerging.<sup>7</sup> In this work, only low pressure ALD processes will be considered but some of the results might also be applicable to the atmospheric pressure ALD processes.

To recapitulate, the surface chemistry rules the growth mechanism of ALD and lends the process its defining characteristics. Gaining a fundamental understanding of the surface chemistry is key in advancing the capabilities of ALD such as expanding the operational envelope and moving to ALD of more complex materials.

### Studying the growth mechanism of ALD

The growth mechanisms of ALD processes are typically studied by investigating the (material) properties of the deposited films, the gas-phase reaction products, or the surface chemistry. The latter is typically more challenging but it is the more direct approach and will be the focus of this work. There are several restrictions on the analysis techniques that can be used to study the surface chemistry during ALD. The surface groups have to be identified and preferably quantified *in-situ*, which implies that the analysis technique has to be compatible with the typical operating conditions of ALD. Furthermore, the analysis technique should be sufficiently sensitive to detect changes in a fraction of a monolayer of material at the surface which has to be isolated from, in most cases, similar but unrelated (bulk) contributions. Information obtained with *inherently surface selective* analysis techniques – i.e. techniques that only probe the surface – have an advantage in this respect since unrelated signals are suppressed or absent. In this work such a *inherently* surface selective technique will be used to study the surface chemistry.

## 1.3 Studying surface chemistry with BB-SFG

The analysis technique of broadband sum-frequency generation (BB-SFG) spectroscopy is based upon the optical process of sum-frequency generation (SFG). Most of the optical processes encountered in every day life, such as the reflection or scattering of light, are so called linear optical processes.<sup>8,9</sup> One of the key features of linear optics is that the polarization in the material, caused by light passing through the material, has the same frequency as the light itself.<sup>8</sup> In practice this means that if multiple colors of light simultaneously pass through the material, then these different “colors” of light do not interact with each other. No new “colors” of light can be generated by these optical processes.

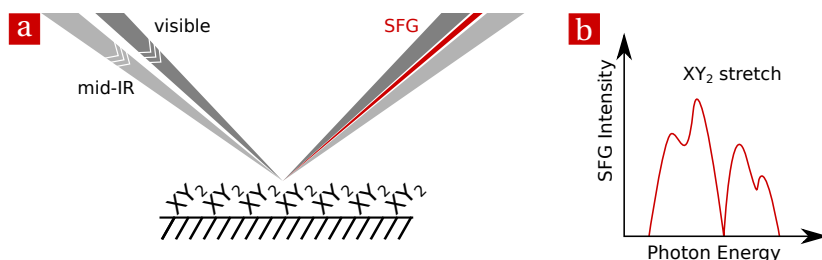


**Figure 1.3:** (a) Illustration of BB-SFG spectroscopy using a visible and mid-IR beam to probe the spectral response of the  $XY_2$  groups on the surface. At the interface, the visible and broadband mid-IR photons generate a new photon which has the sum-frequency of the two driving photons. The SFG process is inherently surface selective on centrosymmetric substrates such as  $c$ -Si and amorphous materials. (b) An illustration of a imaginary spectral shape of the visible BB-SFG signal reflecting the shape of the vibrational fingerprint of the  $XY_2$  groups probed by the mid-IR beam.

This linear description of light-matter interaction is valid for light with a every-day intensity. For light with extremely high intensities, nonlinear optical processes become relevant.<sup>9</sup> In these nonlinear processes, different colors of light do interact which can result in the generation of new “colors” of light. One of these nonlinear optical processes is the aforementioned process of SFG. SFG is a second-order process in which two photons of different energy simultaneously interact with matter generating a new photon. The energy of this new photon is the sum of the energies of the two photons driving the process. It turns out that the SFG process has several practical applications.<sup>9</sup> For example, the family of second-order nonlinear optical processes including SFG are important in the operation of modern laser systems and photonic structures.<sup>10,11</sup> On the other hand, the SFG process is also the basis of SFG spectroscopy. For the SFG process, the selection rules are quite strict and the process only occurs at sites with a low symmetry. As a result, the SFG process is not allowed in the bulk of a centrosymmetric media such as amorphous materials and for example  $c$ -Si.<sup>9</sup> At the surface of such a material, however, the process of SFG is always allowed because of the reduced symmetry. In practice, this makes the SFG process *inherently* surface selective on centrosymmetric substrates. Therefore, the SFG process is ideally suited to probe surface-related phenomena such as surface chemistry.<sup>12,13</sup>

*Vibrational* BB-SFG spectroscopy is an analysis technique based upon the SFG process. By mixing mid-IR light and visible light, the vibrational transitions of surface groups can be probed. The resulting SFG signal is situated in the visible part of the spectrum (convenient for detection) and contains vibrational information of the surface groups.<sup>9,13</sup> Figure 1.3(a) illustrates the interaction of a femtosecond spectrally broadband IR pulse and a picosecond visible pulse with the surface generating the visible SFG signal. Figure 1.3(b) illustrates the resulting (imaginary) spectral shape of the BB-SFG signal which

contains information about the type and the areal density of surface groups excited by the mid-IR beam.

BB-SFG spectroscopy is recognized in the field of surface science as a *state-of-the-art* technique and has been used to successfully address several long standing questions in this field.<sup>14–16</sup> BB-SFG spectroscopy is the go-to technique for these studies because of its *inherent* surface selectivity, its sub-monolayer sensitivity, and its capability to follow the surface chemistry on femtosecond time scales. Due to its all optical nature, BB-SFG spectroscopy is inherently compatible with a wide range of operating conditions including those of typical ALD processes. In this work, BB-SFG spectroscopy will be used, for the first time, to study the surface chemistry during ALD.

## 1.4 Goals, context, and outline

### Goals and objectives

The main goal of this work was to gain a fundamental understanding of the growth mechanism of ALD by studying the surface chemistry using BB-SFG spectroscopy. The first objective was to build an *ex-situ* BB-SFG spectroscopy setup and to gain vital experience with this analysis technique. The second objective was to design and build a BB-SFG setup for *in-situ* studies of the ALD surface chemistry.

Two prototypical ALD processes were studied: thermal ALD of  $\text{Al}_2\text{O}_3$  and thermal ALD of Pt. The choice for these two ALD processes was motivated by several factors. As mentioned before, these two ALD processes are model systems and especially the use of the ALD process of  $\text{Al}_2\text{O}_3$  is widespread. These two rather well-known processes were also chosen to evaluate the merit and flexibility of BB-SFG spectroscopy for studying the surface chemistry during ALD. The growth mechanisms differ in several aspects making these two processes good test cases for BB-SFG spectroscopy. For example, a striking difference is the reliance of the Pt ALD process on the catalytic nature of the Pt surface whereas the  $\text{Al}_2\text{O}_3$  process does not. Moreover, the films deposited by the two different ALD processes also represent extreme cases; i.e. a fully transparent ( $\text{Al}_2\text{O}_3$ ) and a fully opaque (Pt) film which can be used to test the capability of BB-SFG spectroscopy to handle different types of films.

The third objective was to validate the results of BB-SFG spectroscopy by studying the well known growth mechanism of ALD of  $\text{Al}_2\text{O}_3$ . Even though this process is well studied, several open questions were addressed successfully by monitoring the surface chemistry with BB-SFG spectroscopy. Several of these remaining questions were:

- How does the  $-\text{CH}_3$  coverage vary with temperature?
- What is the sticking probability of TMA and  $\text{H}_2\text{O}$ ?
- How do the sticking probabilities depend on temperature?
- Why does the GPC decrease at low temperatures?

The next objective was to study the surface chemistry during the initial growth of  $\text{Al}_2\text{O}_3$  by ALD on various substrates. So far, the initial growth has not been studied in detail, however, a fundamental understanding of the initial growth is becoming increasingly important for e.g. area selective ALD and ALD of ternary or doped materials. Some of the key issues addressed in this work are:

- How do the sticking probabilities evolve during the first few ALD cycles on a  $\text{SiO}_2$  starting surface?
- To which extent is the sticking probability different in the first cycles on  $\text{SiO}_2$  and hydrogen terminated Si(111) from that of steady-state growth?

The Pt ALD process serves as a model system for noble-metal ALD. However, several questions remain about the underlying reaction mechanism. For example, it is not clear which species of hydrocarbon groups are present on the surface and direct measurements of the surface chemistry are lacking. For this ALD process, the objective was to study the surface chemistry answering questions such as:

- Can some of the hydrocarbon groups on the surface after the precursor half-cycle be identified?
- Is there evidence for dehydrogenation of the hydrocarbon groups on the Pt surface?

## Context

This research took place in the *Plasma and Materials Processing* (PMP) group at the department of Applied Physics of the *Eindhoven University of Technology* (TU/e). The PMP group has been in the forefront of the development of ALD processes and their applications. This has led to: (a) The development of, for example, room temperature plasma-enhanced  $\text{Al}_2\text{O}_3$  and Pt ALD processes.<sup>4,17–19</sup> (b) Innovations, such as, the applications of ALD  $\text{Al}_2\text{O}_3$  films in *c*-Si solar cells and in moisture barrier layers.<sup>20,21</sup> This also illustrates the aim of the ALD research in the PMP group: to gain a fundamental understanding of the ALD processes and use that knowledge for the development of novel processes and applications. The purpose of this work was to extend the capabilities of the PMP group with a *state-of-the-art* analysis technique for studying the ALD surface chemistry and to gain fundamental understanding of the ALD growth overall. In this respect, the project was part of the Vici research programme “Nanomanufacturing: atomic level understanding for materials and dimensions control”.

Note that the mechanistic studies performed in this work are part of a long-standing and ongoing effort in the PMP group to understand the growth mechanism of key ALD processes. Especially the investigation of the growth mechanism of the Pt ALD process is a continuation of an earlier effort in the group. In part, these earlier efforts were hampered by the lack of an analysis technique capable of studying the surface chemistry on a (opaque) metallic

surface during ALD. Other processes which have been studied in large detail in the PMP group, using a combination of ab-initio computer simulations and *in-situ* measurements, include plasma-enhanced ALD of Pt, Al<sub>2</sub>O<sub>3</sub> and SiN<sub>x</sub>.<sup>18,22–25</sup>

## Outline

The structure of the dissertation globally follows the main goal and the objectives. The first part of the dissertation is dedicated to BB-SFG spectroscopy. **Chapter 2** describes the fundamentals of the SFG process keeping the specific application of BB-SFG spectroscopy in mind. **Chapter 3** describes the design choices made when building the BB-SFG spectroscopy setup and **Chapter 4** discusses the practical considerations important to employing BB-SFG spectroscopy to study the surface chemistry during ALD.

The second part of the dissertation pertains to the surface chemistry during ALD of Al<sub>2</sub>O<sub>3</sub> and Pt studied with BB-SFG spectroscopy. **Chapter 5** focuses on the initial growth of Al<sub>2</sub>O<sub>3</sub> ALD with Al(CH<sub>3</sub>)<sub>3</sub> (TMA) and H<sub>2</sub>O as reactants. The initial growth was studied on two starting surfaces relevant for the semiconductor industry: a SiO<sub>2</sub> and a hydrogen terminated Si(111) surface. The influence of the starting surface on the surface chemistry of the Al<sub>2</sub>O<sub>3</sub> ALD process was studied on a half-cycle basis. Subtle differences in the reaction cross section were found which were in part responsible for the differences in the GPC during initial growth. This work highlights the use of BB-SFG spectroscopy for studying the surface chemistry during the initial growth. **Chapter 6** focuses on the steady state growth of the Al<sub>2</sub>O<sub>3</sub> ALD process addressing the aforementioned question: What causes the GPC to decrease at low temperatures? A so-far overlooked non-ideality in the ALD process was found to be responsible for the reduced growth at low temperatures. **Chapter 7** takes a more in-depth look at the steady state growth of thermal ALD of Al<sub>2</sub>O<sub>3</sub>. It provides an overview of our current understanding of the Al<sub>2</sub>O<sub>3</sub> growth mechanism and in this context several new insights into the growth mechanism were presented. More particularly, the reaction kinetics of the H<sub>2</sub>O half-cycle was studied revealing a relatively complex behavior. Moreover, several other fundamental issues were addressed such as the self-limiting nature of the reactions, the bonding of the precursor to the surface, and the absence of carbon incorporation into the film.

**Chapter 8** investigates the growth mechanism of ALD of Pt using MeCpPtMe<sub>3</sub> as a precursor and O<sub>2</sub> gas as co-reactant. Direct experimental evidence was found for the presence of CH<sub>3</sub> groups on the surface after the precursor half-cycle. Moreover, the reaction kinetics and the dependence of the surface functionalization after the precursor half-cycle on temperature were studied, confirming several hypothesis made in the past on the basis of studies of the gas-phase reaction products and the general mechanisms reported for hydrocarbon species on the Pt surface in the surface science literature.



## Bibliography

- [1] Choi, Mao, and Chang. Development of hafnium based high-k materials - A review. *Materials Science and Engineering: R: Reports*, 2011. doi:[10.1016/j.mser.2010.12.001](https://doi.org/10.1016/j.mser.2010.12.001).
- [2] Robertson and Wallace. High-K materials and metal gates for CMOS applications. *Materials Science & Engineering R*, 2015. doi:[10.1016/j.mser.2014.11.001](https://doi.org/10.1016/j.mser.2014.11.001).
- [3] van Delft, Garcia-Alonso, and Kessels. Atomic layer deposition for photovoltaics: applications and prospects for solar cell manufacturing. *Semiconductor Science and Technology*, 2012. doi:[10.1088/0268-1242/27/7/074002](https://doi.org/10.1088/0268-1242/27/7/074002).
- [4] Knoop, Potts, Bol, and Kessels. Springer Handbook of Crystal Growth. *Japanese Magazine of Mineralogical and Petrological Sciences*, 2010. doi:[10.2465/gkk.39.193a](https://doi.org/10.2465/gkk.39.193a).
- [5] George. Atomic layer deposition: an overview. *Chemical reviews*, 2010. doi:[10.1021/cr900056b](https://doi.org/10.1021/cr900056b).
- [6] Coburn and Winters. Plasma etching - A discussion of mechanisms. *Journal of Vacuum Science and Technology*, 1979. doi:[10.1116/1.569958](https://doi.org/10.1116/1.569958).
- [7] Poedt, van Lieshout, Illiberi, Knaapen, Roozeboom, and van Asten. On the kinetics of spatial atomic layer deposition. *Journal of Vacuum Science & Technology A: Vacuum, Surfaces, and Films*, 2013. doi:[10.1116/1.4756692](https://doi.org/10.1116/1.4756692).
- [8] Born and Wolf. *Principles of optics : electromagnetic theory of propagation, interference and diffraction of light*. Cambridge University Press, 1999.
- [9] Boyd. *Nonlinear optics*. Elsevier Science Publishing Co Inc, second edition, 1992.
- [10] Koechner. *Solid-State Laser Engineering*. Springer New York, New York, NY, 4th extens edition, 2006. doi:[10.1007/0-387-29338-8](https://doi.org/10.1007/0-387-29338-8).
- [11] Jiang, Liu, Huang, Zhang, Li, Gong, Shen, Liu, and Wu. Valley and band structure engineering of folded MoS2 bilayers. *Nature nanotechnology*, 2014. doi:[10.1038/nnano.2014.176](https://doi.org/10.1038/nnano.2014.176).
- [12] Shen. Surface properties probed by second-harmonic and sum-frequency generation. *Nature*, 1989. doi:[10.1038/337519a0](https://doi.org/10.1038/337519a0).
- [13] Chen, Shen, and Somorjai. Studies of polymer surfaces by sum frequency generation vibrational spectroscopy. *Annual review of physical chemistry*, 2002. doi:[10.1146/annurev.physchem.53.091801.115126](https://doi.org/10.1146/annurev.physchem.53.091801.115126).
- [14] Bonn, Ueba, and Wolf. Theory of sum-frequency generation spectroscopy of adsorbed molecules using the density matrix method - broadband vibrational sum-frequency generation and applications. *Journal of Physics: Condensed Matter*, 2005. doi:[10.1088/0953-8984/17/8/002](https://doi.org/10.1088/0953-8984/17/8/002).
- [15] Guyot-Sionnest, Hunt, and Shen. Sum-frequency vibrational spectroscopy of a Langmuir film: Study of molecular orientation of a two-dimensional system. *Physical Review Letters*, 1987. doi:[10.1103/PhysRevLett.59.1597](https://doi.org/10.1103/PhysRevLett.59.1597).

- [16] Zhang, Shen, and Somorjai. Studies of surface structures and compositions of polyethylene and polypropylene by IR+visible sum frequency vibrational spectroscopy. *Chemical Physics Letters*, 1997. doi:[10.1016/S0009-2614\(97\)01311-0](https://doi.org/10.1016/S0009-2614(97)01311-0).
- [17] van Hemmen, Heil, Klootwijk, Roozeboom, Hodson, van de Sanden, and Kessels. Plasma and Thermal ALD of  $\text{Al}_2\text{O}_3$  in a Commercial 200 mm ALD Reactor. *Journal of The Electrochemical Society*, 2007. doi:[10.1149/1.2737629](https://doi.org/10.1149/1.2737629).
- [18] Mackus, Garcia-Alonso, Knoops, Bol, and Kessels. Room-Temperature Atomic Layer Deposition of Platinum. *Chemistry of Materials*, 2013. doi:[10.1021/cm400274n](https://doi.org/10.1021/cm400274n).
- [19] Macco, van de Loo, and Kessels. Atomic Layer Deposition for High-Efficiency Crystalline Silicon Solar Cells. In Bachmann, editor, *Atomic Layer Deposition in Energy Conversion Applications*. Wiley-VCH Verlag GmbH & Co. KGaA, Weinheim, Germany, 2017. doi:[10.1002/9783527694822.ch2](https://doi.org/10.1002/9783527694822.ch2).
- [20] Hoex, Gielis, van de Sanden, and Kessels. On the c-Si surface passivation mechanism by the negative-charge-dielectric  $\text{Al}_2\text{O}_3$ . *Journal of Applied Physics*, 2008. doi:[10.1063/1.3021091](https://doi.org/10.1063/1.3021091).
- [21] Langereis, Creatore, Heil, van de Sanden, and Kessels. Plasma-assisted atomic layer deposition of  $\text{Al}_2\text{O}_3$  moisture permeation barriers on polymers. *Applied Physics Letters*, 2006. doi:[10.1063/1.2338776](https://doi.org/10.1063/1.2338776).
- [22] Langereis, Bouman, Keijmel, Heil, Van de Sanden, and Kessels. Plasma-assisted ALD of  $\text{Al}_2\text{O}_3$  at Low Temperatures: Reaction Mechanism and Material Properties. *ECS Transactions*, 2008. doi:[10.1149/1.2980000](https://doi.org/10.1149/1.2980000).
- [23] Ande, Knoops, de Peuter, van Drunen, Elliott, and Kessels. Role of Surface Termination in Atomic Layer Deposition of Silicon Nitride. *The Journal of Physical Chemistry Letters*, 2015. doi:[10.1021/acs.jpcllett.5b01596](https://doi.org/10.1021/acs.jpcllett.5b01596).
- [24] Knoops, Braeken, de Peuter, Potts, Haukka, Pore, and Kessels. Atomic Layer Deposition of Silicon Nitride from Bis(tert-butylamino)silane and  $\text{N}_2$  Plasma. *ACS Applied Materials & Interfaces*, 2015. doi:[10.1021/acsami.5b06833](https://doi.org/10.1021/acsami.5b06833).
- [25] Knoops, de Peuter, and Kessels. Redeposition in plasma-assisted atomic layer deposition: Silicon nitride film quality ruled by the gas residence time. *Applied Physics Letters*, 2015. doi:[10.1063/1.4926366](https://doi.org/10.1063/1.4926366).



# Principles of optical sum-frequency generation to study surface chemistry

## 2.1 Introduction

In this chapter a high level overview of the nonlinear optical process of sum-frequency generation (SFG) is given. The SFG process has many practical applications, however, the focus will be on the use of the SFG *process* as the basis of broadband sum-frequency generation (BB-SFG) *spectroscopy*. This chapter should elucidate how SFG spectroscopy can be used to investigate surface reactions, why it is excellently suited to study the surface chemistry ruling atomic layer deposition (ALD), and what sets it apart from other analysis techniques used in the field of ALD to study the surface chemistry. This chapter is by no means a comprehensive overview of nonlinear optics. For an in depth review of nonlinear optical processes the works by [Boyd](#), by [Heinz](#), and by [Shen](#) are highly recommended.<sup>1-3</sup>

This chapter is organized as follows: Section 2 discusses the relevant aspects of the SFG process for spectroscopy on a phenomenological level. Section 3 presents the conventional macroscopic description of the SFG process. Most of the statements made in Section 2 can be understood in the framework of the macroscopic description of the SFG process. Section 4 discusses what determines the spectral shape of the SFG response of a surface and/or a substrate. Several examples of SFG spectra will be shown and discussed. Section 5 describes the model used to reproduce SFG spectra. This model is used to identify and quantify the density of surface groups. To this end, the resonant contributions to the SFG spectra need to be understood, which requires a microscopic description of the SFG process. Section 6 concludes with the discussion of the modeling of a typical BB-SFG spectrum.

## 2.2 Phenomenological description of SFG

A phenomenological description of the key features of the SFG process are given in this section with the particular case of broadband sum-frequency generation (BB-SFG) spectroscopy in mind. This description highlights the merits and the drawbacks of BB-SFG spectroscopy as analysis techniques for in-situ studies of the surface chemistry during ALD. To place BB-SFG spectroscopy in the proper perspective, an overview is given of the analysis techniques most often used to study the surface chemistry during ALD.

The SFG process is a second order nonlinear optical process where two optical electromagnetic (EM) fields with different photon energies,  $\hbar\omega_1$  and  $\hbar\omega_2$ , interact with a material. These two fields induce a polarization of the material with angular velocity  $\omega_3 = \omega_1 + \omega_2$ . This induced polarization generates a new EM-field with photon energy  $\hbar\omega_3$ . Both the *interaction or mixing* of two optical EM-fields and the *generation of a new* EM-field are characteristic for nonlinear optics.

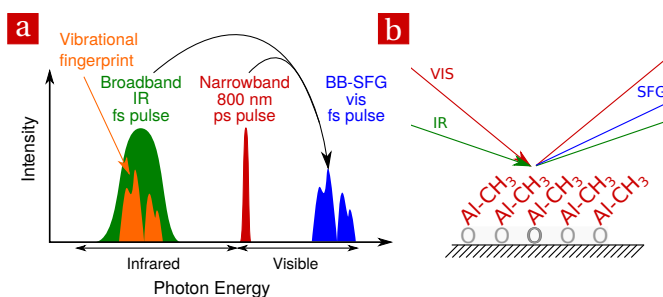


**Figure 2.1:** (a) In BB-SFG spectroscopy a spectrally narrow visible beam and a spectrally broad infrared beam interact simultaneously with the surface groups. The two beams mix at the surface and result in a new signal at the sum-frequency of the two driving beams, i.e. the BB-SFG signal. The mixing is resonantly enhanced by vibrational transitions of surface groups. Therefore, the BB-SFG signal contains the vibrational information in the visible part of the spectrum. (b) An illustration of the geometric arrangement of the different beams with respect to the surface.

In *vibrational* BB-SFG spectroscopy, the mixing of a spectrally narrow visible and spectrally broad mid-IR pulse are used to study the surface groups as is illustrated in Fig. 2.1 (a). Figure 2.1 (b) shows the geometric arrangement of the beams used in this work which is a non-collinear arrangement of the beams. The BB-SFG signal is resonantly enhanced when the infrared light excites a vibrational transition of the surface groups. The resonant enhancement of the SFG process by a vibrational transition is analogous to what occurs in linear optics. In linear optics, the coupling between an external EM field and the induced polarization in the material becomes particularly strong if the energy of the photons matches the energy of an optical transition of the

material. This leads to, for example, the strong absorption of light at specific energies which is the basis of absorption spectroscopy. Similarly, in the SFG process the interaction between the mid-IR photon and the surface groups becomes particularly strong if the energy of the mid-IR photon is close to an allowed optical transition, i.e. when the process is resonant. However, even the resonantly enhanced signals are typically extremely weak compared to the two driving fields (the figure is not to scale).

An energy diagram of the SFG process is given in Fig. 2.2, illustrating both the resonant (thick arrows) and the non-resonant case (thin arrows). When the mid-IR photon matches the energy of a vibrational transition, the signal is resonantly enhanced. In BB-SFG spectroscopy, the surface groups are exposed to photons with a range of energies in the mid-IR part of the spectrum. In essence, a series of parallel SFG processes occurs using different mid-IR photons, resulting in a series of SFG signals. Some of these parallel SFG signals are much stronger due to the resonant enhancement, resulting in a response such as is shown in Fig. 2.1.

The identification of surface species is crucial to the successful application of BB-SFG spectroscopy. In vibrational spectroscopy, surface groups are identified by the (mostly unique) energy of their vibrational transitions. Figure 2.1 illustrates how the detected BB-SFG signal at  $\hbar\omega_{SFG}$  is associated to the mid-IR response where the vibrational transitions are situated. It is convenient to make the association of the detected SFG signal with the mid-IR part of the spectrum more explicit when representing the data. Therefore, the BB-SFG signal detected in the visible part of the spectrum is transformed back to the mid-IR domain. The relation between the SFG signal at  $\hbar\omega_{SFG}$  and the driving visible and mid-IR fields,  $\hbar\omega_{vis}$  and  $\hbar\omega_{IR}$  respectively, is given by  $\hbar\omega_{SFG} = \hbar\omega_{vis} + \hbar\omega_{IR}$ . Subtracting the photon energy of the visible photon (typically 800 nm = 1.55 eV) from the photon energy of the detected signal (ranging from 620 nm = 2 eV up to 650 nm = 1.9 eV) yields the photon energy of the associated mid-IR signal. The conventional quantity for photon energy in vibrational spectroscopy is expressed in “wavenumbers” with units  $\text{cm}^{-1}$ . The spectral width of the visible signal and any uncertainty in the position of the visible signal leads to the uncertainty in the absolute value of the position of a peak in the mid-IR. For example, a uncertainty of  $\sim 1$  nm in the visible beam results in a uncertainty of  $12 \text{ cm}^{-1}$  in the region of interest. Determining the absolute spectral position with sub  $\text{cm}^{-1}$  resolution with BB-SFG is difficult at best.

A key feature of the SFG process is its *inherent* surface selectivity on centrosymmetric substrates such as *c*-Si and amorphous materials. This is caused by the optical selection rules which are quite restrictive for second-order non-linear optical process. It turns out that the SFG process is forbidden at a site with inversion symmetry (in the dipole approximation). Inversion symmetry means that for each atom at coordinate  $(x, y, z)$  there is an identical one at  $(-x, -y, -z)$ . Therefore, “nothing” changes when an inversion operation is applied. Inversion symmetry can occur on a microscopic scale by the arrangement of atoms in a crystal. For example, *c*-Si is an centrosymmetric material

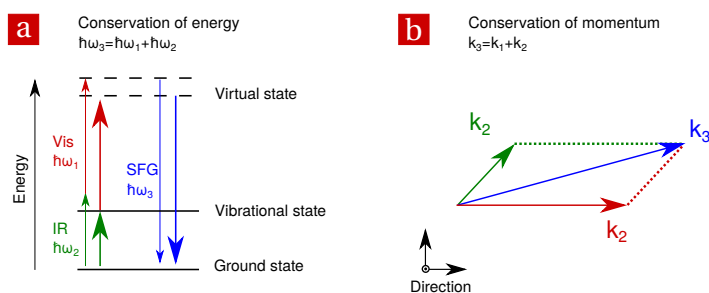


**Figure 2.2:** (a) The energy of the photon generated by the SFG process ( $E = \hbar\omega_3 = \hbar\omega_1 + \hbar\omega_2$ ) is determined by conservation of energy. The visible and IR photon interacting with the system are annihilated and a new photon with the combined energy is generated. The coupling of the mid-IR light with the system is greatly enhanced when the photon energy of the IR photon matches a vibrational transition of the system. This results in a much stronger SFG signal (indicated by the thicker arrow). (b) Conservation of momentum determines the direction of the EM field generated by the SFG process.

which means that it has inversion symmetry. Inversion symmetry can also arise if the material has no long range structure. For example, amorphous solid, gases, and liquids in general have inversion symmetry even though their microscopic structure might not possess inversion symmetry. For SFG spectroscopy on centrosymmetric materials, this means that there will be no bulk contribution. On the other hand, at an interface the inversion symmetry is always broken which gives rise to a SFG signal from the interface, making the SFG process surface selective for centrosymmetric materials.

The description so far has focused on the photon energy of the EM field produced by the SFG process. The directionality of the EM field generated by the SFG process is another aspect that has to be addressed. The direction of the generated SFG beam is determined by conservation of momentum ( $\vec{p} = \hbar\vec{k} = \hbar\omega\vec{c}^{-1}$  for a photon). The generated beam propagates in the direction determined by the vector sum of the momenta of the two driving beams, see Fig. 2.2 (b). For SFG spectroscopy in a non-collinear geometry, this implies that the SFG beam is non-collinear with either of the two driving fields.

Several of the unique properties of the SFG process can be exploited in BB-SFG spectroscopy for studying surface groups and surface chemistry. The interface selectivity ensures that the SFG signal only originates from the surface (groups). Using SFG spectroscopy, a surface can be characterized in a single measurement instead of the two measurements needed in differential techniques (see also panel “Comparing BB-SFG with FTIR spectroscopy”). Moreover, SFG spectroscopy is not affected by changes in the bulk of a material or other environmental factors. It can be performed in vacuum, at ambient pressure, or while the temperature of the sample is changing. For the detection

### Comparing BB-SFG with FTIR spectroscopy

Fourier Transform Infrared (FTIR) absorption spectroscopy is regularly used to study the surface chemistry of ALD. The data obtained by FTIR spectroscopy appears to be quite similar to the data obtained by BB-SFG spectroscopy. However, there is a subtle but important difference between the *inherently* surface selective measurements with BB-SFG spectroscopy and measurements with FTIR absorption spectroscopy.

In FTIR spectroscopy, the small differences in absorption (typically < 1%) due to a changes in the surface groups during ALD are often measured using differential spectra. A transmission spectrum is measured before and after such a change. By subtracting the two spectra, the change in absorption is calculated and the resulting spectrum is called a “difference spectrum”. This procedure eliminates the influence of the unknown and relatively large absorption of other elements in the beam path such as the substrate and the reactor windows. This procedure also eliminates the influence of the unknown intensity of the light source and spectral response of the detector. In BB-SFG spectroscopy, only surface groups can generate a signal and other elements do not significantly influence the results. Furthermore, this signal is background free and therefore a differential measurement is not needed.

Because FTIR is often used in the field of ALD and the results appear to be quite similar, it is insightful to examine in more detail how the two techniques differ. To illustrate this, consider an “ideal” measurement where the surface groups are the only element interacting with the light beam(s). Moreover, the surface groups are only interacting at a well-defined photon energy  $E_s$ , resulting in absorption and SFG mixing. For FTIR spectroscopy, this means that the transmission of the light is attenuated at  $E_s$  if the specific surface groups are present. However, to interpret if there was absorption or not, knowledge of the signal strength before any surface groups were present is required. For the same reason, a subsequent decrease in intensity can only be interpreted/quantified if the intensity before the presence of any surface groups is known. For BB-SFG spectroscopy, the measured signal is directly proportional to the square of the density of the surface groups. So in this case, detection of the SFG photons with energy  $E_s$  is a direct indication of the presence of the surface groups. A subsequent change in the signal strength indicates a quantifiable increase in the number of these surface groups.

In practice, the above means that for a differential technique there has to be *a priori* knowledge and/or several assumptions have to be made to interpret the data, which is not the case for BB-SFG spectroscopy. In most situations, the same information can be measured with both techniques with carefully designed experiments. However, unexpected effects might be obscured in FTIR spectroscopy while they might be revealed with BB-SFG spectroscopy. Apart from that, both techniques have their own strengths and applications.



of the SFG signal it is beneficial that the SFG signal is situated at a different photon energy than either of the driving fields. The SFG photon energy is, to a large extent, determined by the photon energy of the visible beam in the SFG process. An appropriate choice of the photon energy of the visible beam allows the use of highly sensitive spectral detectors which are only available for visible light. Moreover, the SFG signal has a different directionality than the two driving fields due to conservation of momentum. This difference in directionality can be exploited to separate the weak SFG beam from the much stronger driving beams. Due to the conservation of momentum and the collimated nature of the two driving laser beams, the SFG beam is also collimated. The collimated nature of the SFG signal greatly facilitates in-situ spectroscopy. It is difficult to collect a large space angle of light when the source is inside a vacuum chamber far away from the detector or collimating optics. Because of the collimated nature of the SFG beam, it only occupies a small space angle, which allows all the SFG light to be collected. All these features are beneficial when detecting the BB-SFG signal. However, only under these rather ideal conditions is it possible to detect the extremely weak BB-SFG signals.

To place BB-SFG spectroscopy in the proper perspective it should be compared to other in-situ analysis techniques used in the field of ALD. Identifying and quantifying surface groups is key in studying and understanding surface chemistry of an ALD process. Several capabilities are desirable when studying surface chemistry of ALD:

- Identification of the structure of the surface groups.
- Quantification the areal density of the surface groups.
- Identification of the elements in the grown film.
- Sub-monolayer sensitivity.
- Relatively fast acquisition time.
- Surface selectivity, preferably inherent to the analysis techniques.
- Applicable in a wide range of environments such as varying pressure and temperature.
- Applicable to a wide range of substrates.
- Directly interpretable results, i.e. without the need for modeling.

A brief description of analysis techniques commonly used in the field of ALD is given in Table 2.1. The strengths of each of these techniques are highlighted. A more in depth explanation can be found in the references given for each technique. Table 2.2 shows an overview of how well these techniques meet the requirements stated above. From this table it is clear that BB-SFG spectroscopy has several unique properties, such as its inherent interface selectivity and its wide range applicability, which are complementary to other analysis techniques used in the field of ALD.

**Table 2.1:** An overview of the key features of the in-situ analysis techniques used in the field of ALD to study the surface chemistry during of the ALD process.

Name	Description
SE	Spectroscopic ellipsometry measures the (relative) phase and intensity change of light reflecting off a surface. Fitting these data to a model of linear optics allows the determination of linear optical properties such as the complex refractive index and film thickness of thin films. <sup>4,5</sup>
FTIR	Fourier transform infrared spectroscopy measures the absorption of IR light due to vibrational transitions of molecules in the gas-phase, of solids, and of surface groups. This allows the identification and quantification of the chemical structure of (parts of) the molecules. <sup>6-8</sup>
XPS	X-ray photoelectron spectroscopy probes the (mainly) electronic transitions of core electrons. The unique energy of these transitions is used for elemental identification, with in some cases, information on chemical bonding. <sup>9</sup>
QCM	Quartz-crystal microbalance measures the change of the resonance frequency of a quartz crystal due to deposited material on the crystal. This change in frequency is related to the change in mass. If the mass change can be related to a specific surface group (i.e. when the surface chemistry is already known to some extent) this allows the quantification of the areal density of surface groups. <sup>10,11</sup>
QMS	Quadrupole mass spectrometry measures the concentration of gas-phase molecules. The gas-phase molecules are ionized and filtered by their mass to charge ratio. The identity and concentration of gas-phase precursors and reaction products can be studied with this technique. <sup>10,11</sup>

**Table 2.2:** High level overview of key properties of various analysis techniques used to study the surface chemistry of ALD. A not, partially, or fully met criterion is indicated by -, 0, and + respectively. The techniques and their capabilities are also discussed in the text.

	identifies elements	identify ligands	quantify ligands	sub-monolayer sensitivity	surface selectivity	environment independent	substrate flexibility	direct interpretation
BB-SFG	0	+	+	+	+	+	+	+
SE	-	-	-	+	0	+	+	-
FTIR	0	+	+	+	0	0	-	+
XPS	+	0	-	+	+	-	+	+
QCM	-	0	0	0	0	-	0	-
QMS	0	+	0	-	-	0	0	+

## 2.3 Macroscopic model of SFG

The appearance of nonlinear optical effects can be described with the classical EM theory. The electrical field of an EM wave,  $\vec{E}$ , causes a polarization  $\vec{P}$  in matter. The polarization of the matter is a (generally unknown) function of  $\vec{E}$ . This function,  $\vec{P}(\vec{E}) = \vec{f}(\vec{E})$ , can be written as a Taylor series,

$$\vec{P}(\vec{E}) = \underbrace{\vec{P}^{(1)}(\vec{E})}_{\text{Linear optics}} + \underbrace{\vec{P}^{(2)}(\vec{E}, \vec{E})}_{\text{second order optical effects}} + \text{higher orders} \quad (2.1)$$

$$= \epsilon_0(\bar{\chi} : \vec{E}) + \bar{\chi} : \vec{E} \vec{E} + \dots \quad (2.2)$$

Where  $\bar{\chi}$  is the tensor representing the linear term of the function describing how the material polarizes due to the applied electric field. The  $\bar{\chi}$  tensor represents the second-order term of the function describing the polarization of the material due to the external electric field. Both the linear and the second-order susceptibility,  $\bar{\chi}$  and  $\bar{\chi}$ , are material properties and both vary with photon energy but have different units (dimensionless and  $m/V$  respectively). For relatively weak external fields, the magnitude of the first term dominates over the second and higher order terms. Therefore, the response of the material is accurately described by the linear optical response of materials. When the external electric field becomes stronger, the higher order terms start to play an role and lead to detectable signals. To be more precise, the first order and second order terms are roughly equal when the electrical component of the external EM field is in the same order of magnitude as the atomic electric field ( $E_{at} = 5 \times 10^{11} \text{ V/m}$ ).<sup>1</sup>

So far, nothing has been assumed about the frequency of the external electric field. In general, the external electric field  $\vec{E}$  can be written as a superposition of harmonic signals,

$$\vec{E} = \sum_n \vec{A}_n \exp(i\vec{k}_n \cdot \vec{r} - i\omega_n t) + c.c. \quad (2.3)$$

For the linear term in Eq. (2.2), a term of the electric field  $\vec{E}$  with angular velocity  $\omega$  generates a polarization term in  $\vec{P}$  with angular velocity  $\omega$ . On the other hand, the same electric field with angular velocity  $\omega$  generates a polarization with angular velocity  $2\omega$  due to the second order term in Eq. (2.2), i.e.  $\bar{\chi} : \vec{E} \vec{E}$ . This is the process of “second-harmonic generation” (SHG). Moreover, the terms of the external electric field with different angular velocity can start to interact. For two terms with different angular velocity,  $\omega_1$  and  $\omega_2$ , a new term appears due to the second term in Eq. (2.2) with angular velocity  $\omega_1 + \omega_2$  which is the “sum-frequency generation” (SFG) component. Also a term with angular velocity  $\omega_1 - \omega_2$  appears which is the “difference frequency generation” (DFG) component. The polarization produced by each of these second order processes can be described by,

$$\vec{P}(\hbar\omega_3) = \epsilon_0 \bar{\chi} : \vec{E}(\hbar\omega_1) \vec{E}(\hbar\omega_2), \quad (2.4)$$

where the tensor  $\bar{\chi}$  is different for each of the nonlinear processes. In this equation  $\bar{\chi}$  is a tensor with 27 elements describing the nonlinear susceptibility of the material for a specific combination of spatial components of the driving and resulting electric field. This can be made more explicit by writing down the equation for the  $i$  component (e.g. the component in the  $x$  direction) of the polarization caused by the  $j$  component of the  $\omega_1$  electric field and the  $k$  component of the  $\omega_2$  electric field. The polarization is now given by,

$$P_i(\hbar\omega_3) = \epsilon_0 \bar{\chi}_{ijk}(\hbar\omega_3, \hbar\omega_1, \hbar\omega_2) E_j(\hbar\omega_1) E_k(\hbar\omega_2). \quad (2.5)$$

Once the polarization  $\vec{P}(\hbar\omega_3)$  is known, it is possible to calculate the amount of emitted light. The radiation characteristics of an ensemble of dipoles is described by **Born and Wolf**.<sup>12</sup> However, for our purposes it is sufficient to conclude that the strength of the emitted electric field is proportional the strength of the polarization.

At this point, it is possible to show that the SFG process cannot occur at a site with inversion symmetry. The tensor  $\bar{\chi}$  has to have the same symmetry as the material following the Neumann principle.<sup>13</sup> For a site with inversion symmetry, the tensor should also be invariant to this transformation. So the tensor  $\bar{\chi}$  before and the tensor  $\bar{\chi}^*$  after inversion have to be equal. Although (indistinguishable) atoms are swapped, the arrangement and position of the atoms in the crystal remains the same. Applying the inversion transformation on the tensor turns out to be simply a multiplication with  $-1^3$  because the elements of the tensor transform as  $\hat{e}_i \cdot \hat{e}_j \cdot \hat{e}_k \rightarrow -\hat{e}_i \cdot -\hat{e}_j \cdot -\hat{e}_k$ . So for each tensor element it has to hold that,

$$\bar{\chi}_{ijk} = \bar{\chi}_{ijk}^* = -1^3 \cdot \bar{\chi}_{ijk}. \quad (2.6)$$

For this equation to hold, each of the tensor elements has to be zero. The driving fields cannot generate a second order nonlinear polarization and therefore the SFG process does not occur (or in other words no net polarization/EM field is produced). In this derivation, only dipoles were considered as possible sources of SFG light. If quadrupoles (e.g. related to a  $\vec{E}\nabla\vec{E}$  term, related to the variation of the strength of the electric field over an atomic length scale) play an role, this statement is no longer valid in general. The quadrupoles can generate a bulk contribution in a centrosymmetric material. For second-harmonic generation (SHG), it has been shown that these terms are minute but detectable and do play a (minor) role for the nonresonant background of  $c$ -Si.<sup>2,14</sup> If the quadrupole contributions are also present in the SFG response, their influence is small.

An interface or more specifically a surface is inherently different from the bulk from a material since it cannot have inversion symmetry. The different symmetry constraints at a surface have several implications for the tensor describing the SFG process. In the direction perpendicular to the surface, the symmetry is broken. Assuming that the surface is isotropic, which is often the case, and with the normal of the plane pointing towards  $\hat{e}_z$ , it can be shown that only tensor elements which have 1 or 3  $e_z$  elements are non-zero.

Moreover, several of the tensor components are related by symmetry. For example, a 90 degree rotation around the surface normal leaves the system unchanged so  $\bar{\chi}_{zxx} = \bar{\chi}_{zyy}$ . Table 2.3 lists the unique tensor elements accessed by the polarization combinations used in BB-SFG spectroscopy of a surface.<sup>2</sup> The standard convention for the notation of the polarization combinations is followed here:  $Xyz$  stands for  $X$  polarized SFG light driven by  $y$  polarized visible light and  $z$  polarized mid-IR light (the first letter is not capitalized in equations).

**Table 2.3:** Nonzero tensor elements for different polarization combinations in BB-SFG and SFG spectroscopy of an isotropic surface normal to  $\hat{e}_z$ . Note that due to the symmetry the  $x$  component can be exchanged for  $y$ , so  $\bar{\chi}_{zxx} = \bar{\chi}_{zyy}$ .

Polarization	Tensor Elements	Polarization	Tensor Elements
Ppp	$\bar{\chi}_{zzz}, \bar{\chi}_{xxz}, \bar{\chi}_{xzx}, \bar{\chi}_{zxx}$	Spp	$\bar{\chi}_{xxz}, \bar{\chi}_{xzx}$
Psp	$\bar{\chi}_{xxz}, \bar{\chi}_{zxx}$	Ssp	$\bar{\chi}_{xxz}$
Pps	$\bar{\chi}_{xxz}$	Sps	$\bar{\chi}_{xzx}$
Pss	$\bar{\chi}_{zxx}$	Sss	-

## 2.4 Spectral shape of a SFG signal

The spectral shape of the SFG response of a material depends on several factors. To a large part the response is determined by the nonlinear susceptibility,  $\bar{\chi}$ , of the material. Measuring this nonlinear susceptibility is the primary goal of BB-SFG spectroscopy. However, the spectral shape of the SFG signal also depends on the spectral shape of the driving EM fields. It can also be influenced by linear optical effects when the refractive index of the materials varies over the spectral range that is being probed.<sup>15</sup> These (linear optical) effects can be accurately described by the model proposed by Sipe.<sup>16</sup> Moreover, in most cases the materials deposited by ALD do not show any such effects. On the other hand, the influence of thickness on the linear optics are exploited to enhance the signal, which is described in more detail in Chapter 4.

The starting point for describing the spectral shape of the BB-SFG signal is Eq. (2.4). This equation describes the SFG response due to two driving EM fields, each with a discrete angular velocity, i.e. photon energy. In BB-SFG the two driving beams do not have discrete photon energies, see Fig. 2.1, and both beams cover a range of photon energies. In that case, multiple combinations of  $\hbar\omega_1$  and  $\hbar\omega_2$  result in a SFG signal with photon energy  $\hbar\omega_3$ . For example, a SFG signal at 1.9 eV could be generated by: (a) A combination of a driving beams at 1.0 eV and 0.9 eV. (b) But also by a combination of a driving beams at 1.8 eV and 0.1 eV. The SFG response of the material,  $\bar{\chi}$  can differ for scenario (a) and (b). The SFG signal detected at photon energy  $\hbar\omega_3$  can be written as

the sum (integral) over all possible combination of driving fields  $E_{vis}$  and  $E_{ir}$ ,

$$P(\hbar\omega_3) = \epsilon_0 \int_0^\infty d\omega [\bar{\chi}(\hbar\omega_3, \hbar\omega, \hbar(\omega_3 - \omega)) : \vec{E}_{vis}(\hbar\omega), \vec{E}_{ir}(\hbar(\omega_3 - \omega))]. \quad (2.7)$$

This expression allows the identification of several relevant limiting cases:

1. When  $\bar{\chi}$  is independent of photon energy, the result of the integral is simply the convolution of the two driving electric fields.
2. When both driving fields are spectrally narrow (e.g. a delta function  $E(\omega) = \delta(\omega - \omega_{central})$ ), the spectral shape of the SFG signal holds no information. The intensity is determined by the amplitude of  $\bar{\chi}$  and the strength of the driving fields  $E_{vis}$  and  $E_{ir}$ . This is used in “narrowband” SFG spectroscopy.
3. When the  $E_{vis}$  is spectrally narrow and  $E_{ir}$  is spectrally broad, the shape of the SFG signal is determined by the spectral shape of the nonlinear response of the material  $\bar{\chi}$  and the spectral shape of the  $E_{ir}$  field. This is used in BB-SFG spectroscopy.

The other two extremes ( $E_{vis}$  broad,  $E_{ir}$  narrow and both  $E_{vis}$  and  $E_{ir}$  spectrally broad) are typically not used for spectroscopy.

The goal of both “narrowband” SFG (case (2)) and BB-SFG (case (3)) vibrational spectroscopy is to probe the  $\bar{\chi}$  tensor in the mid-IR part of the spectrum. Comparing case (2) and (3) highlights the difference in how this spectral information is acquired: For “narrowband” SFG spectroscopy, the spectral response of  $\bar{\chi}$  tensor is encoded in how the SFG signal strength varies while scanning the driving IR wavelength. With BB-SFG spectroscopy the spectral information of  $\bar{\chi}$  is “directly” represented in the spectral response of the SFG process.

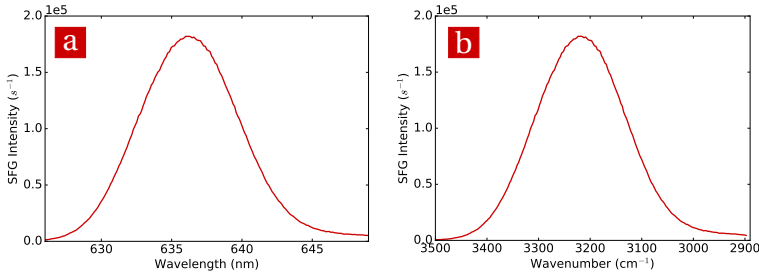
Two types of contributions in  $\bar{\chi}$  can be distinguished: resonant and non-resonant contributions. The resonant contributions have a rapidly varying phase and intensity as a function of photon energy. The non-resonant contribution has a constant (or slowly varying) phase and intensity with photon energy. Examples of both cases will be discussed in the following subsections.

### Non-resonant response in BB-SFG spectra

The non-resonant SFG response of a material, i.e. probed far away from any optically accessible resonances, is spectrally flat. The phase and intensity do not vary (significantly) as a function of photon energy. Although the response is not resonantly enhanced, it can be rather strong for non-centrosymmetric materials. Examples of materials with a strong non-resonant contribution (*c*-GaAs) and a weak non-resonant contribution (*c*-Si) will be discussed.

In the crystalline phase, GaAs is known for its large nonlinear response.<sup>17,18</sup> The SFG process is allowed in the bulk of the material due to the specific crystal structure of GaAs (zincblende,  $F\bar{4}3m$ ) which lacks a center of inversion. The

nonlinear response of the material is expected to be relatively wavelength independent: The 1.42 eV direct band-gap of GaAs is below both the visible signal (1.55 eV) and the SFG signal (1.95 eV, depending on the photon energy of the mid-IR signal) used in the experiment and neither are they close to other optical transitions. There are no resonances present in the spectral range covered by the infrared signal. So neither the visible, the mid-IR, nor the SFG signal can be resonant when changing the wavelength of the mid-IR beam.



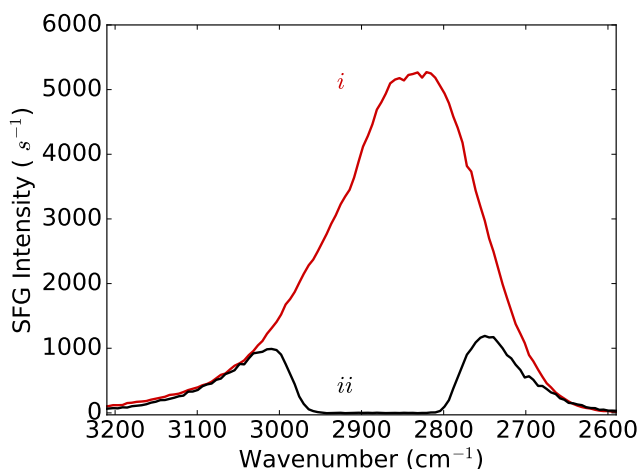
**Figure 2.3:** The measured non-resonant BB-SFG response of a GaAs substrate to 3.2  $\mu\text{m}$  and 800 nm light. This Ppp spectrum was acquired in 100 ms. **(a)** The data as detected. **(b)** The mid-IR part of the spectrum associated with the generated BB-SFG signal. Especially in the case of resonances, representation **(b)** facilitates the interpretation of the spectrum.

Figure 2.3 shows a typical BB-SFG spectrum of a GaAs substrate recorded for Ppp polarization. In this case a spectrally narrow 800 nm beam and a spectrally broad 3.2  $\mu\text{m}$  were used to generate the BB-SFG signal. The BB-SFG signal is indeed detected at the expected wavelength of 635 nm corresponding to 1.95 eV photons matching the sum of photon energy of the two driving beams being 1.55 eV + 0.3 eV. As can be seen in Fig. 2.3 (a) the BB-SFG signal is situated in the visible part of the spectrum. This response observed in the visible part of the spectrum is associated to the response of the material in the mid-IR part of the spectrum. Since the visible beam is spectrally narrow, the spectral shape is due to a combination of the shape of the mid-IR beam and the nonlinear response of GaAs in the probed mid-IR region. Because the response of GaAs is known to be spectrally flat in this region, the shape is mainly due to the spectral shape of the mid-IR beam. Figure 2.3(b) shows the same spectrum after the conversion from detection wavelength to the mid-IR part of the spectrum associated with the response. The spectral shape shown in Fig. 2.3 is a typical example of a non-resonant signal in BB-SFG spectroscopy. For GaAs, a significant part of the nonresonant signal is generated in the bulk of the material. The amount of light generated in the bulk is only limited by the penetration and escape depth of the light and phase matching.

To demonstrate that the BB-SFG signal is indeed related to the mid-IR part of the spectrum, a polyethylene (PE) film is inserted into the mid-IR beam.



Note that this does not probe the nonlinear response of PE; the PE film simply absorbs some of the mid-IR light. The well defined absorption lines of the PE polymer influence the shape of the mid-IR signal. This results in a dip in the spectral shape of the mid-IR beam around  $2900\text{ cm}^{-1}$ . This specific absorption line is caused by the C-H stretch mode of the PE polymer.<sup>19</sup> The mid-IR signal (with the dip) and the visible signal mix on GaAs. As before, the measured spectral shape is that of the mid-IR beam. Figure 2.4 shows the spectra before (*i*) and after (*ii*) insertion of a PE film into the beam path. The expected dip is indeed observed. This shows that the spectral shape of the mid-IR beam is reproduced in the BB-SFG spectrum. More importantly, it shows that the BB-SFG signal is indeed associated with the mid-IR region.



**Figure 2.4:** The BB-SFG response of the GaAs substrate show in spectrum *i* mixing an unaltered mid-IR beam with the narrow visible beam. By inserting a PE film in the mid-IR beam before the sample, parts of the mid-IR beam are absorbed by the PE film. This changes the shape of the mid-IR beam causing the large dip. The visible signals and the mid-IR signal with the dip in its spectral shape are mixed by the GaAs, resulting in a BB-SFG spectrum *ii* with a similar dip. Especially the C-H stretch modes around  $2900\text{ cm}^{-1}$  absorb strongly.

For a centrosymmetric material such as *c*-Si (diamond cubic,  $Fd\bar{3}m$ ), the nonresonant signal is much weaker than that of GaAs. The strong bulk dipole contribution is not present and only a surface contribution is allowed in the bulk dipole approximation for *c*-Si. A spectrum of the nonresonant signal generated by *c*-Si is shown in Fig. 2.5 for the Ppp polarization combination. As expected, the peak shape and width are comparable to the signal observed from GaAs, however, the signal of the *c*-Si is significantly weaker than that of GaAs.

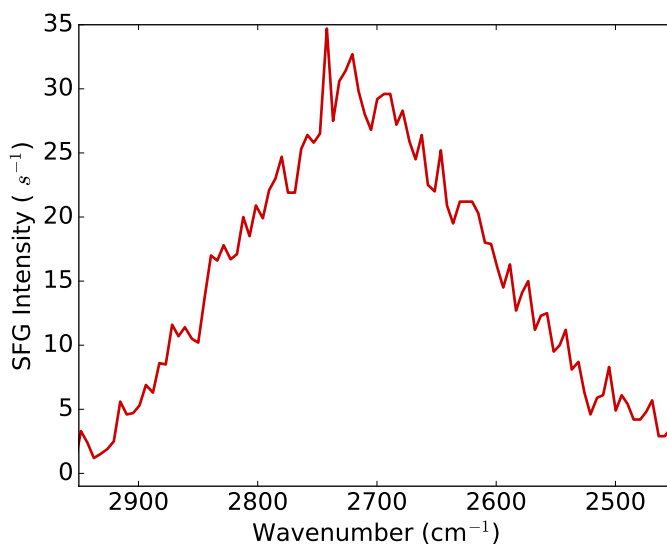


**Figure 2.5:** The nonresonant BB-SFG signal of a Si(100) with a 30 nm ALD grown  $\text{Al}_2\text{O}_3$  film on top.

### Resonant response in BB-SFG spectra

The SFG response of a material probed around an optical transition, i.e. a resonant contributions, shows a strong variation in phase and intensity with photon energy. Two examples of surfaces with surface groups which exhibit such resonances will be discussed: (A) The hydrogen terminated Si(111) surface probing the Si-H stretch mode. (B) The surface of poly(methyl methacrylate) (PMMA) terminated with  $-\text{CH}_3$  and  $\text{CH}_2$  groups of which the C-H stretch modes were probed.

A hydrogen terminated Si(111) surface (H/Si(111)) is nearly atomically smooth and defect free when prepared with wet chemistry.<sup>20</sup> As a result of the ideality of the surface the Si-H stretch mode of the Si-H surface groups is spectrally narrow and intense. The H/Si(111) surface has been studied intensively with a range of analysis techniques including FTIR absorption spectroscopy, SHG spectroscopy, and SFG spectroscopy.<sup>21–25</sup> A BB-SFG spectrum of the Si-H stretch can be seen in Fig. 2.6, showing the strong and narrow peak typical for this surface (the fit in the figure will be discussed later). The full width half maximum (FWHM) observed with FTIR absorption spectroscopy is  $\sim 0.95 \text{ cm}^{-1}$ . This rules out that the width observed in the BB-SFG spectrum is due to the resonance itself. The observed shape is related to the spectral shape of the visible beam. The spectral FWHM of the visible beam of  $\sim 1 \text{ nm}$ , used in this experiment, corresponds to the observed FWHM in the spectrum. In other words the spectral shape is entirely due to instrumental broadening predominantly caused by the spectral width of the visible beam. The ampli-

tude of the peak is related to the number of Si-H groups on the surface. To demonstrate this, the pristine surface is exposed to vapor phase trimethylaluminum (TMA,  $\text{Al}(\text{CH}_3)_3$ ). TMA reacts with the Si-H groups, breaking the Si-H bond and thereby removing the Si-H surface group. The first exposure of TMA results in the middle spectrum in Fig. 2.6 showing a decrease in peak height. The second dose removed all the groups and only the non-resonant contribution of the Si(111) remains. Note that the strength of the non-resonant contribution cannot be compared to Fig. 2.5 as it depends on the polarization combination (here Ssp), the type and doping of the *c*-Si itself, and the timing between the visible and mid-IR pulse.<sup>26,27</sup>

The PMMA surface is the second example of a surface with a resonant contribution in the BB-SFG response. The surface of PMMA is an ideal test case for the BB-SFG setup aimed at studying the surface chemistry during ALD. The surface groups ( $-\text{CH}_3$  and  $-\text{CH}_2$  groups) of PMMA have a strong SFG response.<sup>28-32</sup> Moreover, these groups are similar to the surface groups which occur during the surface chemistry of ALD using metal-organic precursors. Figure 2.7 shows a typical spectrum of a 90 nm PMMA film on *c*-Si prepared by spin coating. The symmetric C-H stretch mode of the  $-\text{CH}_3$  groups dominates the spectrum.<sup>29,32-35</sup> Other C-H stretch modes of the PMMA film can be detected by tuning the mid-IR beam; however, they are much weaker. Figure 2.8 shows a BB-SFG spectrum recorded of a PMMA sample with the mid-IR beam tuned to excite the C-H stretch of the  $\text{CH}_2$  groups which is located at  $\sim 2800 \text{ cm}^{-1}$ . Due to the large cross section of the symmetric stretch, the  $2950 \text{ cm}^{-1}$  peak is still visible. By blocking either the visible beam or the mid-IR beam, it was demonstrated that the measured signals indeed originate from a mixing of the visible and mid-IR beam.

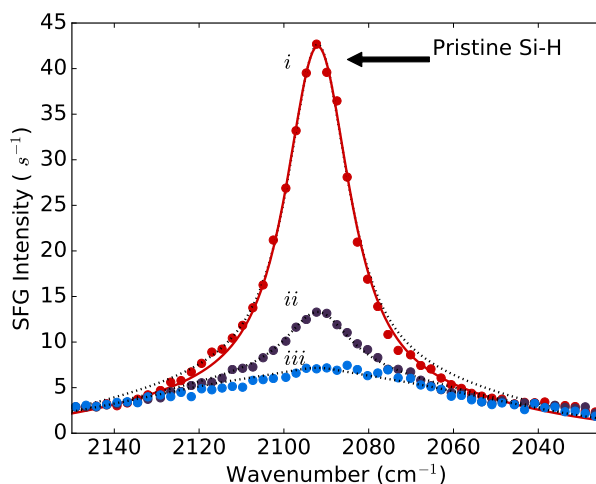


**Figure 2.6:** The measured BB-SFG spectrum (markers) for different coverages of Si-H and the fit of the model to the data (dashed line). The overshoot of the fit for the resonant contribution in the wings of the spectra is due to the spectral profile of the mid-IR beam. For the spectrum with the highest Si-H coverage, an alternative model takes this into account and shows a minor improvement in the reproduction of the data (solid line).

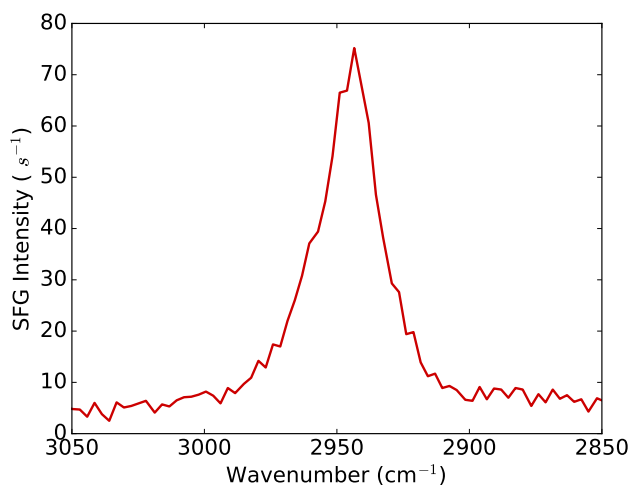


**Figure 2.7:** The BB-SFG response using the Ssp polarization combination of the PMMA surface of a 90 nm PMMA film spin coated on *c*-Si. The C-H stretch mode of the  $-\text{CH}_3$  groups is clearly observed.

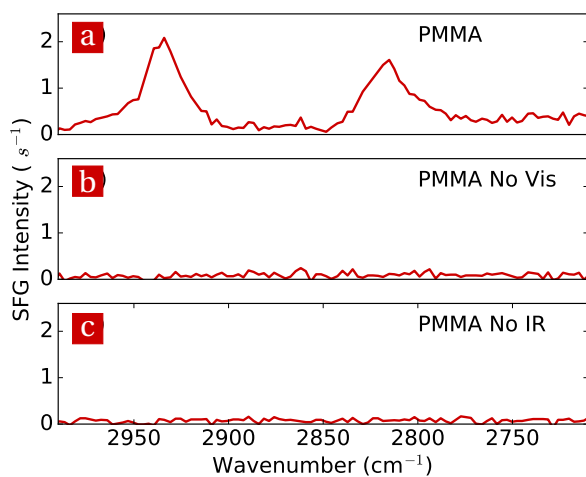


**Figure 2.8:** (a) The BB-SFG response of a 90 nm PMMA film spin coated on *c*-Si for the Ssp polarization combination with the IR beam tuned to show the 2800 cm<sup>-1</sup> resonance of CH<sub>2</sub> groups next to the C-H stretch mode of the -CH<sub>3</sub> groups. (b) and (c) show the spectra recorded with either the visible or the mid-IR beam blocked, demonstrating that the recorded signal is indeed the result of the mixing of the visible and mid-IR beam.

## 2.5 Microscopic description and modeling BB-SFG spectra

A microscopic model of the SFG process yields insight in how the process works. Moreover, it is the justification of the line shape which is used to model the BB-SFG spectra. With this model, the (relative) densities of the surface groups can be determined. First the microscopic model is described focusing on the resulting line shape. This is followed by a discussion of the model used to fit the BB-SFG spectra. To illustrate the fitting procedure an example is discussed.

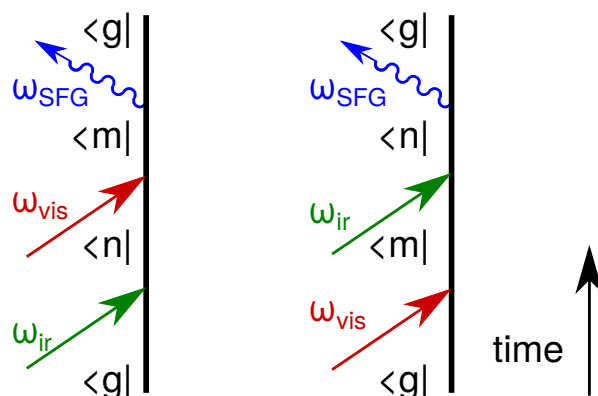


**Figure 2.9:** Two Feynman diagrams associated with the SFG process starting in the ground state  $\langle g |$ . The diagram shows the temporal evolution of the system to states  $\langle n |$  and  $\langle m |$  due to interaction with the IR photon ( $\omega_{ir}$ ) and visible photon ( $\omega_{vis}$ ). For simplicity a single sided Feynman diagram is depicted, other sequences of events and complex conjugates are omitted.

### Microscopic description and line shape of SFG resonances

In the process of SFG a visible and an IR photon are annihilated and a new photon with the combined energy is generated. A quantum mechanical description of the SFG process can be derived with perturbation theory using the density operator.<sup>1,3,36,37</sup> A more visual approach is to use Feynman diagrams to represent the SFG process and derive the quantum-mechanical expression from the diagrams. In a Feynman diagram, the interactions of a system (such as a surface group) with photons is represented graphically. The straight arrows represent the interaction of the system with a photon. The wavy arrow represents the emission of a photon by the system. Each of the steps in the Feynman diagram is associated with a mathematical term, which has to be multiplied to get the final expression. Figure 2.9 shows the Feynman diagrams representing two scenarios resulting in a SFG signal. In the left diagram, the

system first interacts with the mid-IR photon, taking the system from the ground state  $\langle g|$  to state  $\langle n|$ . Subsequently, the visible photon takes the system from state  $\langle n|$  to state  $\langle m|$ . The emission of the SFG photon relaxes the system back to the ground state  $\langle g|$ . Each of these transitions can be resonant if its corresponding state ( $\langle n|$  or  $\langle m|$ ) is an eigenstate (i.e. stable state) of the system, or in other words, if the energy of the absorbed photon matches a optically allowed transition. The sequence of the interactions can be changed leading to, for example, the right diagram in Fig. 2.9. Other sequences are also possible, for example, the SFG photon can be emitted after the first excitation but before the second excitation (not shown). Each of these diagrams is associated with a contribution to the nonlinear susceptibility. The strength of each contribution depends on the occupation of the involved initial state  $\rho_{gg}$ , the damping of the transition from state  $\langle x|$  to state  $\langle y|$  given by  $\Gamma_{xy}$ , the coupling strength of the EM field to the state  $\mu_{xy}$ , and the number of systems contributing to the signal  $N$ . Each diagram in Fig. 2.9 gives rise to a contribution in  $\bar{\chi}$ . For the left diagram in Fig. 2.9 the resonance is described by,

$$\bar{\chi} \propto \frac{N \rho_{gg} \mu_{gm} \mu_{mn} \mu_{ng}}{[(\omega_{mg} \pm (\omega_{vis} + \omega_{ir})) \pm i\Gamma_{mg}][(\omega_{ng} \pm \omega_{ir}) \pm i\Gamma_{ng}]}, \quad (2.8)$$

where  $\omega_{xy}$  is the energy between two eigenstates of the system,  $\omega_{ir}$  represent the energy of the absorbed mid-IR, and  $\omega_{vis}$  represents the energy of the absorption visible photon. The other (relevant) diagrams lead to a similar frequency dependence.

In vibrational SFG spectroscopy the visible and mid-IR wavelengths are chosen such that only the mid-IR photon can be resonant for most substrates. The fact that only the IR transition can be resonant means the first term in the denominator in Eq. (2.8) can be replaced by a constant. Therefore, each resonance can be described by a Lorentzian line shape conforming to Eq. (2.8), sometimes referred to as an excitonic line shape in the field of nonlinear spectroscopy.<sup>38-40</sup> When modeling SFG spectra the expression in Eq. (2.8) is simplified to,

$$\bar{\chi}(\omega_{SFG} = \omega_{vis} + \omega_{ir}) = \frac{h N e^{i\phi}}{\omega_{ir} - \omega_r + i\Gamma}, \quad (2.9)$$

with  $h$  the cross section of the process,  $\phi$  the Lorentzian phase factor, and  $\omega_r$  the resonant frequency. The Lorentzian phase factor  $\phi$  has to be distinguished from the phase of the SFG signal itself: the phase of the SFG signal is a physical quantity given by  $\phi - \arg(\omega_{ir} - \omega_r + i\Gamma)$  and shows a jump of  $\pi$  rad over a resonance, which means it is a function of wavelength. The phase factor  $\phi$  is a mathematical construct associated to the Lorentzian resonance and does not show such a jump. It is a complex number that is related to the orientation of the groups among other factors.<sup>1-3,13</sup> The phase of light cannot be measured directly, however, it plays an important role in the BB-SFG spectra. When two or more contributions are present, the total response is a coherent (i.e.

phase related) superposition of the contributions. To demonstrate the effect of the phase on the interference between a non-resonant background with a resonant signal two cases are examined, see Fig. 2.10. The only difference between the two cases is the phase factor of the resonant contribution. A dramatic change in the spectral response is observed when changing the phase factor from  $\phi = 0$  to  $\phi = \pi$ . Even when the resonant contribution dominates, the interference with the non-resonant background introduces an asymmetry in the intensity spectrum.

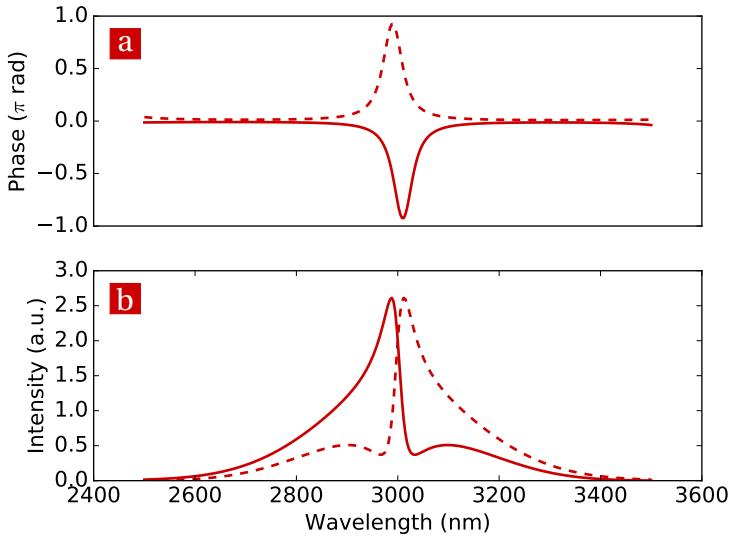


**Figure 2.10:** (a) Phase and (b) intensity of the EM field generated by the coherent superposition of a resonant and a non-resonant contribution. The two contributions are in phase ( $\phi = 0$ , solid line) and out of phase ( $\phi = \pi$ , dashed line).

### Modeling a BB-SFG spectrum

In general, the spectral response can be modeled with Eq. (2.7) multiplied with the appropriate Fresnel factors compensating for linear optical effect. In practice, the integral is omitted, the influence of the spectral variation of the two driving fields is absorbed into the non-resonant contribution, and it is ignored for the resonant contributions. The expression used to describe the BB-SFG spectra is given by,

$$I(\omega_3) \propto A(\omega_3, \omega_1, \omega_2) \cdot |\bar{\chi}_{NR}(\omega_2) + \sum_i \bar{\chi}_{i,res}(\omega_2)|^2 I_{vis} I_{ir} \quad (2.10)$$

with  $A(\dots)$  the influence of linear optics,  $\bar{\chi}_{NR}$  the non-resonant contribution,  $\sum_i \bar{\chi}_{i,res}$  the sum of the resonant contributions, and  $I_{vis}$  and  $I_{ir}$  the intensity



of the two driving fields. The non-resonant contribution is modeled here in most cases with a Gaussian spectral shape and a constant phase. However, any real function which describes the spectral shape can be used. The resonant contributions are modeled as Lorentzian resonances as described in Eq. (2.9) which inherently has a jump in the phase of  $\pi$  rad.

As an illustration this model was applied to the BB-SFG spectra in Fig. 2.6 from the H/Si(111) experiments discussed earlier. The spectra were modeled with a single resonant contribution and a non-resonant contribution. The model was fitted to the data after the transformation from SFG photon energies to IR photon energies by subtracting the visible photon energy. The spectra were fitted with Eq. (2.10) using a Marquardt-Levenberg algorithm. The parameters obtained from the fit are shown in Table 2.4. The resulting parameters for the resonant contribution should be interpreted for (A) the resonant and (B) the non-resonant contribution as follows:

- $h \cdot N$ : The amplitude of the contribution. (A) This parameter is proportional to the density of the surface groups  $N$  causing the resonance for the resonant contribution.  $h$  describes the cross section of the SFG process which is roughly proportional to the absorption cross section multiplied with the Raman cross section. In this case, the spectrum  $i$  had a 1.96 times higher Si-H density than in the spectrum  $ii$ . To obtain the absolute density,  $N$ , the SFG cross section  $h$  has to be known from e.g. a calibration measurement. (B) A constant proportional to  $I_{vis} I_{ir}$ .
- $\omega_0$ : (A) The energy of the vibrational transition. This is related to the nature of the vibration and the species involved. For example, most of the C-H stretches are situated around  $3000 \text{ cm}^{-1}$  whereas Si-H stretch is situated around  $2100 \text{ cm}^{-1}$ . (B) The central wavelength of the mid-IR beam.
- $\Gamma$ : (A) The broadening of the vibrational transition similar to linear optics (e.g. interaction with environment, back bonding). (B) The bandwidth of the visible beam. As discussed before, for the H/Si(111) surface the width of the spectrum is determined by the instrumental broadening.
- $\phi$ : (A) The phase of the resonant contribution which is (in principle) related to the orientation of the groups. Several BB-SFG spectra, differing in e.g. polarization combination, are required to obtain the orientation of the surface groups. (B) The phase of the non-resonant contribution is assumed to be zero.

For the non-resonant contribution, the amplitude has no direct interpretation as it depends on the details of the substrate. The central position and broadening of the non-resonant contribution are determined by the tuning of the mid-IR laser. The phase of the non-resonant contribution is assumed to be constant.

The conventional approach described above is more than sufficient to extract the (relative) density of the surface groups from the BB-SFG spectra. However, this approach ignores the intricate but subtle interplay between the spectral shape of the mid-IR beam probing the SFG response and the

coherent superposition of multiple contributions. Implicitly, it is assumed in the conventional approach that the intensity of the mid-IR does not vary over the spectral range covered by a resonance. Judging from a typical spectral width of the mid-IR beam of  $>200 \text{ cm}^{-1}$  and the broadening of a resonance on the order of  $20 \text{ cm}^{-1}$  this is not a bad approximation, but not entirely correct. Effectively, not all wavelengths are probed with the same strength due to the spectral shape of the mid-IR beam. This skews the effective shape of a resonance which cannot be modeled by the Lorentzian line shape.

A more refined approach would be to determine the spectral shape of the mid-IR beam  $I_{ir}(\omega_2)$  from the NR contribution (if present). Once  $I_{ir}(\omega_2)$  is known the spectrum can then be modeled as,

$$I(\omega_3 = \omega_1 + \omega_2) \propto |\bar{\chi}_{res}(\omega_2) + \bar{\chi}_{NR}|^2 I_{vis} I_{ir}(\omega_2) \quad (2.11)$$

where the resonance is still given by Eq. (2.9). In contrast to Eq. (2.10), the  $\bar{\chi}_{NR}$  tensor is now simply a real constant. This approach leads to a slight improvement in the peak shape of resonant contribution, comparing the solid and the dashed line in Fig. 2.6. However, the main parameter of interest, peak height, is not significantly affected by this procedure. Moreover, in some cases a spectrum with the NR signal cannot be obtained so this approach is not always applicable.

**Table 2.4:** The parameters obtained from the fit of the model to the BB-SFG spectra of Si-H stretch mode in Fig. 2.6. The non-resonant contribution was determined from spectrum (*iii*) assuming that all the Si-H groups were removed. This contribution was used in the modeling of spectrum (*i*) and (*ii*). The coefficient obtained using the alternative model for spectrum (*i*) are also given labeled as the fit of spectrum (*i'*). The parameters labeled with an asterisk (\*) were fixed.

Spectrum	Resonant				Non-resonant		
	$\omega_0 \text{ (cm}^{-1}\text{)}$	$h \cdot N$	$\Gamma \text{ (cm}^{-1}\text{)}$	$\phi \text{ (rad)}$	$\omega_0 \text{ (cm}^{-1}\text{)}$	$h \cdot N$	$\Gamma \text{ (cm}^{-1}\text{)}$
( <i>i</i> )	2092*	21.21	10.59	$\pi^*$	2092.87*	2.51*	81.08*
( <i>ii</i> )	2092*	10.82	10.18	$\pi^*$	2092.87*	2.51*	81.08*
( <i>iii</i> )	-	0*	-	-	2092.87	2.51	81.08
( <i>i'</i> )	2092*	23.52	11.40	$\pi^*$	-	2.26	-

## Bibliography

- [1] Boyd. *Nonlinear optics*. Elsevier Science Publishing Co Inc, second edition, 1992.
- [2] Heinz. Second-order nonlinear optical effects at surfaces and interfaces. *Nonlinear surface electromagnetic phenomena*, 1991.
- [3] Shen. *The Principles of Nonlinear Optics*. John Wiley & Sons, 1984.
- [4] Langereis, Heil, Knoop, Keuning, van de Sanden, and Kessels. In situ spectroscopic ellipsometry as a versatile tool for studying atomic layer deposition. *Journal of Physics D: Applied Physics*, 2009. doi:[10.1088/0022-3727/42/7/073001](https://doi.org/10.1088/0022-3727/42/7/073001).
- [5] Fujiwara. *Spectroscopic ellipsometry : principles and applications*. Wiley, 2007.
- [6] Rai, Vandalon, and Agarwal. Surface Reaction Mechanisms during Ozone and Oxygen Plasma Assisted Atomic Layer Deposition of Aluminum Oxide. *Langmuir*, 2010. doi:[10.1021/la101485a](https://doi.org/10.1021/la101485a).
- [7] Rai, Vandalon, and Agarwal. Influence of surface temperature on the mechanism of atomic layer deposition of aluminum oxide using an oxygen plasma and ozone. *Langmuir : the ACS journal of surfaces and colloids*, 2012. doi:[10.1021/la201136k](https://doi.org/10.1021/la201136k).
- [8] Mirabella. *Internal Reflection Spectroscopy*. CRC Press, 1993.
- [9] Geyer, Methaapanon, Shong, Pianetta, and Bent. In Vacuo Photoemission Studies of Platinum Atomic Layer Deposition Using Synchrotron Radiation. *The Journal of Physical Chemistry Letters*, 2013. doi:[10.1021/jz301475z](https://doi.org/10.1021/jz301475z).
- [10] Rahtu, Alaranta, and Ritala. In Situ Quartz Crystal Microbalance and Quadrupole Mass Spectrometry Studies of Atomic Layer Deposition of Aluminum Oxide from Trimethylaluminum and Water. *Langmuir*, 2001. doi:[10.1021/la010103a](https://doi.org/10.1021/la010103a).
- [11] Heil, van Hemmen, van de Sanden, and Kessels. Reaction mechanisms during plasma-assisted atomic layer deposition of metal oxides: A case study for Al<sub>2</sub>O<sub>3</sub>. *Journal of Applied Physics*, 2008. doi:[10.1063/1.2924406](https://doi.org/10.1063/1.2924406).
- [12] Born and Wolf. *Principles of optics : electromagnetic theory of propagation, interference and diffraction of light*. Cambridge University Press, 1999.
- [13] Reider and Heinz. *Photonic Probes of Surfaces*. Elsevier Science B.V., 1995.
- [14] Gielis, Gevers, Aarts, van de Sanden, and Kessels. Optical second-harmonic generation in thin film systems. *Journal of Vacuum Science & Technology A: Vacuum, Surfaces, and Films*, 2008. doi:[10.1116/1.2990854](https://doi.org/10.1116/1.2990854).
- [15] Backus, Garcia-Araez, Bonn, and Bakker. On the Role of Fresnel Factors in Sum-Frequency Generation Spectroscopy of Metal-Water and Metal-Oxide-Water Interfaces. *The Journal of Physical Chemistry C*, 2012. doi:[10.1021/jp306273d](https://doi.org/10.1021/jp306273d).
- [16] Sipe. New Green-function formalism for surface optics. *Journal of the Optical Society of America B*, 1987. doi:[10.1364/JOSAB.4.000481](https://doi.org/10.1364/JOSAB.4.000481).
- [17] Shoji, Kondo, Kitamoto, Shirane, and Ito. Absolute scale of second-order

- nonlinear-optical coefficients. *Journal of the Optical Society of America B*, 1997. doi:[10.1364/JOSAB.14.002268](https://doi.org/10.1364/JOSAB.14.002268).
- [18] Wilson, Jiang, Carriles, and Downer. Second-harmonic amplitude and phase spectroscopy by use of broad-bandwidth femtosecond pulses. *Journal of the Optical Society of America B*, 2003. doi:[10.1364/JOSAB.20.002548](https://doi.org/10.1364/JOSAB.20.002548).
- [19] Zhang, Shen, and Somorjai. Studies of surface structures and compositions of polyethylene and polypropylene by IR+visible sum frequency vibrational spectroscopy. *Chemical Physics Letters*, 1997. doi:[10.1016/S0009-2614\(97\)01311-0](https://doi.org/10.1016/S0009-2614(97)01311-0).
- [20] Higashi, Chabal, Trucks, and Raghavachari. Ideal hydrogen termination of the Si(111) surface. *Applied Physics Letters*, 1990. doi:[10.1063/1.102728](https://doi.org/10.1063/1.102728).
- [21] Jakob, Chabal, and Raghavachari. Lineshape analysis of the Si-H stretching mode of the ideally H-terminated Si(111) surface: the role of dynamical dipole coupling. *Chemical Physics Letters*, 1991. doi:[10.1016/0009-2614\(91\)90433-A](https://doi.org/10.1016/0009-2614(91)90433-A).
- [22] Burrows, Chabal, Higashi, Raghavachari, and Christman. Infrared spectroscopy of Si(111) surfaces after HF treatment: Hydrogen termination and surface morphology. *Applied Physics Letters*, 1988. doi:[10.1063/1.100053](https://doi.org/10.1063/1.100053).
- [23] Chabal, Dumas, Guyot-Sionnest, and Higashi. Vibrational dynamics of the ideally H-terminated Si(111) surface. *Surface Science*, 1991. doi:[10.1016/0039-6028\(91\)90321-I](https://doi.org/10.1016/0039-6028(91)90321-I).
- [24] Mao, Miranda, Kim, and Shen. Characterization of hydrogen-terminated Si(111) surfaces by sum-frequency surface vibrational spectroscopy. *Applied Physics Letters*, 1999. doi:[10.1063/1.125350](https://doi.org/10.1063/1.125350).
- [25] Dolgova, Fedyanin, Aktsipetrov, and Marowsky. Optical second-harmonic interferometric spectroscopy of Si(111)-SiO<sub>2</sub> interface in the vicinity of E2 critical points. *Physical Review B*, 2002. doi:[10.1103/PhysRevB.66.033305](https://doi.org/10.1103/PhysRevB.66.033305).
- [26] Lagutchev, Lozano, Mukherjee, Hambir, and Dlott. Compact broadband vibrational sum-frequency generation spectrometer with nonresonant suppression. *Spectrochimica acta. Part A, Molecular and biomolecular spectroscopy*, 2010. doi:[10.1016/j.saa.2009.12.066](https://doi.org/10.1016/j.saa.2009.12.066).
- [27] Lagutchev, Hambir, and Dlott. Nonresonant Background Suppression in Broadband Vibrational Sum-Frequency Generation Spectroscopy. *The Journal of Physical Chemistry C*, 2007. doi:[10.1021/jp075391j](https://doi.org/10.1021/jp075391j).
- [28] Chen, Shen, and Somorjai. Studies of polymer surfaces by sum frequency generation vibrational spectroscopy. *Annual review of physical chemistry*, 2002. doi:[10.1146/annurev.physchem.53.091801.115126](https://doi.org/10.1146/annurev.physchem.53.091801.115126).
- [29] Voges, Al-Abadleh, Musorrafiti, Bertin, Nguyen, and Geiger. Carboxylic Acid- and Ester-Functionalized Siloxane Scaffolds on Glass Studied by Broadband Sum Frequency Generation. *The Journal of Physical Chemistry B*, 2004. doi:[10.1021/jp046564x](https://doi.org/10.1021/jp046564x).
- [30] Chen. Investigating buried polymer interfaces using sum frequency generation vibrational spectroscopy. *Progress in polymer science*, 2010.

- doi:[10.1016/j.progpolymsci.2010.07.003](https://doi.org/10.1016/j.progpolymsci.2010.07.003).
- [31] Loch, Ahn, Chen, Wang, and Chen. Sum Frequency Generation Studies at Poly(ethylene terephthalate)/Silane Interfaces: Hydrogen Bond Formation and Molecular Conformation Determination. *Langmuir*, 2004. doi:[10.1021/la0494526](https://doi.org/10.1021/la0494526).
- [32] Chen, Clarke, Wang, and Chen. Comparison of surface structures of poly(ethyl methacrylate) and poly(ethyl acrylate) in different chemical environments. *Physical Chemistry Chemical Physics*, 2005. doi:[10.1039/b501910a](https://doi.org/10.1039/b501910a).
- [33] Wang, Chen, Buck, and Chen. Molecular Chemical Structure on Poly(methyl methacrylate) (PMMA) Surface Studied by Sum Frequency Generation (SFG) Vibrational Spectroscopy. *The Journal of Physical Chemistry B*, 2001. doi:[10.1021/jp013161d](https://doi.org/10.1021/jp013161d).
- [34] Wang, Woodcock, Buck, Chen, and Chen. Different surface-restructuring behaviors of poly(methacrylate)s detected by SFG in water. *Journal of the American Chemical Society*, 2001. doi:[10.1021/ja0164071](https://doi.org/10.1021/ja0164071).
- [35] Loch, Wang, and Chen. Different Molecular Structures at Polymer/Silane Interfaces Detected by SFG. *The Journal of Physical Chemistry B*, 2003. doi:[10.1021/jp035211f](https://doi.org/10.1021/jp035211f).
- [36] Hamm. Principles of Nonlinear Optical Spectroscopy: A Practical Approach. *University of Zurich*, 2005. doi:[10.1021/ja965513d](https://doi.org/10.1021/ja965513d).
- [37] Bonn, Ueba, and Wolf. Theory of sum-frequency generation spectroscopy of adsorbed molecules using the density matrix method - broadband vibrational sum-frequency generation and applications. *Journal of Physics: Condensed Matter*, 2005. doi:[10.1088/0953-8984/17/8/002](https://doi.org/10.1088/0953-8984/17/8/002).
- [38] Dolgova, Schuhmacher, Marowsky, Fedyanin, and Aktsipetrov. Second-harmonic interferometric spectroscopy of buried interfaces of column IV semiconductors. *Applied Physics B: Lasers and Optics*, 2002. doi:[10.1007/s00340-002-0917-5](https://doi.org/10.1007/s00340-002-0917-5).
- [39] Gevers, Gielis, Beijerinck, van de Sanden, and Kessels. Amorphization of Si(100) by Ar<sup>+</sup>-ion bombardment studied with spectroscopic and time-resolved second-harmonic generation. *Journal of Vacuum Science & Technology A: Vacuum, Surfaces, and Films*, 2010. doi:[10.1116/1.3305812](https://doi.org/10.1116/1.3305812).
- [40] Daum. Optical studies of Si/SiO<sub>2</sub> interfaces by second-harmonic generation spectroscopy of silicon interband transitions. *Applied Physics A*, 2007. doi:[10.1007/s00339-007-3913-0](https://doi.org/10.1007/s00339-007-3913-0).

# BB-SFG setup for ALD growth mechanism studies

## 3

### 3.1 Introduction

In this chapter, the design and implementation of a broadband sum-frequency generation (BB-SFG) setup will be described specifically suited for the in-situ study of atomic-layer deposition (ALD) growth mechanism. This BB-SFG setup was constructed in two phases. First, an ex-situ BB-SFG setup was built. By avoiding the additional complexity and constraints of an in-situ setup (at first), valuable experience was gained in working with ultrafast IR optics. For example, obtaining spatial and temporal overlap of femtosecond pulses was new to the PMP group. In this phase important questions could be answered such as:

- What is a reliable procedure to find the correct spatial and temporal overlap?
- What is a good benchmark for the SFG signal strength?

In the second phase, the in-situ setup was built with the goal of studying the surface reactions during ALD. The experience gained from the ex-situ setup was put to good use when designing the optics for the in-situ work. The resulting setup is shown in Fig. 3.1, illustrating the key components of the setup: the laser system, the optical components to tailor the two beams, the vacuum chamber in which ALD was performed, and the detection of the BB-SFG signal.

The structure of this chapter is as follows: First, the main design decisions influencing the capabilities of the setup will be discussed. Then, the setup itself will be described by following the optical pulses through the setup. The following parts of the setup will be discussed: (i) The laser system generating the femtosecond pulses. (ii) The beam tailoring needed to obtain the desired spectral profiles, temporal overlap, and spatial overlap. (iii) The ALD reactor with a (temperature controlled) sample on which the ALD surface chemistry was studied. (iv) The optics and detector needed to detect the BB-SFG signal. In the last section, recommendations will be made for making the current

setup easier to operate. Furthermore, several interesting modifications of the setup will be described which could be relevant for future research.

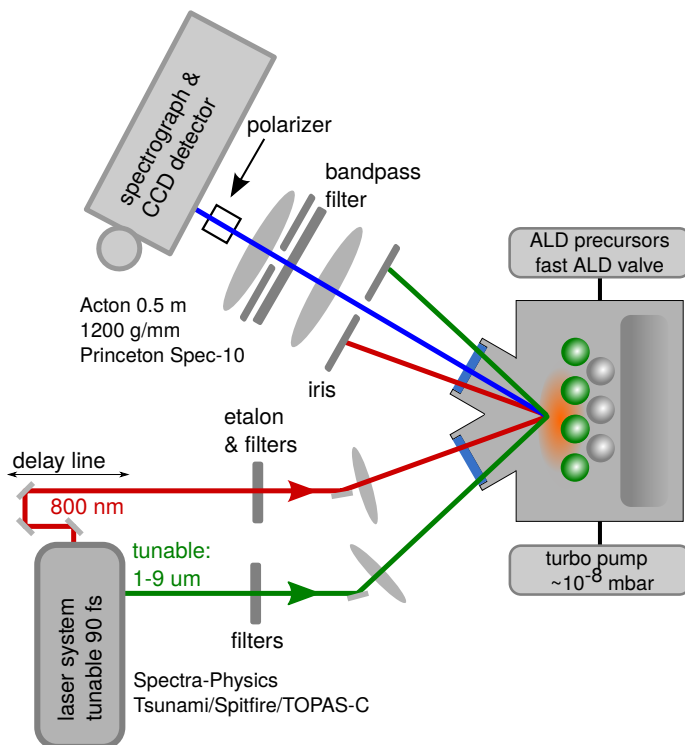


**Figure 3.1:** The main components of the BB-SFG setup built to study the ALD surface chemistry. The key design choices and components of the setup will be discussed in this chapter.

### 3.2 General considerations for vibrational BB-SFG

Identification and quantification of surface groups is a key aspect in studying the ALD surface chemistry with BB-SFG. As explained in the previous chapter, this is achieved in BB-SFG spectroscopy by using the resonant enhancement of the SFG process by exciting a vibrational transition of the surface groups. The energy of these vibrational transitions are unique for each surface group and are typically in the range of 0.4 - 0.1 eV, matching the energy of photons of mid-IR light. This fixed the wavelength of one of the two laser beams driving the BB-SFG process to the mid-IR. In this case, a tunable mid-IR laser was used which generated spectrally broad femtosecond pulses. The choice of the wavelength of the other laser was guided by two considerations: (1) Only the IR signal should be able match a transition between energy levels. This

facilitates interpretation of the spectra as discussed in Chapter 2. (2) The wavelength of the SFG signal should be easily detectable. Both criteria could be met by using wavelengths in the near-IR (800 nm) or visible (532 nm). This would result in an SFG signal in the visible part of the spectrum 600 - 750 nm and 438 - 480 nm respectively. Neither choice would excite resonances in common substrates such as *c*-Si, SiO<sub>2</sub>, and Al<sub>2</sub>O<sub>3</sub>. However, the near-IR was preferred and used in this work as this results in an ideal wavelength to use in combination with readily available and highly sensitive charge-coupled device (CCD) chips for detection of the weak SFG signal.

Pulse duration is an important parameter in BB-SFG which affects the process in several ways. Firstly, it affects the efficiency of the SFG process, and therefore influences the signal-to-noise (S/N) ratio. Secondly, it influences the way spectra are measured. The impact of pulse duration on the efficiency of the SFG process can be elucidated by examining a simple example. In this example, the effects of pulse duration on the spectral width of the pulses is not considered which has already been discussed in the previous chapter. The temporal shape of the pulses is taken to be rectangular. The result obtained can be generalized to more realistic pulse shapes without affecting the outcome. Under these assumptions, the instantaneous SFG intensity  $I_{SFG}$ , generated by the two driving fields with intensities  $I_{vis}$  and  $I_{ir}$ , is described by,

$$I_{SFG} \propto I_{vis} I_{ir}. \quad (3.1)$$

However, the two driving fields are pulsed with a repetition rate  $R$  and have a duration of  $\tau$ . The measured SFG intensity is an time average over many pulses. The time averaged SFG signal (indicated with chevrons) is given by,

$$\langle I_{SFG} \rangle \propto \tau R I_{vis} I_{ir}. \quad (3.2)$$

The sum of the average intensities of the two beams  $\langle I_d \rangle$  is constrained to  $\langle I_d \rangle = \langle I_{vis} \rangle + \langle I_{ir} \rangle$  by, for example, the damage threshold of the sample. With this constraint, one of the beams can take up a fraction of  $\langle I_d \rangle$  given by  $\alpha$ . The intensity of the other beam should than be limited to  $1 - \alpha$ . This results in the following relations,

$$\langle I_{vis} \rangle = \alpha \langle I_d \rangle = \tau R I_{vis}, \quad (3.3)$$

$$\langle I_{ir} \rangle = (1 - \alpha) \langle I_d \rangle = \tau R I_{ir}, \quad (3.4)$$

Combining these equations leads to,

$$\langle I_{SFG} \rangle \propto \frac{\alpha(1-\alpha)\langle I_d \rangle^2}{\tau R}. \quad (3.5)$$

The strongest BB-SFG signal is obtained for  $\alpha \approx 1/2$ . Furthermore, the average SFG signal is inversely proportional to the pulse duration  $\tau$ . Shorter pulses with the same pulse energy lead to stronger average SFG signals. It turns out that the only practical approach for studying surface chemistry with vibrational SFG is to use ultrashort (picosecond and shorter) laser pulses. With



these ultrashort pulses, measurable signals can be obtained from a (partial) monolayer of surface groups while at the same time keeping the (average) power low enough to avoid damaging the surface groups or the substrate.

Most laser systems producing ultrashort pulses generate “bandwidth limited” pulses. This means that the pulses have a spectral bandwidth inversely proportional to their duration as required by the Heisenberg uncertainty principle or the Fourier transform limit. In other words, temporally short pulses have to be spectrally broader than longer pulses. Depending on the spectral width of the pulses there are two possible detection schemes probing a region of the mid-IR response of a sample: “SFG” spectroscopy uses spectrally narrow mid-IR and visible pulses, whereas “BB-SFG” spectroscopy uses a spectrally broad mid-IR beam and a spectrally narrow visible beam. To emphasize how BB-SFG differs from SFG in practice, both cases will be discussed. In “SFG” spectroscopy a spectrum is recorded by probing the SFG response at a series of discrete IR wavelengths using spectrally narrow IR and visible pulses (typically ps in duration).<sup>1,2</sup> There is no vibrational information in the spectral shape of the SFG signal itself. Only the intensity of the SFG signal is used. By recording the SFG intensity at a series of IR wavelengths, i.e. by tuning the laser, a spectrum can be built up. The resolution depends on the bandwidth of the visible and IR pulse. Detection is typically performed with a photomultiplier tube (PMT). The main merits of this method are its relative simplicity and its high spectral resolution. Using shorter pulses, either to follow faster processes or to enhance the S/N ratio, implies sacrificing spectral resolution due to the spectral broadening of the pulses (for the “bandwidth limited” pulses). Using significantly shorter pulses negates the main merit of this approach which is its high spectral resolution.

With the advent of broadband femtosecond laser systems, “BB-SFG” spectroscopy became possible. In the case of BB-SFG, a spectral broad pulse is desired and the broadband nature itself is exploited.<sup>3</sup> The inherently broad IR pulse is used to probe a whole region of the IR spectrum without tuning the laser system. The fact that a whole part of the IR response is probed without tuning the laser system means that the vibrational information is now contained in the spectral shape of the BB-SFG signal. Therefore, a detector is needed which can measure the spectral shape of the BB-SFG signal. Typically, a spectrograph combined with a CCD camera is used for this purpose. To be able to interpret the BB-SFG signal, a spectrally narrow visible beam is used. Having a well defined visible photon energy  $E_{vis}$  makes the assignment of a SFG photon detected at  $E_{SFG}$  to  $E_{IR} = E_{SFG} - E_{vis}$  unique. This is also described with Eq. (2.7). The main drawback of the broadband approach is the increased difficulty of achieving temporal overlap with the much shorter pulses. In practice the spectral resolution is less than that of scanning SFG, however, there is no fundamental limitation to the resolution that can be achieved. There are several key benefits to this approach. It yields better signal-to-noise ratio. The spectra are collected without changing/scanning the output frequency of the IR beam during the experiment. This also allows for spectrally resolved pump probe measurements on fem-

to femtosecond time scales.<sup>4,5</sup> Moreover, it is easier to differentiate between resonant and non-resonant contributions in BB-SFG. It is even possible to suppress the nonresonant contribution in BB-SFG.<sup>6,7</sup> In this work, a broadband scheme was used with a 90 fs mid-IR pulse which was mixed with a spectrally narrow  $\sim 1$  ps visible pulse.

The arrangement of the input beams has a large impact on the capabilities and characteristics of the BB-SFG setup. The two input beams can be arranged in a collinear or a non-collinear geometry. Of the two, the collinear geometry is easier to align. However, the non-collinear geometry offers the advantage that: (1) A separate set of optics can be used for each beam. (2) That mixing can only occur at the sample. (3) That the driving laser beams can be (more) easily separated from the BB-SFG signal after impinging on the sample due to a difference in the propagation direction. Furthermore, BB-SFG can be performed in either transmission or reflection geometry. The latter geometry was chosen, since it allowed for a greater flexibility with respect to sample choice. In reflection mode the sample did not need to be transparent to the SFG light. This allowed the usage of both transparent and opaque samples in the same setup. To summarize, 90 fs IR and  $\sim 1$  ps visible pulses were used in a non-collinear reflection geometry on a planar sample for the BB-SFG experiments presented in this work.

### 3.3 The femtosecond laser system: a tunable mid-IR & visible light source

The laser system generating the femtosecond pulses was a critical part of the BB-SFG setup. The laser system was used to generate two beams: a 90 fs broadband mid-IR beam and a 90 fs broadband 800 nm beam. The spectral and temporal shape of the 800 nm needed to be tailored before it could be used in the BB-SFG experiments. Figure 3.2 shows a schematic of the laser system identifying the main components. The mode of operations of the system will be explained here in broad strokes, for a more detailed description of the fundamental operating principles see [Koechner](#).<sup>8</sup>

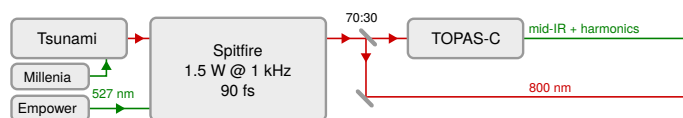


**Figure 3.2:** The main parts of the laser system used for the BB-SFG experiments are indicated together with a simplified representation of the beam paths. During the project two lasers were replaced: The Millenia pump laser was replaced with a newer version of the same laser. The Empower-30 pump laser is the replacement of the Evolution-30 pump laser.

The first step to producing both the mid-IR and visible beams was to gen-

erate a femtosecond pulsed signal. A continuous wave (CW) 5 W intracavity frequency doubled Nd:YLF laser (Spectra Physics Millennia) generating 532 nm light was used to pump the Ti:Sapphire crystal of a modelocked oscillator (*Spectra Physics Tsunami*). The modelocking ensured the generation of femtosecond pulses. The output of the oscillator was a pulse train of 90 fs pulses with a repetition rate of  $\approx 80$  MHz. The average intensity of the light generated by Tsunami was 1 W with a wavelength of 800 nm. The Tsunami laser was actually tunable, but this capability was not used for the BB-SFG experiments. The pulse energy of this system was too weak to be used as either the visible beam in the BB-SFG experiment nor could it be used to (efficiently) generate the mid-IR signal. A chirped regenerative amplifier (*Spectra Physics Spitfire*), again using a Ti:Sapphire crystal was used to amplify a pulse from the 80 MHz pulse train. The crystal in Spitfire was pumped in this case by a ns pulsed 30W intracavity frequency double Nd:YLF laser. The chirped amplifier operated as follows: A femtosecond pulse was selected from the 80 MHz pulse train, stretched temporally, and shot into the cavity of Spitfire. Meanwhile, the crystal in Spitfire has been pumped while, at the same time, the cavity has been prevented from lasing by a Pockels cell. Once the pulse was inside the cavity, the cavity was allowed to lase, greatly amplifying the original pulse. After amplification in the cavity, the pulse was compressed to femtosecond duration. The output of Spitfire was a 1.5 W beam with 90 fs pulses with a repetition rate of 1 kHz. The pulse energy (1.5 mJ) was now high enough to be used in the BB-SFG experiment and to efficiently pump an optical parametric amplifier (OPA).

Of the high intensity 800 nm beam produced by Spitfire 70% was used in the generation of the mid-IR signal. This was done with an two stage optical parametric amplifier (OPA, *Light Conversion TOPAS-C*). In essence difference-frequency generation (DFG) was performed to split a 800 nm photon into two photons which had the same combined energy. This process is often referred to as optical parametric generation (OPG) or optical parametric amplification (OPA). Two signals were generated with OPG in the first stage of TOPAS-C, this process was seeded with white light to enhance efficiency. The signal with the lowest energy photons is called the “idler” and the signal with the highest energy photons is called the “signal”. In the second stage, the “signal” was amplified with the OPA process. After the second stage, next to the depleted 800 nm pump beam, a “signal” and “idler” beam were produced both situated in the near IR part of the spectrum. To generate the mid-IR signals, DFG was performed using the signal and idler beams. When the signal and idler had similar photon energies ( $\sim 1450$  nm and  $\sim 1800$  nm), the difference in photon energy was small and DFG generated photons with energies in the mid-IR part of the spectrum ( $\sim 7500$  nm). The output of TOPAS-C consisted of an array of signals, one of which was the desired mid-IR signal. All of these signals had a similar, but not identical, pointing and some were more intense than the desired mid-IR signal. Careful filtering of the output of TOPAS-C had to be performed to remove these signals such that they did not generate other mixed signals in the same spectral range as the SFG signal.

An essential skill in operating the BB-SFG setup was the daily realignment of the laser system. This was an iterative process, with the most common changes being:

- Tsunami wavelength and bandwidth tuning.
- The chirp compensation in Spitfire.
- The alignment of the out-coupling mirror in Spitfire.
- The alignment of the input beam into TOPAS-C.
- Adjustments to the temporal overlap in the power amplification stage of TOPAS-C.
- Adjustment of the quartz plate before the final DFG stage.

Occasionally, the internal alignment TOPAS-C had to be adjusted to obtain a workable output power. The output power of TOPAS-C could have been used as a metric for the quality of the alignment. However, this was less than ideal since it ignored several pulse parameters that were critical for BB-SFG. Moreover, the other output signals obfuscated the power reading due to less than ideal spectral filtering. If a BB-SFG signal could be obtained with the mid-IR beam, it was found to be best to use the BB-SFG signal itself to do the final alignment of the laser system. As the BB-SFG process was strongly affected by pulse parameters which cannot easily be measured, such as pulse duration, pulse shape, and pulse chirp, it was a good metric for the quality of the OPA output. A strong BB-SFG signal was an indication that a good set of pulse parameters was reached.

The stability of the laser system was of importance when comparing BB-SFG spectra. Changes in output power or pointing over time affected signal strength. This was tested by monitoring the output power of TOPAS-C, tuned to 4720 nm and measured after appropriate filtering, during 30 minutes with a *Ophir 3A-FS-SH* thermal sensor and *Ophir Nova 2* power meter. The peak to peak fluctuations were found to be  $\approx 5\%$ . Figure 3.3 shows the BB-SFG signal of the Si-H stretch mode of a Si-H terminated surface of a Si(111) monitored over time. The peak intensity fluctuated less than 10% during this measurement, in the same range as the relative power fluctuations.

The spectral range covered with the BB-SFG setup was mainly limited by the output power of TOPAS-C at long wavelengths. Figure 3.4 shows the output power of TOPAS-C as a function of wavelength. The system was usable from 2  $\mu\text{m}$ , continuing down to 10  $\mu\text{m}$  with a dip in output power around 6  $\mu\text{m}$ . Figure 3.5 illustrates the bandwidth and spectral range covered with BB-SFG setup. The nonresonant BB-SFG response of a GaAs substrate was measured by stepping through the spectral range of TOPAS-C. The width of each spectrum in Fig. 3.4 illustrates the bandwidth that could be probed at a certain central wavelength without tuning the laser system. A significant and continuous part of the IR spectrum could be probed with BB-SFG by tuning TOPAS-C. Above 6000 nm (below  $\sim 1700\text{ cm}^{-1}$ ) the output power of TOPAS-C decreased significantly. Detection of vibrational modes below  $1700\text{ cm}^{-1}$  was not feasible, except for very strong and narrow resonances. The decrease of

the S/N ratio in Fig. 3.5 at lower wavenumbers was partly due to the lower output power of TOPAS-C and partly due to the spectral response of the GaAs.

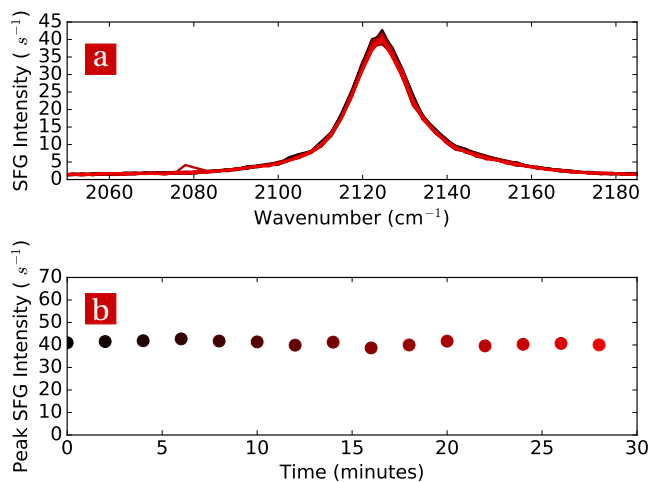


**Figure 3.3:** (a) BB-SFG spectra and (b) amplitude of the Si-H stretch mode of Si-H groups on a Si(111) wafer measured over a period of 30 minutes. The fluctuations here are an indication of the stability of all relevant parameters such as pulse duration, pointing, chirp, and pulse power.

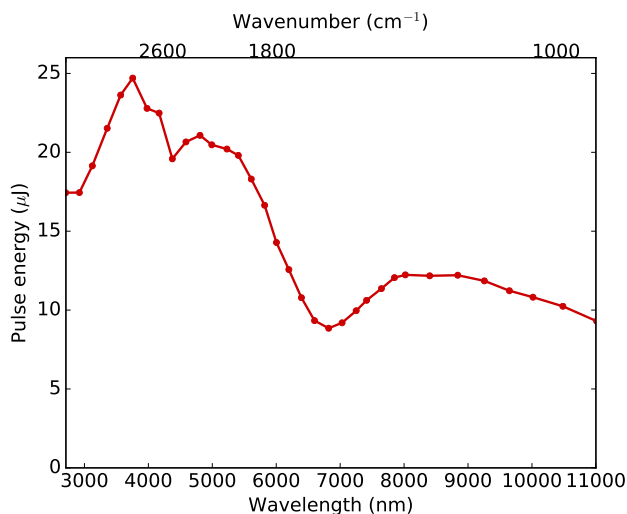


**Figure 3.4:** Indication of wavelength dependence of the output power of the TOPAS-C. Depending on alignment the exact dependence might drop off more steeply when going to longer wavelengths.

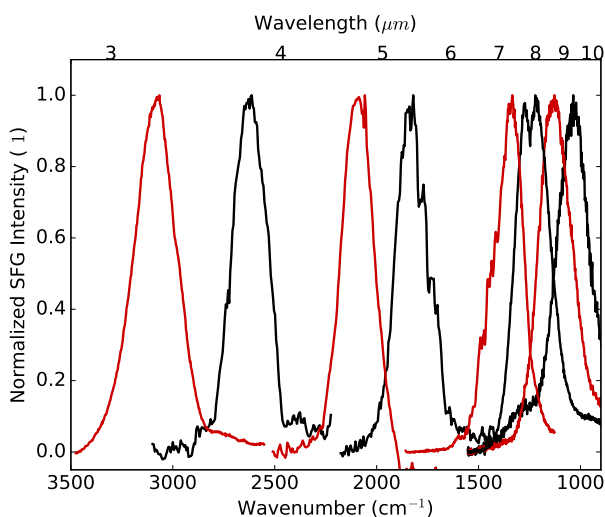


**Figure 3.5:** The nonresonant BB-SFG signal measured on a GaAs wafer for several wavelengths in the continuous tuning range of TOPAS-C. The spectral shape of the pulse is a combination of the spectral shape of the TOPAS-C output together with, for some spectra, the absorption lines of CO<sub>2</sub> and H<sub>2</sub>O.

### 3.4 Beam tailoring to achieve temporal and spatial overlap

The visible beam had to be made spectrally narrow and the unwanted components of the mid-IR beam needed to be filtered out. Subsequently, the beams had to be focused as tightly as possible on the same spot of the sample and the delay between the two pulses had to be such that the pulses arrived at the surface at the same time. The key elements of this part of the setup are shown in Fig. 3.6. The tailoring for the individual beams is discussed first. Then, the procedure is explained that was established to obtain a tight and overlapping focus of the beams on the sample.

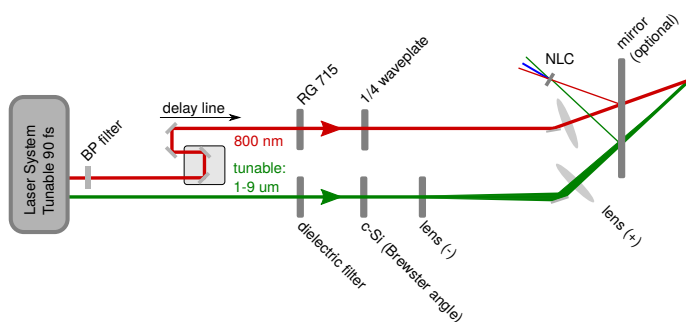


**Figure 3.6:** The main optical components involved in tailoring the mid-IR and visible beams for the BB-SFG experiments. The removable mirror (indicated optional) can be placed to direct the beams towards the nonlinear crystal (NLC) to aid in the alignment.

The visible beam used in the BB-SFG experiment was generated by Spitfire. The characteristics of this beam were changed in several ways. The beam was made spectrally narrow using a spike-filter (*CVI F1.1-800*), reducing the spectral width to approximately 1 nm. This filter is based upon a Fabry-Perot etalon and should introduce asymmetry in the temporal profile of the visible pulse.<sup>6</sup> This was indeed observed in the intensity profile of the BB-SFG when scanning the delay between the visible and mid-IR pulse. The intensity of the visible beam was reduced significantly by this filter and the pulse duration was increased. Performing this step first had the benefit that the remaining optics were exposed to a weaker beam reducing the risk of damage. After the band-pass filter, the beam was passed through a home built delay line using a motorized stage (*Physik Instrumente M-014-D1*) and 4 mirrors. All mirrors, except mentioned otherwise, were protected silver mirrors of the type *Thorlabs PF10-03-P01*. The motorized stage had a repeatability of 2 μm (7 fs) and a step size of 100 nm (0.4 fs) which was sufficient for these experiments. In hind-sight, a stage with a longer range of motion should have been chosen, allow for easier and more accurate alignment of the optical with the axis of

motion of the stage. The length of the beam path of the visible beam had to be manually adjusted to within the range of motion of the stage which was 2.5 cm. Measuring the length of the beam path with this accuracy was difficult given the total length of the beam path (10 m). Moreover, 12 mirrors were used in the visible beam path, increasing the error in the measurement of the path length as the position on each mirror was unknown. A uncertainty of  $\sim 5$  mm in the length measurement was introduced per mirror. The second set of mirrors in the delay line were mounted on optical rails, functioning as a manual delay line with which the coarse adjustments in beam path were made. Subsequently, the visible beam was passed through a variable waveplate (*Alphas PO-TWP-L4-25-UVIR*) which allowed the rotation of the polarization from *p* polarization to *s* if desired.

The mid-IR beam, generated by TOPAS-C, was first filtered using an dielectric filter to remove the strong pump, signal, and idler beams. The remaining relatively weak ( $\sim 20$  mW) signal still contained multiple undesired signals which were filtered out by a *c*-Si wafer (double side polished, low resistivity) under Brewster angle ( $\sim 73^\circ$ ). The mid-IR beam generated by TOPAS-C had a beam diameter of  $\sim 4$  mm. Using a negative lens (*Thorlabs LC5893-E*) was used to make the beam diverge to achieve a better numerical aperture (NA) and therefore better focusing of the mid-IR beam on the sample.

Both beams were focused on the sample in a non-collinear fashion using a separate set of optics. This allowed for the individual optimization of the position and focus point of each of the beams. For the visible beam, a fused silica lens with focal length of 750 mm was used (*Thorlabs LA1978*). This was the shortest length which could be used given the geometry of the vacuum chamber and resulted in a NA of  $\sim 0.01$ . For the mid-IR beam a  $\text{CaF}_2$  lens was used (*Thorlabs LA5956*) with a focal length of 500 mm, which combined with the negative lens, yielded an effective focal length of 750 mm with an acceptable NA of  $\sim 0.01$  and a spot size of  $200 \mu\text{m}$ . If the mid-IR beam was focused on the sample with a single positive lens, a spot size of  $\sim 1$  mm would have been achieved, resulting in a weaker BB-SFG signal. Translating the negative lens perpendicular to the propagation direction of the beam allowed for very accurate positioning of the mid-IR spot on the sample, translating the lens along the propagation direction of the beam allowed an accurate control over the position of the focal point of the mid-IR beam.

To facilitate achieving temporal overlap of the visible and mid-IR pulses, a large removable mirror was placed after the two focusing lenses which reflected both beams simultaneously, see also Fig. 3.6. An iris was placed at the precise position of the mirror image of the focus spot on the sample. This iris was then used to spatially overlap the two beams. Furthermore, the power of both beams was checked after this iris. A typical power was for either the visible beam or the  $3.3 \mu\text{m}$  beams was 5 mW each. Once spatial overlap was achieved, the mirror was rotated such that the beams fall upon a non-linear optical crystal (NLO) which was a barium borate (BBO) crystal. The crystal was oriented appropriately such that mixing of the two signals did occur. The spatial overlap was ensured by the alignment on the iris, so in this step only



the temporal overlap had to be changed. A SFG signal visible to the naked eye was observed once the temporal overlap (i.e. delay) was set correctly. In most cases a visible SFG signal could be found for several delay values. This was probably due to trailing pulses generated by reflection on a thin-film in the optical path and the strongest one was selected.

### 3.5 ALD reaction chamber

The ALD surface chemistry was studied in a vacuum chamber modified for the ALD process. The chamber was equipped with precursors and co-reactants, the sample holder was changed, new electronics were installed, and software was written to run the ALD process. Figure 3.7 shows a side and top view of the reactor. The vacuum chamber was divided into two parts. Each side was equipped with an *Pfeiffer TMU 261P* turbo molecular pump (TMP) and mechanical backing pump. The mechanical pumps were also used as a roughing pumps. The pressure in the reactor was measured with compact full range gauges (*Pfeiffer PKR261*). These gauges employed a sensor based upon the Pirani principle to measure the pressure down to the low vacuum range (10 mbar). For pressures below low vacuum, a cold-cathode probe was automatically switched on and used to measure the pressure. The reactor was equipped with bake out lamps such that a wall temperature of  $\sim 120$  °C can be reached. During normal operations, the reactor walls were heated to  $\sim 80$  °C, unless a lower (sample) temperature was required.

For the ALD experiments, the reactor was equipped with fast ALD valves (*Swagelok 34C-A-GDFG-1KT*). These valves were controlled using an embedded controller with field-programmable gate array (FPGA) (*National Instruments compactRIO*). The FPGA was driving several electronic relays actuating the ALD valves. The operating time of the relays was specified as better than 10 ms, which is slower than the specified response time of the ALD valves of 5 ms. Only pulses of 10 ms or longer were used in the experiments to guarantee a good reproducibility of dose. The precursors were delivered in a vapor drawn configuration, with optional line and precursor-pot heating which was used to prevent precursor condensation in the precursor line. For liquid co-reactants, such as  $\text{H}_2\text{O}$ ,  $\text{D}_2\text{O}$ ,  $\text{CH}_3\text{OH}$ , MeCp, a vapor drawn configuration was used. For oxygen, which was used as a co-reactant in the Pt ALD process, a separate gas line was installed. A needle valve was placed in between the  $\text{O}_2$  source and the ALD valve. This resulted in the smallest possible dead volume reducing the height of the pressure pulse. When both TMPs were used to pump the chamber the ALD saturation doses were found to be very sensitive to minor changes in the sample holder (described later) connecting the two chambers to each other. For the ALD experiments, the isolation valve of the TMP pumping the deposition chamber was closed, effectively operating with 1 TMP. This ensured that the gas-phase reactants could interact with the sample before being pumped out of the reactor.

The sample on which the ALD films were grown was placed in between the

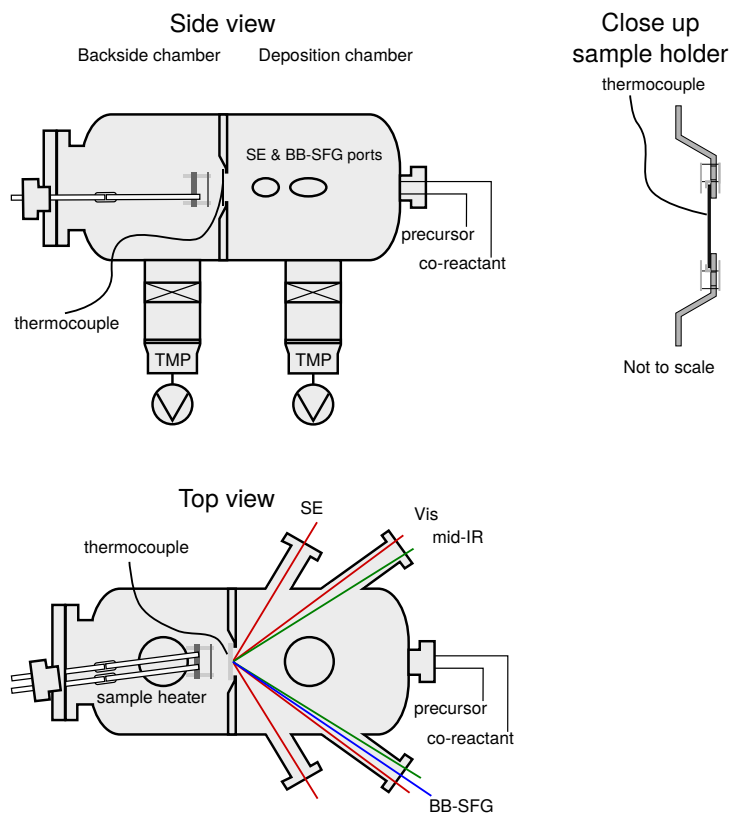


**Figure 3.7:** The geometry of the vacuum chamber used for the in-situ ALD experiments. The main components of the reactor are labeled in the drawing. For scale, the length of the reactor is indicated in the figure.

two compartments of the vacuum chamber. The mount for the sample was designed to accept 2 inch wafers of varying thickness. The samples themselves will be described where relevant. Figure 3.7 shows a cross section of the design of the sample holder as an inset in the figure. Mounting the sample in this fashion ensures that the thickness of the sample did not influence the positioning of the surface significantly. The thickness added by the ALD process it self, typically below 1.5 Å per cycle, was negligible compared to the spot size of either the visible or mid-IR beam. The sample was heated radiatively from the back with a Boralectric heating element (*GE Advanced Ceramics ACSF0073 HTR1002*). Temperature readout and control was performed using a thermocouple (*Thermocoax 2ABAc05/1m/TI/FIM.K*) glued with thermal paste (*RS 186-3600*) to the back side of the sample.

The entrance window used to admit the visible and mid-IR beams driving the SFG process had to be transparent in both the visible and mid-IR part of

the spectrum. To avoid strong nonlinear optical effects in the windows, such as SHG, a material with inversion symmetry was chosen. Typical IR window materials such as ZnS, do not possess such a symmetry and could not be used. Both  $\text{CaF}_2$  and  $\text{BaF}_2$  were suitable materials meeting all the requirements.  $\text{CaF}_2$  windows were chosen (*TSL BVPZ38LACAF2*) because their cubic crystal structure resulting in isotropic optical properties. The concern that these windows would be coated by the ALD processes, leading to a decrease in transmission of either of the beams, was unfounded. After several thousand cycles of  $\text{Al}_2\text{O}_3$  and Pt ALD, the transmission remained virtually unchanged. The only requirement for the exit window was that it should be transparent for the SFG light ( $\sim 740$  nm) which was met by standard fused silica windows. Fused silica also conveniently blocked a part of the mid-IR light.

Complementary to the BB-SFG diagnostic, the reactor was also equipped with in-situ spectroscopic ellipsometry (SE). For these SE measurements, the reactor has been fitted with two stress free windows. SE has been shown to be a valuable tool in characterizing the behavior of the ALD process.<sup>9</sup> In this work SE was mainly used to verify the expected ALD behavior and to determine the growth-per-cycle (GPC). A quadrupole mass spectrometer (QMS) was also available for leak testing purposes. The QMS was not differentially pumped so it could not be used during ALD reactant exposure.

### 3.6 Detection of the BB-SFG signal

To detect the weak (100 photons per second at most) BB-SFG signals required a sensitive detector but also efficient collection of the light with good suppression of undesired light. Figure 3.8 shows the optics used to suppress background light and detect the BB-SFG signal.

The visible, mid-IR and BB-SFG beams exited the vacuum chamber on the detection side. The non-collinear geometry ensured that the beams diverge from each other. At the position where the beams no longer overlap, the direction of the three beams was made parallel by a positive lens (*Thorlabs LA1779*) with its focal point at the position where the SFG occurs. The BB-SFG signal was separated from the undesired and relatively intense visible and mid-IR beams by an iris centered around the BB-SFG signal (this had to be adjusted every time the optical system was realigned). The scattered laser light, predominately from the visible beam due to its shorter wavelength, was removed by using 4 shortpass filters (each with an optical density  $> 5$  above 750 nm, *Thorlabs FES0750*). A second iris was placed around the BB-SFG beam to reduce the stray light further. This detection arm was shielded from unavoidable background light in the darkened lab by a rubberized cloth. Finally the BB-SFG signal was passed through a polarizer (*Thorlabs GL10*) to select the appropriate polarization and the light was focused on the slit of the spectrograph using a lens (*Thorlabs LA1145*).

A spectrograph and CCD camera were used to collect the BB-SFG spectra. The BB-SFG signal, generated from a 800 nm visible pulse and 3-5  $\mu\text{m}$

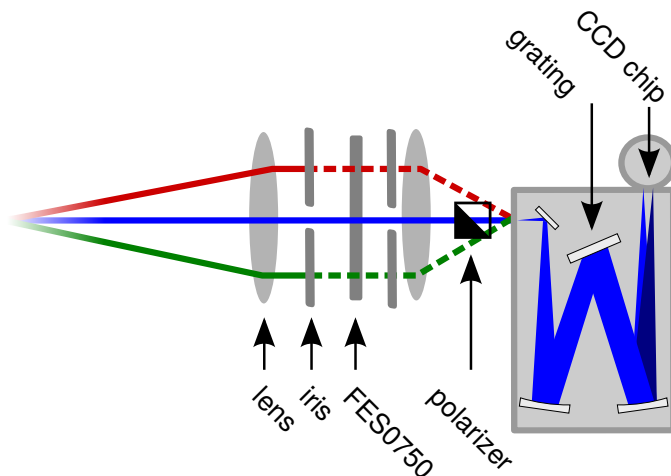


**Figure 3.8:** Sketch of the beam geometry and optics in the detection arm of the BB-SFG setup. The dashed lines represent the path of the visible and mid-IR beams when left unblocked for alignment purposes. A single FES0750 shortpass filter is drawn for simplicity but 4 filters are in use.

mid-IR, was located around 740 nm. This implies that highly sensitive *c*-Si based detectors and efficient spectrograph could be used. A 500 mm spectrograph (*Action Research SP2500*) with a 1200 g/mm grating blazed for 740 nm was used. The efficiency of the grating was  $> 70\%$  at 740 nm and virtually independent on the polarization at this wavelength. The signal was detected with a back-thinned back-illuminated *c*-Si CCD (*Princeton Instruments 100B* excelon coated chip + *Spec-10* LN cooled detector). The quantum efficiency of the chip was  $\sim 0.95$  for the spectral range relevant for BB-SFG spectroscopy. Using the slow readout mode and a gain-setting of 3 of the detector, each photon was roughly proportional to 1 count. The chip, which has 100x1340 pixels, was fully binned in the direction perpendicular to the dispersion direction (i.e. the 100 pixel axis). In the dispersion direction, groups of 4 pixels were binned. A slit width of 200  $\mu\text{m}$  was found to be the most convenient, offering a good balance between reducing stray light and insensitivity to minor changes in alignment of the BB-SFG signal. For a  $-\text{CH}_3$  covered surface during ALD, typically a good S/N was achieved with a 120 s acquisition. For longer acquisition times the number of artifacts induced by “cosmic rays” became too numerous. Depending on the experiment, the acquisition was varied which will be indicated in the text.

Aligning the detection arm was non-trivial since the BB-SFG signal itself was very weak. For most techniques, either a small signal on a strong background needs to be detected, or the detected signals is relatively strong. In the case of BB-SFG neither was the case, so a robust alignment procedure was required. Course alignment was achieved by removing all the optics except

for the two lenses, using a sample which generated a strong SFG signal and closing the slit of the spectrograph. First, the plane in which the mid-IR and visible beams propagate was aligned with the optical plane of the spectrograph. The two detection lenses needed to be adjusted such that both the visible and mid-IR signals fell on the entrance slit of the spectrograph. When both the visible and mid-IR signals are imaged simultaneously on the slit of the spectrograph, there was a good chance that the BB-SFG signal was also imaged on the CCD chip. The long pass filters were placed back before the slit was opened, preventing damage to the optics inside the spectrograph. For the coarse alignment, a slit of  $\sim 1$  mm was found to be most convenient. Once the BB-SFG signal was detected, the slit was narrowed and the focus of the BB-SFG on the slit was re-optimized. Finally, the irises and polarizer were placed back and centered around the BB-SFG signal. The irises were closed to  $\sim 5$  mm aperture without affecting the strength of the BB-SFG signal.

### 3.7 Recommendations for improvements

Several ideas exist to improve the setup which were not executed. In most cases there was no immediate need for these improvements, however these might become very valuable in the future.

- Change reactor geometry so that focal length of  $\sim 5$  cm can be used instead of the current 75 cm. This will greatly improve the signal-to-noise ratio. A more shallow angle of incidence would also be beneficial increasing the electric field perpendicular to the sample surface leading to a stronger SFG signal further enhancing the signal-to-noise ratio.
- Set up a mechanism for dosing a well defined amount of precursor or reactant into the reactor. At the same time, monitor the dosing with a fast well calibrated pressure gauge. This will improve the accuracy with which reaction cross sections can be determined.
- Adding a plasma source (e.g. an electron cyclotron resonance (ECR) source) would allow the study of plasma-enhanced ALD. This is especially interesting because of the much richer chemistry in plasma ALD compared to thermal ALD.
- A continuous reference measurement, preferably with identical optics on a  $\alpha$ -quartz crystal, would allow for an easy comparison of data between different measurement. Moreover, drift in alignment can be detected and no longer influence the outcome of the measurement.
- The software controlling the ALD process and the acquisition of BB-SFG spectra could be integrated. This would facilitate collection of spectra. However, this would not allow higher temporal resolution by simply taking multiple short (e.g. 10 ms) acquisitions and averaging over consecutive ALD cycles. For a good signal to noise ratio an acquisition time of 120 s was needed. In the best case, the same total acquisition time is needed if multiple short acquisitions are used. This would mean

averaging over 12000 cycles, which is not a practical number.

- For initial growth studies, a sample holder needs to be designed which allows one to quickly load a sample. Currently, the sample loading procedure takes roughly an hour including a gluing and a curing step of the thermocouple onto the sample. Loading a fresh sample each experiment is not feasible at the moment, unless the fresh surface could be prepared in-situ (with e.g. vapor phase HF or by evaporating the deposited film).

Several additional capabilities could be interesting for future experiments. The following modifications could be made to the setup relatively easily, offering new capabilities.

- Phase resolved BB-SFG could be implemented in several ways, for a discussion see Shen and Gallmann et al.<sup>10,11</sup> The phase information would facilitate the deconvolution of multiple overlapping peaks. For example, this might be of value deconvoluting the BB-SFG spectra with a complex mixture of CH<sub>x</sub> or OH groups.<sup>12</sup>
- Using a laser system which produces shorter pulses allows one to cover a broader part of the spectrum without tuning the OPA. These systems typically have a comparable output power and this power is spread over a larger part of the spectrum. This will degrade the signal-to-noise as the intensity per cm<sup>-1</sup> will decrease. Depending on the use case this might be valuable or not.
- If higher spectral resolution is needed, various schemes with two broadband pulses are possible.<sup>13</sup> This might be interesting for investigating minor shifts in vibrational frequency due to environmental factors. Alternatively, a more narrow visible beam could be used to enhance spectral resolution at the cost of signal strength.
- Motorizing the variable waveplate and polarizer in the visible, mid-IR, and BB-SFG beams would allow the collection of different polarization combinations on a routine basis. From this information, the orientation and distribution of the surface groups can be determined in some cases.<sup>14,15</sup>

## Bibliography

- [1] Guyot-Sionnest, Hunt, and Shen. Sum-frequency vibrational spectroscopy of a Langmuir film: Study of molecular orientation of a two-dimensional system. *Physical Review Letters*, 1987. doi:[10.1103/PhysRevLett.59.1597](https://doi.org/10.1103/PhysRevLett.59.1597).
- [2] Shen. Surface properties probed by second-harmonic and sum-frequency generation. *Nature*, 1989. doi:[10.1038/337519a0](https://doi.org/10.1038/337519a0).
- [3] Richter, Petralli-Mallow, and Stephenson. Vibrationally resolved sum-frequency generation with broad-bandwidth infrared pulses. *Optics Letters*, 1998. doi:[10.1364/OL.23.001594](https://doi.org/10.1364/OL.23.001594).
- [4] Hsieh, Campen, Vila Verde, Bolhuis, Nienhuys, and Bonn. Ultrafast Reorientation of Dangling OH Groups at the Air-Water Interface Using Femtosecond Vibrational Spectroscopy. *Phys. Rev. Lett.*, 2011. doi:[10.1103/PhysRevLett.107.116102](https://doi.org/10.1103/PhysRevLett.107.116102).
- [5] Ghosh, Smits, Bredenbeck, Dijkhuizen, and Bonn. Femtosecond time-resolved and two-dimensional vibrational sum frequency spectroscopic instrumentation to study structural dynamics at interfaces. *Review Of Scientific Instruments*, 2008. doi:[10.1063/1.2982058](https://doi.org/10.1063/1.2982058).
- [6] Lagutchev, Hambir, and Dlott. Nonresonant Background Suppression in Broadband Vibrational Sum-Frequency Generation Spectroscopy. *The Journal of Physical Chemistry C*, 2007. doi:[10.1021/jp075391j](https://doi.org/10.1021/jp075391j).
- [7] Lagutchev, Lozano, Mukherjee, Hambir, and Dlott. Compact broadband vibrational sum-frequency generation spectrometer with nonresonant suppression. *Spectrochimica acta. Part A, Molecular and biomolecular spectroscopy*, 2010. doi:[10.1016/j.saa.2009.12.066](https://doi.org/10.1016/j.saa.2009.12.066).
- [8] Koechner. *Solid-State Laser Engineering*. Springer New York, New York, NY, 4th extens edition, 2006. doi:[10.1007/0-387-29338-8](https://doi.org/10.1007/0-387-29338-8).
- [9] Langereis, Heil, Knoop, Keuning, van de Sanden, and Kessels. In situ spectroscopic ellipsometry as a versatile tool for studying atomic layer deposition. *Journal of Physics D: Applied Physics*, 2009. doi:[10.1088/0022-3727/42/7/073001](https://doi.org/10.1088/0022-3727/42/7/073001).
- [10] Shen. Phase-sensitive sum-frequency spectroscopy. *Annual review of physical chemistry*, 2013. doi:[10.1146/annurev-physchem-040412-110110](https://doi.org/10.1146/annurev-physchem-040412-110110).
- [11] Gallmann, Steinmeyer, Sutter, Rupp, Iaconis, Walmsley, and Keller. Spatially resolved amplitude and phase characterization of femtosecond optical pulses. *Optics letters*, 2001. doi:[10.1364/OL.26.000096](https://doi.org/10.1364/OL.26.000096).
- [12] Ostroverkhov, Waychunas, and Shen. New Information on Water Interfacial Structure Revealed by Phase-Sensitive Surface Spectroscopy. *Physical Review Letters*, 2005. doi:[10.1103/PhysRevLett.94.046102](https://doi.org/10.1103/PhysRevLett.94.046102).
- [13] McGuire, Beck, Wei, and Shen. Fourier-transform sum-frequency surface vibrational spectroscopy with femtosecond pulses. *Optics letters*, 1999. doi:[10.1109/QELS.2000.902079](https://doi.org/10.1109/QELS.2000.902079).
- [14] Tateishi, Kai, Noguchi, Uosaki, Nagamura, and Tanaka. Local confor-

- mation of poly(methyl methacrylate) at nitrogen and water interfaces. *Polymer Chemistry*, 2010. doi:[10.1039/b9py00227h](https://doi.org/10.1039/b9py00227h).
- [15] Roeterdink, Berg, and Bonn. Frequency- and time-domain femtosecond vibrational sum frequency generation from CO adsorbed on Pt(111). *The Journal of chemical physics*, 2004. doi:[10.1063/1.1802291](https://doi.org/10.1063/1.1802291).





# Practical considerations for BB-SFG spectroscopy studying ALD growth on *c*-Si

## 4.1 Introduction

Broadband sum-frequency generation (BB-SFG) spectroscopy is a state of the art analysis technique and as such it has been successfully employed in the field of surface science to study the surface groups on a wide range of materials. In this project it was used for the first time to study the surface chemistry of atomic layer deposition (ALD). Following the surface chemistry in an ALD reactor came with its own set of challenges.

The first practical question when operating the newly built BB-SFG spectroscopy setup was whether it was capable to detect a sub-monolayer of the surface groups of interest. To evaluate the performance and sensitivity of the BB-SFG setup, several procedures were developed which will be described in this chapter. Some of these procedures were especially suited for benchmarking the setup during daily operation. These benchmarks were used to (quickly) test whether the setup was sufficiently optimized so that a sub-monolayer sensitivity (for groups such as  $-\text{CH}_3$  and  $-\text{OH}$ ) has been reached. The various benchmarks also provided a method to test different types of nonlinear contributions.

In the field of surface science, SFG spectroscopy has been used to study the surface chemistry of several classes of systems: (1) Adsorbates such as CO on for example Pt or Pd.<sup>1,2</sup> (2) Interfaces between different phases (solid, liquid, vapor) of transparent media.<sup>3-5</sup> (3) Highly ordered surfaces such as the terminal groups of self-assembled monolayers<sup>6</sup> and the Si(111)/H surface.<sup>7,8</sup> Reasonably strong signals were obtained from each of these systems due to various reasons. For the metals, the non-resonant background of the metals helped in signal detection although it did complicate the interpretation of the spectral response. For transparent materials, the Fresnel coefficients describing the strength of the fields at the surface were favorable, leading to relative strong SFG signals. For the highly ordered surfaces, there was

negligible cancellation (i.e. destructive interference) due to a large degree of order in e.g. orientation of the surface groups. However, when studying the surface chemistry of ALD on *c*-Si, the sensitivity of BB-SFG spectroscopy was impeded by a combination of factors: (A) A fair amount of random orientation of the surface groups quenched the BB-SFG signal.<sup>9</sup> (B) Unfavorable Fresnel coefficients. (C) A non-resonant background too weak to aid in detection but strong enough to obscure the signals from surface groups. The concurrence of these phenomena made detection of the surface groups involved in the ALD growth mechanism challenging. The first factor was inherent to the surface subject to study and cannot be changed. Factor (B) was addressed by adding an additional spacer layer on top of the *c*-Si. This resulted in more favorable Fresnel coefficients and therefore enhancing the signal strength and sensitivity. The impact of factor (C) was reduced by timing the fs pulses such that the non-resonant contributions were strongly suppressed. Both approaches were key in reaching a sub-monolayer sensitivity for this specific use case.

The structure of this chapter is as follows: Section 2 describes the benchmarks used in this work to evaluate the performance of the setup. In Section 3, the Si-H stretch mode of prototypical and well studied H terminated Si(111) surface was investigated. As a showcase, the reaction kinetics of the dissociation of the Si-H groups on the surface due to exposure of the surface to UV light of two different wavelengths was investigated using the ex-situ setup. Section 4 describes how linear optics were exploited to enhance the signal SFG strength, alleviating one of the aforementioned issues with BB-SFG spectroscopy on *c*-Si. In Section 5, the technique used to suppress the non-resonant signal of the *c*-Si substrate was described and explained. In final section, the main points of attention for BB-SFG spectroscopy with the goal of studying the ALD growth mechanism were summarized.

## 4.2 Suitable benchmarks for the BB-SFG setup

An important part of implementing a new analysis setup was establishing a series of procedures with appropriate reference samples for evaluating the performance of the setup. This ensures that the performance of the setup could be followed over time and also helped when a major change was made to the system. To perform such a check for the current system, the chamber was opened and the appropriate reference sample for that experiment was mounted in the reactor. By monitoring the signal generated by the reference sample, the alignment of the optical components of the setup was optimized. Once a known signal strength was reached, it was fairly certain that the setup should again have the sensitivity to detect a sub-monolayer of e.g.  $-\text{CH}_3$  groups. It is desirable that such a reference sample was stable over time. Moreover, the signal generated by the reference sample should be strong enough such that a spectrum could be acquired within  $\sim 1$  second with a good signal-to-noise ratio. This yielded fast enough feedback on any changes made to the setup, e.g. the orientation of a mirror, to optimize the SFG signal

efficiently. Three types of surfaces were found to be useful as reference samples in this work: The surface of a GaAs crystal, the surface of a Au film, and the surface of a series of polymers. Each of these surfaces served a different purpose and each will be discussed here.

## Bulk GaAs

Crystalline GaAs was selected as one of the benchmark materials. This material was ideal for alignment purposes, allowing a wide spectral range to be inspected without having to change the sample. The crystal structure of GaAs is zincblende ( $F\bar{4}3m$ ) which does not possess inversion symmetry. Therefore GaAs exhibits both a surface contribution and a strong bulk SFG contribution. Considering the penetration and escape depth of the visible, mid IR, and BB-SFG signals, the signal will have a significant bulk contribution limited in part by phase matching.<sup>9</sup> The penetration depth of light with a wavelength  $\lambda = 650$  nm, 800 nm, and 3  $\mu\text{m}$  was 250 nm, 700 nm, and  $>1$   $\mu\text{m}$  respectively. The BB-SFG signal obtained from the GaAs crystals was strong which was very useful for initial alignment. A 2 inch GaAs wafer with a (100) surface and a resistivity of  $2 \cdot 10^{-3}$  Ohm  $\cdot$  cm obtained by Si doping was used as a reference sample in most cases. The GaAs wafer was oriented with the [011] direction parallel to the  $s$  polarization direction of the light. See Fig. 4.1 for an example of a BB-SFG spectrum obtained from a GaAs reference sample. The flat spectral response of GaAs over a wide spectral range (2 - 10  $\mu\text{m}$ ) is due to the absence of any vibrational states in the mid-IR region. This means that the generated BB-SFG spectra reflect the shape of the broadband mid-IR signal as explained in Chapter 2. Multiple polarization combinations can be used on this sample and yield strong SFG signal as can be deduced from the known values for the  $\bar{\chi}$  tensor.<sup>10,11</sup> This includes the Ssp polarization combination which represents the generation of S-polarized SFG light from s-polarized visible light and p-polarized mid-IR light. This Ssp polarization combination is of interest since it is known to generate the strongest SFG signal for the stretch modes of the surface groups relevant for this work ( $-\text{OH}$ ,  $-\text{SiH}$ , and  $-\text{CH}_3$ ) if these groups are oriented perpendicular to the surface.<sup>12</sup>

A target signal strength on GaAs of  $1 \times 10^5$  counts per second per pixel (binning 4 pixels in the dispersion or  $\lambda$  direction) was found to be an appropriate benchmark for the detection of a sub monolayer of  $-\text{CH}_3$  groups using the Ssp polarization combination on a  $c$ -Si substrate with a  $\sim 90$  nm  $\text{SiO}_2$  spacer.

## The gold surface

The surface of gold is known for its large non-resonant nonlinear response and is commonly used as reference samples.<sup>6,13-15</sup> Because of the strong SFG response, this surface is also often used for alignment purposes. However, the surface chemistry at the Au surface itself is also of interest.<sup>2,16</sup> The Au sample used here consisted of a 2 inch  $c$ -Si substrate (Si(100) with native oxide) on which a  $\approx 20$  nm adhesion layer of Ti was evaporated. On this adhesion layer

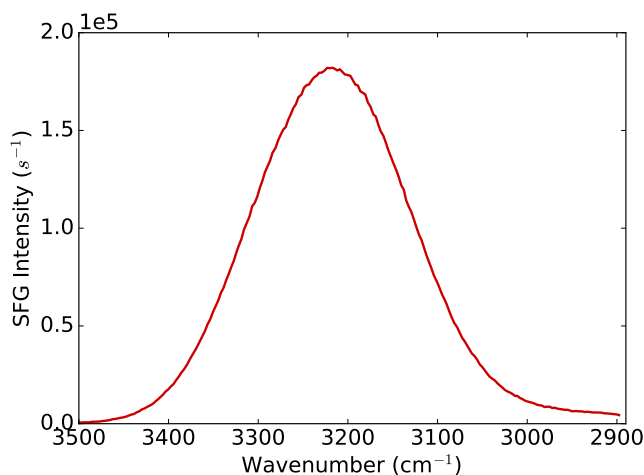


**Figure 4.1:** The BB-SFG signals from a GaAs sample using the Ssp polarization combination. The fairly strong BB-SFG signal makes this sample ideal as a benchmark when aligning the setup after a major change.

a  $\approx 100$  nm Au film was evaporated. In contrast to GaAs, the response of the Au sample originated predominantly from the surface although both surface and bulk contributions were present.<sup>17</sup> The penetration depth of the light into the Au film, for the wavelengths used in the BB-SFG experiments, was less than 50 nm. Figure 4.2 shows a typical BB-SFG spectrum recorded on Au. Due to the conductivity of Au, only electric fields pointing perpendicular to the surface normal can exist near the surface, i.e. p-polarized light. Hence, the spectra recorded of the Au surface were performed using the Ppp polarization combination. Similar to the spectra recorded on GaAs, the spectral shape of the BB-SFG spectrum reflects the spectral shape of the broadband mid-IR beam.

The Au surface has a limited use as a benchmark for BB-SFG spectroscopy since it is constrained to the Ppp polarization combination. Nevertheless, it is one of the prototypical samples and it has to be included in a characterization of the setup. The main benefit of the Au surface over the GaAs wafer is that the signal originates from the surface whereas the GaAs signal is more a bulk signal. Therefore, the alignment will more closely resemble the alignment required for the surface chemistry on *c*-Si. The Au reference sample was used in most cases for the alignment of the setup for experiments using the Ppp polarization combination.

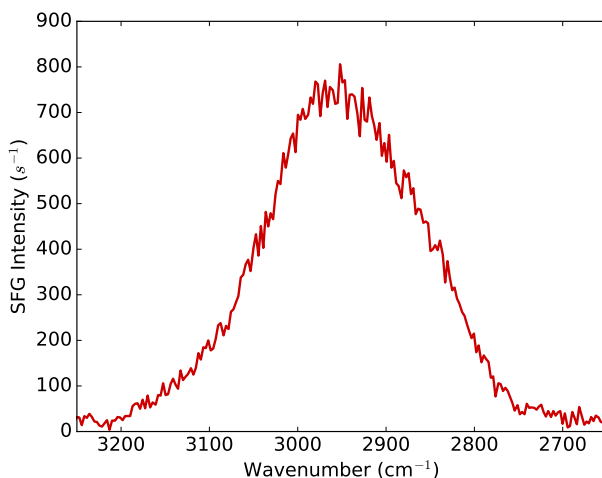


**Figure 4.2:** The BB-SFG signals from a Au sample serve as a benchmark for the setup for Ppp polarization mode. Note that a smaller binning in the  $\lambda$  direction of 2 instead of 4 pixels was used.

### Polymer surfaces

Polymers are useful as reference samples since they offer a wide selection of functional groups and therefore a wide selection of surface terminations. These surfaces provided a convenient benchmark for the detection of resonant BB-SFG signals. Free standing,  $\sim 500 \mu\text{m}$  thick, foils were used of high-density polyethylene (HDPE), polyethylene (PE), polyethylene terephthalate (PET), and polyethylene naphthalate (PEN). A poly (methyl methacrylate) (PMMA) film was prepared by spin coating a solution of PMMA in anisole (A2 solution) onto a Si(100) wafer. This standard procedure resulted in a  $\approx 90 \text{ nm}$  PMMA film on the Si(100) substrate. Figure 4.3 shows a graphical representation of the structure of the polymers investigated with BB-SFG spectroscopy in this work.

For each of these polymers, BB-SFG spectra were collected of the C-H stretching region which is situated around  $3000 \text{ cm}^{-1}$  using both the Ssp and Ppp polarization configuration. The measured BB-SFG spectra for the polymers are shown in Fig. 4.4. For each polymer, the central wavelength of the mid-IR beam was tuned to slightly different to achieve the best signal-to-noise ratio. For each of the polymers, the spectral position of the detected resonances were in agreement with the position reported for linear and non-linear spectroscopy as can be seen in Tab. 4.1. In general, the more rigid the backbone of a  $\text{CH}_x$  groups, e.g. due to a double bond, the larger the vibrational energy (higher wavenumbers) of the C-H stretch mode. A detailed treatment of the mid-IR response (for linear optics) of these polymers, establishing a link between spectral information and the microscopic and macroscopic structure,

is for example given by Koenig.<sup>18</sup> The peak assignment in SFG spectroscopy is often based upon the spectral position of the resonance known from linear (absorption) spectroscopy. However, for PMMA a more in depth study of the peak assignment for SFG spectroscopy was performed by Tateishi et al.<sup>19</sup> Their approach was as follows: They investigated PMMA in which the  $-CH_x$  groups were replaced group-by-group with  $-CD_x$ . The heavier mass of D compared to H shifts the vibrational frequency of the C-H stretch modes.<sup>11</sup> This shift therefore allowed for a direct assignment of the vibrational modes. In general, minor deviations (in the range of  $\sim 20\text{ cm}^{-1}$ ) are observed when comparing the spectral position of stretch modes in SFG spectroscopy with those observed in linear IR spectroscopy. Moreover, some weaker vibrational modes seen with either Raman or absorption spectroscopy have not yet been investigated and/or observed with SFG spectroscopy.

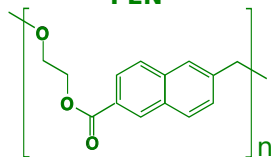
It is important to realize that in most cases the BB-SFG spectra are dominated by one or a few vibrational modes that can overlap and obscure weaker vibrational modes. In some cases, the weaker modes overlapping with a strong mode can be made more visible by selecting a different mid-IR central wavelength. Counter intuitively, it can be beneficial to select a central wavelength away from both the strong and the weak resonance on the side of the weak contribution. This weakens the strong contribution more than the weak contribution due to the Gaussian spectral shape of the mid-IR beam, making the weak contribution easier to discern. The BB-SFG response of the PMMA surface is a good example of this phenomena. The BB-SFG spectrum of the PMMA, typically reported in literature, is shown in Fig. 4.4.<sup>6</sup> However, as demonstrated earlier in Fig. 2.8, other modes are also present. A similar situation arises for CO on Pt, as shown by Lagutchev et al., where two weaker modes associated with CO on Pt actually provide vital insights into the chemistry.<sup>2</sup> These results demonstrate that it is valuable to investigate whether there are any weaker resonances adjacent to the strong resonances readily observed in the BB-SFG spectra.

Often the polymers surfaces and especially the spin coated PMMA surfaces are used in the calibration of the exact mid-IR wavelength associated with the SFG signal because of the well known, well defined, and fairly stable spectral position of such resonances.<sup>6</sup> Without this procedure, only the relative spectral positions can be determined. This procedure was not performed in this work since the benefit was minimal in this case.

**Table 4.1:** Spectral position of the C–H<sub>x</sub> stretch modes of PE, PMMA, PEN, and PET as reported for FTIR absorption spectroscopy. Typically, the spectral position reported for the same groups in SFG spectroscopy shows a offset ( $\sim 20\text{ cm}^{-1}$ ) and a larger variation than the positions reported for FTIR spectroscopy. In the table  $\nu$  sym/asym stand for symmetric stretch and asymmetric stretch respectively.

Polymer	Vibrational mode	Resonance ( $\text{cm}^{-1}$ )	FTIR	BB-SFG
PE	CH <sub>2</sub> asym $\nu$	2920	20	this work, <sup>12,20</sup>
PE	CH <sub>2</sub> sym $\nu$	2850	20	12,20
HDPE	CH <sub>2</sub> asym $\nu$	2920	20	this work, <sup>12,20</sup>
HDPE	CH <sub>2</sub> sym $\nu$	2850	20	12,20
PMMA	CH <sub>2</sub> asym $\nu$	2958	21	19,22
PMMA	CH <sub>2</sub> sym $\nu$	2932	21	19
PMMA	CCH <sub>3</sub> asym $\nu$	3000, 2958	21	-
PMMA	CCH <sub>3</sub> sym $\nu$	2930	21	-
PMMA	OCH <sub>3</sub> asym $\nu$	3025, 3002	21	12,19,22
PMMA	OCH <sub>3</sub> sym $\nu$	2961	21	this work, <sup>6,12,19,22</sup>
PEN	CH $\nu$	3060	23	this work
PEN	CH <sub>2</sub> asym $\nu$	2970	23	-
PEN	CH <sub>2</sub> sym $\nu$	2920	23	-
PET	CH $\nu$	3082	24	this work, <sup>25</sup>
PET	CH <sub>2</sub> asym $\nu$	2970	24	25
PET	CH <sub>2</sub> sym $\nu$	2908	24	25

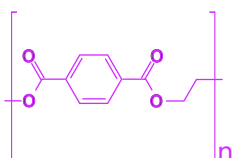
Polyethylene naphthalate  
**PEN**



Polyethylene  
**HDPE & PE**



Polyethylene terephthalate  
**PET**



Poly(methyl methacrylate)  
**PMMA**

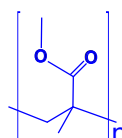


**Figure 4.3:** Chemical structure of the polymer investigated with BB-SFG, with n the chain length. The H atoms are not drawn for brevity and can be inferred from the coordination of the C atoms.



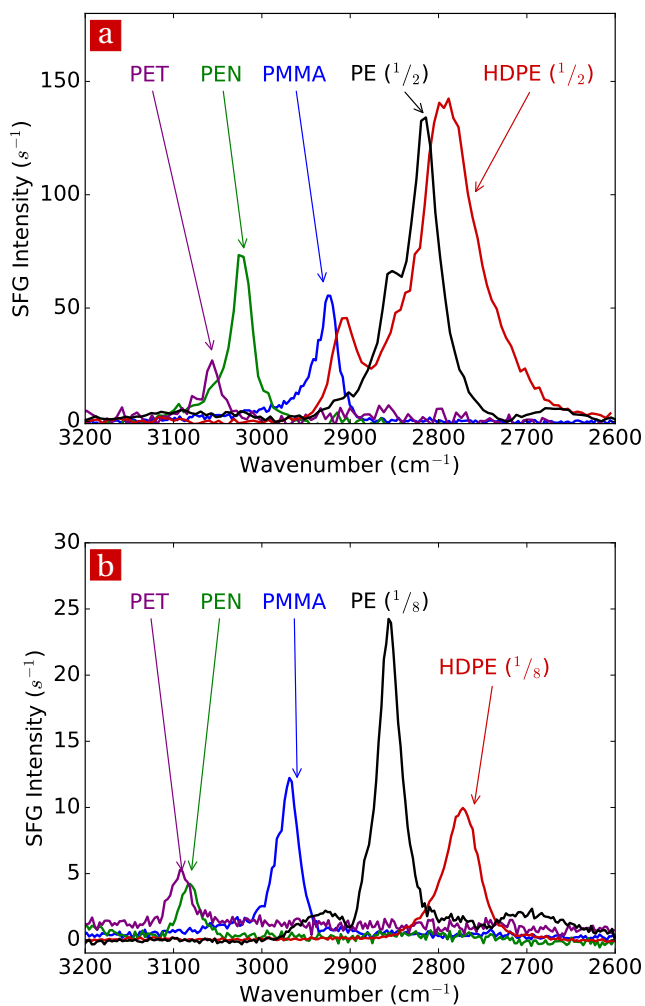


**Figure 4.4:** The BB-SFG response of PET, PEN, PMMA, LDPE, and HDPE in the CH stretch region using (a) the Ssp polarization combination and (b) the Ppp response polarization combination. The intensity of the PE and HDPE spectra were down scaled by multiplying the original intensities by the factors indicated in the figure.

### 4.3 Study case: UV exposure of the H/Si(111) surface

An important step in the production of semiconductor devices is removing the native oxide present on the *c*-Si substrates. This procedure also removes any undesired surface contaminants. Treating *c*-Si with HF acid is one of the industry standards for the removal of native oxide and obtaining a stable H terminated surface for the Si surface.<sup>26</sup> The H terminated Si(111) surface has become a prototypical surface in the field of surface science. This is due to similarities to the industry relevant HF-last Si(100) surface combined with the ideality of the H/Si(111) surface. When prepared correctly, the resulting Si(111) surface is Si-H terminated, atomically flat, and virtually defect free.<sup>27</sup> The Si-H groups on the surface are aligned perpendicular to the surface with negligible angular distribution.<sup>28</sup> It has been shown that the Si-H groups have a very well defined Si-H stretch mode ( $2086\text{ cm}^{-1}$ ) which is extremely narrow ( $0.05\text{ cm}^{-1}$  at 40K).<sup>27-31</sup> Both the IR absorption and the Raman cross section of the Si-H stretch mode are large, making it an ideal subject to be studied with linear,<sup>32-34</sup> and nonlinear vibrational spectroscopy.<sup>8,35,36</sup> Here, this surface was used as a study case to demonstrate the capability of the ex-situ BB-SFG setup to monitor surface chemistry.

When the Si-H groups on the surface of H/Si(111) were exposed to light of sufficiently short wavelength (UV light), the Si-H bond was broken. The reaction kinetics of the dissociation of the Si-H groups due to UV light was studied with the ex-situ BB-SFG setup. Understanding the mechanism responsible for the removal of the Si-H groups is of practical importance for the semiconductor industry. Moreover, it is important to understand how light affects the H/Si(111) surface and the Si-H groups since this surface is often exposed to bright laser pulses in these and other experiments.

So far, the (in)stability of the H/Si(111) surface under UV exposure has received considerable attention. It is known that exposing the H/Si(111) surface to UV light causes the Si-H bond to break.<sup>37-42</sup> The exact microscopic mechanism of this bond breaking is probably complex and several (sometimes quite similar) mechanisms have been reported: (1) Direct photochemical desorption for light with a photon energy above 7.9 eV.<sup>39-41</sup> (2) Photothermal desorption for light with a photon energy  $\sim 4$  eV.<sup>39</sup> (3) Photocleavage of the Si-H bond caused by 4.8 eV photons.<sup>42</sup> (4) Photoinduced oxidation with 1.55 eV photons.<sup>37</sup> The first and second category were studied using  $\sim 25$  ns laser pulses. The third study was performed with a Hg lamp. The fourth study was performed with much shorter (4 ps) laser pulses and with a much higher average intensities than the other experiments. Excluding the last effect, two regimes can be identified with respect to photon energy: Direct photochemical dissociation with a threshold of 6 eV.<sup>39</sup> Mediated bond dissociation for photons with a energy above the bond dissociation energy but below 6 eV. The bond dissociation energy of the Si-H bond is in the range of 3 eV to 4 eV judging from gas-phase data for the dissociation of a Si-H bond in molecules containing such a bond.<sup>37,43</sup> The kinetics of H dissociation in general are com-

plex. For example, for thermal desorption of  $2\text{Si-H} \rightarrow 2\text{Si} + \text{H}_2$ , Reider *et al.* showed that the reaction had an intermediate order of  $m = 1.5 \pm 0.2$ .<sup>44</sup> In this work, the more general term “dissociation” will be used in order to refrain from making a claim about the microscopic process. The reaction kinetics of the Si-H dissociation process, under the influence of either 3.0 eV and 4.8 eV photons, was studied with BB-SFG spectroscopy and the cross section of the process was determined. The two probing laser beams used in the BB-SFG experiments did not affect the H/Si(111) surface itself as was demonstrated in Fig. 3.3.

The H/Si(111) surfaces were prepared following the standard procedure.<sup>29</sup> A Si(111) wafer with native oxide was immersed for 120 s in a buffered hydrofluoric acid (BHF) comprising of 40%  $\text{NH}_4\text{F}$  and 49% HF mixed in a volume ratio of 6:1. After the BHF exposure, the wafer was rinsed in a flow of ultra pure water until the resistivity of the water down stream of the sample reached a resistance  $> 5 \text{ M}\Omega\text{cm}$ . Exposing the Si(111) surface to BHF removed the native oxide and subsequently forms an atomically smooth, Si-H terminated surface which is stable in water.<sup>29</sup> The mechanism responsible for the formation of the atomically flat hydrogen terminated Si(111) is preferential etching of the step edges.<sup>45,46</sup> Considerable reduction of the roughness on the backside of the single side polished wafer was observed which is attributed to the same effect. The removal of the native oxide was confirmed with spectroscopic ellipsometry (SE).

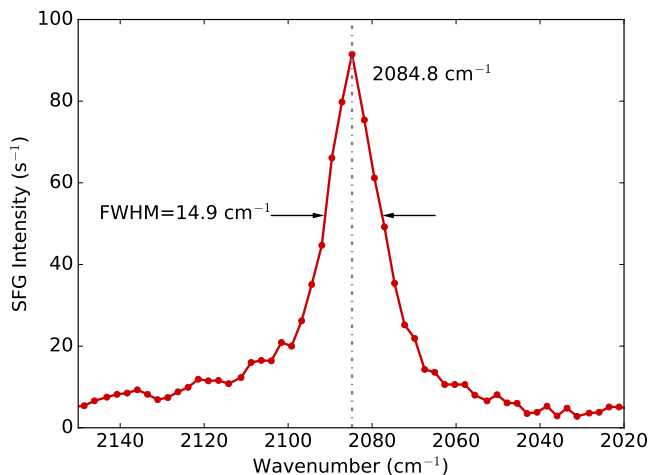


**Figure 4.5:** Ex-situ spectrum of the Si-H stretch mode of a pristine H/Si(111) surface recorded in 10 second.

Figure 4.5 shows a BB-SFG spectrum of the Si-H stretching mode at  $2085 \text{ cm}^{-1}$  of a H/Si(111) prepared as described above. The large SFG cross section of the Si-H stretching mode was reflected by the large intensity of the signal.

The absolute signal strength is larger than the signal of the C–H stretching mode of the polymers, even though the Fresnel coefficients are worse for the H/Si(111) surface. The spectral width of the Si–H peak has been shown to be  $< 1 \text{ cm}^{-1}$ .<sup>29</sup> The peak in Fig. 4.5 is considerably broader which is due to the instrumental broadening as discussed in Chapter 2. After the acquisition of the BB-SFG spectrum of the pristine surface, the sample was exposed to light of a low pressure Hg lamp producing 4.8 eV photons. The next strongest spectral line of this light source has  $\sim 1\%$  of the intensity of the 4.8 eV line and can effectively be neglected. After a 5 second UV exposure, a new BB-SFG spectrum was recorded. This procedure was repeated until the Si-H feature could no longer be discerned. For the second light source, a laser diode producing light with a photon energy of 3.0 eV, the same procedure was used. Table 4.2 lists all the relevant specifications of the two light sources. The Si-H coverage was extracted from the spectra with the procedure discussed in Chapter 2. Figure 4.6 shows the Si–H coverage as a function of the duration of the UV exposure. It is clear that the 3.0 eV photons did not lead to H dissociation whereas the 4.8 eV photons did induce H dissociation despite the lower intensity of the light.

The cross section  $\sigma$  of the dissociation process can be obtained from Fig. 4.6 by modeling the data. The change in Si–H coverage  $\theta$  as a function of time is given by:

$$\frac{d\theta}{dt} = -\sigma\Gamma\theta^n, \quad (4.1)$$

with  $\Gamma$  the photon flux, and  $n$  the order of the reaction. Solving this differential equation assuming first order reaction kinetics ( $n = 1$ ) resulted in an exponential decay of the Si–H coverage with time. The characteristic decay constant of the exponential function was equal to  $\sigma\Gamma$ . This expression was fitted to the data in Fig. 4.6. For comparison, the data was also fitted with the expression which was found assuming that the reaction was second order ( $n = 2$ ) in Si-H coverage. The mean square error of the fit,  $\bar{\chi}_{red}$ , was larger for the latter model suggesting first-order kinetics. For the light source producing 3.0 eV photons no dissociation was observed and therefore the cross section has to be smaller than  $5 \cdot 10^{-19} \text{ cm}^2$ . For the light source generating 4.8 eV photons a cross section of  $8.5 \pm 0.8 \cdot 10^{-17} \text{ cm}^2$  was found. This value is 4 orders of magnitude larger than the cross section reported for the direct photochemical dissociation by [Pusell et al.](#) ( $1.2 \pm 0.8 \times 10^{-20} \text{ cm}^2$ ) and [Vondrak and Zhu](#) ( $2.8 \pm 0.5 \times 10^{-21} \text{ cm}^2$ ) using 7.9 eV photons.<sup>39,40</sup> However, given the photon energy, a different mechanism than photochemical dissociation had to be responsible for the H desorption. [Cicero et al.](#) reported a similar threshold in photon energy for H desorption, however, they did not report a cross section.<sup>42</sup> Moreover, they speculated that a radical-chain reaction is responsible for the oxidation of the Si(111)/H surface exposed to 4.8 eV photons under similar experimental conditions. This radical-chain mechanism was not in agreement with the reaction kinetics shown in Fig. 4.6. The cross section reported by [Bodlaki and Borguet](#) ( $1.7 \pm 0.5 \times 10^{-23} \text{ cm}^2$ ) is significantly smaller and likely

related to a different process in view of the significantly lower photon energy of 1.55 eV.<sup>37</sup>

**Table 4.2:** Details of the two light sources used in the BB-SFG spectroscopy experiments studying the light induced dissociation of Si-H on the H/Si(111) surface. The cross section obtained from the fit to the data in Fig. 4.6 is also given.

		Diode laser	Hg gas discharge
Photon energy	(eV)	3.0	4.8
Intensity	(W m <sup>-2</sup> )	100 ± 10	2.3 ± 0.2
Photon flux	(10 <sup>18</sup> m <sup>-2</sup> s <sup>-1</sup> )	200 ± 20	2.9 ± 0.3
Cross section	(10 <sup>-17</sup> cm <sup>2</sup> )	≪ .05	8.5 ± 0.8

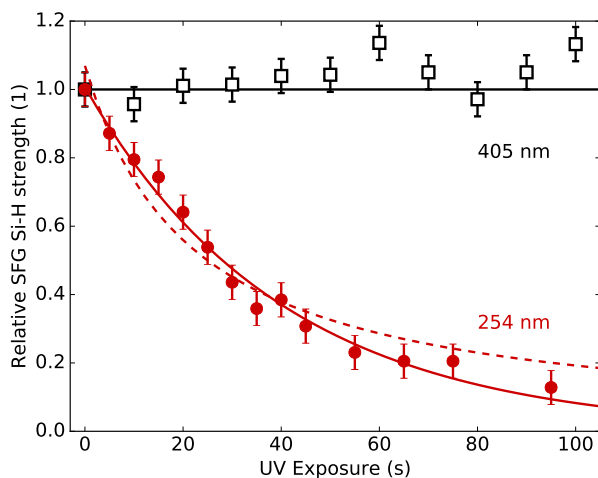


**Figure 4.6:** The Si-H coverage as a function of the exposure to UV light. The wavelength of the light used is indicated in the figure. The solid lines represent exponential fits to the data. For comparison, the dashed line is a fit to the data assuming that the reaction is second order in Si-H coverage.

#### 4.4 Exploiting linear optics for increased sensitivity

The strength of the SFG signal was strongly affected by linear optics. For example, on a bare *c*-Si surface it was difficult to detect the -CH<sub>3</sub> groups involved in the growth of Al<sub>2</sub>O<sub>3</sub> by thermal ALD using Al(CH<sub>3</sub>)<sub>3</sub> and H<sub>2</sub>O. This seems to be in contradiction with the fact that: (1) The Si-H groups on Si(111) were easily detected. (2) The SFG signal from the -CH<sub>x</sub> stretch modes of various polymers was quite strong. (3) The -CH<sub>3</sub> stretch of 90 nm PMMA on

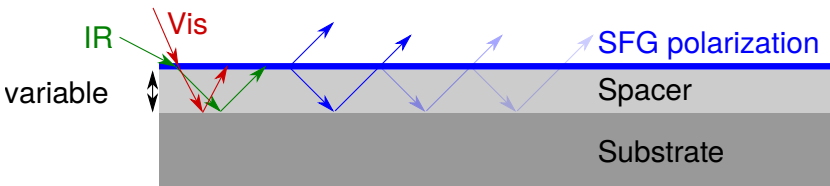
a Si substrate was easily detected. However, for case (1) the SFG cross section was exceptionally large. For cases (2) and (3) the linear optics were much more favorable. To quantify the influence of linear optics on the strength of the SFG signal the “relative probing strength” parameter is introduced. This parameter is a measure for the relative strength of the SFG signal of a group on an arbitrary surface compared to the same group on *c*-Si.

Figure 4.7 shows a schematic of the geometry used in this work. First the effect of linear optics on the driving fields will be discussed, then the influence of linear optics on the escaping SFG light will be treated.

The strength of the two driving electric fields can be calculated for a thin film on a half-infinite substrate using a matrix formalism. Here the approach formulated by Sipe was followed.<sup>47</sup> The strength of the electric field for beam *x* driving the SFG process at the surface of the film is given by,

$$\mathcal{F}_x = 1 + r_{vl} + \frac{t_{vl} r_{ls} t_{lv} \exp(\frac{4i\pi D}{\cos(\theta)\lambda})}{1 - r_{lv} r_{ls} \exp(\frac{4i\pi D}{\cos(\theta)\lambda})} \quad (4.2)$$

where *D* is the thickness of the film,  $\theta$  is the angle of incidence inside the film, and  $r_{ij}$  ( $t_{ij}$ ) represents the Fresnel coefficient for reflection (transmission) of the interface between medium *i* to *j* (with *s* = substrate, *l* = layer, and *v* = vacuum) evaluated at the wavelength  $\lambda$  associated with beam *x* (either *v*is or *i*r).<sup>1</sup>



**Figure 4.7:** The SFG signal is generated by a layer of polarization on the surface (e.g. excited surface groups) of the spacer layer which is on top of the substrate. The driving fields (on the left) are affected by linear optics influencing the strength of the polarization. The polarization layer radiates in two directions: away from the substrate and towards the surface. The upwards signal is detected directly, the downwards signal is only detected after undergoing 1 or more reflections. Interference between the two contributions can enhance or quench the intensity of the SFG signal.

The intensity of the emitted SFG light towards the detector is also affected by linear optics. The dipoles at the surface, caused by the SFG process, produce two electric fields. One field propagates away towards the detector which is labeled  $v_+$ . The other field, labeled  $v_-$ , propagates away from the detector towards the substrate. This light can only be observed after undergoing one

<sup>1</sup>Note that the last term in Eq. (4.2) and Eq. (4.3) can also be written as a sum of contributions using  $\sum_{n=0}^{\infty} x^n = 1 + x + x^2 + \dots = \frac{1}{1-x}$  corresponding more closely to the picture in Fig. 4.7.

or more reflections. The effective field strength is given by,

$$\mathcal{S}_{sfg} = v_+ + v_- \frac{t_{vl} r_{ls} t_{lv} \exp(\frac{4i\pi D}{\cos(\theta)\lambda})}{1 + r_{ls} r_{lv} \exp(\frac{4i\pi D}{\cos(\theta)\lambda})}, \quad (4.3)$$

again following the approach described by Sipe for describing the emission and propagation of light due to a sheet of dipoles inside a stack of thin films.<sup>47</sup> The intensity of the SFG signal  $I_{sfg}$  is then given by:

$$I_{sfg} = |\mathcal{S}_{sfg} \bar{\chi} \mathcal{F}_{vis} \mathcal{F}_{ir}|^2 I_{vis} I_{ir}, \quad (4.4)$$

with  $\bar{\chi}$  the strength of the SFG response,  $I_x$  the intensity of driving field  $x$ . The relative probing strength can now be calculated by simply dividing Eq. (4.4) for a  $c$ -Si substrate with and without a film on top.

Considering the 3 scenarios discussed before, it turns out that for: (1) The effective  $\bar{\chi}$  for the Si-H was extremely large, partly due to the bond itself and partly due to the perfect order, resulting in a fairly strong signal. (2) The polymers without  $c$ -Si substrate had much more favorable Fresnel coefficients. Due to the lower refractive index of the polymer compared to silicon, the  $\mathcal{F}_{ir}$ ,  $\mathcal{F}_{SFG}$  and  $\mathcal{F}_{vis}$  were close to unity. (3) The film thickness for PMMA spin coated on  $c$ -Si was 90 nm, which happens to be the optimal thickness for BB-SFG spectroscopy on a polymer thin-films on a silicon substrate.

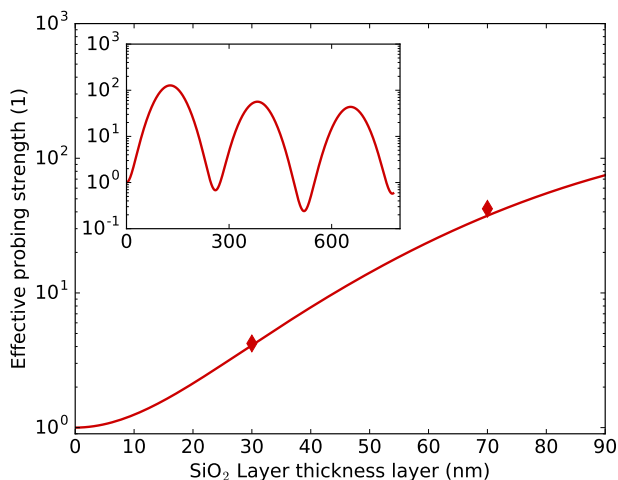


**Figure 4.8:** Enhancement of the BB-SFG signal as a function of spacer thickness as calculated (solid line) and as measured (markers) for a film with a refractive index comparable to  $\text{SiO}_2$ . The inset shows the effective probing strength for a film thickness up to 800 nm.

The effective probing strength of the SFG signal is shown in Fig. 4.8 as a function of the thickness of the  $\text{SiO}_2$  thin-film for such a film on top of  $c$ -Si.

The effective probing strength oscillates with thickness showing several maxima of enhancement at e.g.  $\sim 100$  nm,  $\sim 400$  nm, and  $\sim 650$  nm film thickness. Absorption of the IR light quenches the enhancement, as can be seen from the decreasing maxima with thickness ( see inset in Fig. 4.8). The relation between spacer thickness and effective probing strength was verified by comparing the signal strength of  $-\text{CH}_3$  groups on two different spacer layers. The highly repeatable nature of ALD was exploited to prepare identical  $-\text{CH}_3$  terminated surfaces. Two samples were prepared using Si(100) substrates from the same batch on which a  $\text{SiO}_2$  film was grown with plasma-enhanced chemical vapor deposition (PE-CVD) of 30 and 75 nm thickness respectively. In turn, both samples were mounted in the vacuum chamber. After mounting, a thermocouple was glued to the back of the sample, the chamber was pumped down and the sample was heated to 250 °C. On each sample, 5 ALD cycles were performed to ensure steady state growth, adding a negligible  $\sim 0.5$  nm of  $\text{Al}_2\text{O}_3$  on top of the  $\text{SiO}_2$  spacer. Then the BB-SFG spectra were collected probing the spectral region where the  $-\text{CH}_3$  stretching mode of the chemisorbed precursor ( $\text{Al}(\text{CH}_3)_3$ ) was expected. For each sample, a spectrum was recorded after a saturated TMA exposure and after a saturated  $\text{H}_2\text{O}$  exposure. The spectra obtained by this procedure are shown in Fig. 4.9. The  $-\text{CH}_3$  stretching mode was indeed detected at  $2900\text{ cm}^{-1}$ . The spectral position of the resonance was comparable to the position of the  $-\text{CH}_3$  stretching mode in linear absorption spectroscopy.<sup>11</sup> For both samples, the resonance appeared after TMA exposure and disappeared after  $\text{H}_2\text{O}$  exposure, in agreement with the well known reaction mechanism of this ALD process.<sup>48</sup> The broad spectral feature spanning  $\approx 300\text{ cm}^{-1}$ , which is present in both sets of spectra, was caused by the silicon substrate as was described in detail in the Chapter 2 and 3. The contribution related to the  $-\text{CH}_3$  groups at  $2900\text{ cm}^{-1}$  appeared as a dip in Fig. 4.9(a) and as a peak in Fig. 4.9(b). For the former, the non-resonant background and the resonant contribution were (largely) out of phase, resulting in destructive interference. For the latter spectrum, the resonant contribution was much larger than the non-resonant contribution obscuring the influence of the relative phase between the two contributions. In general, the thickness of the  $\text{SiO}_2$  spacer affects both the *strength* and *phase* of the SFG signal originating from the resonant contribution and the non-resonant contribution differently because the two contributions originate from a different position in the stack. This subtle and intricate interplay between spacer thickness, the phase, and intensity of different contributions can influence the BB-SFG spectra and it is something which should be considered when e.g. designing a new substrate.

The amplitude of the  $-\text{CH}_3$  resonances of both experiments was extracted from the spectra in Fig. 4.9 and plotted on the curve in Fig. 4.8. As can be seen, the experimental results are in good agreement with the predicted enhancement of the probing strength. Minor differences in alignment were the likely cause of the deviation from the theoretical trend. These results indicate that linear optical effects were indeed the main mechanism responsible for the enhancement. Exploiting the optical enhancement using a  $\sim 90$  nm  $\text{SiO}_2$  spacer



– providing the largest possible signal enhancement – was crucial when using BB-SFG to detect  $-\text{CH}_3$  and  $-\text{OH}/-\text{OD}$  surface groups on a silicon based substrate during ALD. Without the enhancement, the surface groups could not be detected using reasonable visible and mid-IR intensities and acquisition times.

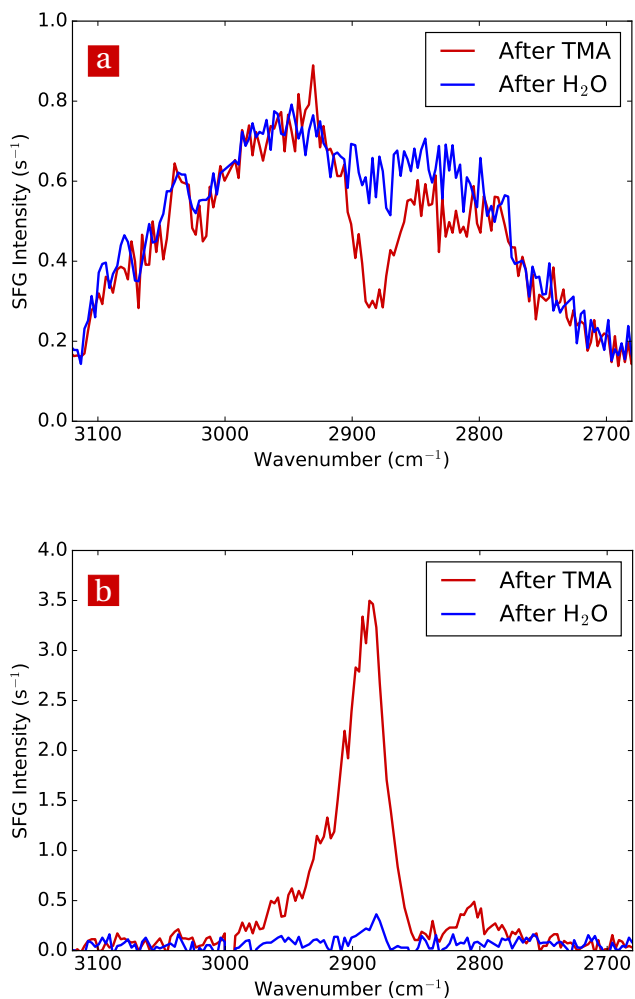


**Figure 4.9:** BB-SFG spectra of a Si(100) substrate with (a) a 30 nm SiO<sub>2</sub> film and (b) a 75 nm SiO<sub>2</sub> film. On these samples ALD is performed, resulting in a -CH<sub>3</sub> terminated surface after the TMA half-cycle and a -OH terminated surface after the H<sub>2</sub>O half-cycle. The resonance due to the C-H stretch mode of the -CH<sub>3</sub> groups is observed at ~2900 cm<sup>-1</sup>, the resonance of the -OH groups falls outside the probed spectral range. In both cases non-resonant suppression was used (see Section 4.5).

## 4.5 Suppression of non-resonant signal

For materials which exhibit a larger non-resonant contribution, such as Au, the non-resonant contribution can be used for (monitoring of) the alignment of the setup. Moreover, the non-resonant contribution enhances the resonant signal because of the cross term in the coherent superposition of the two signals: For a non-resonant signal with amplitude  $E_{nr}$  and a resonant signal  $E_r$  with phase  $\phi$ , the intensity of the combined signal is  $|E_{nr}|^2 + |E_r|^2 + 2 \cos \phi |E_{nr} E_r|$ . The last term in this equation results in an amplification similar to that used in a homodyne amplification scheme.<sup>49</sup> For silicon, the non-resonant signal was too weak to be used in alignment and the enhancement was negligible since both signals were of the same order of magnitude. This means that it was desirable to suppress the non-resonant contribution of the *c*-Si in order to accurately detect the strength of the resonant signals.

For a Au substrate with e.g. adsorbates on top, it has been shown that the non-resonant background can successfully be suppressed by delaying the visible pulse with respect to the mid-IR pulse<sup>13,14,50,51</sup>. Here a similar approach to suppressing the non-resonant contribution of the *c*-Si was taken. The approach was based upon the difference in life time of a resonant contribution (e.g. a stretching vibration) that is typically much longer than the life time of the excitation of a non-resonant contribution. Delaying the visible pulse with respect to the mid-IR pulse – i.e. the visible pulse arrives after the mid-IR pulse – exploits this difference in life time of the excitation. The resonant excitation of the surface groups will still “remember” the 90 fs pulse, whereas, the non-resonant excitation of the silicon does not. See also Fig. 4.10 for an illustration of the timing of the pulses. Typical dephasing times range in the tens of ps for the C-H stretch mode and the Si-H stretch mode.<sup>7,52–54</sup> This approach to suppressing the non-resonant contribution is only possible for BB-SFG spectroscopy and cannot be used for narrowband SFG spectroscopy. The pulse duration needs to be shorter than the life time of the excitation of the resonant contribution (including dephasing) which is typically on the order of picoseconds or less. BB-SFG spectroscopy itself is an excellent tool for measuring processes such as dephasing and decay of excitation in molecules as has been shown by, for example, [Bonn et al.](#)<sup>55</sup>

An experiment was performed to verify whether the non-resonant background can be suppressed by delaying the visible pulse with respect to the mid-IR pulse. At the same time, the SiO<sub>2</sub> spacer described in the previous section was used to enhance the resonant signal on the Si(100) substrate. To prepare the surface, several ALD cycles were performed at 250 °C ending with the TMA exposure to ensure a –CH<sub>3</sub> covered surface. On this surface, a series of BB-SFG spectra was recorded varying the delay between the visible and mid-IR pulse  $\Delta t$ , shown in Fig. 4.11. In a separate experiment using a GaAs substrate the timing corresponding to  $\Delta t = 0$  was determined as the timing with the strongest non-resonant signal. A positive time difference indicates

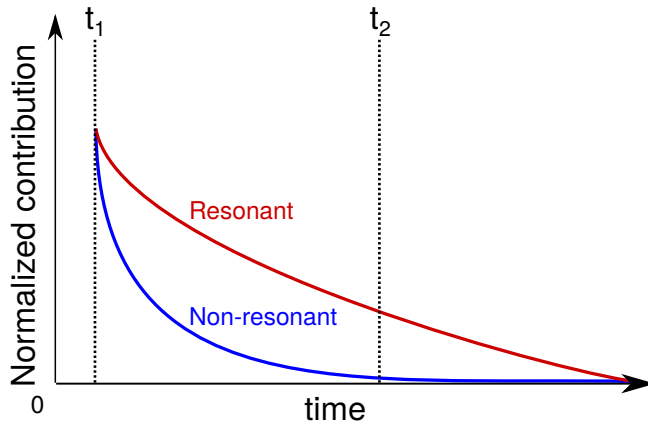


**Figure 4.10:** Illustration of the timing of the pulses used to suppress the non-resonant contribution of silicon. The mid-IR pulse always arrives at  $t_1$ . If the visible pulse also impinges on the surface at time  $t_1$  the non-resonant contribution is relatively strong. Delaying the visible pulse to time  $t_2$  exploits the inherent difference in life time of the resonant and non-resonant contributions. The non-resonant contribution has lost a large part of its excitation caused by the mid-IR pulse due to dissipation at time  $t_2$ . On the other hand, the resonant contribution still retains a large part of the excitation at this time. Therefore, the visible pulse “probes” more of the resonant contribution than of the non-resonant contribution at time  $t_2$  than at time  $t_1$ .

that the visible pulse arrives after the mid-IR pulse and a negative difference indicates the opposite. Comparing the trends in the amplitude of the resonant and non-resonant contributions with respect to delay in Fig 4.11, it can clearly be seen that the non-resonant contribution decays faster than the resonant contribution. The decay of the resonant and the non-resonant contributions were quantified by fitting the spectra in Fig. 4.11 as described in Chapter 2. This results in Fig. 4.12 where the amplitudes of the two contributions are plotted as a function of the delay between the two pulses  $\Delta t$ . The non-resonant signal quickly decreases with  $\Delta t$  for the first data points. Due to the broad nature of the peak, weak non-resonant contributions could not be determined accurately. For a delay larger than 132 fs the amplitude of the non-resonant contribution was set to 0. The trend in the resonant signal suggests that there are three regimes: (1) An exponential increase ( $\exp(t/\tau)$ ) with a time constant  $\tau = 62$  fs. (2) A slow exponential decrease ( $\exp(-t/\tau)$ ) of intensity with delay with a time constant of  $\tau = 908$  fs. (3) A more rapid exponential decay of the resonant signal with delay with a time constant  $\tau = 262$  fs. Regime (1) is probably due to the visible pulse arriving before the mid-IR pulse which is related to dephasing combined with the rise time of the leading edge of the visible pulse. In regime (2) both pulses interact with the sample simultaneously (to a certain degree) depending on the delay between the pulses. In regime (3), the visible pulse arrives after the mid-IR pulse and the time dependence is the result of

the convolution of the temporal shape of the visible pulse over the dephasing behavior of the surface groups. To illustrate the improvement which can be achieved with this approach, Figure 4.13 shows a spectrum of the C-H stretch mode for  $t = 0$  and the optimized timing with a delay of  $t = 132$  fs on the same surface under vacuum conditions. The delay of 132 fs was chosen as the optimal timing in this case. For this timing, the non-resonant contribution is below the detection limit of the setup while at the same time the strength of the resonant contribution was still unaffected.

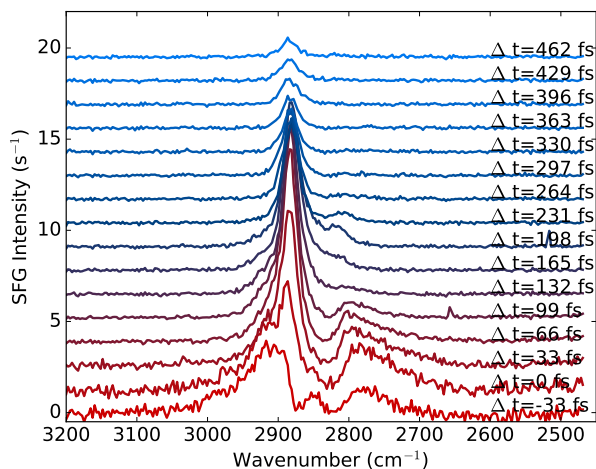


**Figure 4.11:** The BB-SFG spectra showing how the resonant and non-resonant contributions vary as a function of the delay between the mid-IR and visible pulse.

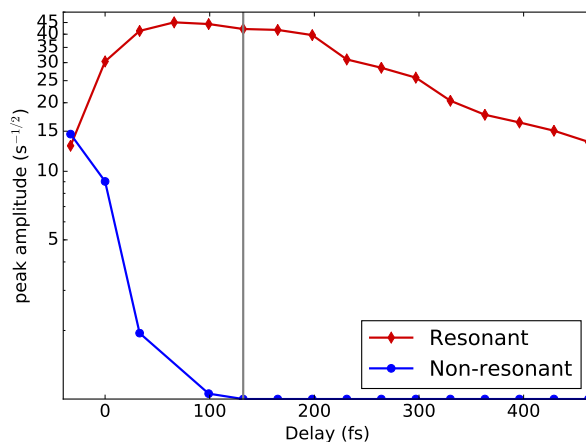


**Figure 4.12:** The non-resonant contribution can be suppressed by delaying the visible pulse with respect to the mid-IR pulse as can be seen in Fig. 4.11. The amplitude of the resonant and non-resonant contribution were quantified and plotted on a logarithmic scale as a function of delay. The solid lines are fits to the data, revealing a characteristic time of 96 fs, 908 fs, and 262 fs. Note that  $t = 0$  was the timing that yielded the strongest SFG signal on GaAs and might not coincide precisely with both pulses arriving at the same time at the surface because of the bulk contribution of the GaAs signal. The vertical line indicates the timing which is also shown in Fig. 4.13 (see also text) and the other lines serve as a guide to the eye.

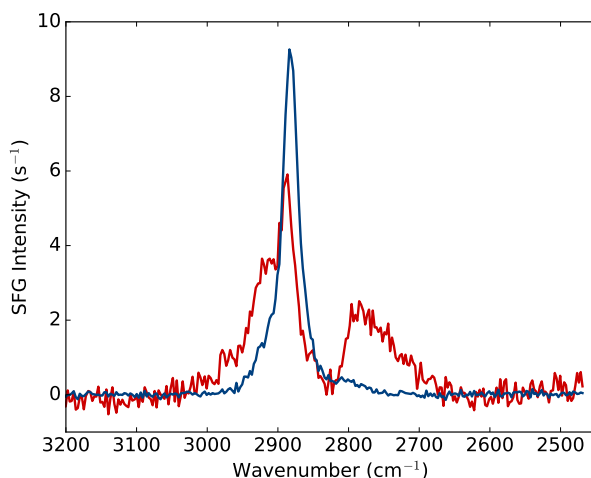


**Figure 4.13:** The effect of the suppression of the non-resonant contribution by delaying the visible pulse with respect to the mid-IR pulse of  $-\text{CH}_3$  groups on a  $c$ -Si substrate with a  $\text{SiO}_2$  spacer layer of 70 nm. A delay of 132 fs shows a significant reduction of the non-resonant contribution while still retaining the resonant contribution.

## 4.6 Summary

The key insights and practical considerations for using BB-SFG spectroscopy to study the surface chemistry of ALD were presented. An important part of implementing a new analysis technique was the selection of good benchmarks with appropriate reference samples. Initially these reference samples served to first achieve sub-monolayer sensitivity towards e.g.  $-\text{CH}_3$  groups. Subsequently, the reference samples were used to regain the sub-monolayer sensitivity if the setup was altered in any way. The key benchmarks were: The non-resonant response of GaAs and Au surfaces; The resonant response of polymers and of H terminated Si(111). Apart from serving as a reference sample, H terminated Si(111) was used as a study case investigating the influence of UV exposure on the Si-H surface groups. It was found that the Si-H groups were not affected by the laser beams (0.4 eV and 1.55 eV photons) used in the BB-SFG setup probing these groups, nor did exposure to 3 eV photons at a much higher intensity affect the Si-H groups. Conversely, exposing the H/Si(111) surface to 4.8 eV photons resulted in the dissociation of the Si-H groups. For this process a cross section of  $8.5 \pm 0.8 \cdot 10^{-17} \text{ cm}^2$  was found, a value comparable to what is reported for direct photochemical dissociation.

Studying the relevant surface groups during ALD directly on *c*-Si yielded very weak signals. To increase the signal strength, a spacer layer was inserted in between the *c*-Si substrate and the surface under investigation. The enhancement of the BB-SFG signal was modeled as a function of spacer layer thickness, taking into account the linear optical properties affecting the three beams (visible, mid-IR, and SFG signal). A broad enhancement of a factor  $\sim 100$  with respect to the SFG signal on *c*-Si (no spacer) was predicted for a  $\text{SiO}_2$  layer thickness between 90 nm and 130 nm. To verify the prediction, a sample with a 30 nm spacer and a sample with a 70 nm spacer were prepared which indeed followed the predicted trend. In subsequent experiments a  $\text{SiO}_2$  spacer layer of 90 nm was used to obtain the strongest possible SFG signal.

The *c*-Si substrate has a non-linear response (mainly due to the lowered symmetry at the surface) which contributes to the BB-SFG spectrum. This non-resonant contribution of the *c*-Si obscures (a part of) the signal of interest. The undesired non-resonant signal of the *c*-Si substrate was quenched by delaying the visible pulse with respect to the mid-IR pulse. The non-resonant contribution decays faster than the resonant contribution which can be exploited to suppress the former. This was verified experimentally and this strategy allowed for a complete suppression of the non-resonant contribution.

In conclusion, combining the enhancement of the SFG signal strength by an appropriate spacer layer and the suppression of the non-resonant *c*-Si contribution allowed the detection of  $-\text{CH}_3$  groups with a sub-monolayer sensitivity during ALD on *c*-Si in the in-situ setup. Furthermore, a (rapid) procedure was developed to ascertain whether the alignment of the setup was sufficient to obtain monolayer sensitivity towards  $-\text{CH}_3$  and  $-\text{OH}$  groups.

## Bibliography

- [1] Kung, Chen, Wei, Shen, and Somorjai. Sum-frequency generation spectroscopic study of CO adsorption and dissociation on Pt(111) at high pressure and temperature. *Surface Science*, 2000. doi:[10.1016/S0039-6028\(00\)00639-7](https://doi.org/10.1016/S0039-6028(00)00639-7).
- [2] Lagutchev, Lu, Takeshita, Dlott, and Wieckowski. Vibrational sum frequency generation studies of CO on Pt(111) electrodes. *The Journal of Chemical Physics*, 2006. doi:[10.1063/1.2359446](https://doi.org/10.1063/1.2359446).
- [3] Zhang, Piatkowski, Bakker, and Bonn. Ultrafast vibrational energy transfer at the water/air interface revealed by two-dimensional surface vibrational spectroscopy. *Nature Chemistry*, 2011. doi:[10.1038/nchem.1158](https://doi.org/10.1038/nchem.1158).
- [4] Hsieh, Campen, Vila Verde, Bolhuis, Nienhuys, and Bonn. Ultrafast Reorientation of Dangling OH Groups at the Air-Water Interface Using Femtosecond Vibrational Spectroscopy. *Phys. Rev. Lett.*, 2011. doi:[10.1103/PhysRevLett.107.116102](https://doi.org/10.1103/PhysRevLett.107.116102).
- [5] Verreault, Kurz, Howell, Koelsch, and Dominique Verreault Volker Kurz. Sample cells for probing solid/liquid interfaces with broadband sum-frequency-generation spectroscopy. *The Review of scientific instruments*, 2010. doi:[10.1063/1.3443096](https://doi.org/10.1063/1.3443096).
- [6] Voges, Al-Abadleh, Musorrafiti, Bertin, Nguyen, and Geiger. Carboxylic Acid- and Ester-Functionalized Siloxane Scaffolds on Glass Studied by Broadband Sum Frequency Generation. *The Journal of Physical Chemistry B*, 2004. doi:[10.1021/jp046564x](https://doi.org/10.1021/jp046564x).
- [7] Guyot-Sionnest, Dumas, and Chabal. Lifetime of an adsorbate-substrate vibration measured by sum frequency generation : H on Si(111). *Journal of Electron Spectroscopy and Related Phenomena*, 1990. doi:[10.1016/0368-2048\(90\)80198-J](https://doi.org/10.1016/0368-2048(90)80198-J).
- [8] Chabal, Dumas, Guyot-Sionnest, and Higashi. Vibrational dynamics of the ideally H-terminated Si(111) surface. *Surface Science*, 1991. doi:[10.1016/0039-6028\(91\)90321-I](https://doi.org/10.1016/0039-6028(91)90321-I).
- [9] Boyd. *Nonlinear optics*. Elsevier Science Publishing Co Inc, second edition, 1992.
- [10] Shoji, Kondo, Kitamoto, Shirane, and Ito. Absolute scale of second-order nonlinear-optical coefficients. *Journal of the Optical Society of America B*, 1997. doi:[10.1364/JOSAB.14.002268](https://doi.org/10.1364/JOSAB.14.002268).
- [11] Wilson, Jiang, Carriles, and Downer. Second-harmonic amplitude and phase spectroscopy by use of broad-bandwidth femtosecond pulses. *Journal of the Optical Society of America B*, 2003. doi:[10.1364/JOSAB.20.002548](https://doi.org/10.1364/JOSAB.20.002548).
- [12] Chen, Shen, and Somorjai. Studies of polymer surfaces by sum frequency generation vibrational spectroscopy. *Annual review of physical chemistry*, 2002. doi:[10.1146/annurev.physchem.53.091801.115126](https://doi.org/10.1146/annurev.physchem.53.091801.115126).
- [13] Curtis, Burt, Calchera, and Patterson. Limitations in the Analysis of Vibrational Sum-Frequency Spectra Arising from the Nonresonant Contribu-



- tion. *The Journal of Physical Chemistry C*, 2011. doi:[10.1021/jp200915z](https://doi.org/10.1021/jp200915z).
- [14] Curtis, Asplund, and Patterson. Use of Variable Time-Delay Sum-Frequency Generation for Improved Spectroscopic Analysis. *The Journal of Physical Chemistry C*, 2011. doi:[10.1021/jp2069368](https://doi.org/10.1021/jp2069368).
- [15] HOMMEL, MA, and ALLE. Broadband Vibrational Sum Frequency Generation Spectroscopy of a Liquid Surface. *Analytical Sciences*, 2001. doi:[10.2116/analsci.17.1325](https://doi.org/10.2116/analsci.17.1325).
- [16] Anfuso, Ricks, Rodríguez-Córdoba, and Lian. Ultrafast Vibrational Relaxation Dynamics of a Rhenium Bipyridyl CO<sub>2</sub> - Reduction Catalyst at a Au Electrode Surface Probed by Time-Resolved Vibrational Sum Frequency Generation Spectroscopy. *The Journal of Physical Chemistry C*, 2012. doi:[10.1021/jp3089098](https://doi.org/10.1021/jp3089098).
- [17] Wang, Rodriguez, Albers, Ahorinta, Sipe, and Kauranen. Surface and bulk contributions to the second-order nonlinear optical response of a gold film. *Physical Review B*, 2009. doi:[10.1103/PhysRevB.80.233402](https://doi.org/10.1103/PhysRevB.80.233402).
- [18] Koenig. *Spectroscopy of Polymers*. Elsevier Science, second edition, 1999.
- [19] Tateishi, Kai, Noguchi, Uosaki, Nagamura, and Tanaka. Local conformation of poly(methyl methacrylate) at nitrogen and water interfaces. *Polymer Chemistry*, 2010. doi:[10.1039/b9py00227h](https://doi.org/10.1039/b9py00227h).
- [20] Zhang, Shen, and Somorjai. Studies of surface structures and compositions of polyethylene and polypropylene by IR+visible sum frequency vibrational spectroscopy. *Chemical Physics Letters*, 1997. doi:[10.1016/S0009-2614\(97\)01311-0](https://doi.org/10.1016/S0009-2614(97)01311-0).
- [21] Dybal and Krimm. Normal-mode analysis of infrared and Raman spectra of crystalline isotactic poly(methyl methacrylate). *Macromolecules*, 1990. doi:[10.1021/ma00207a013](https://doi.org/10.1021/ma00207a013).
- [22] Wang, Chen, Buck, and Chen. Molecular Chemical Structure on Poly(methyl methacrylate) (PMMA) Surface Studied by Sum Frequency Generation (SFG) Vibrational Spectroscopy. *The Journal of Physical Chemistry B*, 2001. doi:[10.1021/jp013161d](https://doi.org/10.1021/jp013161d).
- [23] Miyake. The infrared spectrum of polyethylene terephthalate. II. Polyethylene-d<sub>4</sub> terephthalate. *Journal of Polymer Science*, 1959. doi:[10.1002/pol.1959.1203813420](https://doi.org/10.1002/pol.1959.1203813420).
- [24] Liang and Krimm. Infrared spectra of high polymers: Part IX. Polyethylene terephthalate. *Journal of Molecular Spectroscopy*, 1959. doi:[10.1016/0022-2852\(59\)90048-7](https://doi.org/10.1016/0022-2852(59)90048-7).
- [25] Loch, Ahn, Chen, Wang, and Chen. Sum Frequency Generation Studies at Poly(ethylene terephthalate)/Silane Interfaces: Hydrogen Bond Formation and Molecular Conformation Determination. *Langmuir*, 2004. doi:[10.1021/la0494526](https://doi.org/10.1021/la0494526).
- [26] Grunthaner and Grunthaner. Chemical and electronic structure of the SiO<sub>2</sub>/Si interface. *Materials science reports*, 1986. doi:[10.1016/S0920-2307\(86\)80001-9](https://doi.org/10.1016/S0920-2307(86)80001-9).
- [27] Jakob, Chabal, and Raghavachari. Lineshape analysis of the Si-H stretching mode of the ideally H-terminated Si(111) surface: the role of dynam-

- cal dipole coupling. *Chemical Physics Letters*, 1991. doi:[10.1016/0009-2614\(91\)90433-A](https://doi.org/10.1016/0009-2614(91)90433-A).
- [28] Tully, Chabal, Raghavachari, Bowman, and Lucchese. Infrared linewidths and vibrational lifetimes at surfaces: H on Si(100). *Physical Review B*, 1985. doi:[10.1103/PhysRevB.31.1184](https://doi.org/10.1103/PhysRevB.31.1184).
- [29] Higashi, Chabal, Trucks, and Raghavachari. Ideal hydrogen termination of the Si(111) surface. *Applied Physics Letters*, 1990. doi:[10.1063/1.102728](https://doi.org/10.1063/1.102728).
- [30] Dumas, Chabal, and Higashi. Coupling of an adsorbate vibration to a substrate surface phonon: H on Si(111). *Physical Review Letters*, 1990. doi:[10.1103/PhysRevLett.65.1124](https://doi.org/10.1103/PhysRevLett.65.1124).
- [31] Frank, Chabal, and Wilk. Nucleation and interface formation mechanisms in atomic layer deposition of gate oxides. *Applied Physics Letters*, 2003. doi:[10.1063/1.1585129](https://doi.org/10.1063/1.1585129).
- [32] Niwano. Infrared spectroscopic study of initial stages of ultraviolet ozone oxidation of Si(100) and Si(111) surfaces. *Journal of Vacuum Science & Technology A: Vacuum, Surfaces, and Films*, 1994. doi:[10.1116/1.579264](https://doi.org/10.1116/1.579264).
- [33] Michalak, Rivillon, Chabal, Esteve, and Lewis. Infrared spectroscopic investigation of the reaction of hydrogen-terminated, (111)-oriented, silicon surfaces with liquid methanol. *The journal of physical chemistry B*, 2006. doi:[10.1021/jp0624303](https://doi.org/10.1021/jp0624303).
- [34] Michalak, Amy, Aureau, Dai, Esteve, and Chabal. Nanopatterning Si(111) surfaces as a selective surface-chemistry route. *Nature materials*, 2010. doi:[10.1038/nmat2611](https://doi.org/10.1038/nmat2611).
- [35] Guyot-Sionnest, Lin, and Hiller. Vibrational dynamics of the Si-H stretching modes of the Si(100)/H:2x1 surface. *The Journal of Chemical Physics*, 1995. doi:[10.1063/1.469474](https://doi.org/10.1063/1.469474).
- [36] Lupke. Characterization of semiconductor interfaces by second-harmonic generation. *Surface Science Reports*, 1999. doi:[10.1016/S0167-5729\(99\)00007-2](https://doi.org/10.1016/S0167-5729(99)00007-2).
- [37] Bodlaki and Borguet. Photoreactivity of Si(111)-H in Ambient. *Journal of Physical Chemistry C*, 2007. doi:[10.1021/jp0639546](https://doi.org/10.1021/jp0639546).
- [38] Bodlaki. In situ second-harmonic generation measurements of the stability of Si(111)-H and kinetics of oxide regrowth in ambient. *Journal of Applied Physics*, 2004. doi:[10.1063/1.1664024](https://doi.org/10.1063/1.1664024).
- [39] Pusel, Wetterauer, and Hess. Photochemical Hydrogen Desorption from H-Terminated Silicon(111) by VUV Photons. *Physical Review Letters*, 1998. doi:[10.1103/PhysRevLett.81.645](https://doi.org/10.1103/PhysRevLett.81.645).
- [40] Vondrak and Zhu. Dissociation of a Surface Bond by Direct Optical Excitation: H-Si(100). *Physical Review Letters*, 1999. doi:[10.1103/PhysRevLett.82.1967](https://doi.org/10.1103/PhysRevLett.82.1967).
- [41] Vondrak and Zhu. Direct Photodesorption of Atomic Hydrogen from Si(100) at 157 nm: Experiment and Simulation. *The Journal of Physical Chemistry B*, 1999. doi:[10.1021/jp990636g](https://doi.org/10.1021/jp990636g).
- [42] Cicero, Linford, and Chidsey. Photoreactivity of Unsaturated Compounds with Hydrogen-Terminated Silicon(111). *Society*, 2000. doi:[10.1021/la9911990](https://doi.org/10.1021/la9911990).

- [43] Luo. *Comprehensive Handbook of Chemical Bond Energies*. CRC Press, 2007. doi:[10.1201/9781420007282](https://doi.org/10.1201/9781420007282).
- [44] Reider, Hořlífer, and Heinz. Desorption kinetics of hydrogen from the Si(111) 7x7 surface. *The Journal of Chemical Physics*, 1991. doi:[10.1063/1.460660](https://doi.org/10.1063/1.460660).
- [45] Allongue, Kieling, and Gerischer. Etching mechanism and atomic structure of H-Si(111) surfaces prepared in ceNH<sub>4</sub>F. *Electrochimica Acta*, 1995. doi:[10.1016/0013-4686\(95\)00071-L](https://doi.org/10.1016/0013-4686(95)00071-L).
- [46] Allongue, Henry de Villeneuve, Morin, Boukherroub, and Wayner. The preparation of flat H-Si(111) surfaces in 40% ceNH<sub>4</sub>F revisited. *Electrochimica Acta*, 2000. doi:[10.1016/S0013-4686\(00\)00610-1](https://doi.org/10.1016/S0013-4686(00)00610-1).
- [47] Sipe. New Green-function formalism for surface optics. *Journal of the Optical Society of America B*, 1987. doi:[10.1364/JOSAB.4.000481](https://doi.org/10.1364/JOSAB.4.000481).
- [48] George. Atomic layer deposition: an overview. *Chemical reviews*, 2010. doi:[10.1021/cr900056b](https://doi.org/10.1021/cr900056b).
- [49] Dadap, Shan, Weling, Misewich, and Heinz. Homodyne detection of second-harmonic generation as a probe of electric fields. *Applied Physics B*, 1999. doi:[10.1007/s003400050628](https://doi.org/10.1007/s003400050628).
- [50] Lagutchev, Hambir, and Dlott. Nonresonant Background Suppression in Broadband Vibrational Sum-Frequency Generation Spectroscopy. *The Journal of Physical Chemistry C*, 2007. doi:[10.1021/jp075391j](https://doi.org/10.1021/jp075391j).
- [51] Lagutchev, Lozano, Mukherjee, Hambir, and Dlott. Compact broadband vibrational sum-frequency generation spectrometer with nonresonant suppression. *Spectrochimica acta. Part A, Molecular and biomolecular spectroscopy*, 2010. doi:[10.1016/j.saa.2009.12.066](https://doi.org/10.1016/j.saa.2009.12.066).
- [52] Lin, Chen, Chang, Tsai, Lin, and Wang. The vibrational dephasing and relaxation of CH and CD stretches on diamond surfaces: An anomaly. *The Journal of Chemical Physics*, 1996. doi:[10.1063/1.472271](https://doi.org/10.1063/1.472271).
- [53] van der Voort, Rella, van der Meer, Akimov, and Dijkhuis. Dynamics of Si-H Vibrations in an Amorphous Environment. *Physical Review Letters*, 2000. doi:[10.1103/PhysRevLett.84.1236](https://doi.org/10.1103/PhysRevLett.84.1236).
- [54] Ueba. Vibrational relaxation and pump-probe spectroscopies of adsorbates on solid surfaces. *Progress in Surface Science*, 1997. doi:[10.1016/S0079-6816\(97\)00021-X](https://doi.org/10.1016/S0079-6816(97)00021-X).
- [55] Bonn, Kleyn, and Kroes. Real time chemical dynamics at surfaces. *Surface Science*, 2002. doi:[DOI: 10.1016/S0039-6028\(01\)01550-3](https://doi.org/10.1016/S0039-6028(01)01550-3).

# Initial growth of Al<sub>2</sub>O<sub>3</sub> by atomic layer deposition studied with vibrational sum-frequency generation

## Abstract

The initial growth during atomic-layer deposition (ALD) of Al<sub>2</sub>O<sub>3</sub> using trimethylaluminum (TMA) and water was studied on two starting surfaces: SiO<sub>2</sub> and H/Si(111). By *in-situ* spectroscopy ellipsometry (SE), it was observed that Al<sub>2</sub>O<sub>3</sub> growth started virtually immediately on both surfaces but for H/Si(111) with a somewhat reduced growth-per-cycle (GPC) compared to steady-state growth. The underlying surface chemistry during the initial cycles of ALD was monitored with *in-situ* broadband sum-frequency generation (BB-SFG). For the SiO<sub>2</sub> surface, the –CH<sub>3</sub> surface groups were followed revealing that only the initial TMA half-cycle deviates from steady-state growth. The reaction cross section of the initial TMA half-cycle ( $\sigma_{TMA} = 2.0 \pm 0.2 \cdot 10^{-18} \text{cm}^2$ ) was a factor of 3 lower than for the TMA half-cycle during steady-state ALD ( $\sigma_{TMA} = 6.5 \pm 0.6 \cdot 10^{-18} \text{cm}^2$ ). Each of the H<sub>2</sub>O half-cycles showed the same reaction cross section ( $\sigma_{H_2O} = 4.0 \pm 0.4 \cdot 10^{-20} \text{cm}^2$ ) equal to that of steady-state growth, in agreement with the SE data. For the H/Si(111) surface the chemisorption of TMA on the Si-H surface groups was studied by monitoring the Si-H groups. The reaction cross section ( $\sigma_{TMA} = 3.1 \pm 0.3 \cdot 10^{-18} \text{cm}^2$ ) during the first TMA half-cycle on H/Si(111) was a factor two lower than during steady-state growth of Al<sub>2</sub>O<sub>3</sub>. These results show that the initial growth of Al<sub>2</sub>O<sub>3</sub> ALD on SiO<sub>2</sub> and H/Si(111) shows subtle but measurable differences with respect to steady-state growth.

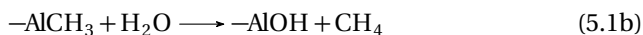
## 5.1 Introduction

In microelectronics and related fields, many key advances in dry etching and thin-film deposition have been the result of detailed insight into the underlying fundamental surface reactions. The pioneering work by **Coburn and Winters** has been exemplary for the approach used today in mechanistic studies in semiconductor processing by etching and deposition.<sup>1</sup> The value of this approach was demonstrated by their seminal work on Si etching.<sup>1-4</sup> They introduced a methodology combining the systematic aspects of fundamental surface-science studies with the close-to-actual operation conditions and the non-ideal surfaces used in the etch processes.<sup>1-4</sup> On these non-ideal surfaces, additional processes can occur that are critical for understanding the etching mechanism. Similar non-idealities can play a key role in the growth of thin-film deposition by processes such as atomic-layer deposition (ALD). A comparable approach to that of **Coburn and Winters** has been adopted in the field of ALD to study its growth mechanism. These studies have led to a good understanding of the fundamental growth mechanism of ALD processes during steady-state growth.<sup>5-7</sup> Conversely, the growth mechanism during the initial growth of thin-films by ALD has not received as much attention. Initial growth, also referred to as “nucleation” in the ALD community, can be defined as a transient phase lasting 1 or more ALD cycles in which growth deviates from the steady-state film growth. This can manifest itself as: (i) the same reaction mechanism with different reaction rates, due to e.g. a different reactivity or density of the surface groups; and/or (ii) a different reaction mechanism, e.g. involving different types of surface groups. Independent hereof, initial growth might show up as a deviation in the growth-per-cycle (GPC); a deviation in the dose required for saturation, or a growth delay.<sup>8,9</sup> Initial growth phenomena can affect many of the applications of ALD, which often require films of only several nm thickness. Therefore, a slightly reduced initial growth can have a relatively large impact on this aspect.<sup>10</sup> Initial growth phenomena also play a key role in depositing doped films and ternary compounds by combining two or more ALD processes. For these complex ALD processes, initial growth phenomena occur basically each time a switch is made to the alternate ALD chemistry.<sup>11-13</sup> For example, when depositing Al doped ZnO, a marked decrease in the GPC or even etching was observed when switching from the Al<sub>2</sub>O<sub>3</sub> ALD process to the ZnO ALD process.<sup>11,12</sup> On the other hand, differences in the initial growth and nucleation behavior can also be exploited to grow metal nano-particles.<sup>14</sup> Moreover, understanding initial growth is important for area selective deposition processes, where lack of growth or large differences in the GPC on different substrates can be exploited to achieve selectivity.<sup>9,15,16</sup>

So far, only a small number of publications focused on the direct study of the (changes in the) underlying reaction mechanism during initial growth. Since such a detailed understanding of changes in the surface chemistry during initial growth remains elusive even for the prevalent ALD processes,

more insight into the surface chemistry during this phase of the ALD process is needed.

This work focuses on the initial growth of ALD of  $\text{Al}_2\text{O}_3$  using  $\text{Al}(\text{CH}_3)_3$  (trimethylaluminum, TMA) and  $\text{H}_2\text{O}$  as precursor and co-reactant, respectively. As the prototypical metal-oxide ALD process, the steady-state reaction mechanism of this ubiquitous ALD process has been investigated with a wide range of techniques. This includes gas-phase and surface FTIR spectroscopy,<sup>17,18</sup> quadrupole-mass spectrometry (QMS),<sup>19</sup> and quartz-crystal microbalance.<sup>20</sup> The main reaction pathway during steady-state growth for this ALD process can be described by,



where a hyphen (–) indicates a surface group and were all other molecules are in the gas or vapor phase.<sup>17–23</sup> The initial growth on two different surfaces will be studied: -OH terminated  $\text{SiO}_2$  and H terminated Si(111). For the growth of  $\text{Al}_2\text{O}_3$  on the -OH terminated  $\text{SiO}_2$  surface, a difference in -OH density and a difference in the reactivity of the -OH groups might lead to minor changes in the GPC during the initial ALD cycle(s). For the growth of  $\text{Al}_2\text{O}_3$  on H terminated Si(111), no -OH groups are present so the growth must occur via a different reaction pathway. Frank et al. reported that TMA chemisorbs on this surface forming either a Si-Al bond or a Si-O-Al bond.<sup>24</sup> Such differences in the surface chemistry are expected to affect the reaction cross section of TMA as well as the GPC of the ALD process to a certain degree during the initial cycles.

The choice for these two surfaces is motivated by their pervasiveness in the semiconductor industry and research. The Si(100) /  $\text{SiO}_2$  interface is known for its high electronic quality.<sup>25–27</sup> Often, functional layers are grown on top of a (ultrathin)  $\text{SiO}_2$  film exploiting its high quality interface to silicon. On the other hand, H terminated Si is another ubiquitous starting surface for thin-film growth when a direct interface with the Si is desired.<sup>25</sup> Especially the H terminated Si(111) surface (H/Si(111)) is of interest as it has become a prototypical surface in the field of surface science due to its ideal properties.<sup>28–34</sup> The H/Si(111) surface is atomically flat, virtually defect free, stable in ambient conditions, and has perfectly aligned surface groups when prepared with care.<sup>35,36</sup>

*In-situ* vibrational broadband sum-frequency generation (BB-SFG) spectroscopy was used to study the surface chemistry during the ALD process on these two surfaces. For the initial growth on the  $\text{SiO}_2$  surface, the density of  $-\text{CH}_3$  surface groups was monitored during the first 3 ALD cycles as a function of precursor and co-reactant exposure. Emphasis was placed on the reaction kinetics of the ALD chemistry and the determination of the reaction cross section  $\sigma$ . For initial growth on the H/Si(111) surface, the relative density of Si-H on the surface as a function of TMA exposure was measured. This revealed the reaction kinetics of the precursor chemisorption on H/Si(111)

and allowed the determination of the reaction cross section of this process.

## 5.2 Vibrational broadband sum-frequency generation

Vibrational BB-SFG spectroscopy is a second-order nonlinear optical technique with which the surface chemistry can be monitored *in-situ* with sub-monolayer sensitivity and fairly fast acquisition times. The SFG process itself is illustrated in Fig. 5.1. In short, the electric field of a spectrally narrow visible light pulse,  $\vec{E}(\omega_{vis})$  and a broadband femtosecond mid-IR pulse  $\vec{E}(\omega_{IR})$  interact with surface groups, causing a polarization of the surface groups with a frequency equal to the sum frequency of the two driving fields. The resulting polarization  $\vec{P}$  is given by,

$$P_i(\omega_{sfg} = \omega_{vis} + \omega_{ir}) = \epsilon_0 \bar{\chi}_{ijk} E_j(\omega_{vis}) E_k(\omega_{ir}) \quad (5.2)$$

with  $i, j, k$  the Cartesian components of the fields, and  $\bar{\chi}_{ijk}(\omega_{sfg}, \omega_{vis}, \omega_{ir})$  the second-order susceptibility.<sup>37</sup> The intensity of the emitted SFG light,  $I$  is proportional to  $|P|^2$ .<sup>37</sup> Transitions between vibrational levels of the surface groups give rise to a resonant enhancement of the SFG signal, i.e. an increase of the amplitude of  $\bar{\chi}_{ijk}$  at the characteristic frequencies associated with these vibrational modes. Therefore, the IR fingerprint of the surface groups is present in the spectral shape of the BB-SFG signal emitted in the visible part of the spectrum. The selection rules of the SFG process are quite strict. It turns out that the BB-SFG spectroscopy is inherently surface selective when used to study the surface chemistry on materials with inversion symmetry such as amorphous materials and crystalline Si.<sup>37,38</sup> This unique combination of inherent surface selectivity, sub-monolayer sensitivity, and fast acquisition times ( $\sim 120$  s for a sensitivity better than 10 % of a monolayer of  $-\text{CH}_3$ ) makes BB-SFG spectroscopy ideally suited to study the surface chemistry during ALD.

In our previous work, BB-SFG was employed to study the steady-state growth of thermal ALD of  $\text{Al}_2\text{O}_3$ . Both the  $-\text{CH}_3$  and the  $-\text{OH}$  surface groups, ruling the reaction mechanism of the  $\text{Al}_2\text{O}_3$  ALD process, could be detected with BB-SFG spectroscopy.<sup>39</sup> By monitoring the  $-\text{CH}_3$  density as a function of the precursor and co-reactant exposure, the reaction kinetics in both half-cycles were revealed over a large temperature range (100 °C up to 300 °C).<sup>22,39</sup> Moreover, the unique properties of BB-SFG spectroscopy allowed for the detection of *persistent*  $-\text{CH}_3$  groups present on the surface at low temperatures which are no longer reactive towards  $\text{H}_2\text{O}$ .<sup>22</sup> The observation of these persistent  $-\text{CH}_3$  groups confirmed the inertness of isolated  $-\text{CH}_3$  groups towards  $\text{H}_2\text{O}$ , as predicted with ab-initio simulations.<sup>40,41</sup> Furthermore, it was demonstrated that the *persistent*  $-\text{CH}_3$  groups are the cause of a lower GPC which is commonly observed at low temperatures for ALD of  $\text{Al}_2\text{O}_3$ .<sup>22</sup>

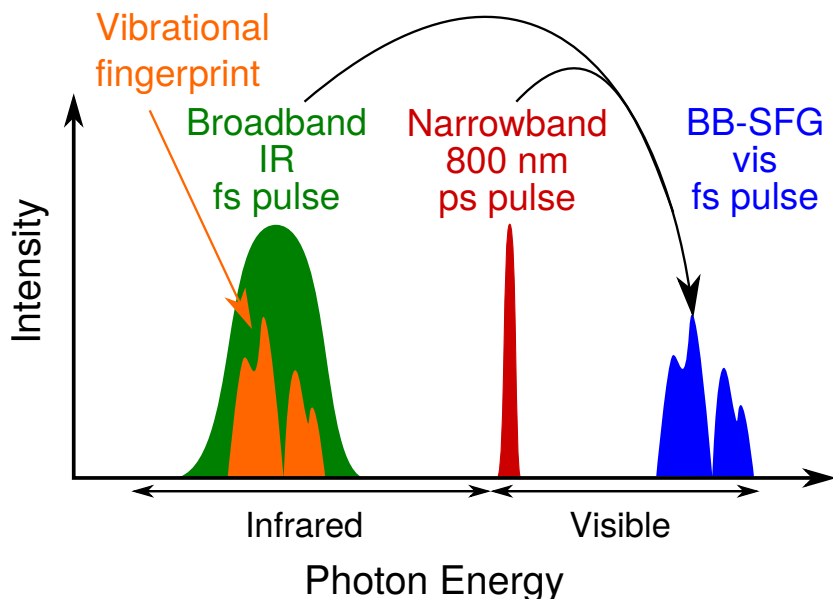


**Figure 5.1:** The vibrational transitions of the surface groups are probed with BB-SFG by exposing the surface groups simultaneously to a broadband femtosecond IR pulse and a narrowband visible pulse. The two pulses interact resulting in the emission of a SFG signal. The efficiency of the mixing is resonantly enhanced by the vibrational transitions of the surface groups, and as a result the vibrational fingerprint is contained in the SFG signal in the visible part of the spectrum.

## 5.3 Experimental details

### ALD setup and substrate preparation

The BB-SFG experiments were performed in a home-built ALD reactor. The ALD reactor consisted of a vacuum chamber which was equipped with 2 turbomolecular pumps (Pfeiffer TMU 261P) reaching a base pressure better than  $1 \cdot 10^{-6}$  mbar. The vapor drawn precursor and co-reactant were dosed using “fast ALD” valves (Swagelok 34C-A-GDFG-1KT). The reactor walls were heated to 80 °C. For the experiments at 100 °C, the sample was heated radiatively using a Boralectric heating element (GE Advanced Ceramics ACSF0073 HTR1002). The sample temperature was measured using a thermocouple (Thermocoax 2ABAc05/1m/TI/FIM.K) glued to the sample with thermally conductive adhesive (RS 186-3600). The temperature sensor was also used as input for the custom electronics controlling the sample temperature by modulating the power dissipation in the heating element.

The samples for the initial growth studied with BB-SFG spectroscopy and SE were prepared as follows: The substrates with the SiO<sub>2</sub> surface were prepared by depositing 90 nm of SiO<sub>2</sub> on a Si(100) substrate with plasma-



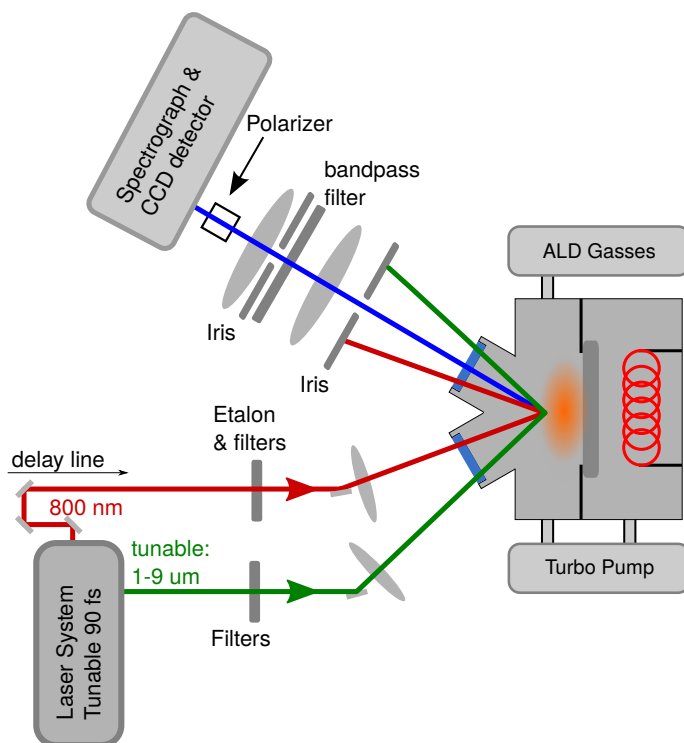


**Figure 5.2:** Schematic of the main components of the BB-SFG setup and the ALD setup employed to study the surface chemistry during ALD of  $\text{Al}_2\text{O}_3$ .

enhanced chemical-vapor deposition (PE-CVD) at  $300^\circ\text{C}$  using  $\text{SiH}_4 - \text{O}_2$  plasma. Both the SE and BB-SFG spectroscopy experiments on this type of sample were performed at  $100^\circ\text{C}$ . The substrates with the H/Si(111) surface were prepared by the procedure as described by Higashi et al.<sup>42</sup> A Si(111) wafer with native oxide was immersed for 120 s in a buffered hydrofluoric acid (BHF) comprising of 40%  $\text{NH}_4\text{F}$  and 49% HF mixed in a volume ratio of 6:1. After the BHF exposure, the wafer was rinsed in a flow of ultra-pure water until the resistivity of the water down stream of the wafer reached a resistance  $> 5 \text{ M}\Omega\text{cm}$ . Exposing the Si(111) surface to BHF removed the native oxide and subsequently formed an atomically smooth, Si-H terminated surface which is stable in water and ambient.<sup>42</sup> The BB-SFG spectroscopy experiments on this type of sample were performed at  $80^\circ\text{C}$  and the SE experiments were performed at  $100^\circ\text{C}$ .

## Optical setup, BB-SFG experiments, and modeling

The optical setup for the *in-situ* BB-SFG spectrometry experiments built around the ALD reactor is shown schematically in Fig. 5.2. Three main components can be identified: the laser system, the optical components used to tailor the beam, and the detection system. The laser system generating the 90 fs pulses consisted of an optical oscillator (Spectra-Physics Tsunami) and amplifier (Spectra-Physics Spitfire) producing a 1.8 W beam of visible (795 nm) light with a repetition rate of 1 kHz. Of this visible signal, 70 % was used to pump an optical-parametric amplifier (OPA, Light Conversion TOPAS-C) generating the tunable mid-IR signal (3–8  $\mu\text{m}$ ). The mid-IR beam generated in the OPA was directed towards the ALD system and focused onto the substrate situated in the vacuum chamber. The remaining 30 % of the visible beam was made spectrally narrow by a spike filter (CVI F1.1-800 spike-filter) which lengthened the pulses to  $\sim 1$  ps duration and significantly reduced its intensity. At the sample, both beams had an average power of 5 mW each. To synchronize the visible and mid-IR pulses, a home built delay line was incorporated into the visible beam path (Physik Instrumente M-014-D1). The visible beam was focused onto the same spot as the mid-IR beam in a non-collinear geometry. The BB-SFG signal generated at the sample was separated from the 2 laser beams driving the SFG process using spatial filtering (2 apertures of  $\sim 2$  mm placed  $\sim 30$  cm apart) and spectral filtering (4 Thorlabs FES0750 filters each with an optical density  $> 5$ ). To select the polarization of the SFG light, the beam was passed through a Glan-laser polarizer (Thorlabs GL10A). The BB-SFG signal was focused onto the entrance slit of the spectrograph (Acton Research SP2500) and detected by a liquid nitrogen cooled CCD chip (Princeton Instruments Spec-10).

The BB-SFG spectra were collected using an acquisition time of 120s. The so-called “Ssp” polarization mode was used which is the most sensitive mode for  $-\text{CH}_3$  and Si-H groups. In this mode,  $p$  polarized mid-IR and  $s$  polarized visible light are used to drive the SFG process while the  $s$  component of the SFG (denoted as capital S) signal is detected. To obtain information about the density of a surface groups, the BB-SFG spectra have to be fitted to a model. The SFG response of a surface group with coverage  $\rho$  is given by,

$$I(\omega_{ir}) \propto \left| \bar{\chi}_{NR} + \rho \frac{A_{res} \exp(i\phi)}{\omega_{ir} - \omega_{res} + i\Gamma} \right|^2 \quad (5.3)$$

with  $A_{res}$  the cross section of the SFG process of a single surface group for a resonance at  $\omega_{ir}$ , and  $\Gamma$  the broadening of the resonance. The parameter  $\bar{\chi}_{NR}$  aggregates the nonresonant contributions to the SFG signal and  $\phi$  describes the phase of the resonant contribution. The relative density of the surface groups can be determined from a fit of this model to the data using the least-squares approach with a Levenberg-Marquardt algorithm. This procedure was used to obtain the relative densities reported in this work. See the supporting information in the appendix for a figure with both the measured and modeled data.

### **In-situ SE measurements and modeling**

The initial growth of Al<sub>2</sub>O<sub>3</sub> ALD was followed using *in-situ* SE (J. A. Woollam Co. M2000X) on a commercial ALD reactor (Oxford Instruments FlexAL). To obtain the thickness of the deposited Al<sub>2</sub>O<sub>3</sub> film, a model was made to fit the SE data. The substrates was parameterized using the *in-situ* SE spectra recorded before the start of the deposition. The wavelength dependence of the optical constants of the Al<sub>2</sub>O<sub>3</sub> film itself were described with a Cauchy model. The parameters of the Cauchy model were determined from the *in-situ* SE spectrum recorded after 50 ALD cycles, i.e. with the thickest film deposited in the experiment. The Al<sub>2</sub>O<sub>3</sub> films had a refractive index of  $n = 1.6$  at 2 eV which is typical for these ALD films.<sup>43</sup> Using this model, with only the thickness of the Al<sub>2</sub>O<sub>3</sub> film as a fitting parameter, all the intermediate SE spectra were fitted resulting in data as shown in Fig. 5.3.

The GPC during the initial growth has to be calculated from the thickness increase caused by a single ALD cycle since the GPC is expected to change from cycle to cycle. However, care has to be taken to correctly interpret thickness changes measured with SE caused by single half-cycle. When measuring thickness changes as small as those caused by 1 ALD cycle, the role of the surface groups on the SE spectra has to be considered. Both the -OH and -CH<sub>3</sub> surface groups have an unknown (but fairly high) refractive index resulting in an apparent thickness similar to the GPC. Therefore, if *both* material is added and the surface groups are changed, it is not possible to separate the two contributions. As shown by Langereis et al., for steady-state growth this means that the thickness change between different half-cycles cannot be used to calculate the GPC because of the change in surface groups. Conversely, the thickness change after a full ALD cycle does correspond to the GPC since the same surface groups were present during both measurements.

For initial growth, the same reasoning can be applied depending on the starting surface. Because the SiO<sub>2</sub> surface starts out -OH terminated, the change in surface groups after a full ALD cycle (TMA followed by H<sub>2</sub>O) is minimal since the surface is again -OH terminated. When modeling the SE response the sample before ALD, the influence of the -OH groups is incorporated in the fitting parameter of e.g. the SiO<sub>2</sub> film. The SE spectrum of the same sample after a full ALD cycle only differs in the contribution of the deposited Al<sub>2</sub>O<sub>3</sub> layer. The surface is still -OH terminated and the influence of the -OH groups will still be included in the optical model of the Si(100)/SiO<sub>2</sub> sample. As a result, the thickness of the Al<sub>2</sub>O<sub>3</sub> film will be accurate. The same reasoning holds for the subsequent ALD cycles and the GPC can be calculated from the change in the thickness of the Al<sub>2</sub>O<sub>3</sub> film for each cycle. For this reason, the GPC data for the Si(100)/SiO<sub>2</sub> substrate was determined using the spectra recorded after the H<sub>2</sub>O half-cycle resulting in an -OH terminated surface. For the H/Si(111) surface, it is not possible to exclude the influence of a change in surface functionalization (from Si-H to -OH) in the first cycle(s). Also for this sample the GPC was calculated using the thickness obtained from the SE spectra recorded after the H<sub>2</sub>O half-cycle but the first GPC value will

be affected by a change in surface groups.

## 5.4 Results

### Growth-per-cycle during initial growth

The initial growth of  $\text{Al}_2\text{O}_3$  ALD on a  $\text{SiO}_2$  and a H/Si(111) surface was followed with *in-situ* SE. Changes in surface chemistry during the initial growth can affect the amount of material deposited per cycle, i.e. result in a change in GPC during the early cycles. For both cases, an *in-situ* SE spectrum was taken of the bare substrate before deposition. During the ALD process a SE spectrum was recorded after each half-cycle resulting in the data shown in Fig. 5.3 (a). The GPC was calculated using the thickness data, resulting in Fig. 5.3 (b). For the  $\text{SiO}_2$  surface, the first cycle shows a GPC of 2.7 Å whereas all subsequent cycles exhibit a GPC of 0.8 Å. The latter is in agreement with what is typically reported for this ALD process when thicker films are considered.<sup>43</sup> This result suggests that the initial growth phenomena might be restricted to the first ALD cycle only.

Using the same procedure for the H/Si(111) surface, Fig. 5.3 (b) shows that the first 20 cycles are affected compared to the steady-state growth. However, after this initial growth phase, a GPC of 0.8 Å was measured which is again in agreement with the reported GPC for steady state growth of  $\text{Al}_2\text{O}_3$  by ALD.<sup>43</sup>

### –CH<sub>3</sub> coverage during initial growth on SiO<sub>2</sub>

The initial growth of  $\text{Al}_2\text{O}_3$  by ALD on the  $\text{SiO}_2$  surface was studied with BB-SFG spectroscopy by monitoring the –CH<sub>3</sub> surface groups related to chemisorbed TMA for the first 3 ALD cycles. A BB-SFG spectrum was recorded for the bare  $\text{SiO}_2/c$ -Si substrate probing the spectral region around 3000  $\text{cm}^{-1}$  in which the C-H stretch mode of –CH<sub>3</sub> groups is situated. Figure 5.4 (a) shows the broad spectral signature of the non-resonant SFG response from the substrate. From this point on, for every measurement the non-resonant background was suppressed to facilitate the interpretation of the BB-SFG spectra. This suppression was achieved by delaying the visible pulse with respect to the mid-IR pulse, similar to the approach used by Lagutchev et al. to reduce the non-resonant contribution of a Au surface.<sup>45</sup>

The first ALD cycle on the sample was started with the TMA half-cycle. Instead of using one relatively long precursor exposure, the TMA dose was divided up into shorter exposures of 20 ms each. This allowed us to follow the surface chemistry during the half-cycles. In every measurement, the surface was exposed to 20 ms of TMA and once the vacuum chamber was pumped down a BB-SFG spectrum was collected. In Fig. 5.4 (b) spectrum *i* is taken after the first exposure and this spectrum clearly shows the appearance of a resonant feature at 2890  $\text{cm}^{-1}$  which is indicative of the –CH<sub>3</sub> groups of chemisorbed TMA on the surface. This procedure was repeated several

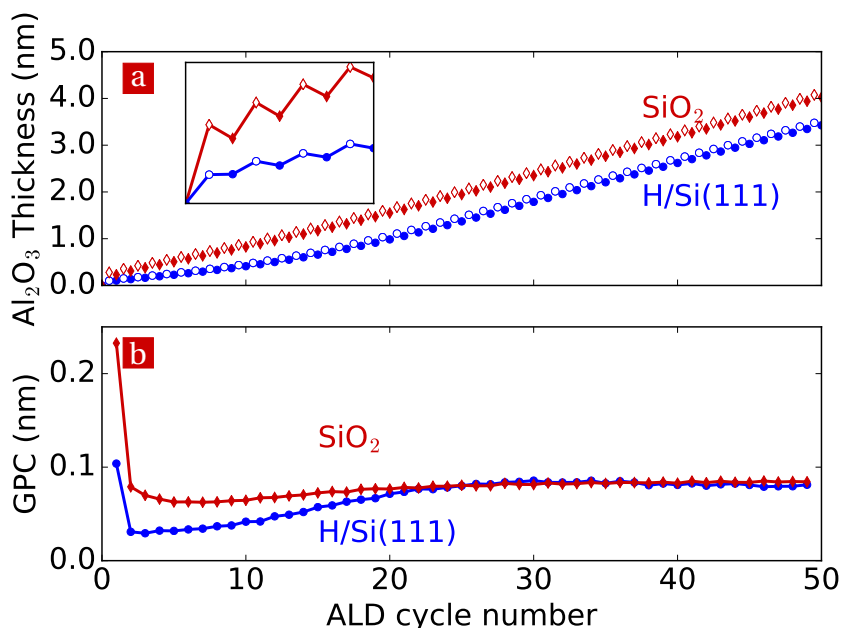


**Figure 5.3:** (a) The thickness of a  $\text{Al}_2\text{O}_3$  film grown by ALD measured with *in-situ* SE plotted as a function of the number of cycles for a  $\text{SiO}_2$  and a  $\text{H/Si}(111)$  starting surface. Data was collected after both the TMA (open markers) and the  $\text{H}_2\text{O}$  (solid markers) half-cycle. The inset shows the first 4 cycles in more detail. (b) The GPC plotted as a function of the ALD cycle number for ALD of  $\text{Al}_2\text{O}_3$  on both the  $\text{SiO}_2$  and  $\text{H/Si}(111)$  surface.

times and spectra *ii* up to *v* show an increase in the strength of the feature assigned to the  $-\text{CH}_3$  groups. From spectrum *v* on, the feature related to the  $-\text{CH}_3$  groups no longer changes. This indicates that additional TMA could no longer adsorb on the surface and that saturation was reached. The  $\text{H}_2\text{O}$  half-cycle following the TMA half-cycle was studied using the same procedure, exposing the surface to 20 ms of  $\text{H}_2\text{O}$  multiple times and recording a BB-SFG spectrum after each exposure. A decrease in  $-\text{CH}_3$  coverage on the surface was observed as a function of  $\text{H}_2\text{O}$  exposure (spectra not shown). The *persistent*  $-\text{CH}_3$  groups present during steady-state growth of  $\text{Al}_2\text{O}_3$  at  $100^\circ\text{C}$ <sup>22</sup> were also observed after the first  $\text{H}_2\text{O}$  half-cycle. These *persistent*  $-\text{CH}_3$  groups are not reactive towards  $\text{H}_2\text{O}$  and therefore remain on the surface after the  $\text{H}_2\text{O}$  half-cycle. Hence, they limit the TMA uptake in the subsequent TMA half-cycle.

The relative  $-\text{CH}_3$  coverage during the ALD half-cycles was determined from the spectra shown in Fig. 5.4 by a fitting procedure. The top two panels of Fig. 5.5 show the  $-\text{CH}_3$  coverage as a function of precursor and co-reactant exposure in the first ALD cycle. The 2 subsequent ALD cycles were also mon-

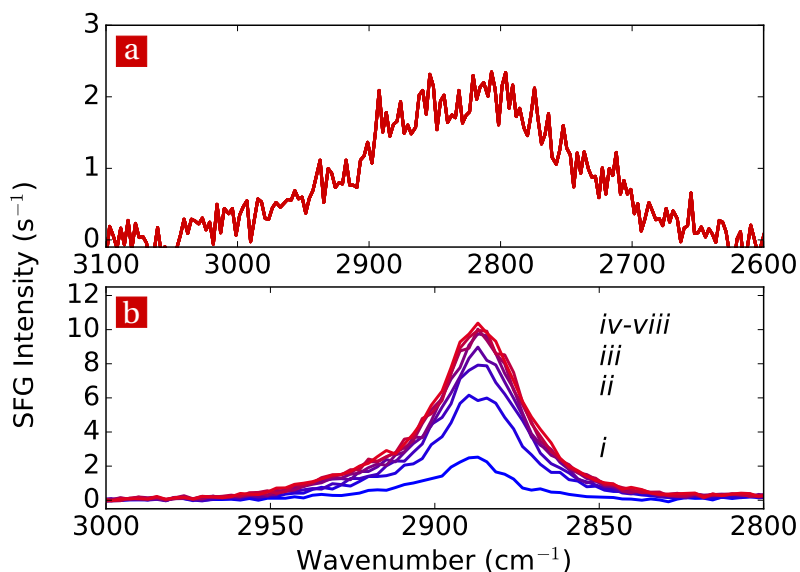


**Figure 5.4:** (a) A BB-SFG spectrum recorded of the pristine  $\text{SiO}_2$  surface revealing a non-resonant  $c$ -Si background resulting in the broad spectral feature reflecting the spectral shape of the mid-IR beam used in the experiment. By delaying the visible pulse with respect to the mid-IR pulse, this contribution was suppressed in all subsequent experiments. (b) BB-SFG spectra of the C-H stretch region (i) after the first TMA exposure. The characteristic peak around  $2900\text{ cm}^{-1}$  is indicative of the  $-\text{CH}_3$  groups of chemisorbed TMA on the surface. The amount of chemisorbed TMA increases for subsequent exposures (ii–iv), and eventually saturates (v–viii).

itored using the same approach, and the results are also plotted in Fig. 5.5. Each of the half-cycles was driven to saturation before the next half-cycle was commenced. From Fig. 5.5 it is clear that the reaction kinetics of the first TMA half-cycle deviates significantly from the reaction kinetics of the steady state growth. Yet, the reaction kinetics of the TMA half-cycles for the second and third ALD cycle are virtually identical to the reaction kinetics observed for the steady state growth (also shown in Fig. 5.5). Furthermore, the relative amount of  $-\text{CH}_3$  after the TMA half-cycle did not vary from cycle-to-cycle. For the  $\text{H}_2\text{O}$  step, all the half-cycles show reaction kinetics identical to that of the steady state growth. The relative coverage of the *persistent*  $-\text{CH}_3$  groups left after the saturated  $\text{H}_2\text{O}$  half-cycles is  $\sim 60\%$ . The amount of *persistent* groups was the same for the first, second, and third cycle and is similar to what has been observed for steady state growth at  $100\text{ }^\circ\text{C}$ .<sup>22</sup> To summarize, these data show that only the reaction kinetics of the first TMA half-cycle is affected when growing on a  $\text{SiO}_2$  surface. This is in line with the immediate

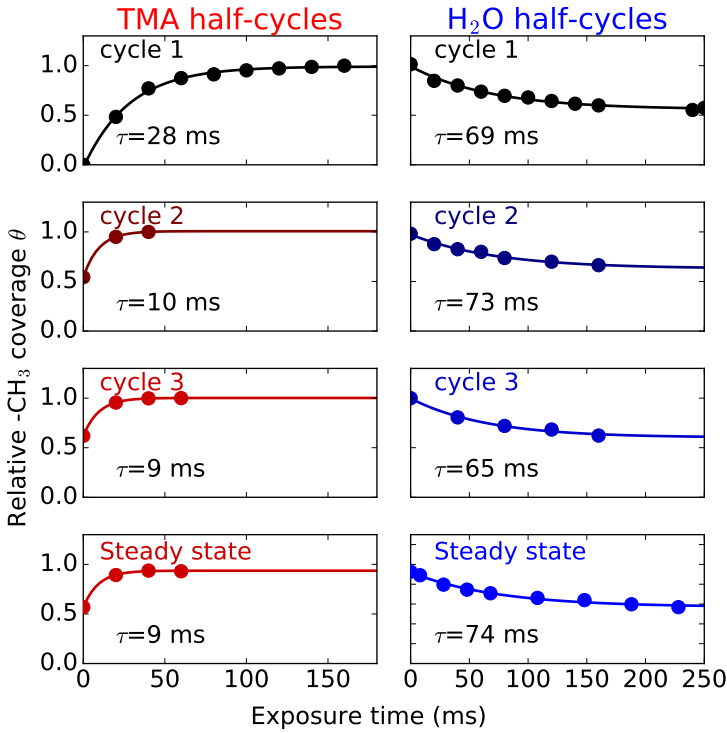


**Figure 5.5:** The  $-\text{CH}_3$  coverage as a function of the TMA and  $\text{H}_2\text{O}$  exposure for the first 3 cycles on the  $\text{SiO}_2$  surface for ALD of  $\text{Al}_2\text{O}_3$  at  $100^\circ\text{C}$  obtained from modeling the BB-SFG spectra. For comparison, the steady-state reaction kinetics, reported elsewhere,<sup>22</sup> are also given in the figure. The data is normalized to the  $-\text{CH}_3$  coverage reached after the first TMA half-cycle and the solid lines are fits to the data used to determine the reaction cross section.

growth observed for ALD of  $\text{Al}_2\text{O}_3$  on the  $\text{SiO}_2$  surface in Fig. 5.3 which is also typically reported in literature.<sup>18,46</sup>

The reaction cross section was determined from the reaction kinetics, i.e. the curves in Fig. 5.5. Assuming that the reaction in the TMA and  $\text{H}_2\text{O}$  half-cycle can be described by a first order reactions, the  $-\text{CH}_3$  coverage  $\theta_{\text{CH}}$  and  $-\text{OH}$  coverage  $\theta_{\text{OH}}$  are given by:

$$\frac{d\theta_{\text{OH}}}{dt} = -\sigma_{\text{TMA}}\Gamma_{\text{TMA}}\theta_{\text{OH}}, \quad (5.4a)$$

$$\frac{d\theta_{\text{CH}}}{dt} = -\sigma_{\text{H}_2\text{O}}\Gamma_{\text{H}_2\text{O}}\theta_{\text{CH}}, \quad (5.4b)$$

with  $\sigma_{\text{TMA}}$  and  $\sigma_{\text{H}_2\text{O}}$  the reaction cross section of TMA and  $\text{H}_2\text{O}$  during the TMA and  $\text{H}_2\text{O}$  half-cycle, respectively. For the relative  $-\text{OH}$  and  $-\text{CH}_3$  coverage,

**Table 5.1:** The reaction cross-section  $\sigma_{TMA}$  and  $\sigma_{H_2O}$  of the reactions taking place in the TMA and H<sub>2</sub>O half-cycles during the first 3 ALD cycles on the SiO<sub>2</sub> surface for the initial TMA half-cycle on H/Si(111). For comparison, the steady state cross sections are also listed. A surface coverage of  $6 \cdot 10^{14} \text{ cm}^{-2}$  was assumed in the calculation of the initial sticking probability for both the -OH and the -CH<sub>3</sub> groups.<sup>21,47</sup> For the H/Si(111) surface a coverage of  $7.8 \cdot 10^{14} \text{ cm}^{-2}$  was used.<sup>48</sup> The “random error” is listed in the table, the systematic error might be larger but only introduces a scaling factor and does not affect the trend in the data.

Starting Surf.	Cycle	$\sigma_{TMA}$ ( $10^{-18} \text{ cm}^2$ )	$S_0^{TMA}$ ( $\cdot 10^{-3}$ )	$\sigma_{H_2O}$ ( $10^{-18} \text{ cm}^2$ )	$S_0^{H_2O}$ ( $\cdot 10^{-3}$ )
H/Si(111)	1st.	$3.1 \pm 0.3$	$2 \pm 0.2$	-	-
SiO <sub>2</sub>	1st.	$2.0 \pm 0.2$	$1 \pm 0.1$	$0.040 \pm 0.004$	$0.02 \pm 0.002$
SiO <sub>2</sub>	2nd.	$6.0 \pm 0.6$	$4 \pm 0.4$	$0.039 \pm 0.004$	$0.02 \pm 0.002$
SiO <sub>2</sub>	3rd.	$6.0 \pm 0.6$	$4 \pm 0.4$	$0.040 \pm 0.004$	$0.02 \pm 0.002$
<b>steady state</b>	$\infty$	$6.5 \pm 0.6$	$4 \pm 0.4$	$0.037 \pm 0.004$	$0.02 \pm 0.002$

the relation  $\theta_{OH} + \theta_{CH} = 1$  holds. The Hertz-Knudsen equation was used to determine the flux of H<sub>2</sub>O ( $\Gamma_{H_2O} = 3.5 \cdot 10^{20} \text{ cm}^{-2}\text{s}^{-1}$ ) and TMA ( $\Gamma_{TMA} = 1.7 \cdot 10^{19} \text{ cm}^{-2}\text{s}^{-1}$ ) towards the substrate from the pressure in the reactor during dosing. The reaction cross section was determined from the fit of the simple exponential function described by Eq. (5.4) to the data in Fig. 5.5. The main uncertainty in the cross section was caused by a systematic error in the absolute magnitude of the flux which only introduces a scaling factor in the absolute value of the cross section. Therefore, this does not affect the interpretation of relative differences between the cross sections. The “random error” in the data is better than 10% which is a conservative estimate from the fluctuations in the strength of the SFG signal over time.

Table 5.1 lists the reaction cross sections obtained from the fits to the data in Fig. 5.5 for both half-cycles during the first 3 ALD cycles. The reaction cross section of the initial TMA half-cycle,  $\sigma_{TMA} = 2.0 \pm 0.2 \cdot 10^{-18} \text{ cm}^2$ , was found to be a factor of three lower than that of steady state growth. The corresponding initial sticking probability  $S_0^{TMA}$ , related to the reaction cross section by  $S_0^{TMA} = \sigma_{TMA} \cdot \theta_{OH}$ , was calculated assuming an absolute -OH surface coverage of  $6 \cdot 10^{14}$  groups per  $\text{cm}^2$ .<sup>47</sup> The initial sticking probability of  $S_0^{TMA} = 0.001$  indicates that a TMA molecule has approximately 1000 interactions with -OH groups on the SiO<sub>2</sub> surface before the TMA molecule chemisorbs. The reaction cross-section and initial sticking probability of the subsequent TMA half-cycles,  $\sigma_{TMA} = 6.0 \cdot 10^{-18} \text{ cm}^2$  and  $S_0^{TMA} = 0.004$ , was the same as that of the steady state growth. For the H<sub>2</sub>O half-cycles, the cross section did not vary with cycle number and it was found to be  $\sigma_{H_2O} = 4.0 \pm 0.4 \cdot 10^{-20} \text{ cm}^2$  which is identical to that of the steady-state growth. This yields a initial sticking probability of  $S_0^{H_2O} = 2 \cdot 10^{-5}$  assuming a -CH<sub>3</sub> coverage of  $6 \cdot 10^{14} \text{ cm}^{-2}$ .<sup>21</sup>



### Si-H coverage during initial chemisorption of TMA on H/Si(111)

The initial chemisorption of TMA on the H/Si(111) surface was studied with BB-SFG spectroscopy by monitoring the stretching mode of the Si-H groups on the surface. A BB-SFG spectrum of the pristine surface was collected after the reactor was pumped down and is shown in Fig. 5.6. A sharp resonance at  $2090\text{ cm}^{-1}$  was observed which is typical for the stretching vibration of Si-H groups on the H/Si(111) surface. In FTIR spectroscopy the stretching mode of Si-H on the H/Si(111) surface is commonly observed at  $2086\text{ cm}^{-1}$  and is known for its extremely narrow spectral width of  $0.05\text{ cm}^{-1}$  at 40K.<sup>24,35,36,42,49</sup> However, in the BB-SFG spectra, the spectral width of the Si-H feature is entirely due to the instrumental broadening, see also appendix. To test repeatability of the measurement and the stability of the surface, a second spectrum is recorded after waiting 120 s. The overlap between the two spectra in Fig. 5.6 shows the excellent repeatability of the measurement. After the collection of the BB-SFG spectrum of the pristine surface, the sample was exposed to TMA by opening the ALD valve for a duration of 10 ms. After pumping down the vacuum chamber a new BB-SFG spectrum was collected. The amplitude of the Si-H feature decreased, as can be seen in Fig. 5.6. This indicated that TMA has reacted with the Si-H groups, in agreement with the observation of Frank et al.<sup>24</sup> Again a second spectrum was collected after 120 s to verify the stability of the surface. This entire procedure of dosing TMA for 10 ms and recording two BB-SFG spectra was repeated until the Si-H feature could not longer be discerned.

The Si-H coverage was determined from a fit to the BB-SFG spectra in Fig. 5.6 using the aforementioned procedure. The resulting Si-H coverage was plotted as a function of TMA exposure in Fig. 5.7, showing an exponential decrease of Si-H coverage with TMA exposure. This indicated that the reaction of TMA with the Si-H groups is first order in the Si-H coverage. The reactor cross section  $\sigma_{TMA}$  was found from fitting the exponential function described by Eq. (5.4b) to the data (replacing  $\theta_{OH}$  by  $\theta_{SiH}$ ). The TMA flux was  $\Gamma_{TMA} = 1.7 \cdot 10^{19}\text{ cm}^{-2}\text{s}^{-1}$ . The reaction cross section of TMA chemisorption on H/Si(111),  $\sigma_{TMA} = 3.1 \cdot 10^{-18}\text{ cm}^2$ , was found to be slightly smaller than the cross section of the steady state growth but larger than the reaction cross section of the initial chemisorption on a  $\text{SiO}_2$  surface.

## 5.5 Concluding remarks

The subtle differences in the surface chemistry and the reaction kinetics during the initial growth of  $\text{Al}_2\text{O}_3$  by ALD on the  $\text{SiO}_2$  surface and the H/Si(111) surface were studied with *in-situ* BB-SFG spectroscopy.

For the  $\text{SiO}_2$  surface, the density of  $-\text{CH}_3$  groups was monitored during the first 3 ALD cycles with BB-SFG spectroscopy. The reactivity of TMA towards the  $\text{SiO}_2$  surface, i.e. the reaction cross section, in the first ALD cycle was found to be a factor of 3 lower than during steady-state growth. This suggests a

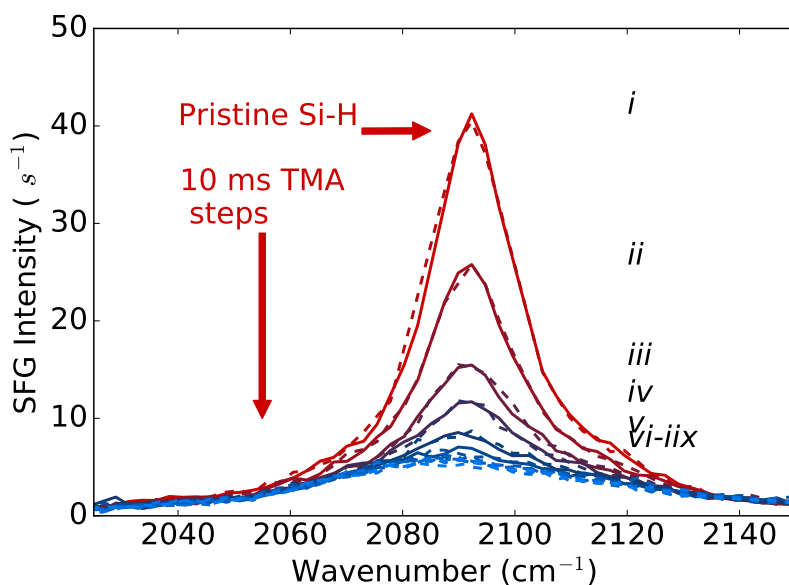


**Figure 5.6:** (i) A BB-SFG spectrum of a pristine H/Si(111) surface showing the typical Si-H stretch for this surface situated at  $2900\text{ cm}^{-1}$ . In (ii) through (ix) the Si-H signal decreases due to subsequent TMA exposures. The stability of the surface and reproducibility of the measurement was verified by the overlap between the spectrum recorded after the TMA dose (solid lines) and the spectrum recorded after a dwell time of 120s (dashed lines).

lower reactivity of the -OH groups back bonded to Si compared to -OH groups back bonded to Al. The subsequent TMA half-cycles showed a reactivity comparable to steady-state growth. All three  $\text{H}_2\text{O}$  half-cycles, including the  $\text{H}_2\text{O}$  step in the first ALD cycle, showed a reactivity comparable to steady-state growth and seem to be unaffected by initial growth phenomena. Apparently, the environment and therefore the reactivity of the  $-\text{CH}_3$  groups towards  $\text{H}_2\text{O}$  is not affected significantly during the initial growth. The relative amount of  $-\text{CH}_3$  groups after the TMA half-cycle did not vary from cycle-to-cycle. The relative density of *persistent*  $-\text{CH}_3$  groups after the  $\text{H}_2\text{O}$  half-cycle also did not vary from cycle-to-cycle and was comparable to the relative density reported for steady-state growth. Moreover, the presence of the persistent surface groups has the side-effect that the TMA uptake during the first ALD cycle is significantly higher than in the subsequent ALD cycles. The larger TMA uptake in the first ALD cycle is also reflected in the *in-situ* SE data, showing a significantly higher GPC ( $2.3\text{ \AA}$  compared to  $0.8\text{ \AA}$  for steady-state growth) approximately matching the increase in TMA uptake deduced from the BB-SFG spectra. Moreover, the *in-situ* SE data shows that only the first ALD cycle

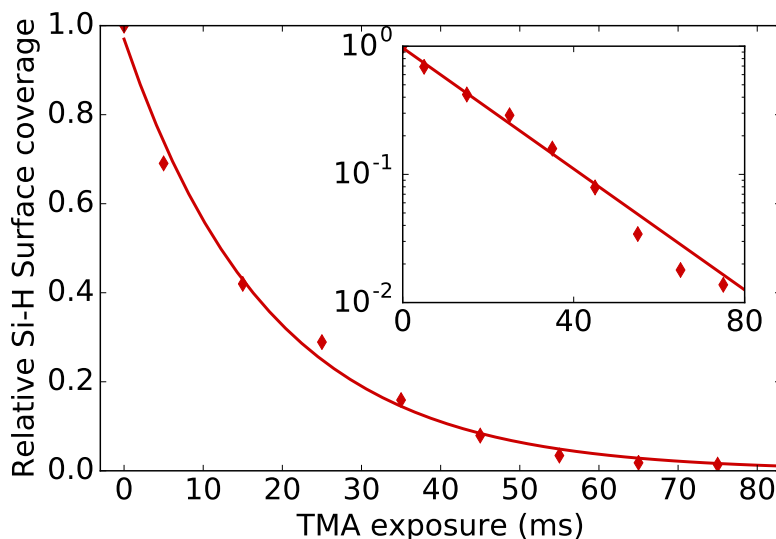


**Figure 5.7:** The Si-H coverage of a H/Si(111) surface as a function of TMA exposure determined from the BB-SFG spectra. The inset shows the same data plotted on a logarithmic scale.

was affected by initial growth phenomena and that all subsequent cycles exhibit steady-state growth, in line with the trend in the reaction cross section determined with BB-SFG spectroscopy. The surface chemistry for  $\text{Al}_2\text{O}_3$  ALD on the  $\text{SiO}_2$  surface is likely fairly independent of the techniques with which the  $\text{SiO}_2$  was formed. Yet, annealed  $\text{SiO}_2$  surfaces are expected to exhibit a different surface termination (with a lower density of -OH groups due to thermally induced dehydroxylation). This can result in a different reaction mechanism with different surface species, such as TMA chemisorption on Si-O-Si bridges,<sup>50</sup> that will lead to different reaction kinetics.

The chemisorption of TMA onto the H/Si(111) surface during the first TMA half-cycle was followed with BB-SFG spectroscopy by probing the Si-H groups. The TMA chemisorption onto the Si-H groups showed a slightly smaller reaction cross section than that of steady-state growth. Moreover, the reaction was observed to be first order in the Si-H coverage. It was not possible to measure the  $-\text{CH}_3$  groups on the H/Si(111) surface due to less favorable Fresnel coefficients leading to a reduced sensitivity on this surface. Yet, the cross section determined from measurements of either the Si-H groups or the  $-\text{CH}_3$  groups lead to similar results. With *in-situ* SE, immediate growth was observed however, the first  $\sim 20$  cycles show a lower GPC with respect to the steady-state growth, in line with the lower reactivity measured with BB-SFG

spectroscopy.

There is no simple or direct relation between the reaction cross section and the number of ALD cycles affected by initial growth phenomena. The reaction cross section is a measure of how reactive the precursor is towards the surface, but this is only a part of the picture. During the initial growth phase, the type and areal density of the dominant surface groups is changing cycle-by-cycle. The higher cross section for TMA chemisorption on H/Si(111) surface than on the SiO<sub>2</sub> surface should be seen in this light. TMA chemisorbs more readily on H/Si(111) than it does on -OH groups on the SiO<sub>2</sub> surface. However, the TMA uptake is probably lower and it takes longer to reach steady-state conditions.

For a better understanding of initial growth during ALD, the surface chemistry needs to be studied both qualitatively and quantitatively. First, the (surface) groups involved in the ALD process need to be determined. Then, both the reaction cross section and the areal density of the surface groups needs to be quantified. In this work, it was demonstrated that BB-SFG spectroscopy is a feasible technique for quantifying these characteristic of the surface chemistry. When complemented with other analysis techniques, determining e.g. gas-phase reaction products and GPC, this can yield fundamental insights into the underlying growth mechanisms of the initial growth phase of ALD.

## Acknowledgements

The authors would like to thank J.J.A. Zeebregts, J.J.L.M. Meulendijks, C.A.A. van Helvoirt, and C.O. van Bommel for their skillful technical support. This work was supported by the Dutch Technology Foundation STW and the Netherlands Organization for scientific Research (NWO, VICI Program on “Nanomanufacturing.”).

## 5.A Appendix

### Modeling the BB-SFG spectra

Figure 5.8 shows the same BB-SFG spectra as shown in Fig. 5.4 but in this case with an vertical offset applied to the spectra for clarity. A good agreement between the measured data and the fit of the model described in the main manuscript, used to obtain the relative  $-\text{CH}_3$  density, can be seen in the figure.

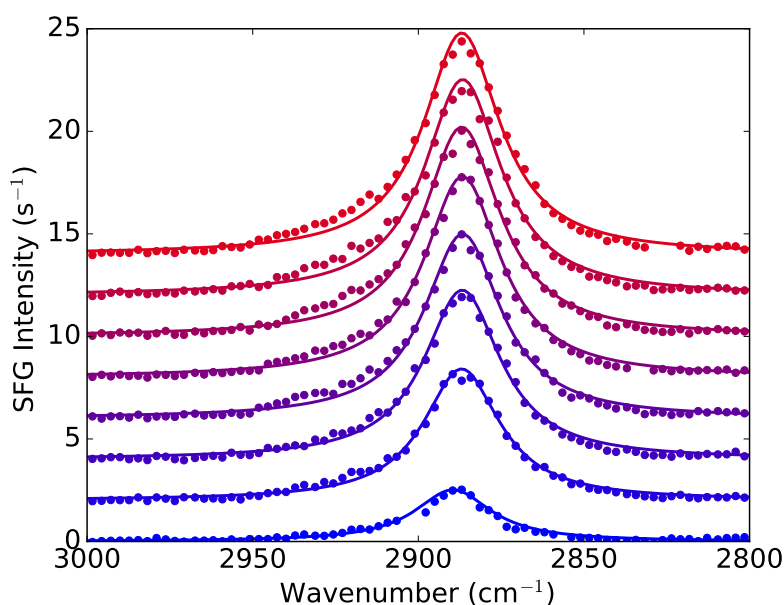


**Figure 5.8:** BB-SFG spectra showing the  $-\text{CH}_3$  resonance, identical to the data in Fig. 5.4. The measured data (markers) and the fit to the data (solid lines) are both shown. An offset has been applied to the spectra for clarity.

### Spectral shape of the Si-H stretch mode

The spectral resolution of BB-SFG spectroscopy is limited by the spectral width of the visible pulse. In the SFG process a mid-IR photon with energy  $\omega_{ir}$  mixes with a visible photon with energy  $\omega_{vis}$ . This produces a new photon with photon energy  $\omega_{sfg} = \omega_{vis} + \omega_{ir}$ . A variation of  $\omega_{vis}$  of  $\delta\omega_{vis}$  results in a variation in the SFG photon,  $\delta\omega_{sfg} = \delta\omega_{vis}$ . The visible pulse used in this work had a spectral width of 1 nm centered around 795 nm, i.e. 1.25%. For a (infinitely narrow) resonance at  $2090\text{ cm}^{-1}$  this corresponds to a full-width half-maximum (FWHM) of  $25\text{ cm}^{-1}$  in the IR domain, in excellent agreement with the FWHM of  $\sim 25\text{ cm}^{-1}$  observed experimentally.

## Bibliography

- [1] Coburn and Winters. Plasma etching - A discussion of mechanisms. *Journal of Vacuum Science and Technology*, 1979. doi:[10.1116/1.569958](https://doi.org/10.1116/1.569958).
- [2] Winters and Coburn. Surface science aspects of etching reactions. *Surface Science Reports*, 1992. doi:[10.1016/0167-5729\(92\)90009-Z](https://doi.org/10.1016/0167-5729(92)90009-Z).
- [3] Winters. Surface processes in plasma-assisted etching environments. *Journal of Vacuum Science & Technology B: Microelectronics and Nanometer Structures*, 1983. doi:[10.1116/1.582629](https://doi.org/10.1116/1.582629).
- [4] Winters and Coburn. Plasma-assisted etching mechanisms: The implications of reaction probability and halogen coverage. *Journal of Vacuum Science & Technology B*, 1985. doi:[10.1116/1.582996](https://doi.org/10.1116/1.582996).
- [5] Knoops, Potts, Bol, and Kessels. Springer Handbook of Crystal Growth. *Japanese Magazine of Mineralogical and Petrological Sciences*, 2010. doi:[10.2465/gkk.39.193a](https://doi.org/10.2465/gkk.39.193a).
- [6] George, Ott, and Klaus. Surface Chemistry for Atomic Layer Growth. *The Journal of Physical Chemistry*, 1996. doi:[10.1021/jp9536763](https://doi.org/10.1021/jp9536763).
- [7] George. Atomic layer deposition: an overview. *Chemical reviews*, 2010. doi:[10.1021/cr900056b](https://doi.org/10.1021/cr900056b).
- [8] Frank, Chabal, Green, Delabie, Brijs, Wilk, Ho, da Rosa, Baumvol, and Stedile. Enhanced initial growth of atomic-layer-deposited metal oxides on hydrogen-terminated silicon. *Applied Physics Letters*, 2003. doi:[10.1063/1.1595719](https://doi.org/10.1063/1.1595719).
- [9] Mackus, Thissen, Mulders, Trompenaars, Verheijen, Bol, and Kessels. Direct-write atomic layer deposition of high-quality Pt nanostructures: Selective growth conditions and seed layer requirements. *Journal of Physical Chemistry C*, 2013. doi:[10.1021/jp402260j](https://doi.org/10.1021/jp402260j).
- [10] Wilson, Grubbs, and George. Nucleation and Growth during Al<sub>2</sub>O<sub>3</sub> Atomic Layer Deposition on Polymers. *Chem. Mater.*, 2005. doi:[10.1021/cm050704d](https://doi.org/10.1021/cm050704d).
- [11] Elam and George. Growth of ZnO/Al<sub>2</sub>O<sub>3</sub> alloy films using atomic layer deposition techniques. *Chemistry of Materials*, 2003. doi:[10.1021/cm020607+](https://doi.org/10.1021/cm020607+).
- [12] Wu, Potts, Hermkens, Knoops, Roozeboom, and Kessels. Enhanced doping efficiency of Al-doped ZnO by atomic layer deposition using dimethylaluminum isopropoxide as an alternative aluminum precursor. *Chemistry of Materials*, 2013. doi:[10.1021/cm402974j](https://doi.org/10.1021/cm402974j).
- [13] Mackus, MacIsaac, Kim, and Bent. Incomplete elimination of precursor ligands during atomic layer deposition of zinc-oxide, tin-oxide, and zinc-tin-oxide. *The Journal of Chemical Physics*, 2017. doi:[10.1063/1.4961459](https://doi.org/10.1063/1.4961459).
- [14] Weber, MacKus, Verheijen, van der Marel, and Kessels. Supported core/shell bimetallic nanoparticles synthesis by atomic layer deposition. *Chemistry of Materials*, 2012. doi:[10.1021/cm301206e](https://doi.org/10.1021/cm301206e).
- [15] Mackus, Verheijen, Leick, Bol, and Kessels. Influence of Oxygen Exposure on the Nucleation of Platinum Atomic Layer Deposition: Consequences

- for Film Growth, Nanopatterning, and Nanoparticle Synthesis. *Chemistry of Materials*, 2013. doi:[10.1021/cm400562u](https://doi.org/10.1021/cm400562u).
- [16] Mameli, Kuang, Aghaee, Ande, Karasulu, Creatore, Mackus, Kessels, and Roozeboom. Area-Selective Atomic Layer Deposition of  $\text{In}_2\text{O}_3\text{:H}$  Using a  $\hat{\text{A}}\text{t}$ -Plasma Printer for Local Area Activation. *Chemistry of Materials*, 2017. doi:[10.1021/acs.chemmater.6b04469](https://doi.org/10.1021/acs.chemmater.6b04469).
- [17] Dillon, Ott, Way, and George. Surface chemistry of  $\text{Al}_2\text{O}_3$  deposition using  $\text{Al}(\text{CH}_3)_3$  and  $\text{H}_2\text{O}$  in a binary reaction sequence. *Surface Science*, 1995. doi:[10.1016/0039-6028\(95\)90033-0](https://doi.org/10.1016/0039-6028(95)90033-0).
- [18] Ott, McCarley, Klaus, Way, and George. Atomic layer controlled deposition of  $\text{Al}_2\text{O}_3$  films using binary reaction sequence chemistry. *Applied Surface Science*, 1996. doi:[10.1016/S0169-4332\(96\)00503-X](https://doi.org/10.1016/S0169-4332(96)00503-X).
- [19] Rahtu, Alaranta, and Ritala. In Situ Quartz Crystal Microbalance and Quadrupole Mass Spectrometry Studies of Atomic Layer Deposition of Aluminum Oxide from Trimethylaluminum and Water. *Langmuir*, 2001. doi:[10.1021/la010103a](https://doi.org/10.1021/la010103a).
- [20] Elam, Groner, and George. Viscous flow reactor with quartz crystal microbalance for thin film growth by atomic layer deposition. *Review of Scientific Instruments*, 2002. doi:[10.1063/1.1490410](https://doi.org/10.1063/1.1490410).
- [21] Ott, Klaus, Johnson, and George.  $\text{Al}_3\text{O}_3$  thin film growth on Si(100) using binary reaction sequence chemistry. *Thin Solid Films*, 1997. doi:[10.1016/S0040-6090\(96\)08934-1](https://doi.org/10.1016/S0040-6090(96)08934-1).
- [22] Vandalon and Kessels. What is limiting low-temperature atomic layer deposition of  $\text{Al}_2\text{O}_3$ ? A vibrational sum-frequency generation study. *Applied Physics Letters*, 2016. doi:[10.1063/1.4939654](https://doi.org/10.1063/1.4939654).
- [23] Mitsui, Hill, Curtis, and Ganz. Initial stages of Al growth from dimethylaluminum hydride on silicon. *Physical Review B*, 1999. doi:[10.1103/PhysRevB.59.8123](https://doi.org/10.1103/PhysRevB.59.8123).
- [24] Frank, Chabal, and Wilk. Nucleation and interface formation mechanisms in atomic layer deposition of gate oxides. *Applied Physics Letters*, 2003. doi:[10.1063/1.1585129](https://doi.org/10.1063/1.1585129).
- [25] Grunthaner and Grunthaner. Chemical and electronic structure of the  $\text{SiO}_2/\text{Si}$  interface. *Materials science reports*, 1986. doi:[10.1016/S0920-2307\(86\)80001-9](https://doi.org/10.1016/S0920-2307(86)80001-9).
- [26] Deal. The Current Understanding of Charges in the Thermally Oxidized Silicon Structure. *Journal of The Electrochemical Society*, 1974. doi:[10.1149/1.2402380](https://doi.org/10.1149/1.2402380).
- [27] Deal, Sklar, Grove, and Snow. Characteristics of the Surface-State Charge ( $Q_{ss}$ ) of Thermally Oxidized Silicon. *Journal of The Electrochemical Society*, 1967. doi:[10.1149/1.2426565](https://doi.org/10.1149/1.2426565).
- [28] Niwano. Infrared spectroscopic study of initial stages of ultraviolet ozone oxidation of Si(100) and Si(111) surfaces. *Journal of Vacuum Science & Technology A: Vacuum, Surfaces, and Films*, 1994. doi:[10.1116/1.579264](https://doi.org/10.1116/1.579264).
- [29] Michalak, Rivillon, Chabal, Esteve, and Lewis. Infrared spectroscopic investigation of the reaction of hydrogen-terminated, (111)-oriented, silicon surfaces with liquid methanol. *The journal of physical chemistry*.

- B*, 2006. doi:[10.1021/jp0624303](https://doi.org/10.1021/jp0624303).
- [30] Michalak, Amy, Aureau, Dai, Esteve, and Chabal. Nanopatterning Si(111) surfaces as a selective surface-chemistry route. *Nature materials*, 2010. doi:[10.1038/nmat2611](https://doi.org/10.1038/nmat2611).
- [31] Chabal, Dumas, Guyot-Sionnest, and Higashi. Vibrational dynamics of the ideally H-terminated Si(111) surface. *Surface Science*, 1991. doi:[10.1016/0039-6028\(91\)90321-I](https://doi.org/10.1016/0039-6028(91)90321-I).
- [32] Guyot-Sionnest, Lin, and Hiller. Vibrational dynamics of the Si-H stretching modes of the Si(100)/H:2x1 surface. *The Journal of Chemical Physics*, 1995. doi:[10.1063/1.469474](https://doi.org/10.1063/1.469474).
- [33] Lupke. Characterization of semiconductor interfaces by second-harmonic generation. *Surface Science Reports*, 1999. doi:[10.1016/S0167-5729\(99\)00007-2](https://doi.org/10.1016/S0167-5729(99)00007-2).
- [34] Allongue, Kieling, and Gerischer. Etching mechanism and atomic structure of H-Si(111) surfaces prepared in  $\text{ceNH}_4\text{F}$ . *Electrochimica Acta*, 1995. doi:[10.1016/0013-4686\(95\)00071-L](https://doi.org/10.1016/0013-4686(95)00071-L).
- [35] Jakob, Chabal, and Raghavachari. Lineshape analysis of the Si-H stretching mode of the ideally H-terminated Si(111) surface: the role of dynamical dipole coupling. *Chemical Physics Letters*, 1991. doi:[10.1016/0009-2614\(91\)90433-A](https://doi.org/10.1016/0009-2614(91)90433-A).
- [36] Tully, Chabal, Raghavachari, Bowman, and Lucchese. Infrared linewidths and vibrational lifetimes at surfaces: H on Si(100). *Physical Review B*, 1985. doi:[10.1103/PhysRevB.31.1184](https://doi.org/10.1103/PhysRevB.31.1184).
- [37] Boyd. *Nonlinear optics*. Elsevier Science Publishing Co Inc, second edition, 1992.
- [38] Heinz. Second-order nonlinear optical effects at surfaces and interfaces. *Nonlinear surface electromagnetic phenomena*, 1991.
- [39] Vandalon and Kessels. Chapter 7 of this thesis.
- [40] Shirazi and Elliott. Cooperation between adsorbates accounts for the activation of atomic layer deposition reactions. *Nanoscale*, 2015. doi:[10.1039/C5NR00900F](https://doi.org/10.1039/C5NR00900F).
- [41] Weckman and Laasonen. First principles study of the atomic layer deposition of alumina by TMA- $\text{H}_2\text{O}$ -process. *Phys. Chem. Chem. Phys.*, 2015. doi:[10.1039/C5CP01912E](https://doi.org/10.1039/C5CP01912E).
- [42] Higashi, Chabal, Trucks, and Raghavachari. Ideal hydrogen termination of the Si(111) surface. *Applied Physics Letters*, 1990. doi:[10.1063/1.102728](https://doi.org/10.1063/1.102728).
- [43] van Hemmen, Heil, Klootwijk, Roozeboom, Hodson, van de Sanden, and Kessels. Plasma and Thermal ALD of  $\text{Al}_2\text{O}_3$  in a Commercial 200 mm ALD Reactor. *Journal of The Electrochemical Society*, 2007. doi:[10.1149/1.2737629](https://doi.org/10.1149/1.2737629).
- [44] Langereis, Heil, Knoops, Keuning, van de Sanden, and Kessels. In situ spectroscopic ellipsometry as a versatile tool for studying atomic layer deposition. *Journal of Physics D: Applied Physics*, 2009. doi:[10.1088/0022-3727/42/7/073001](https://doi.org/10.1088/0022-3727/42/7/073001).
- [45] Lagutchev, Hambir, and Dlott. Nonresonant Background Suppression in Broadband Vibrational Sum-Frequency Generation Spectroscopy. *The*



- Journal of Physical Chemistry C*, 2007. doi:[10.1021/jp075391j](https://doi.org/10.1021/jp075391j).
- [46] Higashi and Fleming. Sequential surface chemical-reaction limited growth of high-quality  $\text{Al}_2\text{O}_3$  dielectrics. *Applied Physics Letters*, 1989. doi:[10.1063/1.102337](https://doi.org/10.1063/1.102337).
- [47] Zhuravlev. Concentration of hydroxyl groups on the surface of amorphous silicas. *Langmuir*, 1987. doi:[10.1021/la00075a004](https://doi.org/10.1021/la00075a004).
- [48] Dinger, Lutterloh, and Kuppers. Interaction of hydrogen atoms with Si(111) surfaces: Adsorption, abstraction, and etching. *The Journal of Chemical Physics*, 2001. doi:[10.1063/1.1351158](https://doi.org/10.1063/1.1351158).
- [49] Dumas, Chabal, and Higashi. Coupling of an adsorbate vibration to a substrate surface phonon: H on Si(111). *Physical Review Letters*, 1990. doi:[10.1103/PhysRevLett.65.1124](https://doi.org/10.1103/PhysRevLett.65.1124).
- [50] Puurunen. Surface chemistry of atomic layer deposition: A case study for the trimethylaluminum/water process. *Journal of Applied Physics*, 2005. doi:[10.1063/1.1940727](https://doi.org/10.1063/1.1940727).

# What is limiting low-temperature atomic layer deposition of $\text{Al}_2\text{O}_3$ ? A vibrational sum-frequency generation study

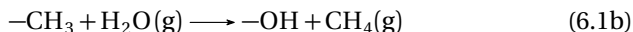
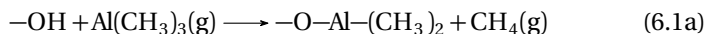
## Abstract

The surface reactions during atomic layer deposition (ALD) of  $\text{Al}_2\text{O}_3$  from  $\text{Al}(\text{CH}_3)_3$  and  $\text{H}_2\text{O}$  have been studied with broadband sum-frequency generation (BB-SFG) to reveal what is limiting the growth at low temperatures. The  $-\text{CH}_3$  surface coverage was measured for temperatures between 100 and 300 °C and the absolute reaction cross sections, describing the reaction kinetics, were determined for both half-cycles. It was found that  $-\text{CH}_3$  groups persisted on the surface after saturation of the  $\text{H}_2\text{O}$  half-cycle. From a direct correlation with the growth per cycle it was established that the reduced reactivity of  $\text{H}_2\text{O}$  towards  $-\text{CH}_3$  is the dominant factor limiting the ALD process at low temperatures.

## 6.1 Introduction

Atomic layer deposition (ALD) has become an enabling technology in the fabrication of semiconductor and photovoltaic devices due to its unique capability to conformally deposit ultra-thin films with sub-nanometer thickness precision.<sup>1</sup> In recent years, the adoption of ALD as the method of choice in numerous applications has sparked a drive towards the development of new ALD processes. Simultaneously, the operating range of existing processes are being explored with the main goal of obtaining greater flexibility in deposition conditions, while at the same time retaining all the merits of ALD. Of especial interest is low temperature ALD,<sup>2,3</sup> enabling deposition on temperature sensitive samples. When exploring a new process or extending the operating range of an established process, insight into the surface chemistry that is governing ALD is key. Yet gaining understanding of ALD film growth by directly studying the surface groups, ruling the ALD chemistry, requires highly sensitive in-situ diagnostic techniques.

This work focuses on the ubiquitous thermal ALD process of  $\text{Al}_2\text{O}_3$ , using trimethylaluminum ( $\text{Al}(\text{CH}_3)_3$ , TMA) as precursor and water as co-reactant and addresses the question what limits  $\text{Al}_2\text{O}_3$  growth at low temperature. The steady-state growth mechanism of this ALD process has been studied extensively with techniques such as quadrupole mass spectrometry,<sup>4</sup> spectroscopic ellipsometry,<sup>4</sup> quartz-crystal microbalance,<sup>5</sup> and Fourier-transform infrared (FTIR) absorption spectroscopy.<sup>6-8</sup> The generally accepted and dominant reaction mechanism for steady-state growth is as follows:



where an "-" symbol designate surface species. In addition to hydroxyls which form the most important chemisorption site for TMA, it has been reported that TMA can chemisorb on bridged oxygen on a dehydroxylated  $\text{Al}_2\text{O}_3$  surface,<sup>9</sup> formates,<sup>10</sup> and carbonates.<sup>11</sup> One of the unresolved issues in understanding the growth of  $\text{Al}_2\text{O}_3$  by ALD is the exact cause of the decrease in growth per cycle (GPC) reported at low temperatures.<sup>2,3</sup> Figure 6.1 shows the GPC of  $\text{Al}_2\text{O}_3$  ALD in terms of Al atoms deposited as a function of deposition temperature as measured with Rutherford back-scattering spectrometry (RBS, this metric gives more insight than the GPC in terms of thickness). Comparing the GPC of this thermal process with its plasma enhanced counterpart using  $\text{O}_2$  plasma instead of  $\text{H}_2\text{O}$ , also included in Fig. 6.1, shows that the decrease in GPC at low temperatures only occurs for the thermal process while the GPC of the plasma process keeps increasing when going to lower temperatures.<sup>3,11</sup> Because both processes only differ in the co-reactant, the likely cause of the lower GPC for the  $\text{H}_2\text{O}$ -based process is the lack of reactivity of the co-reactant at low temperatures. However, the precise ALD surface chemistry related to

this lower reactivity is unclear. So far, the aforementioned diagnostic techniques have not been able to resolve this issue and therefore a new approach is needed.

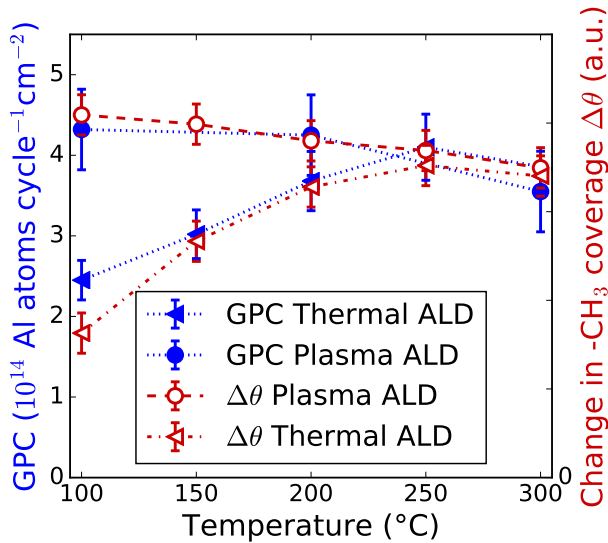


**Figure 6.1:** The growth-per-cycle (GPC) as a function of temperature for thermal ALD of  $\text{Al}_2\text{O}_3$  with  $\text{Al}(\text{CH}_3)_3$  and  $\text{H}_2\text{O}$  as well as for the plasma-enhanced ALD process with  $\text{Al}(\text{CH}_3)_3$  and  $\text{O}_2$  plasma. The GPC is given in terms of Al atoms per  $\text{cm}^2$  per cycle as obtained by RBS measurements (solid markers). At low temperatures, the thermal process shows a significant decrease in the GPC, whereas the plasma process does not. The trends in the GPC can also be predicted by the change in  $-\text{CH}_3$  coverage measured with BB-SFG (open markers). The measured and predicted GPC data show a good agreement.

## 6.2 Experimental details

In this work, the surface chemistry of ALD  $\text{Al}_2\text{O}_3$  is investigated with the technique of broadband sum-frequency generation (BB-SFG). BB-SFG is a state-of-the-art nonlinear optical technique used predominantly in surface science and which is used here to study ALD chemistry. BB-SFG is inherently interface selective with a sub-monolayer sensitivity for  $-\text{CH}_3$  groups and with fairly short acquisition times (120 s for a sensitivity better than 10% of a  $-\text{CH}_3$  monolayer). One of the key features of BB-SFG is that the measured signals are directly correlated to the absolute surface density, revealing more information than so-called differential techniques (such as FTIR) from which only changes

in surface coverage can be extracted. By its very nature, the surface selectivity of BB-SFG leads to the simultaneous detection of species which are changing after an ALD half-cycle and species which are persistent over the ALD half-cycles. In this Letter, it will be shown that these persistent surface species play a key role in ALD of  $\text{Al}_2\text{O}_3$  at low temperatures. Water is not reactive enough at low temperatures to remove all the  $-\text{CH}_3$  groups from the surface; even when saturation conditions are reached a significant amount of  $-\text{CH}_3$  groups persist on the surface. These persistent  $-\text{CH}_3$  groups limit the uptake of TMA in the next half-cycle causing the reduction in GPC. The reduction in the areal density of the Al atoms deposited per cycle is found to be directly proportional to the persistent  $-\text{CH}_3$  coverage.

### 6.3 Results

ALD of  $\text{Al}_2\text{O}_3$  was studied with BB-SFG in a setup designed and built for this purpose. The setup consisted of a vacuum chamber equipped with two turbomolecular pumps (base pressure below  $10^{-7}$  mbar) and fast ALD valves to dose the vapor drawn reactants. A pump down step of  $\sim 140$  s reaching a pressure below  $10^{-6}$  mbar was performed after dosing the reactants. The sample was heated radiatively from the back side and the temperature of the sample was controlled with a thermocouple glued to the substrate within 5 mm of the spot measured with BB-SFG. The sample itself was a free-standing 2 inch Si(100) wafer with a 90 nm  $\text{SiO}_2$  film on top for optical enhancement purposes of the BB-SFG signal, see appendix. The sample was mounted such that BB-SFG could be performed in reflection mode. The laser system used for the experiments produced a  $\sim 90$  fs pulsed IR ( $3.3 \mu\text{m}$ ) beam and visible (800 nm) beam with a repetition rate of 1 kHz. A band-pass filter was used to reduce the bandwidth of the visible pulse to  $\sim 1$  nm. Both the IR and visible beams (pulse energy  $\sim 5 \mu\text{J}$  each) were focused on the sample in a non-collinear geometry. The spectra shown in this work were acquired with an integration time of 120 s to reach a noise level of  $< 1\%$  for typical signals. Except for dark-field subtraction and the removal of features due to cosmic rays, the data is presented as-obtained.

The surface chemistry occurring during both ALD half-cycles was monitored with BB-SFG by probing the spectral region of the C-H stretching modes. The C-H stretching mode of  $-\text{CH}_3$  was successfully detected at  $\sim 2890 \text{ cm}^{-1}$  after precursor exposure, similar to what is typically observed with FTIR for chemisorbed TMA.<sup>6</sup> The mode is in the same range as, for example,  $-\text{CH}_3$  groups of self-assembled monolayers (SAM) when probing them with BB-SFG.<sup>12</sup> BB-SFG was used to detect the  $-\text{CH}_3$  groups during steady-state ALD at  $200^\circ\text{C}$ . Recording a spectrum after a saturated  $\text{H}_2\text{O}$  dose shows no  $-\text{CH}_3$  groups as can be deduced from the featureless spectrum in Fig. 6.2a. This corresponds to a fully  $-\text{OH}$  terminated surface.<sup>6-8</sup> Subsequently, the  $-\text{OH}$  covered surface was exposed to a pulse of TMA by activating the ALD valve for 20 ms. As expected from Eq. (6.1a), the spectrum recorded after the TMA expo-

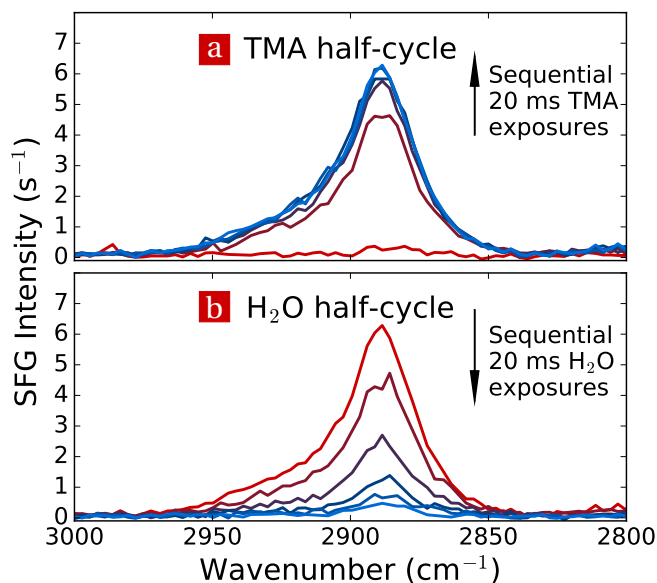


**Figure 6.2:** BB-SFG spectra showing the C-H stretching mode of  $-CH_3$  surface groups on the surface, recorded as a function of (a) subsequent TMA and (b)  $H_2O$  exposures during ALD at a sample temperature of  $200^\circ C$ .

sure shows the spectral feature indicative of the C-H stretching mode of  $-CH_3$  groups on the surface. A subsequent 20 ms pulse yields only a slight increase in peak height indicating a small additional uptake of TMA. Ensuing TMA pulses do not show any change in  $-CH_3$  coverage, implying that saturation has already been reached. When continuing with the  $H_2O$  half-cycle after the TMA half-cycle, the first 20 ms  $H_2O$  exposure results in a significant decrease in the amount of  $-CH_3$  on the surface as can be seen in Fig. 6.2b. Subsequent pulses of water remove  $-CH_3$  groups from the surface until all  $-CH_3$  groups have disappeared. To recapitulate, the surface chemistry at  $200^\circ C$  is described by Eq. (6.1) which is reflected by the uptake and removal of  $-CH_3$  for the TMA and water half-cycle, respectively. This happens in a self-limiting fashion as is characteristic for ALD.

In order to reveal how the sample temperature influences the surface chemistry during steady-state film growth, the experiments have been carried out at temperatures ranging between  $100^\circ C$  and  $300^\circ C$ . A set of saturation plots was obtained for each temperature yielding the dependence of the  $-CH_3$  coverage on the precursor and co-reactant dose as shown in Fig. 6.3. In this figure, the BB-SFG spectra were normalized for each temperature to the  $-CH_3$  coverage obtained after a saturated TMA exposure. The reason is that the acquisition of the spectra for these experiments was relatively time consuming

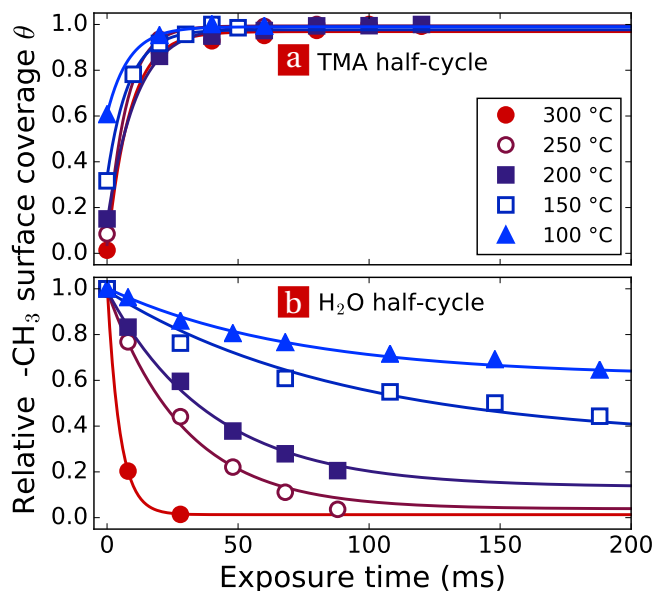


**Figure 6.3:** Relative  $-\text{CH}_3$  surface coverage  $\theta$ , extracted from the BB-SFG spectra as a function of (a) TMA and (b)  $\text{H}_2\text{O}$  exposure for various temperatures. The solid lines represent fits to the data in order to extract information about the reaction kinetics.

and necessary day-to-day adjustments of the laser system influenced the optical alignment, preventing a direct comparison of absolute intensities between measurements at different temperatures. As can be seen from the figure, the saturation of the TMA half-cycle is fast and the dose for which saturation is achieved is independent of temperature. For low temperatures, the initial  $-\text{CH}_3$  coverage is not equal to zero and both  $-\text{OH}$  and  $-\text{CH}_3$  groups coexist on the surface at the beginning of the TMA half-cycle. This  $-\text{CH}_3$  can be traced back to the reactivity of the  $\text{H}_2\text{O}$  co-reactant as can be seen in Fig. 6.3b. This figure shows that water is reactive towards the  $-\text{CH}_3$  groups at high temperatures and quickly removes all the  $-\text{CH}_3$ . However, for lower temperatures the reaction slows down. Furthermore, below 200 °C there are  $-\text{CH}_3$  groups which are no longer reactive towards  $\text{H}_2\text{O}$  and these  $-\text{CH}_3$  groups therefore persist on the surface. In other words, the half-cycle saturates while there are still  $-\text{CH}_3$  groups present on the surface. An additional check with two extra-long  $\text{H}_2\text{O}$  exposures of 400 and 800 ms at 150 °C (not shown) did not yield an additional decrease of the  $-\text{CH}_3$  signal. This implies that during thermal ALD of  $\text{Al}_2\text{O}_3$  at low temperatures, there is a significant amount of  $-\text{CH}_3$  present on the surface at the beginning of the TMA half-cycle.

To obtain more quantitative information on the influence of the temperature on the ALD process, a less time consuming experiment was carried out

such that the  $-\text{CH}_3$  coverages for different temperatures could be compared with each other. Instead of recording saturation curves, spectra were only recorded after a saturated half-cycle. Figure 6.4 shows the BB-SFG spectra of the C-H stretch mode after the TMA and  $\text{H}_2\text{O}$  half-cycles. Again, at high temperatures the  $-\text{CH}_3$  surface groups added to the surface during the TMA half cycle are completely removed in the water half cycle, while at lower temperatures  $-\text{CH}_3$  groups persist. Moreover, the influence of temperature induced dehydroxylation is observed in the  $-\text{CH}_3$  coverage after a saturated TMA.<sup>8</sup> Due to dehydroxylation, fewer reactive sites are available for TMA chemisorption at high temperature than at low temperature, hence the  $-\text{CH}_3$  coverage shows a decrease with temperature.

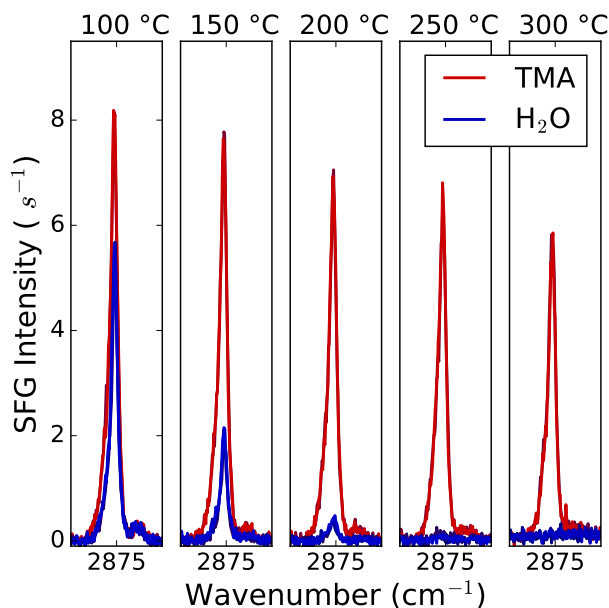


**Figure 6.4:** BB-SFG spectra recorded after the TMA and  $\text{H}_2\text{O}$  half-cycle at various temperatures. For each temperature, data for four half-cycles are shown (i.e. subsequent TMA,  $\text{H}_2\text{O}$ , TMA,  $\text{H}_2\text{O}$  exposures) revealing the excellent reproducibility of the data.

The trend in growth per cycle shown in Fig. 6.1 can be reproduced using the data in Fig. 6.4. The density of Al atoms deposited per cycle is proportional to the TMA uptake in the TMA half-cycle. The TMA uptake is directly related to the change in  $-\text{CH}_3$  coverage if the number of  $-\text{CH}_3$  ligands,  $n$ , which remain attached to the Al atom after chemisorption is temperature independent. QCM studies showed that this is indeed the case over the temperature range investigated here.<sup>9,13</sup> For the thermal ALD process, the TMA uptake will be limited by the persistent  $-\text{CH}_3$  groups in the  $\text{H}_2\text{O}$  half-cycle. Therefore, the TMA uptake should be proportional to the difference in  $-\text{CH}_3$  coverage



between the TMA and H<sub>2</sub>O half-cycles. The increase in –CH<sub>3</sub> coverage caused by the TMA exposure was determined from Fig. 6.4, and the predicted GPC from this change in –CH<sub>3</sub> coverage was plotted in Fig. 6.1. The validity of this procedure can be evaluated by also predicting the GPC of the plasma process. For the plasma process, there should be no persistent groups due to the high reactivity of the O<sub>2</sub> plasma. In this case, the change in –CH<sub>3</sub> coverage is equal to the –CH<sub>3</sub> coverage after TMA exposure. This result is also plotted in Fig. 6.1 on the same scale as the data set for thermal ALD. Both data sets indeed show a good agreement with GPC determined by RBS. The agreement between the measured and predicted GPC for ALD of Al<sub>2</sub>O<sub>3</sub> using TMA and H<sub>2</sub>O corroborates therefore that the persistent –CH<sub>3</sub> groups are the limiting factor in the Al<sub>2</sub>O<sub>3</sub> ALD process at low temperatures.

The underlying cause of the persistent –CH<sub>3</sub> groups can be studied in more detail by considering the reaction kinetics. The kinetics of the reactions in Eq. (6.1) were determined from Fig. 6.3 by fitting the dependence of –CH<sub>3</sub> coverages on the reactant exposure time with an exponential function, see appendix. Briefly, the exponential time constant is equal to the reaction cross section multiplied with the (known) impinging flux of reactant species on the surface. Figure 6.5 shows the temperature dependence of the reaction cross section in both half-cycles and the related initial reaction probability (i.e. the reaction probability when the reactant TMA or H<sub>2</sub>O interacts with a surface that is fully covered with –OH or –CH<sub>3</sub> groups respectively). The figure also shows the fraction of persistent surface groups as a function of temperature obtained from the fits to the saturation plots (Fig. 6.5c). Considering the order of magnitude of the initial reaction probabilities, it can be concluded that the values of 10<sup>-3</sup> for TMA and 10<sup>-4</sup> for H<sub>2</sub>O fall inside the range of values in reported literature.<sup>14,15</sup> However, those literature values vary over several orders of magnitude for different studies. The study of the reaction kinetics in this work, i.e. by directly measuring the surface coverage, is expected to yield very accurate results. The main uncertainty, the systematic error in the calculation of the reactant flux, introduces only a scaling factor and does not affect the trend in the data with temperature. Examining the temperature dependence in Fig. 6.5a more closely reveals that the reaction cross-section - and hence the initial reaction probability - during the TMA half-cycle is independent of temperature. This confirms that chemisorption of TMA on the predominantly –OH terminated surface is a barrierless process which is not thermally activated. For the H<sub>2</sub>O half-cycle the reaction cross-section in Fig. 6.5b does depend on the temperature and the behavior is more complex. The increase in reactivity at high temperatures during the H<sub>2</sub>O half-cycle suggests a thermally activated reaction for this half-cycle.

Although the reactions described by Eq. (6.1) suggest simple reaction kinetics, the data in Fig. 6.3 and Fig. 6.5 show a more intricate chemistry during the H<sub>2</sub>O half-cycle especially at low temperatures: A pseudo first order reaction can describe the chemistry at high temperatures but it cannot describe the kinetics at low temperatures due to the presence of persistent surface groups. A possible explanation for the persistent surface groups can be found in the

recent ab-initio studies using density functional theory (DFT) performed by Shirazi and Elliott.<sup>16</sup> They proposed that so-called cooperative effects play an important role in the surface chemistry of ALD. For  $-\text{CH}_3$  surface groups reacting with  $\text{H}_2\text{O}$ , they found a significantly higher activation barrier for isolated  $-\text{CH}_3$  groups than for clusters of  $-\text{CH}_3$ . An independent DFT study from Weckman et al. also reports a high activation barrier for isolated  $-\text{CH}_3$  and cooperative effects for this ALD process.<sup>17</sup> Such a cooperative effect could explain the persistence of  $-\text{CH}_3$  groups at low temperatures and hence this work can be seen as experimental evidence of the cooperative effect.

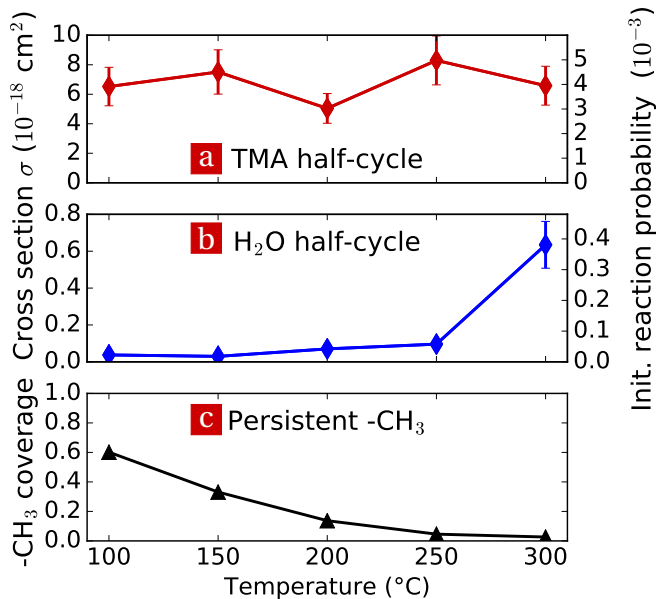


**Figure 6.5:** Temperature dependence of the reaction cross sections  $\sigma$  and the initial reaction probability for the (a) TMA and (b)  $\text{H}_2\text{O}$  half-cycle. Panel (c) shows the fraction of  $-\text{CH}_3$  groups persisting after  $\text{H}_2\text{O}$  exposure as a function of temperature.

## 6.4 Conclusion

In conclusion, we have addressed the question of what is causing the reduced GPC of thermal ALD of  $\text{Al}_2\text{O}_3$  at low temperatures using the nonlinear optical technique of BB-SFG. It was found that water is not reactive enough to remove all  $-\text{CH}_3$  groups at low temperatures which leads to a significant amount of persistent  $-\text{CH}_3$  groups. These persistent  $-\text{CH}_3$  groups limit the TMA uptake and hence they limit the GPC. This was also corroborated by the fact that the predicted GPC, using the measured  $-\text{CH}_3$  coverage as input, showed an

excellent agreement with the GPC measured with RBS if the persistent groups were accounted for. These persistent  $-\text{CH}_3$  groups are not incorporated in the film as is evidenced by the high-quality, virtually carbon-free material which is generally grown with the thermal ALD process at low temperatures.<sup>2,3</sup> Furthermore, from the reaction kinetics it was determined that for the TMA half-cycle the reaction cross-section is temperature independent indicating barrierless reaction. On the other hand, the temperature dependent reaction cross-section in the  $\text{H}_2\text{O}$  half-cycle indicates a thermally activated reaction. Finally, since the combination of  $\text{H}_2\text{O}$  as co-reactant and metal atoms with organic ligands as precursor are quite commonplace in other ALD chemistries, the presence of persistent surface groups reported in this work could play a role in other ALD processes.

## Acknowledgements

The authors would like to thank J.J.A. Zeebregts, J.J.L.M. Meulendijks, C.A.A. van Helvoirt, and C.O. van Bommel for their technical support. This work is supported by the Dutch Technology Foundation STW and the Netherlands Organization for scientific Research (NWO, VICI program on “Nanomanufacturing”. )

## 6.A Appendix

### Sample details and ALD procedure

The sample used in the ALD growth studies consisted of a Si(100) wafer on which a 90 nm  $\text{SiO}_2$  film was grown with plasma-enhanced chemical vapor deposition (PECVD). The thickness of the  $\text{SiO}_2$  film was determined by spectroscopic ellipsometry (SE) using a *J.A. Woollam Co. Inc. M-2000U*. The main purpose of this  $\text{SiO}_2$  film was to enhance the BB-SFG signal strength by maximizing the strength of the driving fields and enhancing the efficiency of the out coupling of the BB-SFG light.

The ALD cycle consisted of a TMA and a  $\text{H}_2\text{O}$  half-cycle each with sufficiently long pumping steps to remove the gas-phase reaction products and excess reactant. Each half-cycle comprised of 1 or more dosing steps. A dosing step consisted of actually dosing a reactant pulse ( $< 40$  ms), followed by a pump down step of  $\sim 140$  s. During this pump down step, 20 s of waiting time is observed to ensure that the majority of the gas-phase species are pumped away while the remaining 120 s are used for the acquisition of the data. The timing of all dosing steps was the same and irrespective of the half-cycle. The sample was heated radiatively with a *BORALECTRIC* element (*GE Advanced Ceramics ACSF0073 HTR1002*). To regulate the temperature of the sample, the power dissipated in the heating element was computer controlled using a temperature reading from the sample with a thermocouple (*Thermocoax type-k shielded*) glued to the surface with a baked out silver paste (*RS 186-3600*). Before each experiment, the sample was heated to the desired deposition temperature and the

$\text{Al}_2\text{O}_3$  surface was prepared by running 5 cycles of ALD to ensure steady state growth. For selected temperatures, the ALD growth was monitored with in-situ SE and these measurements revealed the expected ALD behavior.

### Modeling of BB-SFG data to extract $-\text{CH}_3$ coverage

The intensity  $I$  of a SFG signal for surface groups with density  $N$  having a resonance due to a vibrational transition at scales with,<sup>18</sup>

$$I \propto \|NR + N \frac{Ae^{-i\phi}}{\omega - \omega_{res} - i\gamma}\|^2 I_{vis} I_{IR} \quad (6.2)$$

where  $A$  is proportional to the SFG cross section (in first approximation the Raman cross section multiplied with the IR cross section),  $\omega$  the probed IR frequency,  $\phi$  the phase of the resonant contribution with respect to the non-resonant contribution NR signal, and  $\gamma$  is the broadening parameter of the resonance. This relation shows that the intensity of the BB-SFG signal scales with the square of the density of the surface groups  $N$  when the non-resonant contribution is negligible small. The spectra are fitted with Eq. (6.2) by nonlinear least-squares regression, allowing the determination of surface group density  $N$ . For an example of a data set with fits to Eq. (6.2), see Fig. 6.6.

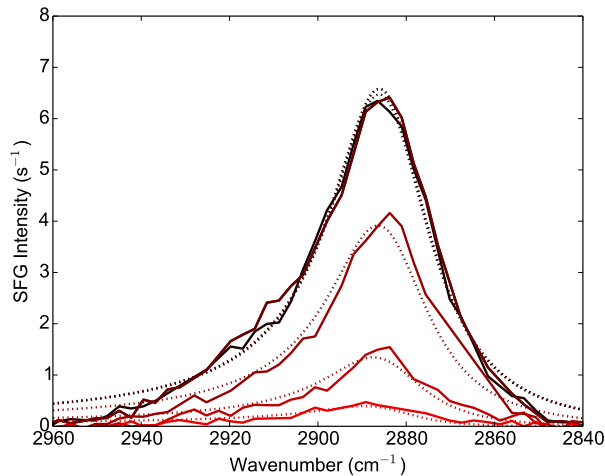


**Figure 6.6:** A series of BB-SFG spectra showing the  $-\text{CH}_3$  resonance for several consecutive  $\text{H}_2\text{O}$  exposures (solid lines) as well as the fits to the spectra (dotted lines).

### Reaction kinetics

The reaction kinetics can be derived from the saturation plots in Fig. 6.3 by analyzing the relation between precursor/co-reactant exposure and relative surface coverage. The relative surface coverage  $\theta_{CH}$  is a dimensionless quantity with  $\theta_{CH} = 1$  corresponding

to the  $-\text{CH}_3$  the coverage after saturation of the TMA half-cycle. The normalized hydroxyl coverage  $\theta_{OH}$  is complementary to the  $-\text{CH}_3$  coverage,  $\theta_{CH} = 1 - \theta_{OH}$  with  $\theta_{OH}$  corresponding to the coverage after the saturated  $\text{H}_2\text{O}$  half-cycle when all  $-\text{CH}_3$  groups have been removed. Here, it is assumed that the active groups undergo pseudo first order reactions. So, for the TMA half-cycle, the  $-\text{CH}_3$  coverage of the active groups depends on the TMA flux  $\Phi_{TMA}$  as follows,

$$\frac{d\theta_{CH}}{dt} = \sigma_{TMA}\Phi_{TMA}\theta_{OH} = \sigma_{TMA}\Phi_{TMA}(1 - \theta_{CH}) \quad (6.3)$$

where  $\sigma_{TMA}$  is the reaction cross section for the reaction occurring in the TMA half-cycle. Solving this differential equation yields,

$$\theta_{CH}(t) = 1 - e^{-\sigma_{TMA}\Phi_{TMA}t} \quad (6.4)$$

For the  $\text{H}_2\text{O}$  half-cycle, the relative  $-\text{CH}_3$  coverage of the reactive surface groups exposed to a flux of  $\text{H}_2\text{O}$  represented by  $\Phi_{H2O}$  depends on reactant exposure as follows,

$$\frac{d\theta_{CH}}{dt} = -\sigma_{H2O}\Phi_{H2O}\theta_{CH} \quad (6.5)$$

where  $\sigma_{H2O}$  is the reaction cross section for the reaction occurring in the  $\text{H}_2\text{O}$  half-cycle. Solving this differential equation yields,

$$\theta_{CH} = e^{-\sigma_{H2O}\Phi_{H2O}t} \quad (6.6)$$

At high temperatures this description is sufficient to model the saturation curves. At low temperatures, the presence of persistent surface groups calls for a modification of Eq. (6.4) and Eq. (6.6). The total  $-\text{CH}_3$  coverage can be divided in two categories: (i) The  $-\text{CH}_3$  groups that are active and take part in the ALD reactions as described by Eq. (1). (ii) The  $-\text{CH}_3$  groups that are persistent, i.e. do not react, and are not described by the ALD chemistry in Eq. (6.1). An offset is  $A$  added to Eq. (6.4) and Eq. (6.6) to account for the persistent surface groups. Moreover, it is important to ensure that the final coverage in the co-reactant half-cycle is the same as starting coverage in the precursor half-cycle and vice versa. This is implemented in the fitting routine by simultaneously analyzing a set of two saturation curves (for each temperature a TMA and a  $\text{H}_2\text{O}$  curve) such that the fitting parameter  $A$  can be shared between the two half-cycles. In the fit, the following relation was used for the TMA half-cycle,

$$\theta_{CH} = A + (1 - A)(1 - e^{-t/\tau_1}) \quad (6.7)$$

with exponential time constant  $\tau_1$ . This was used in conjunction with,

$$\theta_{CH} = A + (1 - A)e^{-t/\tau_2} \quad (6.8)$$

for the  $\text{H}_2\text{O}$  half-cycle with exponential time constant  $\tau_2$ . The impinging reactant fluxes  $\Phi_{TMA}$  and  $\Phi_{H2O}$  were determined using the Hertz-Knudsen equation,<sup>19</sup> which in this case means that only the partial pressures of the reactants had to be determined.

Because the partial pressure of reactant was large compared to the partial pressure of the gas-phase reaction products, it was sufficient to measure the total pressure. The pressure was measured with *Pfeiffer PKR261* during both reactant precursor and co-reactant dosing; a TMA flux of  $1.7 \cdot 10^{19} \text{ c m}^{-2} \text{ s}^{-1}$  and a  $\text{H}_2\text{O}$  flux of  $3.5 \cdot 10^{20} \text{ cm}^{-2} \text{ s}^{-1}$  were found. The initial reaction probabilities was calculated by multiplying the cross section with the initial (full) surface coverage of  $-\text{OH}$  and  $-\text{CH}_3$  groups (both  $\sim 6 \cdot 10^{14} \text{ cm}^{-2}$  as estimated from the  $-\text{OH}$  coverages reported by [Zhuravlev](#) and [Ott et al.](#)<sup>20,21</sup> while inferring equal  $-\text{OH}$  and  $-\text{CH}_3$  coverage from stoichiometric arguments). The reaction cross-section, the initial reaction probability, and the relative coverage of persistent  $-\text{CH}_3$  groups are shown in [Fig. 6.5](#).

## Bibliography

- [1] Knoops, Potts, Bol, and Kessels. Springer Handbook of Crystal Growth. *Japanese Magazine of Mineralogical and Petrological Sciences*, 2010. doi:[10.2465/gkk.39.193a](https://doi.org/10.2465/gkk.39.193a).
- [2] Groner, Fabreguette, Elam, and George. Low-Temperature Al<sub>2</sub>O<sub>3</sub> Atomic Layer Deposition. *Chemistry of Materials*, 2004. doi:[10.1021/cm0304546](https://doi.org/10.1021/cm0304546).
- [3] Potts, Keuning, Langereis, Dingemans, van de Sanden, and Kessels. Low Temperature Plasma-Enhanced Atomic Layer Deposition of Metal Oxide Thin Films. *Journal of The Electrochemical Society*, 2010. doi:[10.1149/1.3428705](https://doi.org/10.1149/1.3428705).
- [4] Heil, Kudlacek, Langereis, Engeln, van de Sanden, and Kessels. In situ reaction mechanism studies of plasma-assisted atomic layer deposition of Al<sub>2</sub>O<sub>3</sub>. *Applied Physics Letters*, 2006. doi:[10.1063/1.2357886](https://doi.org/10.1063/1.2357886).
- [5] Wind and George. Quartz Crystal Microbalance Studies of Al<sub>2</sub>O<sub>3</sub> Atomic Layer Deposition Using Trimethylaluminum and Water at 125C. *The Journal of Physical Chemistry A*, 2010. doi:[10.1021/jp9049268](https://doi.org/10.1021/jp9049268).
- [6] Langereis, Keijmel, van de Sanden, and Kessels. Surface chemistry of plasma-assisted atomic layer deposition of Al<sub>2</sub>O<sub>3</sub> studied by infrared spectroscopy. *Applied Physics Letters*, 2008. doi:[10.1063/1.2940598](https://doi.org/10.1063/1.2940598).
- [7] Frank, Chabal, and Wilk. Nucleation and interface formation mechanisms in atomic layer deposition of gate oxides. *Applied Physics Letters*, 2003. doi:[10.1063/1.1585129](https://doi.org/10.1063/1.1585129).
- [8] Dillon, Ott, Way, and George. Surface chemistry of Al<sub>2</sub>O<sub>3</sub> deposition using Al(CH<sub>3</sub>)<sub>3</sub> and H<sub>2</sub>O in a binary reaction sequence. *Surface Science*, 1995. doi:[10.1016/0039-6028\(95\)90033-0](https://doi.org/10.1016/0039-6028(95)90033-0).
- [9] Puurunen. Correlation between the growth-per-cycle and the surface hydroxyl group concentration in the atomic layer deposition of aluminum oxide from trimethylaluminum and water. *Applied Surface Science*, 2005. doi:[10.1016/j.apsusc.2004.10.003](https://doi.org/10.1016/j.apsusc.2004.10.003).
- [10] Kwon, Dai, Halls, and Chabal. Detection of a Formate Surface Intermediate in the Atomic Layer Deposition of High-k Dielectrics Using Ozone. *Chemistry of Materials*, 2008. doi:[10.1021/cm703667h](https://doi.org/10.1021/cm703667h).
- [11] Rai, Vandalon, and Agarwal. Surface Reaction Mechanisms during Ozone and Oxygen Plasma Assisted Atomic Layer Deposition of Aluminum Oxide. *Langmuir*, 2010. doi:[10.1021/la101485a](https://doi.org/10.1021/la101485a).
- [12] Voges, Al-Abadleh, Musorrafiti, Bertin, Nguyen, and Geiger. Carboxylic Acid- and Ester-Functionalized Siloxane Scaffolds on Glass Studied by Broadband Sum Frequency Generation. *The Journal of Physical Chemistry B*, 2004. doi:[10.1021/jp046564x](https://doi.org/10.1021/jp046564x).
- [13] Rahtu, Alaranta, and Ritala. In Situ Quartz Crystal Microbalance and Quadrupole Mass Spectrometry Studies of Atomic Layer Deposition of Aluminum Oxide from Trimethylaluminum and Water. *Langmuir*, 2001. doi:[10.1021/la010103a](https://doi.org/10.1021/la010103a).
- [14] Knoops, Langereis, van de Sanden, and Kessels. Conformality of Plasma-

- Assisted ALD: Physical Processes and Modeling. *Journal of The Electrochemical Society*, 2010. doi:[10.1149/1.3491381](https://doi.org/10.1149/1.3491381).
- [15] Elam and George. Growth of ZnO/Al<sub>2</sub>O<sub>3</sub> alloy films using atomic layer deposition techniques. *Chemistry of Materials*, 2003. doi:[10.1021/cm020607+](https://doi.org/10.1021/cm020607+).
- [16] Shirazi and Elliott. Cooperation between adsorbates accounts for the activation of atomic layer deposition reactions. *Nanoscale*, 2015. doi:[10.1039/C5NR00900F](https://doi.org/10.1039/C5NR00900F).
- [17] Weckman and Laasonen. First principles study of the atomic layer deposition of alumina by TMA-H<sub>2</sub>O-process. *Phys. Chem. Chem. Phys.*, 2015. doi:[10.1039/C5CP01912E](https://doi.org/10.1039/C5CP01912E).
- [18] Bonn, Ueba, and Wolf. Theory of sum-frequency generation spectroscopy of adsorbed molecules using the density matrix method - broadband vibrational sum-frequency generation and applications. *Journal of Physics: Condensed Matter*, 2005. doi:[10.1088/0953-8984/17/8/002](https://doi.org/10.1088/0953-8984/17/8/002).
- [19] Kolasinski. *Surface Science*. John Wiley & Sons, Ltd, Chichester, UK, 2012. doi:[10.1002/9781119941798](https://doi.org/10.1002/9781119941798).
- [20] Zhuravlev. Concentration of hydroxyl groups on the surface of amorphous silicas. *Langmuir*, 1987. doi:[10.1021/la00075a004](https://doi.org/10.1021/la00075a004).
- [21] Ott, Klaus, Johnson, and George. Al<sub>3</sub>O<sub>3</sub> thin film growth on Si(100) using binary reaction sequence chemistry. *Thin Solid Films*, 1997. doi:[10.1016/S0040-6090\(96\)08934-1](https://doi.org/10.1016/S0040-6090(96)08934-1).





# Revisiting the growth mechanism of atomic layer deposition of $\text{Al}_2\text{O}_3$ : a vibrational sum-frequency generation study

## Abstract

The growth mechanism of the prototypical atomic layer deposition (ALD) process of  $\text{Al}_2\text{O}_3$  using  $\text{Al}(\text{CH}_3)_3$  (TMA) and  $\text{H}_2\text{O}$  has been revisited on the basis of insights obtained with the nonlinear optical analysis technique of broadband sum-frequency generation (BB-SFG). With BB-SFG spectroscopy, both the  $-\text{CH}_3$  and  $-\text{OH}$  surface groups ruling the growth of  $\text{Al}_2\text{O}_3$  by ALD were detected and could be monitored during the ALD process with sub-monolayer sensitivity. Several remaining questions pertaining to the growth mechanism of  $\text{Al}_2\text{O}_3$  were addressed. The reaction kinetics of the  $\text{H}_2\text{O}$  half-cycle were studied for ALD between 100 °C and 300 °C and the reaction cross section  $\sigma$  was determined. The cross section at 300 °C was fairly large ( $\sigma = 3 \cdot 10^{-19} \text{ cm}^2$ ) and it decreased with decreasing temperature. Below 200 °C, the cross section also clearly varied with the surface coverage. For example, at 100 °C the cross section started at  $\sigma = 1 \cdot 10^{-20} \text{ cm}^2$  for a full  $-\text{CH}_3$  coverage and decreased to  $\sigma = 3 \cdot 10^{-21} \text{ cm}^2$  for a 60% coverage. This coverage dependence of the reaction kinetics also explains the presence of the *persistent*  $-\text{CH}_3$  groups at low temperatures which are no longer reactive towards  $\text{H}_2\text{O}$ . By a dedicated study using X-ray photo-emission spectroscopy (XPS) it was demonstrated that the *persistent*  $-\text{CH}_3$  groups were not incorporated into the film. The absolute  $-\text{CH}_3$  coverage was measured for ALD between 100 °C and 450 °C. With this data, steric hindrance was ruled as the cause of the self-limiting behavior in the TMA half-cycle on basis of the decrease observed in the  $-\text{CH}_3$  coverage with temperature. The self limiting behavior was attributed to the depletion of under coordinated O during the TMA half-cycle. Moreover, the chemisorption of TMA on the  $-\text{OH}$  surface groups during the TMA half-cycle was investigated. On average 1.5  $-\text{CH}_3$  ligands remained on the surface per deposited Al atom after the TMA half-cycle at 300 °C and this number decreased to 0.8 at 100 °C. These insights into the underlying growth mechanism augment the understanding of the  $\text{Al}_2\text{O}_3$  ALD and reveals several nuances in this well studied ALD process.

## 7.1 Introduction

Atomic-layer deposition (ALD) of ultra-thin metal-oxide films is an enabling technology in the fabrication of semiconductor devices. For these applications, the capability of ALD to conformally coat complex 3D structures while yielding sub-nanometer control over the film-thickness is crucial.<sup>1</sup> These aspects of the ALD process are inherent to its growth mechanism. In essence, ALD consists of a sequence of self-limiting surface reactions which together deposit an “atomic layer” of material.<sup>1</sup> The sequence of steps is called an ALD cycle which can be repeated to grow a film with sub-nanometer thickness control. Moreover, it is these self-limiting reactions that give ALD some of its unique capabilities such as its inherent conformality and uniformity.<sup>1</sup> Currently, there is a push towards even more demanding applications for ALD films. A good example of this trend is the deposition of ALD films on temperature sensitive substrates requiring the development of low temperature or even room temperature ALD processes.<sup>2-4</sup> In order to meet these ever more demanding requirements in a systematic way, a better understanding of the surface reactions governing the ALD process is essential.

This work focuses on the surface chemistry of the prototypical ALD process growing  $\text{Al}_2\text{O}_3$  using trimethylaluminum (TMA) as precursor and water as co-reactant. This process serves as a model system for ALD of metal-oxides with metal-organic precursors. Moreover, it is one of the more ubiquitous ALD processes.<sup>2,5-11</sup> Higashi and Fleming introduced the ALD process of  $\text{Al}_2\text{O}_3$  and they reported on its key aspects as well as the noteworthy properties of the resulting  $\text{Al}_2\text{O}_3$  films.<sup>5</sup> Ensuing, many details of this ALD process have been studied intensively and as a result the growth mechanism is fairly well understood as will be addressed in the next section.<sup>6-8,12,13</sup> Nevertheless, new insights into some of the fundamental mechanisms of this ALD process can be gained. For example, in our previous work we reported on the fundamental mechanism causing the commonly observed decrease in growth-per-cycle (GPC) at low temperatures. It was demonstrated that this decrease in GPC was caused by *persistent*  $-\text{CH}_3$  groups present on the surface at low temperatures.<sup>14</sup> Basically, these *persistent*  $-\text{CH}_3$  groups limit the TMA uptake and therefore result in a lower GPC. Ensuing, it was demonstrated by others that these *persistent* groups play a key role in other ALD processes as well.<sup>15</sup>

For the  $\text{Al}_2\text{O}_3$  ALD process, several open questions pertaining to the growth mechanism were identified and investigated here: Firstly, the origin of the self-limiting behavior in the precursor half-cycle is still debated in the literature.<sup>8,9,16</sup> The conclusions drawn from experiments have been contradictory,<sup>8,9</sup> and recently this topic has been studied using density functional theory (DFT) indicating the need for further experimental work.<sup>16</sup> Secondly, how TMA chemisorbs on the  $-\text{OH}$  terminated surface is of interest. So far, indirect measurements by quadrupole mass spectrometry (QMS) and quartz-crystal microbalance (QCM) have shed some light on this topic, however, a more direct measurement is desirable.<sup>12</sup> Thirdly, in our previous work the tempera-

ture dependence of the reaction kinetics were found to be relatively complex and it was concluded that they should be studied in more detail.<sup>14</sup> Finally, the apparent paradox between virtually carbon free Al<sub>2</sub>O<sub>3</sub> films, as typically reported for ALD,<sup>17</sup> and the presence of the *persistent* –CH<sub>3</sub> groups at low temperatures needs to be addressed.

The nonlinear optical technique of broadband sum-frequency generation (BB-SFG) was used to study the surface chemistry during ALD of Al<sub>2</sub>O<sub>3</sub>. BB-SFG spectroscopy is a state of the art technique, predominantly used in the field of surface science, which is now utilized to study the surface chemistry of ALD in this work. BB-SFG spectroscopy is ideally suited for this task because of its sub-monolayer sensitivity, inherent surface selectivity, and fairly short acquisition times. In short, the BB-SFG signal is generated by simultaneously exposing the surface groups to a picosecond visible pulse and a femtosecond broadband mid-IR pulse.<sup>18,19</sup> These two pulses mix, generating a new signal in the visible part of the spectrum. The mixing is resonantly enhanced for mid-IR photons exciting a vibrational transition of the surface groups.<sup>18</sup> As a result, a part of the vibrational fingerprint of the surface groups is present in the visible BB-SFG signal. The surface groups can be identified by the unique spectral position of the resonances and the density of the surface groups is proportional to the strength of those resonant signals. For example, the C-H stretch mode of –CH<sub>3</sub> groups at ~2900 cm<sup>-1</sup> can be used to identify the presence of these groups and to study their density on the surface. A key merit of BB-SFG spectroscopy is that the detected signals are proportional to the square of the absolute surface coverage. Moreover, because of its inherent surface selectivity, differential spectra are not required. This allows a more direct interpretation of the data and requires less prior knowledge of the system under investigation than a differential technique such as Fourier transform IR (FTIR) absorption spectroscopy.

Because BB-SFG spectroscopy is not yet established in the field of ALD, it is valuable to explore its capabilities and verify whether the –CH<sub>3</sub> and –OH surface groups resulting from TMA and H<sub>2</sub>O exposure during ALD could be detected. For this purpose, an isotope study using H<sub>2</sub>O, D<sub>2</sub>O, Al(CH<sub>3</sub>)<sub>3</sub>, and Al(CD<sub>3</sub>)<sub>3</sub> was performed subsequently. The aforementioned open questions were investigated with BB-SFG spectroscopy. The reaction kinetics during the H<sub>2</sub>O half-cycle was studied by BB-SFG spectroscopy by measuring the –CH<sub>3</sub> density as a function of co-reactant exposure, i.e. a type of saturation curve was established. To address the influence of temperature on the reaction kinetics, these experiments were performed at different temperatures ranging from 100°C up to 300°C. To gain more quantitative information about the surface chemistry, the absolute areal density of –CH<sub>3</sub> surface groups was determined after both half-cycles for ALD between 100 °C and 450 °C. This data yielded insights into the origin of the self-limiting nature of the ALD reactions and the chemisorption of TMA itself. A separate X-ray photo-emission spectroscopy (XPS) experiment was performed to study the possible incorporation of carbon into the film from –CH<sub>3</sub> groups remaining at the surface after the H<sub>2</sub>O step.

The manuscript is organized as follows: A brief recapitulation of the growth

mechanism of Al<sub>2</sub>O<sub>3</sub> ALD is given in Section 2. This provides the necessary background for the interpretation of the experimental results and puts the results in their proper perspective. In Section 3, the experimental details are given. In section 4, the results are presented and discussed. The section is divided into 4 parts: basic surface chemistry, reaction kinetics, quantification of the –CH<sub>3</sub> coverage, and carbon incorporation. In Section 5, the main conclusions are given.

## 7.2 Growth mechanism of ALD of Al<sub>2</sub>O<sub>3</sub>

The growth of Al<sub>2</sub>O<sub>3</sub> during steady-state ALD is ruled by surface chemistry involving predominantly –CH<sub>3</sub> and –OH groups. A schematic representation of the growth mechanism is shown in Fig. 7.1. At the beginning of the TMA half-cycle, the surface is –OH terminated. This surface is exposed to vapor phase TMA which chemisorbs on the -OH groups. Each chemisorbed TMA molecule reacts with one or two –OH groups. This ligand exchange reaction releases gas-phase CH<sub>4</sub> as a volatile reaction product. After a sufficiently large precursor exposure, no more TMA can chemisorb on the surface. This is the self-limiting aspect of the chemistry and the half-cycle is said to be “in saturation” resulting in a –CH<sub>3</sub> terminated surface. At the end of the TMA half-cycle, the gas-phase reaction products (CH<sub>4</sub>) and excess precursor are removed from the reactor by purging and/or pumping. In the ensuing H<sub>2</sub>O half-cycle, vapor phase H<sub>2</sub>O reacts with the –CH<sub>3</sub> groups on the surface. This ligand exchange reaction replaces the –CH<sub>3</sub> groups with –OH groups and again releases gas-phase CH<sub>4</sub>. This reaction is also self-limiting and at the end of this half-cycle the remaining co-reactant molecules and gas-phase reaction products are again removed by purging and/or pumping. The surface is now -OH terminated while a layer of Al<sub>2</sub>O<sub>3</sub> is deposited, and the cycle can be repeated. In their simplest form, these reaction can be summarized by,



In these equations, the “–” sign indicates a surface species and  $x$  represents the number of –CH<sub>3</sub> ligands bonded to Al remaining after chemisorption. There exist several secondary reaction pathways with e.g. different reactive sites that might contribute to the ALD growth. For example, TMA chemisorption has been shown to occur on Al–O–Al bridges,<sup>9</sup> carbonates,<sup>20,21</sup> and formates.<sup>22</sup> However, the growth via these secondary reaction paths is generally small compared to the growth via the reaction path in Eq. (7.1).

The surface chemistry of Al<sub>2</sub>O<sub>3</sub> ALD has been studied extensively with Fourier transform infrared (FTIR) absorption spectroscopy. These measurements confirmed that the surface chemistry was dominated by the –CH<sub>3</sub> and –OH groups when employing TMA and H<sub>2</sub>O. It is insightful to provide some background information on FTIR spectroscopy before discussing a typical result. To study the surface chemistry of ALD with FTIR absorption spectroscopy,

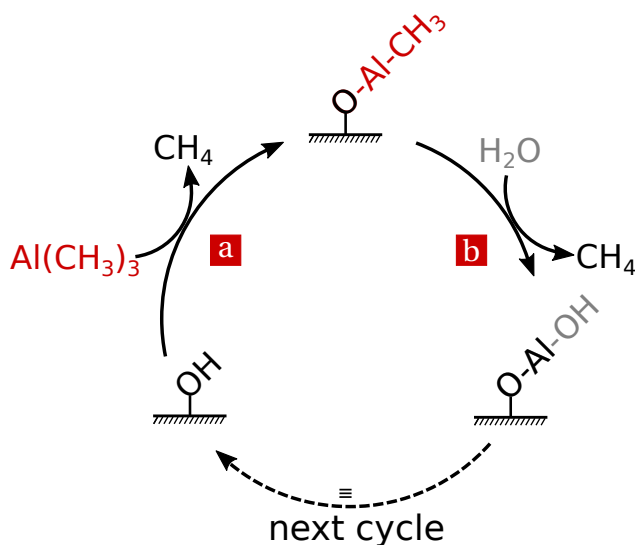


**Figure 7.1:** The cyclical ALD process for  $\text{Al}_2\text{O}_3$  can be divided into a TMA and a  $\text{H}_2\text{O}$  half-cycle. (a) In the TMA half-cycle, vapor phase TMA ( $\text{Al}(\text{CH}_3)_3$ ) reacts with the  $\text{-OH}$  groups on the surface depositing a submonolayer of Al atoms terminated by  $\text{-CH}_3$  groups. (b) In the ensuing  $\text{H}_2\text{O}$  half-cycle, water vapor reacts with the  $\text{-CH}_3$  groups converting the surface layer into  $\text{Al}_2\text{O}_3$  and recuperating a  $\text{-OH}$  terminated surface. Gas-phase  $\text{CH}_4$  is released in both the TMA and the  $\text{H}_2\text{O}$  half-cycle as a reaction product that is removed from the reactor by pumping and/or purging before the next ALD half-cycle.

the absorption of infrared radiation by a monolayer of  $\text{-CH}_3$  or  $\text{-OH}$  groups needs to be detected. This contribution is small compared to other optical elements absorbing infrared radiation such as the bulk of the substrate on which ALD is performed. To eliminate the contributions by other elements not related to the surface groups and to facilitate the interpretation of the data it is convenient to work with so called “difference spectra”. Such a difference spectrum is calculated from a spectrum recorded directly before and after a half-cycle. The main difference between the two spectra is the absorption due to the *change* in surface groups, hence the difference of the two spectra will emphasize these changes. A positive (negative) peak in a difference spectrum indicates the increase (decrease) in the presence of a specific surface group. Note that this approach will only reveal species that are *changing*.

Ott et al. used this approach to study which surface groups are involved in the growth of  $\text{Al}_2\text{O}_3$  by ALD.<sup>8</sup> Figure 7.2 shows the FTIR difference spectra they reported in their work for both the TMA and  $\text{H}_2\text{O}$  half-cycle.<sup>8</sup> For the TMA half-cycle, an increased absorption in the C–H stretch region around  $2900\text{ cm}^{-1}$  can be seen. This implies an increase in the number of  $\text{-CH}_3$

groups on the surface. The negative peak in the O–H stretch region around  $3700\text{ cm}^{-1}$  indicates that the number of –OH groups has decreased after TMA exposure. From these observations it can be inferred that TMA has chemisorbed on the –OH site as described in Eq. (7.1a).<sup>8,23</sup> For the  $\text{H}_2\text{O}$  half-cycle the opposite trends are observed involving the same surface groups: After the  $\text{H}_2\text{O}$  exposure the number of – $\text{CH}_3$  groups decreased and the number of –OH groups increased. This indicates that vapor phase  $\text{H}_2\text{O}$  reacted with – $\text{CH}_3$  groups, removing the – $\text{CH}_3$  groups from the surface and forming –OH groups.<sup>8,23</sup> This observation is in line with Eq. (7.1b).

Evidence for the gas-phase reaction products can also be obtained with FTIR using an alternative measurement scheme. In this scheme, the gas-phase reaction products need to be present during the acquisition of one FTIR spectrum and absent during another acquisition. The difference spectrum now contains information about the gas-phase species which were present. It is possible to follow the progress of the reactions during a half-cycle, by exposing the surface to multiple consecutive short exposures instead of a single long exposure. Figure 7.3 shows a set of FTIR spectra identifying the gas-phase species formed during ALD. For the TMA half-cycle shown in Fig. 7.3(a), the first TMA exposure produces mainly  $\text{CH}_4$  identified by its unique IR fingerprint.<sup>20</sup> A trace of unreacted TMA can also be seen in the figure.<sup>20,24</sup> Both the second and the third TMA exposure show less  $\text{CH}_4$  production and the signature of (unreacted) TMA becomes more evident. During the  $\text{H}_2\text{O}$  half-cycle shown in Fig. 7.3(b), both gas-phase  $\text{CH}_4$  and vapor phase  $\text{H}_2\text{O}$  were seen after the first  $\text{H}_2\text{O}$  exposure. Again less  $\text{CH}_4$  was produced in the subsequent exposures. These results show that the observed gas-phase reaction products are in line with Eq. (7.1). Moreover, the trends in the amount of gas-phase reaction products and the consumption of the precursor and co-reactant are in agreement with the self-limiting nature of the ALD reactions.

Complementary to FTIR spectroscopy, QMS is often used to identify and monitor the gas-phase reaction products. In QMS, gas-phase species are first ionized and subsequently filtered on the basis of their mass-to-charge ratio ( $m/z$ ). Figure 7.4 shows the QMS signals recorded during ALD of  $m/z$  ratios of 15, 18, and 57 corresponding predominantly to  $\text{CH}_3^+$ ,  $\text{H}_2\text{O}^+$ , and  $\text{Al}(\text{CH}_3)_2^+$  respectively. In this case, the QMS signal strength scales with the partial pressure of the specific gas-phase molecule. In the precursor half-cycle, TMA was dosed in 5 consecutive exposures of 40 ms each. The top panel in Fig. 7.4 shows the  $m/z = 57$  signal corresponding to  $\text{Al}(\text{CH}_3)_2^+$  which is indicative of TMA. The first two exposures of TMA do not give rise to a peak in the  $m/z = 57$  signal, indicating that all the TMA is consumed before it can reach the mass spectrometer. This is similar to the result in Fig. 7.3 where the majority of the TMA was also consumed in the first exposure. Each time the sample was exposed to TMA, an increase in the  $m/z = 15$  signal was observed corresponding to  $\text{CH}_3^+$ . This ion can be produced by ionization of either gas phase  $\text{CH}_4$  or gas phase TMA depending on their ionization cross section. For each TMA half-cycle, 5 consecutive TMA exposures were performed. Assuming that no TMA was consumed in the last exposure and thereby ascribing the

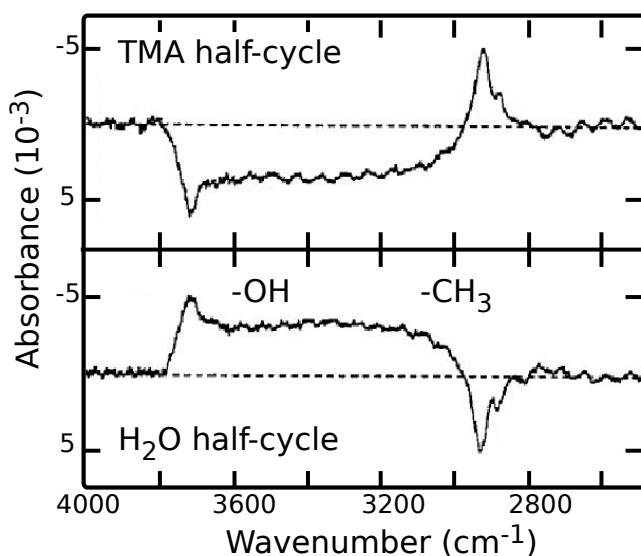


**Figure 7.2:** FTIR absorption spectra showing the change in absorption (i.e. a difference spectrum) related to the change in surface species caused by TMA or H<sub>2</sub>O exposure. During the TMA half-cycle, TMA chemisorbs on the -OH groups leading to a decrease in the number of -OH groups (negative peak with respect to the baseline) and an increase in the number of -CH<sub>3</sub> groups (positive peak with respect to the baseline) on the surface. During the H<sub>2</sub>O half-cycle, vapor phase H<sub>2</sub>O reacts with the -CH<sub>3</sub> groups which are removed forming new -OH groups appear. Adapted from Ott et al.<sup>8</sup>

entire signal to TMA yields an upper limit for the contribution of TMA to the CH<sub>3</sub><sup>+</sup> signal. From Fig. 7.4 it can be seen that the TMA contribution to the CH<sub>3</sub><sup>+</sup> signal is indeed small. In the co-reactant half-cycle, H<sub>2</sub>O was dosed in 5 consecutive exposures of 100 ms each. The lower panel of Fig. 7.4 shows the  $m/z = 18$  signal indicative of H<sub>2</sub>O. Again, gas-phase CH<sub>4</sub> was observed as a reaction product. In this half-cycle there is no ambiguity in the assignment of the  $m/z = 15$  signal as no TMA was present. The  $m/z = 18$  signal shows H<sub>2</sub>O molecules reaching the QMS apparatus even in the first exposure. This is different from the TMA half-cycle, where no TMA reached the detector in the first two exposures. This difference is caused in part by the lower reactivity of H<sub>2</sub>O towards -CH<sub>3</sub> groups than TMA to -OH groups. To recapitulate, the gas-phase reaction product measured with both FTIR and QMS are in line with the reactions given in Eq. (7.1).

A key step in the characterization of an ALD process is to verify that the surface chemistry is indeed self-limiting. This is often done by measuring the influence of the precursor and co-reactant exposure on the GPC. If the ALD process is well behaved, the GPC approaches an horizontal asymptotic value for sufficiently long exposures and purge steps, i.e. the GPC shows saturation. Figure 7.5 shows the variation in the GPC as a function of precursor exposure,



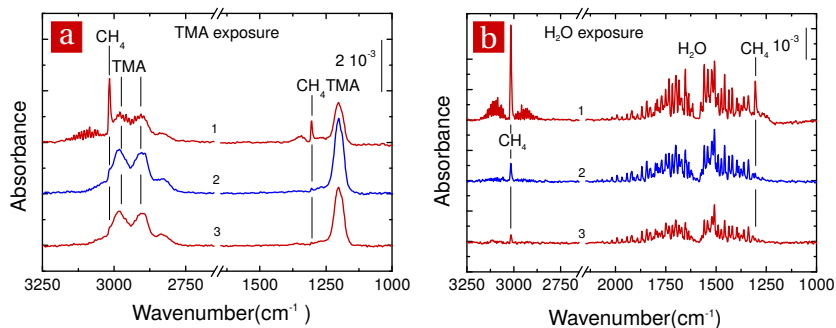


**Figure 7.3:** Gas-phase reaction products during ALD of Al<sub>2</sub>O<sub>3</sub> measured with infrared absorption spectroscopy for three consecutive precursor and co-reactant exposures labeled chronologically in (a) a TMA half-cycle and (b) a H<sub>2</sub>O half-cycle. The peak assignment are given in the figure. For both half-cycles the produced amount of CH<sub>4</sub> decrease with each exposure as a result of the self-limiting nature of the reactions. These experiments were carried out in a home built reactor ALD-I at 145 °C.<sup>24</sup>

co-reactant exposure, and purge time measured with spectroscopic ellipsometry (SE).<sup>25</sup> To study the influence of a single parameter in these experiments, all other steps were made sufficiently long to ensure their saturation. The GPC showed saturation for a precursor exposure of >~ 20 ms and a co-reactant exposure of >~ 10 ms. For the purge steps, saturation was observed for purges of >~ 1 s. The GPC for the optimized ALD cycle was ~1.0 Å, a typical value for Al<sub>2</sub>O<sub>3</sub> ALD at a deposition temperature of 250 °C.

The deposition temperature has a significant influence on the ALD process.<sup>2,8,26–28</sup> The lowest practical temperature for Al<sub>2</sub>O<sub>3</sub> ALD is ~ 150 °C. At lower temperatures, the ALD cycle becomes quite long because H<sub>2</sub>O is difficult to remove at low temperatures resulting in extremely long purge steps. Also the mass density of the deposited Al<sub>2</sub>O<sub>3</sub> decreases significantly for deposition temperatures below 150 °C.<sup>2</sup> For example, Groner et al. showed that a deposition at 33 °C requires a cycle time of ~200 s (compared to e.g. 4 s) and the mass density of the film is ~20 % less than for films grown at high temperatures.<sup>2</sup> Temperature also has an impact on the GPC of the Al<sub>2</sub>O<sub>3</sub> ALD process. The GPC in Fig. 7.5 was expressed in thickness, labeled here as GPC(nm), which is a suitable parameter if e.g. a certain thickness is required for an application. Moreover, it can be measured in-situ with commonly available techniques such as SE. Alternatively, the GPC can be expressed as the number of atoms deposited per surface area, labeled as GPC(at). This quantity is more closely related to e.g. the number of precursor molecules chemisorbing on the surface per cycle. For mechanistic studies, the GPC(at) is therefore more suited. Basically, the GPC(at) can be calculated from the GPC(nm) if the atomic density (atoms/m<sup>3</sup>) and the stoichiometry of the film are known. A direct method of determining the GPC(at) is Rutherford backscattering spectrometry (RBS).<sup>3</sup>

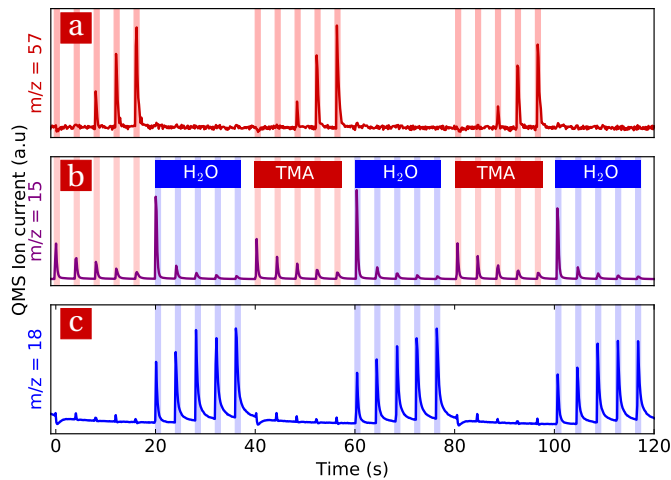


**Figure 7.4:** Gas-phase species measured with QMS as a function of time for ALD using consecutive exposures of TMA and H<sub>2</sub>O. **(a)** For the TMA half-cycle, the first 2 TMA exposures (out of 5) were fully consumed by the reaction with surface groups, as can be seen from the  $m/z = 57$  signal due to  $\text{Al}(\text{CH}_3)_2^+$  and indicative of TMA. **(b)** For both the TMA and H<sub>2</sub>O exposures, a peak was observed in the  $m/z = 15$  signal that is mainly due to  $\text{CH}_3^+$  and indicative of gas-phase reaction product  $\text{CH}_4$ . **(c)** For the H<sub>2</sub>O half-cycle, all H<sub>2</sub>O exposures resulted in a clear peak in the  $m/z = 18$  signal that is mainly due to  $\text{H}_2\text{O}^+$  and indicative of H<sub>2</sub>O. These experiments were carried out in a *Oxford Instruments FlexAL* reactor with a sample and wall temperature of 100 °C.

In RBS, the areal density of a specific atom is measured. Dividing the areal density by the number of ALD cycles used to prepare the film results in the  $\text{GPC}(\text{at})$ . On the other hand, as stated before, the  $\text{GPC}(\text{at})$  is given by the atomic density multiplied by the  $\text{GPC}(\text{nm})$ . Both the atomic density and the  $\text{GPC}(\text{nm})$  can be measured with X-ray reflectivity (XRR),<sup>2</sup> or more indirectly with SE using the Lorentz-Lorenz relation.<sup>8,17,26,29</sup> Figure 7.6 shows the  $\text{GPC}(\text{at})$  based on the values reported in the literature for both thermal  $\text{Al}_2\text{O}_3$  ALD and the related plasma-enhanced ALD (PE-ALD) process of  $\text{Al}_2\text{O}_3$  using the same precursor. The temperature trend in the  $\text{GPC}(\text{at})$  for the thermal process shows an increase with temperature up to  $\sim 200$  °C. For temperatures above  $\sim 250$  °C, the  $\text{GPC}(\text{at})$  decreases steadily with temperature. For the PE-ALD process, the  $\text{GPC}(\text{at})$  decreases monotonically with temperature. The cause of these trends will be discussed later. General consensus is lacking on the exact upper temperature limit at which it is no longer possible to achieve self-limiting growth and hence ALD. However, it has been reported that the precursor starts to decompose above  $\sim 450$  °C.<sup>6,30</sup>

The deposition temperature also influences the density and stoichiometry of the ALD  $\text{Al}_2\text{O}_3$  films to a certain extent. The  $\text{Al}_2\text{O}_3$  films deposited by ALD,

i.e. typically below 450 °C, are all amorphous. The structure of this amorphous material changes with temperature, going from a local structure similar to that of  $\alpha$ -Al<sub>2</sub>O<sub>3</sub> at high temperatures to a structure closer to amorphous aluminum oxide hydroxide (AlO(OH)) for deposition at low temperatures.<sup>31</sup> This trend is also reflected in the stoichiometry of the films which are slightly O rich at high temperatures.<sup>2,3,17,28,32</sup> At lower temperatures, the films become even more O rich,<sup>2,3,17,28,31,32</sup> in line with the AlO(OH) structure. The films prepared with thermal ALD are generally carbon free, even when deposited at low temperatures.<sup>17</sup> Furthermore, an increasing amount of H and –OH in the bulk of the films is reported with decreasing temperature.<sup>2,17</sup> The mass density of the Al<sub>2</sub>O<sub>3</sub> prepared with ALD is reported to decrease from 3.0 g/cm<sup>3</sup> at 300 °C to approximately 2.8 g/cm<sup>3</sup> at 100 °C.<sup>2,3,17</sup> For comparison, the density of (crystalline)  $\alpha$ -Al<sub>2</sub>O<sub>3</sub> and  $\gamma$ -Al<sub>2</sub>O<sub>3</sub> are 3.99 g/cm<sup>3</sup> and 3.97 g/cm<sup>3</sup>, respectively.<sup>33</sup>

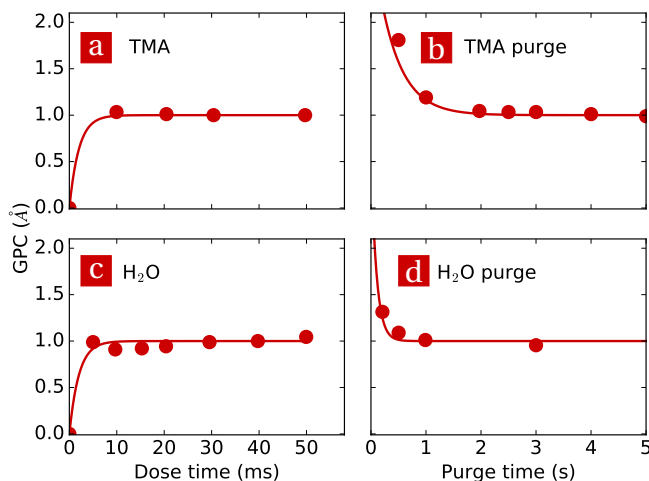


**Figure 7.5:** The so-called saturation curves for thermal ALD of Al<sub>2</sub>O<sub>3</sub> at 250 °C. The growth-per-cycle (GPC(nm)) as a function of (a) the TMA and (c) the H<sub>2</sub>O dose and (b,d) their corresponding purge steps. The lines serve as a guide to the eye. The experiments were carried out in a *Oxford Instruments OpAL* reactor and the data was taken from [Dingemans and Kessels](#).<sup>25</sup>

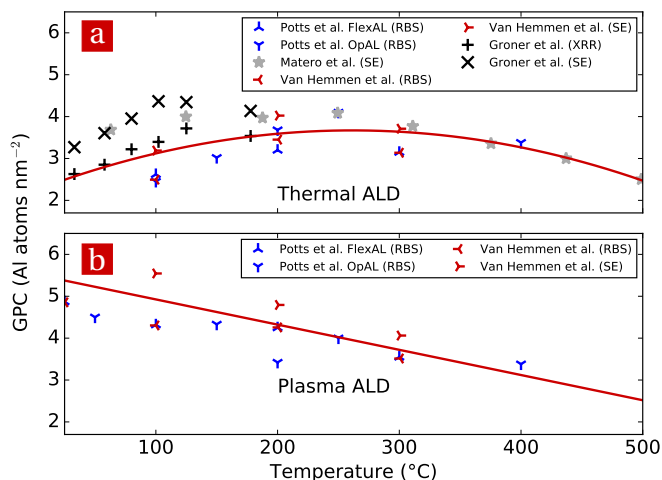


**Figure 7.6:** The growth per cycle in terms of Al atoms per surface area (GPC(at)) for (a) thermal and (b) PE-ALD as reported in the literature. For the data obtained with RBS and XRR, the data was used as reported. For the GPC(at) determined with SE, the GPC(at) was calculated from the refractive index and the GPC(nm) reported in the respective publications. The data was taken from [Matero et al.](#), [van Hemmen et al.](#), [Groner et al.](#), and [Potts et al.](#)<sup>2,3,17,26</sup> The solid line serves as a guide to the eye.

## 7.3 Experimental details

### ALD setup and sample preparation

The growth mechanism of ALD was studied using BB-SFG spectroscopy in a purpose-built ALD reactor. The reactor chamber consisted of two parts, both were equipped with a turbo molecular pump (*Pfeiffer TMU 261P*) with an individual backing pump. Both parts reached a base pressure of  $< 1 \cdot 10^{-6}$  mbar. The backing pumps were also used as roughing pumps. The ALD precursors ( $\text{Al}(\text{CH}_3)_3$  and  $\text{Al}(\text{CD}_3)_3$ ) and co-reactants ( $\text{H}_2\text{O}$  and  $\text{D}_2\text{O}$ ) were dosed into the front part of the reactor with fast ALD valves (*Swagelok 34C-A-GDFG-1KT*) each attached to the reactor with an individual line. The sample was situated at the interface between the two reactor parts and it was heated radiatively from the backside with a Borelectric heating element (*GE Advanced Ceramics ACSF0073 HTR1002*). Sample temperature was computer controlled using a temperature readout from a thermocouple (*Thermocoax 2ABAc05/1m/TI/FIM.K*) glued with thermal paste (*RS 186-3600*) to the back side of the sample as input.

The sample used in the BB-SFG experiments consisted of a Si(100) wafer on which a 90 nm thick  $\text{SiO}_2$  film was deposited with plasma-enhanced chemical vapor deposition (PE-CVD) for optical enhancement of the BB-SFG signal.

## BB-SFG spectroscopy and quantification

In BB-SFG spectroscopy, the surface groups are simultaneously irradiated with a spectrally narrow visible pulse and a broadband mid-IR pulse. The visible laser pulses were generated using a regenerative amplifier (*Spectra-Physics Spitfire*) producing pulses with a duration of  $\sim 90$  fs at a repetition rate of 1 kHz. This amplifier was seeded with a mode-locked oscillator (*Spectra-Physics Tsunami*) and pumped with intracavity doubled, diode-pumped Nd:YLF laser (*Spectra-Physics Evolution 30*). The average output power of *Spitfire* was 1.5 W. From this output beam, 30% of this light was used as the visible pulse in the BB-SFG experiment. To get the desired spectral and temporal shape, the visible light was passed through an etalon (*CVI F1.1-800*). The mid-IR laser pulse was generated from the remaining  $\sim 70\%$  of the visible light using an optical parametric amplifier (*Spectra-Physics TOPAS-C*) with an additional difference-frequency mixer. The mid-IR beam and the visible beams were directed towards the ALD reactor, synchronized with a delay line, and focused non-collinearly onto the sample. A separate set of optics was used for each of the two beams. For the mid-IR beam a combination of a positive and a negative  $\text{CaF}_2$  lens were used. This combination of lenses improved the numerical aperture and allowed a tighter focus (effective focal length 750 mm). The visible beam, which was much larger in diameter than the mid-IR beam, was focused on the sample with a single lens (focal length 750 mm). A  $\text{CaF}_2$  window was used to admit the two pulses into the ALD reactor. After passing through all optical components, the average power was  $\sim 5$  mW for each of the two laser beams. The two pulses impinged on the sample in a reflection geometry at an angle of incidence  $\sim 30$  degrees from the surface normal.

The BB-SFG signal exited the reactor through a fused silica window and was filtered spatially (using 2 irises of  $\sim 4$  mm) and spectrally (using 4 *Thorlabs FES0750* filters each with an optical density  $> 5$ ). The S-polarized component of the BB-SFG beam was selected with a polarizer and focused on the slit of the spectrometer. The BB-SFG signal was detected with a *Acton Research SP2500* spectrograph and *Princeton Instruments 100B* CCD camera. The polarization combination of the BB-SFG signal recorded in this work are *Ssp* (S-polarized SFG, s-polarized visible, and p-polarized mid-IR light).

The relative surface coverage  $\rho$  of the measured groups was determined from the BB-SFG spectra. The resonant contribution caused by a vibrational mode of a surface group, e.g. the C-H stretch mode of a  $-\text{CH}_3$  group, was modeled using an Lorentzian line shape. Furthermore, a small non-resonant contribution  $\bar{\chi}_{NR}$  had to be included. The spectral shape of the BB-SFG signal  $I(\omega)$  for a single resonance was described by,

$$I(\omega) \propto |\bar{\chi}_{NR} + \rho \frac{Ae^{-i\phi}}{\omega - \omega_{res} + i\Gamma}|^2 I_{vis} I_{ir}, \quad (7.2)$$

with  $I_{vis}$  and  $I_{ir}$  the intensity of the visible and mid-IR beams exciting the surface groups. The resonant contribution was described by:  $A$  the cross section

of the SFG process for the specific resonance,  $\phi$  the phase of the resonance,  $\omega_{res}$  the resonance frequency, and  $\Gamma$  the broadening of the resonance. The spectra were modeled by fitting this equation to the data using a least-squares algorithm.

## 7.4 Results and Discussion

### Basic surface chemistry

The C-H stretch region of the BB-SFG response was probed after the TMA and H<sub>2</sub>O half-cycle during steady-state ALD growth of Al<sub>2</sub>O<sub>3</sub> at 250 °C. To ensure steady-state growth, 5 ALD cycles were performed before recording a BB-SFG spectrum. After this preparation, an ALD cycle was performed and a BB-SFG spectrum was recorded after each half-cycle with the mid-IR laser tuned to 2850 cm<sup>-1</sup>, see Fig. 7.7. After the TMA half-cycle, the C-H stretch mode of the -CH<sub>3</sub> surface groups was indeed observed at 2890 cm<sup>-1</sup>. After the H<sub>2</sub>O cycle, a flat spectral response was recorded in this region, indicating that all the -CH<sub>3</sub> groups were removed by the H<sub>2</sub>O exposure. The O-H stretch mode of the -OH surface groups (3690 cm<sup>-1</sup>) falls outside of the spectral region probed with the mid-IR laser tuned to 2850 cm<sup>-1</sup>. In principle it was possible to tune the laser to a different wavelength and probe the O-H stretch region. However, for such a measurement the beam path (~ 10 m) would need to be purged with e.g. dry nitrogen to remove ambient H<sub>2</sub>O. More importantly, it is preferable to probe both -CH<sub>3</sub> and -OH groups with the same laser pulses without tuning the laser system, allowing a comparison of the relative -CH<sub>3</sub> and -OH peak height eliminating an exhaustive and error prone calibration procedure. Replacing H<sub>2</sub>O with D<sub>2</sub>O conveniently shifts the vibrational frequency of the O-H stretch mode into the spectral range probed with the laser tuned to 2850 cm<sup>-1</sup>. This shift is related to the heavier mass of D compared to H which should shift the stretch mode towards lower wavenumbers by a factor of  $\sim \sqrt{M_D/M_H} \approx \sqrt{2}$ .<sup>34</sup> Figure 7.7 shows the BB-SFG spectra recorded for ALD with either H<sub>2</sub>O or D<sub>2</sub>O, with all other factors unchanged. The BB-SFG spectrum for the TMA half-cycle for the TMA/H<sub>2</sub>O process was identical to that of the TMA/D<sub>2</sub>O process. This demonstrates that the surface chemistry was not affected when H<sub>2</sub>O was replaced with D<sub>2</sub>O. The -OD groups were successfully detected after the D<sub>2</sub>O half-cycle at 2725 cm<sup>-1</sup>. Note that the spectral position and shape of the resonance indicate that the -OD groups on a surface have negligible D-bridges. Such bonding would induce a shift and a significant broadening (spanning > 200 cm<sup>-1</sup>) of the peak otherwise.<sup>35,36</sup> To recapitulate, both the -CH<sub>3</sub> and the -OD groups were observed with BB-SFG with a sensitivity better than 10% of a monolayer.

To study the influence of temperature on the surface groups, BB-SFG spectra were also collected for ALD at 150 °C using TMA and D<sub>2</sub>O. Comparing the BB-SFG spectra recorded after the TMA half-cycle in Fig 7.8 for ALD at 150 °C and 250 °C reveals a stronger -CH<sub>3</sub> signal at 150 °C indicating that more -CH<sub>3</sub>

groups are present on the surface. This was attributed to thermally induced dehydroxylation which increases with temperature, resulting in a lower -OD coverage at high temperatures and therefore a lower TMA uptake.<sup>6</sup> Furthermore, it is known from our earlier work that for ALD of  $\text{Al}_2\text{O}_3$  at temperatures below  $\sim 200$  °C there are *persistent*  $-\text{CH}_3$  groups remaining on the surface after the  $\text{H}_2\text{O}$  half-cycle.<sup>14</sup> The persistent  $-\text{CH}_3$  groups were also observed in this experiment for ALD at 150 °C and absent at 250 °C. The spectrum recorded after the  $\text{D}_2\text{O}$  half-cycle for ALD at 150 °C clearly showed both  $-\text{CH}_3$  and  $-\text{OD}$  groups. The interpretation of the small differences in shape and area of the  $-\text{OH}$  signal at 150 °C and 250 °C is not straightforward and beyond the scope of this work.<sup>37</sup>

Replacing TMA with a fully deuterated molecule (D-TMA,  $\text{Al}(\text{CD}_3)_3$ ) should lead to a shift of the stretch mode of the  $-\text{CH}_3$  groups by a factor of  $\sim \sqrt{2}$  towards lower wavenumbers. Figure 7.9 shows the signal of the C–D stretch mode of the  $-\text{CD}_3$  groups which was detected at  $2125\text{ cm}^{-1}$  which is indeed shifted by a factor of  $\sim \sqrt{2}$  compared to stretch mode of  $-\text{CH}_3$  at  $2890\text{ cm}^{-1}$ . The signal-to-noise level is rather poor due to the lower output power of the mid-IR laser at this wavelength used to probe the surface groups. Possibly, the signal-to-noise ratio was reduced even more by a lower SFG cross section due to the deuteration.<sup>34,38</sup> Nevertheless, not only did the  $-\text{CD}_3$  signal appear at the expected position, it also behaved as described in Eq. (7.1). The  $-\text{CD}_3$  signal appeared after the D-TMA half-cycle and disappeared after the  $\text{D}_2\text{O}$  half-cycle. This additional evidence corroborates the assignment of the signal at  $2890\text{ cm}^{-1}$  to the C-H stretch mode of  $-\text{CH}_3$  surface groups.

To summarize, at high temperatures the chemistry of  $\text{Al}_2\text{O}_3$  ALD is described accurately by Eq. (7.1): After the TMA half-cycle, the surface is covered by  $-\text{CH}_3$  groups. After the  $\text{H}_2\text{O}$  half-cycle, there are only  $-\text{OH}$  groups on the surface. For ALD at low temperatures, only  $-\text{CH}_3$  groups were observed after the TMA half-cycle. However, after the  $\text{H}_2\text{O}$  half-cycle both  $-\text{OD}$  and *persistent*  $-\text{CH}_3$  groups were present on the surface.

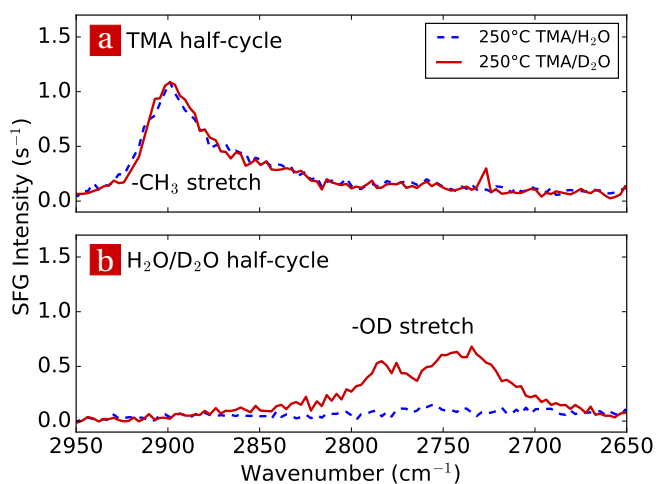


**Figure 7.7:** BB-SFG spectra recorded after a TMA and a H<sub>2</sub>O half-cycle for ALD of Al<sub>2</sub>O<sub>3</sub> at 250 °C. **(a)** The stretch mode of the –CH<sub>3</sub> groups was visible after the TMA half-cycle. Replacing H<sub>2</sub>O with D<sub>2</sub>O shows an identical spectrum for the TMA half-cycle. **(b)** The stretch mode of the –OH groups after the H<sub>2</sub>O half-cycle cannot be observed as it falls outside of the spectral range of the measurement. In the D<sub>2</sub>O half-cycle, a broad feature around 2725 cm<sup>-1</sup> is visible which is the stretch mode of –OD groups on the surface.



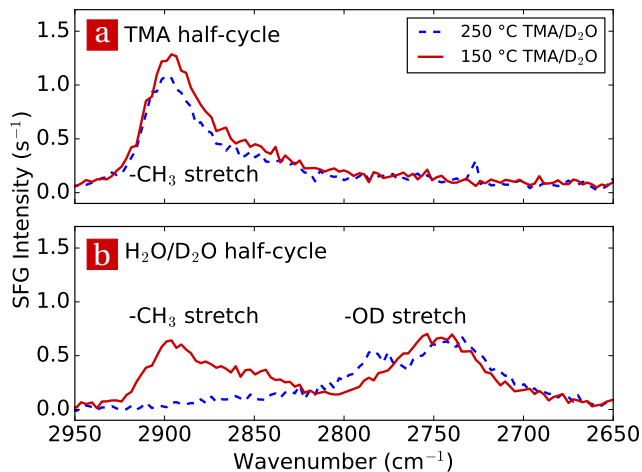


**Figure 7.8:** BB-SFG spectra for ALD at 150 °C and 250 °C using TMA and D<sub>2</sub>O. **(a)** At 250 °C the –CH<sub>3</sub> groups appear after TMA exposure and –OD groups appear after D<sub>2</sub>O exposure. At 150 °C the ALD process shows a slightly higher –CH<sub>3</sub> density after the TMA half-cycle and **(b)** both –OD and *persistent* –CH<sub>3</sub> groups are present on the surface after the D<sub>2</sub>O half-cycle.

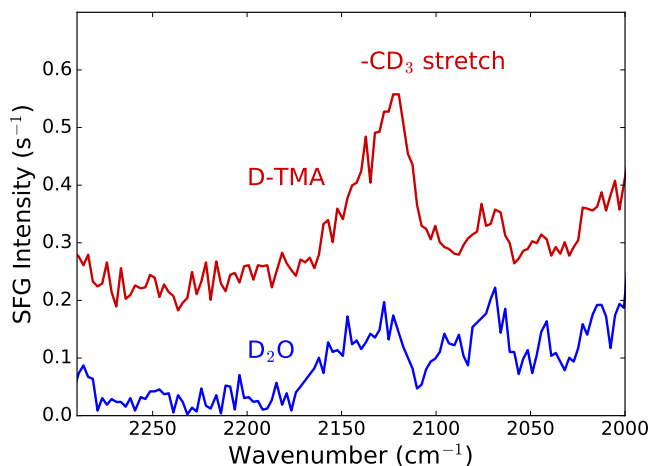


**Figure 7.9:** Using deuterated TMA (D-TMA, Al(CD<sub>3</sub>)<sub>3</sub>) and D<sub>2</sub>O at 200 °C, the stretch mode of the –CD<sub>3</sub> groups was detected at 2125 cm<sup>-1</sup>. The feature appeared after D-TMA exposure and disappeared after D<sub>2</sub>O exposure similar to the –CH<sub>3</sub> signal observed when using TMA. The signal-to-noise ratio is rather poor due to a relatively low laser intensity at this wavelength.

## Reaction kinetics

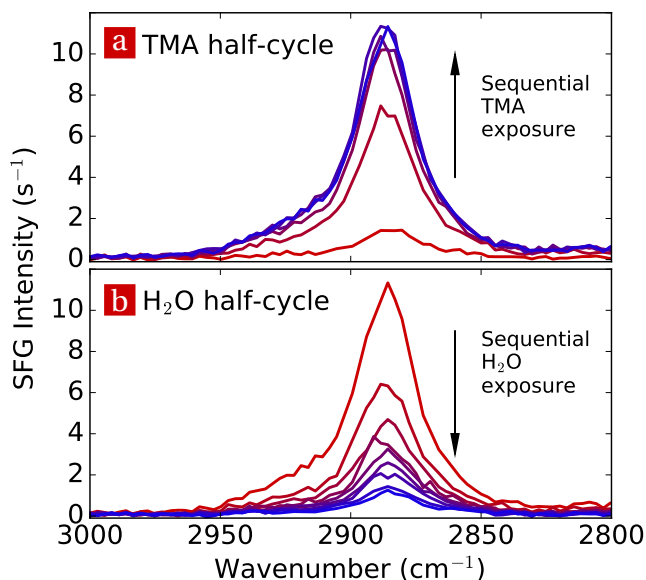
Fundamental insight into the surface reactions ruling ALD can be gained by studying the reaction kinetics and their temperature dependence. By definition, the reaction kinetics describe how the reaction rate depends on the reactant exposure. The reaction kinetics of steady-state ALD were measured for both half-cycles by monitoring the  $-\text{CH}_3$  signal as a function of precursor and co-reactant exposure. Note that for this experiment the central wavelength of the mid-IR laser was re-tuned to obtain the best possible signal-to-noise ratio for the  $-\text{CH}_3$  signal. Figure 7.10 shows how the  $-\text{CH}_3$  signal varied as a function of TMA and  $\text{H}_2\text{O}$  exposure during ALD at  $150^\circ\text{C}$ . For ALD at  $150^\circ\text{C}$ , the surface is covered with both  $-\text{OH}$  and *persistent*  $-\text{CH}_3$  groups at the start of the TMA half-cycle. This can be seen in Fig. 7.10 from the non-zero  $-\text{CH}_3$  signal at the end of the  $\text{H}_2\text{O}$  half-cycle and at the start of the TMA half-cycle. This surface, terminated with both  $-\text{OH}$  and  $-\text{CH}_3$  groups, was exposed to TMA by pulsing the ALD valve for 20 ms. The increase in the intensity of the  $-\text{CH}_3$  signal in Fig. 7.10(a) reflected an increase in the amount of  $-\text{CH}_3$  groups on the surface. This procedure was repeated until the  $-\text{CH}_3$  signal no longer increased, i.e. saturation was reached. The surface at the end of the TMA half-cycle is the starting surface for the subsequent  $\text{H}_2\text{O}$  half-cycle. A BB-SFG spectrum was recorded at the beginning of the  $\text{H}_2\text{O}$  half-cycle, see also the top spectrum in Fig. 7.10(b). Then, the surface was exposed to vapor phase  $\text{H}_2\text{O}$  by pulsing the ALD valve for 40 ms, resulting in the removal of a part of the  $-\text{CH}_3$  groups. This procedure was repeated until the  $-\text{CH}_3$  coverage no longer changed indicating that saturation was reached. The  $-\text{CH}_3$  groups still present on the surface were no longer reactive towards  $\text{H}_2\text{O}$ , i.e. *persistent*  $-\text{CH}_3$  groups.

Figure 7.11 shows the relative  $-\text{CH}_3$  density  $\theta_{\text{CH}}$  as a function of the duration of the  $\text{H}_2\text{O}$  exposure. The relative  $-\text{CH}_3$  density was determined from the BB-SFG spectra in Fig. 7.10 by fitting the spectra with the appropriate peak shape.<sup>14,19,39</sup> The experiment was performed at temperatures between  $100^\circ\text{C}$  and  $300^\circ\text{C}$  to determine how temperature affected the reaction kinetics. For high temperatures, the reaction in the  $\text{H}_2\text{O}$  half-cycle was fast and removed all the  $-\text{CH}_3$  groups. Whereas, for lower temperatures the reaction slowed down and saturated before all the  $-\text{CH}_3$  groups were removed, resulting in the aforementioned *persistent*  $-\text{CH}_3$  groups. An additional check with a prolonged  $\text{H}_2\text{O}$  exposure of 400 and 800 ms exposure (not shown) was performed at  $150^\circ\text{C}$  and did not reveal an additional  $-\text{CH}_3$  removal.

The reaction kinetics plotted in Fig. 7.11 describe the relation between the  $\text{H}_2\text{O}$  flux,  $\Gamma_{\text{H}_2\text{O}}$ , and the change in  $-\text{CH}_3$  coverage,  $\frac{d\theta_{\text{CH}}}{dt}$ . The reaction in the  $\text{H}_2\text{O}$  half-cycle, given by Eq. (7.1b), can be described by the following equation,

$$\frac{d\theta_{\text{CH}}}{dt} = -\sigma_{\text{H}_2\text{O}}\theta_{\text{CH}}\Gamma_{\text{H}_2\text{O}}, \quad (7.3)$$

in which  $\sigma_{\text{H}_2\text{O}}$  is the reaction cross section. The reaction cross section (with



**Figure 7.10:** BB-SFG spectra showing the stretch mode of the  $-\text{CH}_3$  groups on the surface during ALD at  $150\text{ }^\circ\text{C}$ . The number of  $-\text{CH}_3$  groups is reflected by the strength of the resonance at  $2890\text{ cm}^{-1}$ . **(a)** During the TMA half-cycle, the number of  $-\text{CH}_3$  groups increased until saturation was reached. **(b)** During the  $\text{H}_2\text{O}$  half-cycle, initially the  $\text{H}_2\text{O}$  exposure removed  $-\text{CH}_3$  from the surface. However, this reaction saturated even though there were  $-\text{CH}_3$  groups on the surface. These  $-\text{CH}_3$  groups were no longer reactive with  $\text{H}_2\text{O}$  and were labeled as *persistent*  $-\text{CH}_3$  groups.

units  $\text{cm}^2$ ) is closely related to the initial reaction (or sticking) probability  $S_0 = \sigma N_{\text{CH}}^{\text{full}}$ , with  $N_{\text{CH}}^{\text{full}}$  the absolute  $-\text{CH}_3$  coverage after a saturated TMA step.  $S_0$  represents the probability that a  $\text{H}_2\text{O}$  molecule reacts with a  $-\text{CH}_3$  group when it impinges on a fully  $-\text{CH}_3$  covered surface. More complex models describing the reaction kinetics are treated in the supplementary information as they introduce more unknowns and did not yield more insight. The solution of Eq. (7.3) is given by an exponential function ( $\exp(-\sigma_{\text{H}_2\text{O}} \Gamma_{\text{H}_2\text{O}} t)$ ) and describes the reaction kinetics at high temperatures. The decay seen at low temperatures (below  $200\text{ }^\circ\text{C}$ ) cannot be described by this exponential function alone. The reaction saturates before all the  $-\text{CH}_3$  groups are removed, i.e. the *persistent*  $-\text{CH}_3$  groups on the surface. This means that at low temperatures the reaction kinetics cannot be described with a single first-order reaction with a constant cross section.

To explain these reaction kinetics, two models are proposed. Either there are two kinds of  $-\text{CH}_3$  groups or the reactivity of the  $-\text{CH}_3$  groups is coverage dependent. In the first model, each of the two kinds of  $-\text{CH}_3$  groups has its

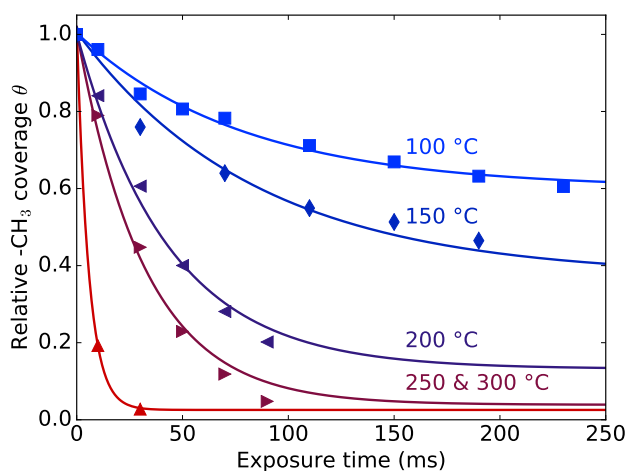


**Figure 7.11:** The relative  $-\text{CH}_3$  coverage as a function of  $\text{H}_2\text{O}$  dose for ALD at 100 °C up to 300 °C obtained from fits to the BB-SFG spectra. At high temperatures, the reaction is fast and removes all  $-\text{CH}_3$ . At lower temperatures the reaction slows down and saturates before all  $-\text{CH}_3$  is removed leaving *persistent*  $-\text{CH}_3$  on the surface.

own reaction and Eq. 7.1b consists in fact of two parallel reaction paths. The reaction for the *reactive* type of  $-\text{CH}_3$  has a low activation energy and occur at typical ALD temperatures. The reaction for the *persistent*  $-\text{CH}_3$  groups has a higher activation energy such that this reaction only occurs at elevated temperatures resulting in *persistent*  $-\text{CH}_3$  at low temperatures. In this model, the relative coverage of the *reactive* groups are described by an exponential function of the  $\text{H}_2\text{O}$  exposure (assuming this reaction is a first order reaction). The *persistent* groups are described by a variable at low temperature (or an exponential function with a very large time constant). This model was also discussed in Chapter 6 of this Thesis. The underlying microscopic cause for the two types of  $-\text{CH}_3$  groups might be due to different reactivity of various surface site of the  $-\text{CH}_3$  groups, similar to reactions at step edges and terraces on crystalline surfaces. On these ideal surfaces, large differences in reactivity are observed. For example, the reaction rate of  $\text{H}_2$  dissociation on a Pt surface that depends on the crystal face, e.g. Pt(100) versus Pt(111), and on the step-edge density.<sup>40</sup>

The second model, a coverage dependent reactivity of the  $-\text{CH}_3$  groups, is also known from the field of surface science. This occurs, for example, for the oxidation of CO on a rhodium surface where a strong coverage dependence in the reactivity was found.<sup>41,42</sup> A similar effect was reported for the dimethylamine precursor in chemical vapor deposition (CVD), where the adsorption of the precursor showed a coverage dependent reaction cross section.<sup>43</sup> Moreover, support for the existence of this mechanism in ALD can

be found in recent ab-initio work by Shirazi and Elliott.<sup>16</sup> In their density-functional theory (DFT) simulations, isolated  $-\text{CH}_3$  groups are not reactive towards  $\text{H}_2\text{O}$  (i.e. a high activation energy). On the other hand, clusters of 3  $-\text{CH}_3$  groups are reactive towards  $\text{H}_2\text{O}$ . If the microscopic reaction cross section depends on number of neighboring  $-\text{CH}_3$  groups it is likely that the macroscopic cross section depends on the surface coverage. This model, assuming a non-constant reaction cross section  $\sigma(\theta)$ , leads to an change in Eq. (7.3) for the  $\text{H}_2\text{O}$  half-cycle, substituting  $\sigma_{\text{H}_2\text{O}}$  by  $\sigma_{\text{H}_2\text{O}}(\theta_{\text{CH}}) = f(\theta_{\text{CH}})$ . The coverage dependent cross section can be calculated from the data in Fig. 7.10 by rearranging Eq. (7.3). Note that the unknowns in the resulting expression for  $\sigma_{\text{H}_2\text{O}}(\theta_{\text{CH}})$  – namely  $\Gamma$ ,  $\theta_{\text{CH}}$  and  $\frac{d\theta_{\text{CH}}}{dt}$  – were all measured in the experiment which means that  $\sigma$  can be calculated from this data set. Figure 7.12 shows the reaction cross section of the  $\text{H}_2\text{O}$  half-cycle as a function of surface coverage calculated from the data in Fig. 7.11. For ALD at higher temperatures, the cross section is independent of the surface coverage. For lower temperatures, the value of the cross section decreases and below 200 °C the cross section shows a coverage dependence. For comparison, the reaction cross section of the TMA half-cycle reported in our previous work was  $\sigma = 6.5 \cdot 10^{-18} \text{ cm}^2$ . For TMA, the cross section was found to be independent on surface coverage and did not vary with temperature in the investigated range between 100 °C and 300 °C.<sup>14</sup>

The activation energy of the reaction in the  $\text{H}_2\text{O}$  half-cycle was determined from the temperature dependence of the sticking probability. Figure 7.13 shows an Arrhenius plot of the initial sticking probability. The linear fit to the data revealed an activation energy of 0.27 eV. This is quite close to the activation energy of the surface reaction predicted by DFT simulations. Shirazi and Elliott reported an activation energy of 0.25 eV for a cluster of 3  $\text{CH}_3$  groups undergoing the reaction  $3 \text{ Al}-\text{CH}_3 + \text{H}_2\text{O} \longrightarrow 2 \text{ Al}-\text{CH}_3 + \text{Al}-\text{OH} + \text{CH}_4$  and a very high activation energy for the reaction of an isolated  $-\text{CH}_3$  group with  $\text{H}_2\text{O}$ .<sup>16</sup> Weckman and Laasonen found a activation energy of 0.44 eV for the reaction  $\text{Al}-(\text{CH}_3)_2 + \text{H}_2\text{O} \longrightarrow \text{Al}-\text{CH}_3\text{OH} + \text{CH}_4$ , 0.67 eV for  $\text{Al}-\text{CH}_3\text{OH} + \text{H}_2\text{O} \longrightarrow \text{Al}-(\text{OH})_2 + \text{CH}_4$ .<sup>44</sup> For the reaction  $\text{Al}-\text{CH}_3 + \text{H}_2\text{O}$  no direct route was found in their work.<sup>44</sup>

To summarize, at high temperatures the reactions in the  $\text{H}_2\text{O}$  half-cycle obey first-order reaction kinetics. Below 200 °C, the reaction kinetics can no longer be described as a first-order reaction and *persistent*  $-\text{CH}_3$  groups remain on the surface. Two possible models were proposed to account for these observations: (1) There are two types of  $-\text{CH}_3$  groups each with its own reactivity. (2) The reactivity of the  $-\text{CH}_3$  groups depends on the surface coverage at low temperatures. Both models are established in the field of surface science, they can equally well describe the data, and both models are not necessarily mutually exclusive. However, we prefer the coverage dependent model because this effect has been observed in the related deposition process of CVD and was it actually predicted for the  $\text{Al}_2\text{O}_3$  ALD process by ab-initio DFT simulations.

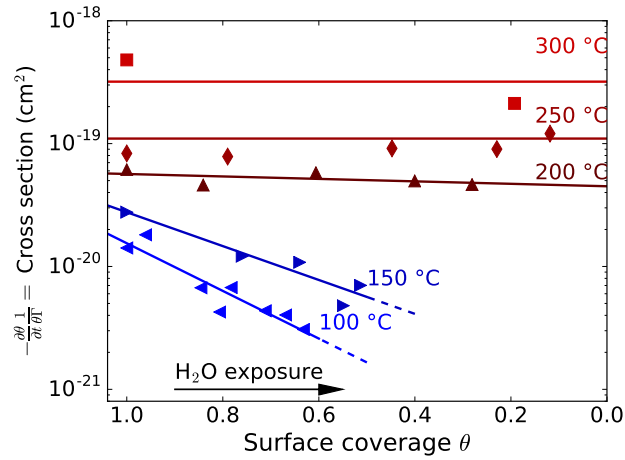


**Figure 7.12:** The reaction cross section determined for the H<sub>2</sub>O half-cycle as a function of surface coverage for ALD at 100 °C up to 300 °C. At high temperatures, the cross section is constant resulting in an exponential decrease of -CH<sub>3</sub> coverage as function of H<sub>2</sub>O dose. Below 200 °C the cross section clearly depends on the surface coverage. Due to the fast reaction only two data points were available at 300 °C. The solid lines is a guide to the eye.

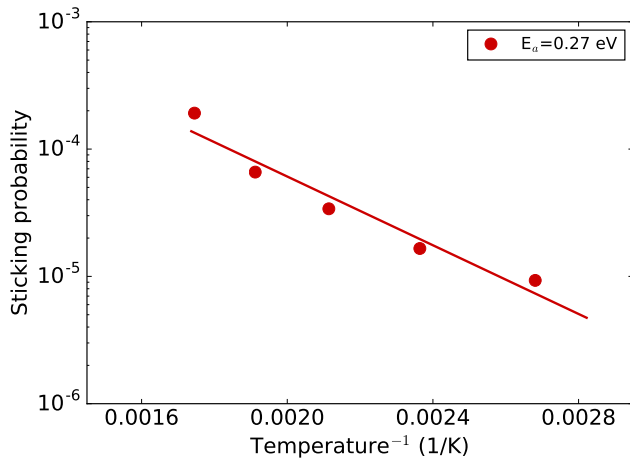


**Figure 7.13:** An Arrhenius plot of the initial sticking probability versus temperature revealing the activation energy for the reaction in the H<sub>2</sub>O half-cycle.

## Quantification of the $-\text{CH}_3$ density

The relative  $-\text{CH}_3$  coverage after the TMA and the  $\text{H}_2\text{O}$  half-cycle was measured with BB-SFG spectroscopy for ALD between 100 °C and 450 °C. At each temperature, 5 ALD cycles were performed to ensure steady-state growth at that temperature. During the subsequent ALD cycle, BB-SFG spectra were collected after each half-cycle. Then the temperature was raised by 50 °C and the measurement procedure repeated after the temperature had settled. It was not practical to simultaneously investigate the reaction kinetics and determine the  $-\text{CH}_3$  coverage in a single experiment. BB-SFG spectra can only be compared if the optical alignment of the setup remained unaltered. The daily adjustments to the setup limited the number of spectra which could be measured in a single run. To cover a wider temperature range in a single run, spectra were only collected after a saturated half-cycle. With this approach it was possible to measure the  $-\text{CH}_3$  coverage from 100 °C up to 300 °C in one run and from 300 °C up to 450 °C in a second run. By measuring the  $-\text{CH}_3$  coverage at 300 °C twice, the influence of possible changes to the optical alignment could be determined. The spectra recorded in this fashion are shown in Fig. 7.14. For the TMA half-cycle, a gradual decrease of the  $-\text{CH}_3$  signal with temperature was observed. Comparing the spectra for the TMA half-cycle recorded at 300 °C revealed a small difference in signal strength. For the  $\text{H}_2\text{O}$  half-cycle, *persistent*  $-\text{CH}_3$  groups were observed at low temperatures.

The relative  $-\text{CH}_3$  density was determined by fitting the spectra in Fig. 7.14. Because the two data sets were measured on different days, the two series were joined by scaling the high temperature data such that the extracted  $-\text{CH}_3$  coverages at 300 °C overlap. The SFG amplitude, which is proportional to the  $-\text{CH}_3$  density, is plotted on the left axis of Fig. 7.15. These data were made absolute, i.e. calibrated, by assuming a  $-\text{CH}_3$  areal density of  $5.5 \cdot 10^{14} \text{ cm}^{-2}$  after the TMA half-cycle for ALD at 300 °C. This assumption is based upon data presented by Rahtu et al. indicating that 1.5  $-\text{CH}_3$  groups per Al atom are left after TMA chemisorption at this temperature combined with the GPC(at) of  $3.6 \text{ nm}^{-2}$ .<sup>12</sup> Care was taken to select an appropriate temperature for the calibration procedure as the accuracy of the data is only as good as the calibration. At 300 °C the calibration data are not affected by low temperature effects such as precursor condensation and persistent surface groups nor by high-temperature effects such as precursor decomposition. The right axis of Fig. 7.15 shows the absolute  $-\text{CH}_3$  density as a function of temperature for both half-cycles resulting from this procedure. Note that the trend in the relative  $-\text{CH}_3$  data is independent of the calibration. The  $-\text{CH}_3$  density after the TMA half-cycle decreases with temperature up to 400 °C, dropping off more rapidly above 400 °C. The trend up to 400 °C can be attributed to temperature induced dehydroxylation leading to a reduction of the density of the  $-\text{OH}$  groups.<sup>6</sup> The sharp drop can be a combination of decomposition of the chemisorbed TMA, e.g. demethylation, and precursor desorption.<sup>6,30</sup> For the  $\text{H}_2\text{O}$  half-cycle, the persistent  $-\text{CH}_3$  groups are observed at low temperatures and absent above  $\sim 200$  °C.

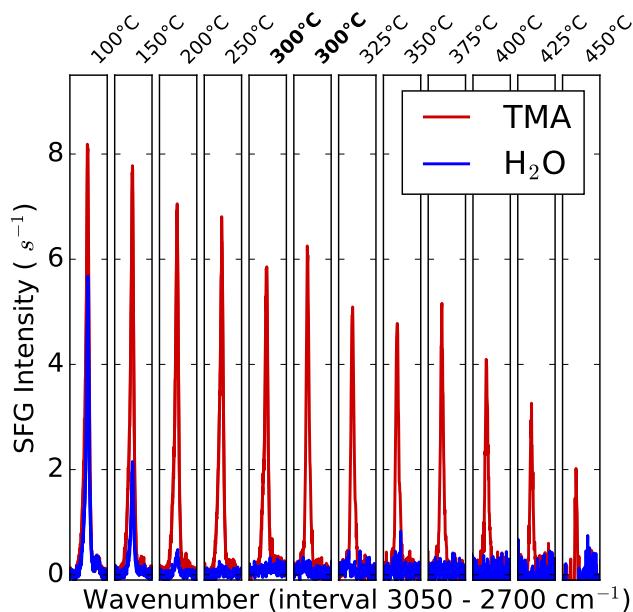


**Figure 7.14:** BB-SFG spectra of the  $-\text{CH}_3$  signal after a saturated TMA and  $\text{H}_2\text{O}$  dose for ALD between  $100\text{ }^\circ\text{C}$  and  $450\text{ }^\circ\text{C}$ . This data was collected in two separate experimental runs ( $100\text{--}300\text{ }^\circ\text{C}$  and  $300\text{--}450\text{ }^\circ\text{C}$ ).

The temperature trend in the  $-\text{CH}_3$  coverage yields insight into the mechanism causing the self limiting nature of the TMA half-cycle. For  $\text{Al}_2\text{O}_3$  ALD, two key mechanisms have been proposed: (1) Steric hindrance. (2) Depletion of “reactive sites”.<sup>9</sup> There are proponents for both mechanisms. For example, **Puurunen** attributed the self-limiting nature of the surface reactions in the TMA half-cycle to steric hindrance.<sup>9</sup> On the other hand, **Shirazi and Elliott** concluded from their DFT simulations that for the TMA half-cycle the depletion of undercoordinated oxygen sites is the cause of saturation.<sup>16</sup> Both the trend in the  $-\text{CH}_3$  coverage with temperature and the absolute values of the coverage point towards the depletion of “reactive sites”. The absolute  $-\text{CH}_3$  densities reached after the TMA half-cycle,  $\leq 6\text{ nm}^{-2}$  as shown in Fig. 7.15, are not high enough for steric hindrance. For example, on  $\text{Si}(111)$  densities as high as  $8\text{ }-\text{CH}_3$  groups per  $\text{nm}^2$  have been observed.<sup>45,46</sup> A stronger argument that does not depend on the absolute densities can be found in the temperature trend of the  $-\text{CH}_3$  density in Fig. 7.15. For small and immobile surface groups such as the  $-\text{CH}_3$  groups, the surface area that these groups occupy is temperature independent.<sup>9</sup> This implies that if steric hindrance is the limiting factor, the same  $-\text{CH}_3$  coverage should be observed at all temperatures. If, for the sake of argument, it is assumed that steric hindrance is the limiting factor at  $100\text{ }^\circ\text{C}$  it follows that at higher temperatures a different



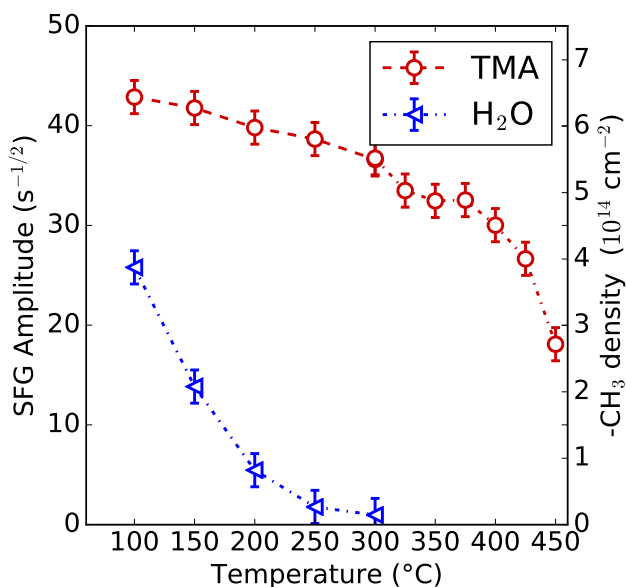


**Figure 7.15:** The BB-SFG amplitude of the  $-\text{CH}_3$  signal after the TMA and  $\text{H}_2\text{O}$  half-cycle as a function of substrate temperature obtained from fit of the BB-SFG spectra in Fig. 7.14. (right axis) The corresponding absolute  $-\text{CH}_3$  coverage is also given (see text). At low temperatures the persistent  $-\text{CH}_3$  groups after the  $\text{H}_2\text{O}$  exposure are visible. The density of *persistent*  $-\text{CH}_3$  groups was determined from fits to the saturation curves in Fig. 7.11 for better accuracy. Above 400 °C effects such as precursor decomposition and precursor desorption might affect the data.

mechanism must be responsible for the self-limiting behavior. Apart from steric hindrance, the self-limiting nature of the TMA half-cycle can be caused by depletion of “reactive sites”. This can be subdivided into two categories: (1) Depletion of protons/H-atoms. (2) Depletion of under-coordinated O atoms. The first factor, depletion of protons, can be ruled out from the fact that these  $\text{Al}_2\text{O}_3$  films are known to contain a significant amount of hydrogen, partly in the form of  $-\text{OH}$  in the bulk of the film.<sup>17,47,48</sup> This leaves the depletion of under-coordinated O sites as the likely reason for the self-limiting nature of the TMA half-cycle which is in agreement with mechanism proposed by Shirazi and Elliott.<sup>16</sup>

Another topic that can be addressed with these data is the chemisorption of TMA on the  $-\text{OH}$  groups. TMA can chemisorb on a  $-\text{OH}$  covered surface in several configurations: TMA can chemisorb monofunctional, i.e. react with a single  $-\text{OH}$  group leaving two  $-\text{CH}_3$  groups attached to the Al atom. Alternatively, TMA can chemisorb bifunctionally, i.e. react with two  $-\text{OH}$  groups leaving a single  $-\text{CH}_3$  group attached to the Al atom. It is not likely that TMA reacts with three  $-\text{OH}$  groups upon chemisorption.<sup>16,44</sup> The number of re-

maintaining  $-\text{CH}_3$  groups after chemisorption was calculated from the change in  $-\text{CH}_3$  groups  $\Delta\theta_{CH}$  during the TMA half-cycle divided by the number of Al atoms deposited per surface area. The GPC(at) data were not available for the temperature range used in this work from a single source, and therefore the data was taken from [Gröner et al.](#) and [Matero et al.](#) using XRR and SE respectively.<sup>10,26</sup> The  $\Delta\theta_{CH}$  was calculated from the data in Fig. 7.15. For the thermal ALD process at low temperature,  $\Delta\theta_{CH}$  equals the coverage reached after TMA minus the *persistent*  $-\text{CH}_3$  coverage. At higher temperatures, no *persistent*  $-\text{CH}_3$  are present and  $\Delta\theta_{CH}$  is equal to the coverage reached in the TMA half-cycle. Figure 7.16 shows the  $\Delta\theta_{CH}$  to Al ratio for the  $\text{Al}_2\text{O}_3$  ALD process. At low temperatures, TMA chemisorbs bifunctionally, i.e. with 1  $-\text{CH}_3$  group remaining after chemisorption. The number of  $-\text{CH}_3$  groups remaining after TMA chemisorption gradually increases towards 1.5 for higher temperatures. The related process of PE-ALD of  $\text{Al}_2\text{O}_3$  can be treated in a similar fashion. For the PE-ALD process, it is expected that even at low temperatures the plasma is reactive enough to completely remove all the  $-\text{CH}_3$  groups. This was demonstrated in our previous work, where the GPC(at) of the PE-ALD process could be predicted accurately from the  $-\text{CH}_3$  coverage with this assumption.<sup>14</sup> Figure 7.16 also shows the  $-\text{CH}_3$  to Al ratio for PE-ALD of  $\text{Al}_2\text{O}_3$ . For the PE-ALD process, 1.5  $-\text{CH}_3$  groups remain attached to the Al atom after chemisorption. The number of  $-\text{CH}_3$  groups remaining on the surface after the chemisorption of TMA is independent of temperature up to 400 °C for PE-ALD. Above this temperature, precursor decomposition and desorption might affect the data.

The trend observed for thermal ALD could be explained by a cooperative effect in TMA chemisorption proposed by [Shirazi and Elliott](#).<sup>16</sup> Their DFT results show that when a single TMA molecule chemisorbs on a fully  $-\text{OH}$  covered surface, it is likely to adsorb monofunctionally. On the other hand, if there is already TMA chemisorbed on the surface, new TMA can adsorb bifunctionally. A similar mechanism could be responsible for the transition from monofunctional to bifunctional chemisorption seen for the thermal ALD process at lower temperatures. At low temperatures, the presence of persistent  $-\text{CH}_3$  ensures that TMA can chemisorb bifunctionally. At higher temperatures the surface starts out  $-\text{OH}$  covered and no  $-\text{CH}_3$  groups are present. Therefore, TMA chemisorbs mono-functionally initially. The chance of bifunctional chemisorption increases with TMA uptake because the already chemisorbed TMA allows new TMA to chemisorb bifunctionally. The average of the monofunctional and bifunctional adsorption could result in the average of 1.5  $-\text{CH}_3$  groups per Al atom as observed at high temperatures.

To summarize, from the quantification of the  $-\text{CH}_3$  coverage it was possible to deduce that the self-limiting nature of the TMA half-cycle is caused by depletion of under-coordinated O sites. Moreover, for thermal ALD at low temperatures it was shown that (excluding persistent  $-\text{CH}_3$ ) TMA retains one of its  $-\text{CH}_3$  ligands after chemisorption. This increases to 1.5  $-\text{CH}_3$  ligands at higher temperatures.

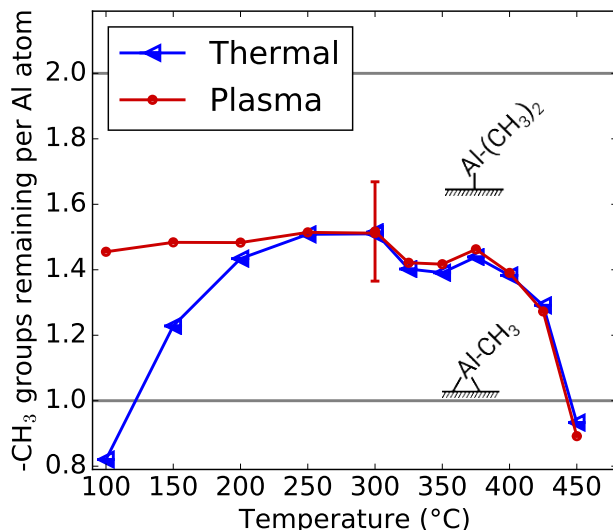


**Figure 7.16:** The number of reactive  $-\text{CH}_3$  groups attached to Al after TMA chemisorption, calculated by dividing the non-persistent  $-\text{CH}_3$  coverage (Fig. 7.15) by the number of Al atoms deposited per cycle (Fig. 7.6). The thermal process shows a trend towards bi-functional adsorption when going to low temperatures, i.e. the Al atom is twofold coordinated to O and has a single  $-\text{CH}_3$  group. The related  $\text{O}_2$  plasma process shows a constant number of remaining  $-\text{CH}_3$  groups after chemisorption as a function of temperature. Above  $400^\circ\text{C}$  thermal decomposition and desorption of TMA might influence the result for both thermal and plasma ALD.

## Carbon incorporation

The  $\text{Al}_2\text{O}_3$  films have been reported to be carbon-free even when deposited with ALD at low temperatures.<sup>2,3,17,28</sup> This suggests that the *persistent*  $-\text{CH}_3$  groups are not incorporated into the film. Therefore, an dedicated experiment was designed to test the hypothesis that  $-\text{CH}_3$  groups are not incorporated into the film. This was done by intentionally leaving  $-\text{CH}_3$  groups on the surface by not saturating the  $\text{H}_2\text{O}$  half-cycle for ALD. Two samples were prepared by performing 300 cycles of ALD of  $\text{Al}_2\text{O}_3$  at a deposition temperature of  $200^\circ\text{C}$ . The first sample, labeled “saturated”, consisted of a Si(100) substrate on which an  $\text{Al}_2\text{O}_3$  film was deposited using the normal process parameters with each process step in saturation. The preparation of the second sample differed only in the duration of the  $\text{H}_2\text{O}$  exposure. The  $\text{H}_2\text{O}$  exposure was chosen to be roughly half of the exposure needed for saturation. This sample was labeled “unsaturated”. The film thickness and optical properties of the  $\text{Al}_2\text{O}_3$  films after deposition were determined with SE and are listed in Table

**7.1.** The  $\text{Al}_2\text{O}_3$  film thickness of the “unsaturated” sample is roughly 60% of the  $\text{Al}_2\text{O}_3$  thickness found for the “saturated” sample. For both samples, a similar refractive index was found for the  $\text{Al}_2\text{O}_3$  film, which is an indication of a similar atomic density. This shows that indeed the  $\text{H}_2\text{O}$  exposure was not saturated for the “unsaturated” sample but that nevertheless high quality  $\text{Al}_2\text{O}_3$  was grown in both cases.

The elemental composition of both the samples was analyzed by XPS. The Al2p, C1s, and O1s contributions were measured and the atomic O to Al ratio and the C content of the material were calculated from the area of the peaks using the appropriate sensitivity factors. A depth profile was made by stepwise sputtering the  $\text{Al}_2\text{O}_3$  film with Ar ions and measuring an XPS spectra after each sputter step. The [O] to [Al] atomic ratio and the atomic C percentage are shown in Fig 7.17 as a function of etch time. At the surface (before the first etch step) adventitious carbon was observed which is not related to the ALD process. From the first etch step on, the carbon signal for both samples was below the detection limit of the setup which is  $\sim 1\%$ . The  $\text{Al}_2\text{O}_3$  layer was stoichiometric throughout the film with an O to Al ratio of 3:2, in agreement with what is reported for  $\text{Al}_2\text{O}_3$  ALD at this temperature.<sup>2,17</sup>

For comparison, the expected C content of the “unsaturated” sample was calculated assuming the worst-case scenario: i.e. full incorporation of unreacted  $-\text{CH}_3$  groups. Judging from the 40% reduction of the GPC(nm), roughly 40% of  $-\text{CH}_3$  groups were left on the surface after the  $\text{H}_2\text{O}$  half-cycle during ALD on the “unsaturated” sample. For each Al atom which is deposited,  $\sim 1.5$   $-\text{CH}_3$  groups will be on the surface after TMA chemisorption. For the “unsaturated” sample, this means that 0.6  $-\text{CH}_3$  groups per Al atom will be left on the surface after the unsaturated  $\text{H}_2\text{O}$  exposure. If all of these C atoms would be incorporated, the stoichiometry of the film would be significantly affected. The composition would be: 32 at. % Al, 19 at. % C, and 48 at. % O. The carbon content was evidently much lower for the “unsaturated” sample. Moreover, there were no significant differences between the “saturated” and “unsaturated” samples with respect to film composition.

This experiment clearly showed that  $-\text{CH}_3$  groups present on the surface after the  $\text{H}_2\text{O}$  half-cycle do not necessarily lead to carbon incorporation. Similarly, operating very close to or slightly below saturation is not (necessarily) detrimental to film composition. Obviously, it might affect uniformity and will affect conformality. In industry, ALD is occasionally operated slightly below saturation to optimize the efficiency of precursor usage and the throughput of the ALD system.<sup>31</sup> A plausible reason for the absence of carbon incorporation for thermal ALD of  $\text{Al}_2\text{O}_3$  can be found in the reaction mechanism; for thermal ALD of  $\text{Al}_2\text{O}_3$  both half-cycles consist of a single elemental reaction. In other words, either  $\text{H}_2\text{O}$  reacts with  $-\text{CH}_3$  in a reaction without any reaction intermediates and a single transitions state or the reaction does not occur at all. For a non-elementary reaction, the reaction might have a carbon containing reaction intermediate. If the reaction intermediate is reactive towards the precursor and remains on the surface it could easily be incorporated into the film. In PE-ALD of  $\text{Al}_2\text{O}_3$  and ALD of  $\text{Al}_2\text{O}_3$  using  $\text{O}_3$  instead of  $\text{H}_2\text{O}$ , for

example, carbonates and formates have been observed as reaction intermediates.<sup>20–22,49</sup> Moreover, these reaction intermediates have been shown to act as a chemisorption site of TMA.<sup>20,21</sup> When TMA chemisorbs on such a site, this can lead to carbon incorporation. For PE-ALD, carbon incorporation is indeed observed for short (i.e. undersaturated) plasma exposures. Furthermore, the plasma exposure needs to be longer than the duration needed for saturation of the GPC to obtain carbon free films.<sup>48,50</sup> On the other hand, thermal ALD of  $\text{Al}_2\text{O}_3$  does not show such a relation between the  $\text{H}_2\text{O}$  exposure and carbon incorporation.

**Table 7.1:** Film thickness, refractive index and GPC determined with spectroscopic ellipsometry for two samples deposited by 300 cycles of ALD. The sample labeled “saturated” was prepared using an optimized ALD process, while the sample labeled “unsaturated” was prepared with the same process with a smaller  $\text{H}_2\text{O}$  dose such that the  $\text{H}_2\text{O}$  dose was insufficient to reach saturation.

Sample	Thickness (nm)	GPC ( $\text{\AA}$ )	$n$ 589 nm
“saturated”	30.0	1.00	1.67
“unsaturated”	16.5	0.55	1.67

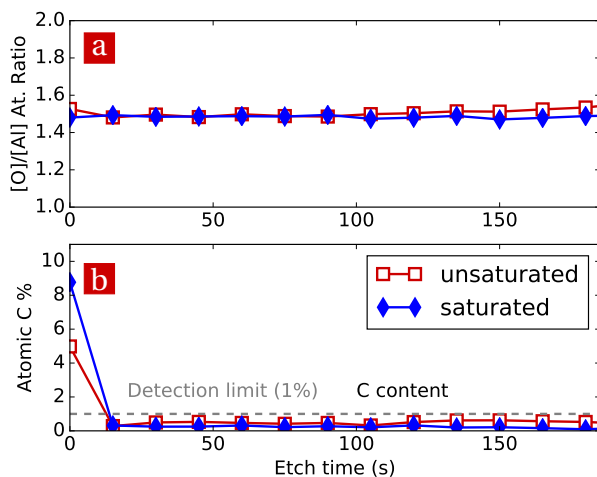


**Figure 7.17:** XPS depth profile of two samples with an ALD  $\text{Al}_2\text{O}_3$  film on Si(100) prepared at 200 °C. The sample labeled “saturated” was prepared using an ALD recipe where both half-cycles were fully saturated. The sample labeled “unsaturated” was prepared with the same recipe with a shortened  $\text{H}_2\text{O}$  exposure which resulted in  $\sim 60\%$  of the normal GPC. (a) Both films were stoichiometric throughout. (b) In both cases the carbon content was below the XPS detection limit. The carbon seen at  $t=0$  is adventitious carbon unrelated to the ALD process. The samples were prepared in an *Oxford Instruments FlexAL* and examined with a *Thermo Scientific K-Alpha XPS*.

## 7.5 Conclusion

The growth mechanism of the prototypical ALD process of  $\text{Al}_2\text{O}_3$  was studied with BB-SFG spectroscopy. Several dedicated experiments were performed to elucidate several key elements of  $\text{Al}_2\text{O}_3$  ALD process: the reaction kinetics, the origin of the self-limiting nature of the surface reactions, the number of -OH groups consumed by the chemisorption of TMA, and the apparent paradox between *persistent*  $-\text{CH}_3$  groups at low temperatures and negligible carbon incorporation into the  $\text{Al}_2\text{O}_3$  films.

The overall surface chemistry was monitored for ALD using either  $\text{Al}(\text{CH}_3)_3$  (TMA) or  $\text{Al}(\text{CD}_3)_3$  (D-TMA) as precursor and  $\text{H}_2\text{O}$  or  $\text{D}_2\text{O}$  as co-reactant. Comparing BB-SFG spectra of the C-H region using TMA and  $\text{H}_2\text{O}$  versus TMA and  $\text{D}_2\text{O}$  at 250 °C demonstrated that at this temperature the ALD process showed virtually ideal behavior: TMA chemisorb on the  $-\text{OH}$  sites and  $\text{H}_2\text{O}$  is reactive enough to remove all  $-\text{CH}_3$  groups. At 150 °C, TMA did chemisorb on the  $-\text{OH}$  groups. However,  $\text{H}_2\text{O}$  was not reactive enough at this temperature to remove all  $-\text{CH}_3$  groups. Both  $-\text{OD}$  groups and *persistent*  $-\text{CH}_3$  groups were present on the surface after the  $\text{D}_2\text{O}$  half-cycle. Replacing TMA with D-TMA showed the typical isotope shift in the C-H / C-D stretch mode of the

–CH<sub>3</sub> groups. These experiments established that both the –CH<sub>3</sub> and the –OD groups could be monitored with sub-monolayer sensitivity with BB-SFG spectroscopy.

The reaction kinetics of the growth mechanism was investigated with BB-SFG spectroscopy by monitoring the –CH<sub>3</sub> coverage during the H<sub>2</sub>O half-cycle. At high temperatures the reaction during the H<sub>2</sub>O half-cycle was fast, removed all –CH<sub>3</sub> groups, and obeyed first-order reaction kinetics. At lower temperatures, the reaction slowed down and *persistent* –CH<sub>3</sub> groups remained on the surface. The initial sticking probability and the reaction cross section were quantified. An initial sticking probability  $S_0 = 1 \times 10^{-4}$  (cross section  $\sigma = 1 \times 10^{-18}$  cm<sup>2</sup>) was found for the reactions in the H<sub>2</sub>O half-cycle at 300 °C. This decreased rapidly with temperature, with a initial sticking probability of  $S_0 = 1 \times 10^{-6}$  (cross section  $\sigma = 1 \times 10^{-20}$  cm<sup>2</sup>) at 100 °C. For comparison, the reaction cross section in the TMA half-cycle reported in our previous work was  $\sigma = 6.5 \cdot 10^{-18}$  cm<sup>2</sup> and independent of temperature.

Both the reaction kinetics and the *persistent* surface groups could be interpreted in two ways: either two “kinds” of –CH<sub>3</sub> exist (e.g. different sites) leading to different reaction paths or the reaction cross section was coverage dependent. Both models could describe the data. The coverage dependent reaction cross sections were determined from the data. From the temperature dependence of the reaction cross section, an activation energy of 0.27 eV was found for the reaction in the H<sub>2</sub>O half-cycle. This is comparable to what has been predicted in recent DFT studies (0.25–0.62 eV). In these DFT studies, a coverage dependent reactivity is also reported. Furthermore, in the related process of CVD, such a coverage dependence is also observed. These facts support the coverage dependent model, making this the preferred model.

The –CH<sub>3</sub> coverage was measured with BB-SFG after the TMA and H<sub>2</sub>O half-cycles for deposition temperatures between 100 °C and 450 °C. The trend in the –CH<sub>3</sub> coverage after the TMA step showed that the self-limiting behavior in the TMA half-cycle cannot be caused by steric hindrance. The most likely mechanism responsible for the self-limiting nature in the TMA half-cycle is the depletion of under-coordinated O atoms. Furthermore, the –CH<sub>3</sub> coverage was quantified in absolute terms and the number of –OH groups consumed in the chemisorption of a TMA molecule on the surface could be determined as a function of temperature. It was found that at 100 °C TMA chemisorbs bifunctionally on the –OH groups with one –CH<sub>3</sub> group remaining on the surface after chemisorption. With increasing temperature this increases to 1.5 –CH<sub>3</sub> groups remaining on the surface after TMA chemisorption at 250 °C.

Possible incorporation of the *persistent* –CH<sub>3</sub> groups into the Al<sub>2</sub>O<sub>3</sub> films was studied with XPS. Virtually carbon free films were found when intentionally trying to incorporate –CH<sub>3</sub> groups. This result demonstrated that the persistent –CH<sub>3</sub> groups are not incorporated in the film and do not necessarily lead to carbon impurities.

Overall, these results demonstrate that BB-SFG spectroscopy can be used to obtain fundamental insight into subtle and intricate elements of the surface chemistry of ALD. The combination of sub-monolayer sensitivity, inher-

ent surface selectivity, and relatively short acquisition times make BB-SFG spectroscopy ideally suited for mechanistic studies of ALD processes with metal-organic reactants.

## Acknowledgements

The authors would like to thank J.J.A. Zeebregts, J.J.L.M. Meulendijks, C.A.A. van Helvoirt, and C.O. van Bommel for their skillful technical support. This work was supported by the Dutch Technology Foundation STW and the Netherlands Organization for scientific Research (NWO, VICI Program on “Nanomanufacturing.”).

## 7.A Appendix

### Literature overview GPC(at)

The GPC(at) data taken from the literature and was summarized in Fig. 7.6 where the number of Al atoms deposited per cycle per surface area is plotted as a function of temperature. When Rutherford backscattering spectroscopy (RBS) data is available, the GPC(at) is known. For most other methods, the GPC(at) is determined from the GPC(nm) and the atomic density (Al atoms per volume). In most cases the GPC(nm) is determined with spectroscopic ellipsometry (SE) or X-ray reflectivity (XRR). The atomic density can be measured with for example XRR. On the other hand, the SE measurement used to determine the thickness also yields the refractive index. The density can be estimated from refractive index using the Lorentz-Lorenz or Clausius-Mossotti relations.<sup>8,29</sup> In some cases, depending on how the SE measurement was performed, there can be a strong correlation between the determined thickness and the refractive index. The data taken from Groner et al. shows an exceptionally high GPC(nm) and a relatively low refractive index.<sup>2</sup> These two parameters are strongly correlated in the SE measurement. Our hypothesis is that this correlation mistakenly lead to the high GPC(nm) and relatively low refractive index. This was compensated for by assuming the refractive index typically reported for these films and adjusting the GPC(nm) accordingly keeping the product of the two constant, see Fig. 7.6 (for the uncorrected data see Fig. 7.18). It is important to note that both the uncorrected and the corrected data taken from Groner et al. show a strong drop in Al atoms deposited per cycle with decreasing temperature.

### Reaction kinetics: standard models and the rate limiting step

The reaction kinetics observed in the H<sub>2</sub>O half-cycle during ALD were compared to several standard models. Most of these standard models, except most notably the first order Langmuir model, have a coverage dependent reaction cross section, and several of these models will be discussed here.<sup>51,52</sup> In some cases a model of the surface



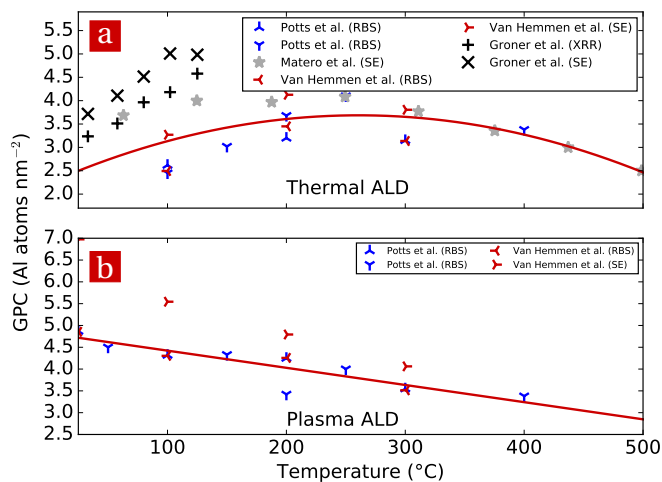


**Figure 7.18:** All data sets are the same as in Fig. 7.6 except for the GPC(at) from Groner et al..<sup>2</sup>

chemistry is related to a standard model of the reaction kinetics. For example, adsorption of  $O_2$  on Rh(111) can occur by a dissociative reaction ( $O_2(g) \rightarrow 2O(ads)$ ) or non-dissociative reaction ( $O_2(g) \rightarrow O_2(ads)$ ).<sup>51,53</sup> When first-order reaction kinetics are observed, this is evidence for the non-dissociative reaction in the Rh(111) case. Note that the observation of a certain type of reaction kinetics does not suggest a model of the surface chemistry by itself. For the reactions during the  $H_2O$  half-cycle, there are no clear cut models beyond the first-order reaction given in Eq. (7.1b). Nevertheless, it is important to be aware of the standard models and how they relate to the data. Once a clear model is available, and only then, can any conclusions be drawn from this comparison. The following standard models for reaction kinetics will be discussed:

- First, second, and third order reaction kinetics (Langmuir adsorption model)
- Second order reaction kinetics of dissociation with mobile dissociation products. These products can hop to the nearest neighbors.
- Precursor-mediated adsorption, with the gas-phase adsorbent first adsorbing in a “precursor” state which subsequently can desorb or adsorb.

Even more complex models (with more unknown variables) exist such as the Eley-Rideal (in short, a gas-phase molecule reacts directly with an adsorbed gas-phase molecule on the surface) and the Langmuir-Hinshelwood (in short, two gas-phase molecules absorb and react on the surface) mechanism,<sup>31</sup> but they are only in part applicable to the growth mechanism of ALD of  $Al_2O_3$ . For this discussion it is more convenient to work with sticking probability  $S(\theta, T)$  as a function of surface coverage  $\theta$  and temperature  $T$  than with the reaction cross section  $\sigma(\theta, T)$ . Historically the standard models are postulated in the context of sticking probability. Often the temperature dependence and the coverage dependence are assumed to be independent, with  $S(\theta, T) = AS(\theta)\exp(-E_{act}/k_B T)$  with  $A$  the pre-exponential factor and  $E_{act}$  the activation energy of the adsorption.

The Langmuir models can be described by a sticking probability of,<sup>51,52</sup>

$$S(\theta) = (1 - \theta)^n \quad (7.4)$$

with  $n$  the order of the reaction. To include dissociation to  $z$  nearest neighbors this is modified to,<sup>51,52</sup>

$$S(\theta) = \frac{z}{z - \theta} (1 - \theta)^n, \quad (7.5)$$

For a precursor-mediated adsorption (precursor as in “state” not in “molecule”), the sticking probability is given by,<sup>51,52</sup>

$$S(\theta) = \frac{(1 + K)(1 - \theta)^2}{1 + K(1 - \theta)^2} \quad (7.6)$$

with  $K = k_a/k_d$  the ratio of the adsorption and desorption rate coefficient. This precursor mediated mechanism can have 2 different activation energies, one for the precursor state and one for the adsorbent state.

For these models the corresponding saturation curve was calculated by (numerical) integration, see Fig. 7.19(a). For the Langmuir model with  $n > 1$  a more gradual decrease in  $\theta$  with time is observed than an exponential function. However, all curves have a similar time scale. The Langmuir model including the effect of dissociation to nearest neighbors (Langmuir-m in the figure) slightly deviates from the Langmuir model (an exponential decay). The precursor mediated model exhibits a shape quite similar to first order reaction kinetics. It is important to note that all of these models have a cross section that varies with surface coverage except for the Langmuir model with  $n = 1$ , see Fig. 7.19(b).

For the model to be viable, it has to explain both the reaction kinetics at low and high temperatures including the “persistent”  $-\text{CH}_3$  groups. This means that the model should accurately reproduce the shape of Fig. 7.12 and Fig. 7.11. Comparing the trends in the cross section as a function of  $\theta$  in Fig. 7.19(b) with Fig. 7.12 it is clear that the precursor mediated model and the Langmuir model taking nearest neighbors effects into account show an upward trend in the cross section which is not observed in the experimental data. The standard Langmuir model would describe the data if *both* the order of the reaction  $n$  and the time constant (not visible due to normalization) varied with temperature. At high temperatures, the experimental data can be represented by a first order reaction. The saturation curves and reaction cross section for ALD below 200 °C can be described by a second-order reaction of which the reactivity slows down with decreasing surface coverage and which is never driven to saturation for realistic  $\text{H}_2\text{O}$  dose times. As stated before, the observation that the experimental data can be described by a Langmuir model with a varying reaction order is in itself not a new insights into the growth mechanism. It is nothing more than a (mathematical) description of the experimental data.

Another possible mechanism that was ruled out was a change in the rate-limiting step during the  $\text{H}_2\text{O}$  half-cycle from mass-transport limited to reaction-limited. For the surface reaction, it is probable that the reaction rate is higher at high temperatures. Therefore, the consumption of the vapor phase  $\text{H}_2\text{O}$  is larger at high temperatures. Furthermore, the consumption of vapor phase  $\text{H}_2\text{O}$  is higher at the beginning of a half-cycle because there are more unreacted  $-\text{CH}_3$  groups on the surface. This means that the reactions are more likely mass transport limited at high temperatures and at the beginning of the half-cycle. If the reactions are indeed mass-transfer limited, this

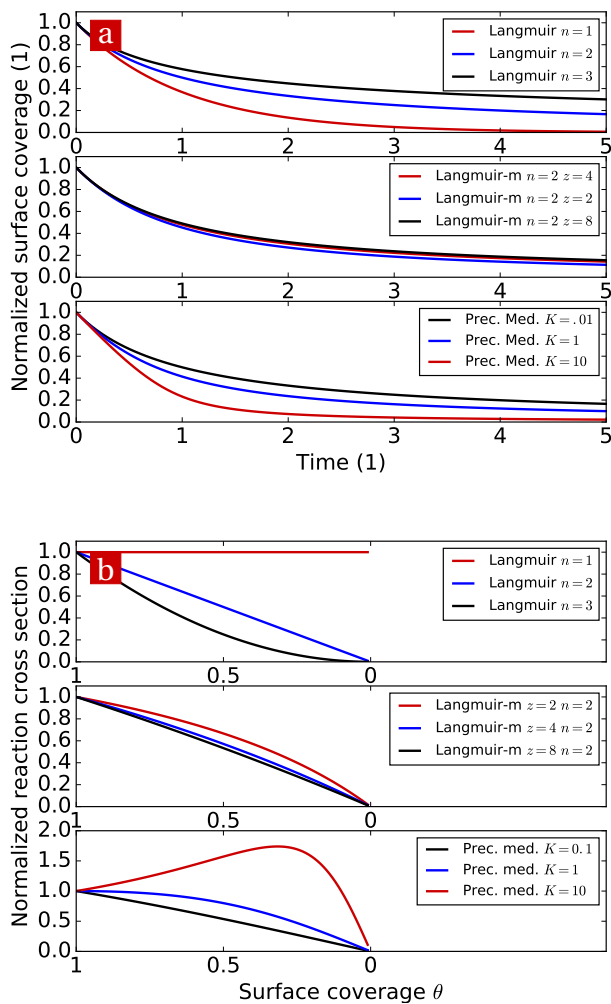


**Figure 7.19:** (a) The trend in the surface coverage  $\theta$  with time for different models describing the reaction kinetics. Langmuir-m is the Langmuir model taking into account adsorption with dissociation onto nearest neighbors. Prec. Med. is the precursor mediated model. (b) The reaction cross section as a function of surface coverage associated with the models.

effectively means that the flux  $\Gamma$  of  $\text{H}_2\text{O}$  was lower than estimated at the beginning of the  $\text{H}_2\text{O}$  half-cycle at high temperatures.<sup>1</sup> Compensating for this effect would skew the trends in Fig. 7.12 even further. Moreover, the mass-transfer limit can be ruled out as the rate-limiting step simply on basis of the temperature trend. The mass-transfer limit does not vary with temperature for a given flux. A strong increase in the reaction cross section was seen with temperature and therefore the mass-transfer limit cannot be the rate-limiting step at low temperatures.

---

<sup>1</sup>The flux  $\Gamma$  was calculated using the Hertz-Knudsen equation is inversely proportional to the square root of gas temperature  $T$  and proportional with pressure  $p$ , i.e.  $\Gamma \propto \frac{p}{\sqrt{T}}$

## Bibliography

- [1] Knoops, Langereis, van de Sanden, and Kessels. Conformality of Plasma-Assisted ALD: Physical Processes and Modeling. *Journal of The Electrochemical Society*, 2010. doi:[10.1149/1.3491381](https://doi.org/10.1149/1.3491381).
- [2] Groner, Fabreguette, Elam, and George. Low-Temperature Al<sub>2</sub>O<sub>3</sub> Atomic Layer Deposition. *Chemistry of Materials*, 2004. doi:[10.1021/cm0304546](https://doi.org/10.1021/cm0304546).
- [3] Potts, Keuning, Langereis, Dingemans, van de Sanden, and Kessels. Low Temperature Plasma-Enhanced Atomic Layer Deposition of Metal Oxide Thin Films. *Journal of The Electrochemical Society*, 2010. doi:[10.1149/1.3428705](https://doi.org/10.1149/1.3428705).
- [4] Mackus, Garcia-Alonso, Knoops, Bol, and Kessels. Room-Temperature Atomic Layer Deposition of Platinum. *Chemistry of Materials*, 2013. doi:[10.1021/cm400274n](https://doi.org/10.1021/cm400274n).
- [5] Higashi and Fleming. Sequential surface chemical-reaction limited growth of high-quality Al<sub>2</sub>O<sub>3</sub> dielectrics. *Applied Physics Letters*, 1989. doi:[10.1063/1.102337](https://doi.org/10.1063/1.102337).
- [6] Dillon, Ott, Way, and George. Surface chemistry of Al<sub>2</sub>O<sub>3</sub> deposition using Al(CH<sub>3</sub>)<sub>3</sub> and H<sub>2</sub>O in a binary reaction sequence. *Surface Science*, 1995. doi:[10.1016/0039-6028\(95\)90033-0](https://doi.org/10.1016/0039-6028(95)90033-0).
- [7] Ott, McCarley, Klaus, Way, and George. Atomic layer controlled deposition of Al<sub>2</sub>O<sub>3</sub> films using binary reaction sequence chemistry. *Applied Surface Science*, 1996. doi:[10.1016/S0169-4332\(96\)00503-X](https://doi.org/10.1016/S0169-4332(96)00503-X).
- [8] Ott, Klaus, Johnson, and George. Al<sub>2</sub>O<sub>3</sub> thin film growth on Si(100) using binary reaction sequence chemistry. *Thin Solid Films*, 1997. doi:[10.1016/S0040-6090\(96\)08934-1](https://doi.org/10.1016/S0040-6090(96)08934-1).
- [9] Puurunen. Surface chemistry of atomic layer deposition: A case study for the trimethylaluminum/water process. *Journal of Applied Physics*, 2005. doi:[10.1063/1.1940727](https://doi.org/10.1063/1.1940727).
- [10] Groner, Elam, Fabreguette, and George. Electrical characterization of thin Al<sub>2</sub>O<sub>3</sub> films grown by atomic layer deposition on silicon and various metal substrates. *Thin Solid Films*, 2002. doi:[10.1016/S0040-6090\(02\)00438-8](https://doi.org/10.1016/S0040-6090(02)00438-8).
- [11] Miikkulainen, Leskela, Ritala, and Puurunen. Crystallinity of inorganic films grown by atomic layer deposition: Overview and general trends. *Journal of Applied Physics*, 2013. doi:[10.1063/1.4757907](https://doi.org/10.1063/1.4757907).
- [12] Rahtu, Alaranta, and Ritala. In Situ Quartz Crystal Microbalance and Quadrupole Mass Spectrometry Studies of Atomic Layer Deposition of Aluminum Oxide from Trimethylaluminum and Water. *Langmuir*, 2001. doi:[10.1021/la010103a](https://doi.org/10.1021/la010103a).
- [13] Elam, Groner, and George. Viscous flow reactor with quartz crystal microbalance for thin film growth by atomic layer deposition. *Review of Scientific Instruments*, 2002. doi:[10.1063/1.1490410](https://doi.org/10.1063/1.1490410).
- [14] Vandalon and Kessels. What is limiting low-temperature atomic layer deposition of Al<sub>2</sub>O<sub>3</sub>? A vibrational sum-frequency generation study. *Applied Physics Letters*, 2016. doi:[10.1063/1.4939654](https://doi.org/10.1063/1.4939654).

- [15] Mackus, Weber, Thissen, Garcia-Alonso, Vervuurt, Assali, Bol, Verheijen, and Kessels. Atomic layer deposition of Pd and Pt nanoparticles for catalysis: on the mechanisms of nanoparticle formation. *Nanotechnology*, 2016. doi:[10.1088/0957-4484/27/3/034001](https://doi.org/10.1088/0957-4484/27/3/034001).
- [16] Shirazi and Elliott. Cooperation between adsorbates accounts for the activation of atomic layer deposition reactions. *Nanoscale*, 2015. doi:[10.1039/C5NR00900F](https://doi.org/10.1039/C5NR00900F).
- [17] van Hemmen, Heil, Klootwijk, Roozeboom, Hodson, van de Sanden, and Kessels. Plasma and Thermal ALD of  $\text{Al}_2\text{O}_3$  in a Commercial 200 mm ALD Reactor. *Journal of The Electrochemical Society*, 2007. doi:[10.1149/1.2737629](https://doi.org/10.1149/1.2737629).
- [18] Boyd. *Nonlinear optics*. Elsevier Science Publishing Co Inc, second edition, 1992.
- [19] Voges, Al-Abadleh, Musorrafiti, Bertin, Nguyen, and Geiger. Carboxylic Acid- and Ester-Functionalized Siloxane Scaffolds on Glass Studied by Broadband Sum Frequency Generation. *The Journal of Physical Chemistry B*, 2004. doi:[10.1021/jp046564x](https://doi.org/10.1021/jp046564x).
- [20] Rai, Vandalon, and Agarwal. Surface Reaction Mechanisms during Ozone and Oxygen Plasma Assisted Atomic Layer Deposition of Aluminum Oxide. *Langmuir*, 2010. doi:[10.1021/la101485a](https://doi.org/10.1021/la101485a).
- [21] Rai, Vandalon, and Agarwal. Influence of surface temperature on the mechanism of atomic layer deposition of aluminum oxide using an oxygen plasma and ozone. *Langmuir : the ACS journal of surfaces and colloids*, 2012. doi:[10.1021/la201136k](https://doi.org/10.1021/la201136k).
- [22] Kwon, Dai, Halls, and Chabal. Detection of a Formate Surface Intermediate in the Atomic Layer Deposition of High-k Dielectrics Using Ozone. *Chemistry of Materials*, 2008. doi:[10.1021/cm703667h](https://doi.org/10.1021/cm703667h).
- [23] Langereis, Keijmel, van de Sanden, and Kessels. Surface chemistry of plasma-assisted atomic layer deposition of  $\text{Al}_2\text{O}_3$  studied by infrared spectroscopy. *Applied Physics Letters*, 2008. doi:[10.1063/1.2940598](https://doi.org/10.1063/1.2940598).
- [24] Langereis, Bouman, Keijmel, Heil, Van de Sanden, and Kessels. Plasma-assisted ALD of  $\text{Al}_2\text{O}_3$  at Low Temperatures: Reaction Mechanism and Material Properties. *ECS Transactions*, 2008. doi:[10.1149/1.2980000](https://doi.org/10.1149/1.2980000).
- [25] Dingemans and Kessels. Status and prospects of  $\text{Al}_2\text{O}_3$ -based surface passivation schemes for silicon solar cells. *J. Vac. Sci. Technol. A*, 2012. doi:[10.1116/1.4728205](https://doi.org/10.1116/1.4728205).
- [26] Matero, Rahtu, Ritala, Leskela, and Sajavaara. Effect of water dose on the atomic layer deposition rate of oxide thin films. *Thin Solid Films*, 2000. doi:[10.1016/S0040-6090\(00\)00890-7](https://doi.org/10.1016/S0040-6090(00)00890-7).
- [27] Langereis, Heil, Knoops, Keuning, van de Sanden, and Kessels. In situ spectroscopic ellipsometry as a versatile tool for studying atomic layer deposition. *Journal of Physics D: Applied Physics*, 2009. doi:[10.1088/0022-3727/42/7/073001](https://doi.org/10.1088/0022-3727/42/7/073001).
- [28] Potts, Dingemans, Lachaud, and Kessels. Plasma-enhanced and thermal atomic layer deposition of  $\text{Al}_2\text{O}_3$  using dimethylaluminum isopropoxide,  $\text{Al}(\text{CH}_3)_2(\mu\text{-O}^i\text{Pr})_2$ , as an alternative aluminum precursor. *Journal*

- of Vacuum Science & Technology A: Vacuum, Surfaces, and Films*, 2012. doi:[10.1116/1.3683057](https://doi.org/10.1116/1.3683057).
- [29] Born and Wolf. *Principles of optics : electromagnetic theory of propagation, interference and diffraction of light*. Cambridge University Press, 1999.
- [30] Squire. Mechanistic studies of the decomposition of trimethylaluminum on heated surfaces. *Journal of Vacuum Science & Technology B: Microelectronics and Nanometer Structures*, 1985. doi:[10.1116/1.582976](https://doi.org/10.1116/1.582976).
- [31] Pooldt, van Lieshout, Illiberi, Knaapen, Roozeboom, and van Asten. On the kinetics of spatial atomic layer deposition. *Journal of Vacuum Science & Technology A: Vacuum, Surfaces, and Films*, 2013. doi:[10.1116/1.4756692](https://doi.org/10.1116/1.4756692).
- [32] Potts and Kessels. Energy-enhanced atomic layer deposition for more process and precursor versatility. *Coordination Chemistry Reviews*, 2013. doi:[10.1016/j.ccr.2013.06.015](https://doi.org/10.1016/j.ccr.2013.06.015).
- [33] Luo and Kerr. Bond dissociation energies. *CRC Handbook of Chemistry and Physics*, 2007.
- [34] Wilson, Decius, and Cross. *Molecular Vibrations*. Dover Publications Inc, 1980.
- [35] Du, Superfine, Freysz, and Shen. Vibrational spectroscopy of water at the vapor/water interface. *Physical Review Letters*, 1993. doi:[10.1103/PhysRevLett.70.2313](https://doi.org/10.1103/PhysRevLett.70.2313).
- [36] Miranda, Xu, Shen, and Salmeron. Icelike Water Monolayer Adsorbed on Mica at Room Temperature. *Physical Review Letters*, 1998. doi:[10.1103/PhysRevLett.81.5876](https://doi.org/10.1103/PhysRevLett.81.5876).
- [37] Boulesbaa and Borguet. Vibrational Dynamics of Interfacial Water by Free Induction Decay Sum Frequency Generation (FID-SFG) at the Al<sub>2</sub>O<sub>3</sub>(1120)/H<sub>2</sub>O Interface. *The Journal of Physical Chemistry Letters*, 2014. doi:[10.1021/jz401961j](https://doi.org/10.1021/jz401961j).
- [38] Maeda and Nakamura. Infrared spectroscopic study of hydrogenated and deuterated silicon nitride films prepared from plasma-enhanced deposition. *Journal of Applied Physics*, 1984. doi:[10.1063/1.333302](https://doi.org/10.1063/1.333302).
- [39] Bonn, Ueba, and Wolf. Theory of sum-frequency generation spectroscopy of adsorbed molecules using the density matrix method - broadband vibrational sum-frequency generation and applications. *Journal of Physics: Condensed Matter*, 2005. doi:[10.1088/0953-8984/17/8/002](https://doi.org/10.1088/0953-8984/17/8/002).
- [40] Groot, Kleyn, and Juurlink. Separating Catalytic Activity at Edges and Terraces on Platinum: Hydrogen Dissociation. *The Journal of Physical Chemistry C*, 2013. doi:[10.1021/jp401355c](https://doi.org/10.1021/jp401355c).
- [41] Tait, Dohnalek, Campbell, and Kay. N-alkanes on MgO(100). I. Coverage-dependent desorption kinetics of n-butane. *Journal of Chemical Physics*, 2005. doi:[10.1063/1.1883629](https://doi.org/10.1063/1.1883629).
- [42] Hopstaken and Niemantsverdriet. Structure sensitivity in the CO oxidation on rhodium: Effect of adsorbate coverages on oxidation kinetics on Rh(100) and Rh(111). *Journal of Chemical Physics*, 2000. doi:[10.1063/1.1289764](https://doi.org/10.1063/1.1289764).
- [43] Okada and George. Adsorption and desorption kinetics of tetrakis

- (dimethylamino) titanium and dimethylamine on TiN surfaces. *Applied surface science*, 1999. doi:[10.1016/S0169-4332\(98\)00375-4](https://doi.org/10.1016/S0169-4332(98)00375-4).
- [44] Weckman and Laasonen. First principles study of the atomic layer deposition of alumina by TMA-H<sub>2</sub>O-process. *Phys. Chem. Chem. Phys.*, 2015. doi:[10.1039/C5CP01912E](https://doi.org/10.1039/C5CP01912E).
- [45] Terry, Linford, Wigren, Cao, Pianetta, and Chidsey. Alkyl-terminated Si(111) surfaces: A high-resolution, core level photoelectron spectroscopy study. *Journal of Applied Physics*, 1999. doi:[10.1063/1.369473](https://doi.org/10.1063/1.369473).
- [46] Fidélis, Ozanam, and Chazalviel. Fully methylated, atomically flat (111) silicon surface. *Surface Science*, 2000. doi:[10.1016/S0039-6028\(99\)01065-1](https://doi.org/10.1016/S0039-6028(99)01065-1).
- [47] Dingemans, van Helvoirt, Pierreux, Keuning, and Kessels. Plasma-Assisted ALD for the Conformal Deposition of SiO<sub>2</sub>: Process, Material and Electronic Properties. *Journal of The Electrochemical Society*, 2012. doi:[10.1149/2.067203jes](https://doi.org/10.1149/2.067203jes).
- [48] Verlaan, van den Elzen, Dingemans, Van De Sanden, and Kessels. Composition and bonding structure of plasma-assisted ALD Al<sub>2</sub>O<sub>3</sub> films. *Physica Status Solidi (C) Current Topics in Solid State Physics*, 2010. doi:[10.1002/pssc.200982891](https://doi.org/10.1002/pssc.200982891).
- [49] Goldstein, McCormick, and George. Al<sub>2</sub>O<sub>3</sub> Atomic Layer Deposition with Trimethylaluminum and Ozone Studied by in Situ Transmission FTIR Spectroscopy and Quadrupole Mass Spectrometry. *The Journal of Physical Chemistry C*, 2008. doi:[10.1021/jp804296a](https://doi.org/10.1021/jp804296a).
- [50] Potts, Profijt, Roelofs, and Kessels. Room-Temperature ALD of Metal Oxide Thin Films by Energy-Enhanced ALD. *Chemical Vapor Deposition*, 2013. doi:[10.1002/cvde.201207033](https://doi.org/10.1002/cvde.201207033).
- [51] Oura, Katayama, Zotov, Lifshits, and Saranin. Elementary Processes at Surfaces I. Adsorption and Desorption. In *Surface Science*. Springer, 2003. doi:[10.1007/978-3-662-05179-5\\_12](https://doi.org/10.1007/978-3-662-05179-5_12).
- [52] Holloway. Dynamics of gas-surface reactions. *Surface Science*, 1994. doi:[10.1016/0039-6028\(94\)90687-4](https://doi.org/10.1016/0039-6028(94)90687-4).
- [53] Brault, Range, and Toennies. Molecular beam studies of sticking of oxygen on the Rh(111) surface. *The Journal of Chemical Physics*, 1997. doi:[10.1063/1.473951](https://doi.org/10.1063/1.473951).





# Surface chemistry during atomic-layer deposition of Pt studied with vibrational sum-frequency generation

## Abstract

The reaction mechanism of Pt atomic-layer deposition (ALD) from MeCpPtMe<sub>3</sub> and O<sub>2</sub> was investigated with vibrational broadband sum-frequency generation (BB-SFG) spectroscopy. This ALD process has been considered a model system for noble metal ALD. However, several questions remain about the underlying reaction mechanism. For example, it is not clear which species of hydrocarbon groups are present on the surface during ALD. In this work, direct evidence for the presence of CH<sub>3</sub> groups was found. Moreover, a contribution assigned to species containing C=C bonds was observed. This assignment was confirmed in a series of experiments exposing different surfaces (Pt and SiO<sub>2</sub>) to either the MeCpPtMe<sub>3</sub> precursor or to CH<sub>3</sub>-C<sub>5</sub>H<sub>7</sub>, a molecule similar to the MeCp ligand. For ALD at 250 °C, both the CH<sub>3</sub> and the C=C groups were observed on the surface after the precursor half-cycle and both were removed in the subsequent O<sub>2</sub> half-cycle. The relative CH<sub>3</sub> and C=C coverage after the precursor half-cycle was studied from 80 °C up to 300 °C. The CH<sub>3</sub> coverage showed a monotonic decrease with temperature whereas the C=C coverage was fairly constant. Furthermore, the reaction kinetics during the precursor half-cycle were studied, revealing that the saturation of C=C groups occurred ~ 3 times faster than that of the CH<sub>3</sub> groups. Both the temperature trend and the reaction kinetics are evidence of the dehydrogenation of some of the hydrocarbon species on the Pt surface during ALD.

## 8.1 Introduction

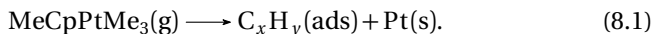
Ultrathin films or nanoparticles of noble metals have a wide range of (potential) applications because of the chemical stability, catalytic nature, and high work function of the noble metals.<sup>1-6</sup> Atomic-layer deposition (ALD) is gaining an increasing interest for the synthesis of these ultrathin films and nanoparticles because of its unique combination of capabilities. For example, ALD combines sub-nanometer thickness control with the capability to conformally coat complex 3D structures.<sup>5,7-10</sup>

Insight into the growth mechanism of these noble metal ALD processes is essential for extending the operating conditions or for enabling new applications. For example, once it was understood what was limiting Pt ALD at low temperatures, it was possible to modify the process by introducing a new step.<sup>11</sup> This resulted in the capability to deposit high quality material even at room temperature.<sup>11</sup> Moreover, the insight that these noble metal ALD processes depend on the catalytic nature of the surface for growth was exploited to make the Pt ALD process area selective.<sup>11</sup> These examples demonstrate that a fundamental and detailed understanding of the growth mechanism is paramount in developing these ALD processes further.

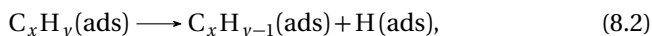
A model system for noble-metal ALD is the Pt ALD process using MeCpPtMe<sub>3</sub> as precursor and O<sub>2</sub>(g) as co-reactant. As such, the steady-state growth mechanism of this ALD process has been studied extensively. So far, the main emphasis has been on investigating the gas-phase reaction products of this process in detail.<sup>12-16</sup> Figure 8.1 shows the growth mechanism of the Pt ALD process as reported by Mackus *et al.* inferred from the gas-phase reaction products combined with insights from the field of surface science and catalysis.<sup>11</sup> Broadly speaking, at the beginning of the precursor half-cycle the Pt surface is covered to some extent by adsorbed O.<sup>8,12,17-21</sup> The MeCpPtMe<sub>3</sub> precursor adsorbs on this Pt surface and some of the ligands might detach from the Pt atom. It is possible that some of the ligand undergo a catalytic reaction with the Pt surface. Therefore, the term “fragments” is sometimes used instead of ligands. Overall, gas-phase CH<sub>4</sub>, CO<sub>2</sub>, and H<sub>2</sub>O are released but the majority of the precursor fragments remain on the surface as hydrocarbon species, C<sub>x</sub>H<sub>y</sub>, after the precursor half-cycle.<sup>12,14,16,21</sup> Even for this prototypical ALD process, direct evidence of the nature of the surface groups is lacking. Geyer *et al.* showed evidence for the presence of a carbonaceous layer after the precursor half-cycle with photoemission (PE) spectroscopy using synchrotron radiation.<sup>22</sup> They also showed that the carbonaceous layer was removed in the subsequent O<sub>2</sub> co-reactant half-cycle, however, the exact nature of the surface groups remained unclear.<sup>22</sup> In the co-reactant half-cycle, the surface is exposed to O<sub>2</sub>(g) which dissociates on the Pt surface and combusts the hydrocarbon species. Moreover, the adsorbed O is replenished after the co-reactant half-cycle.

Looking more closely at the precursor half-cycle, several key steps can be discerned. The precursor adsorbs onto the Pt surface and undergoes (partial)

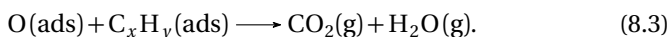
catalytic fragmentation forming  $C_xH_y$  groups on the surface.<sup>12,23</sup> Although the exact configuration of the Pt and the bonding of the ligands is not known, this reaction can be summarized as,



The hydrocarbon fragments can dehydrogenate on the catalytic Pt surface,<sup>12,23</sup>



increasing the amount of adsorbed H on the surface. The extent to which this dehydrogenation takes place is not known. For example, it is not clear if all precursor ligands undergo dehydrogenation reactions. In addition to the dehydrogenation reaction, the precursor fragments can react with other adsorbed species. If adsorbed O is present on the Pt surface the hydrocarbons can “combust” forming the aforementioned  $\text{CO}_2$  and  $\text{H}_2\text{O}$ . This reaction can be described by,<sup>12,23</sup>



Since the nature of the hydrocarbon species is not known, the reactions are not given as balanced equations. If adsorbed H is present, e.g. formed by the dehydrogenation reaction, the hydrocarbons can recombine with  $\text{H}(\text{ads})$  to a volatile reaction product. So far, the only hydrocarbon observed as a gas-phase reaction product is  $\text{CH}_4(\text{g})$ . Higher hydrocarbons (including the MeCp group) have not been observed as a gas-phase reaction product.<sup>12,16,21</sup> The formation of  $\text{CH}_4(\text{g})$  is the result of the following reaction,<sup>12,23</sup>



The reaction kinetics of the gas-phase products show that the formation of  $\text{CO}_2(\text{g})$  precedes the formation of  $\text{CH}_4(\text{g})$  during the precursor exposure.<sup>12</sup> This is in line with the hypothesis that dehydrogenation reactions take place on the surface (Eq. (8.2)). Quantitatively,  $\sim 9$  times more carbon is lost to the gas-phase as  $\text{CH}_4(\text{g})$  than to  $\text{CO}_2(\text{g})$ .<sup>12,16</sup> Saturation of the precursor half-cycle is apparently reached when a carbonaceous layer is formed that blocks further precursor adsorption.<sup>12,23</sup>

For the co-reactant half-cycle, the reaction mechanism relies on the catalytic nature of the Pt surface to dissociate molecular  $\text{O}_2$  to atomic O, making the O reactive enough for the combustion of the hydrocarbon species. It was postulated that at low temperatures this dissociation does not occur when the carbonaceous layer is present.<sup>12,23</sup> This has been ascribed to the blocking of the sites needed for dissociation of  $\text{O}_2(\text{g})$  at low temperatures by the carbonaceous layer, e.g. poisoning of the catalytic Pt surface.<sup>12,23</sup> For the temperatures at which dissociation does take place,  $\text{O}(\text{ads})$  is formed and the precursor fragments are combusted, as described by Eq. (8.3).<sup>12,23</sup> This results again in gas-phase  $\text{CO}_2(\text{g})$ , and vapor phase  $\text{H}_2\text{O}(\text{g})$ . No  $\text{CH}_4(\text{g})$  or higher hydrocarbons could be observed during the co-reactant half-cycle. Saturation is

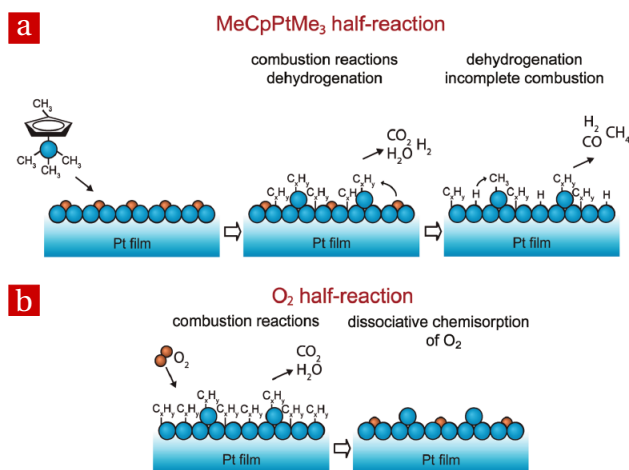


**Figure 8.1:** Schematic representation of the growth mechanism of Pt ALD using MeCpPtMe<sub>3</sub> as precursor and O<sub>2</sub> as co-reactant as proposed by Mackus et al. **(a)** At the start of the precursor half-cycle there is a significantly amount of adsorbed O on the surface. The precursor adsorbs on the Pt surface. This results in the deposition hydrocarbon species and Pt atoms. These hydrocarbon species are either dehydrogenated, combusted by O (ads) forming CO<sub>2</sub> and H<sub>2</sub>O, or released as CH<sub>4</sub>(g) to the gas-phase. **(b)** During the co-reactant half-cycle, molecular O<sub>2</sub> is dissociated on the catalytic Pt surface forming atomic O. The atomic oxygen combusts the hydrocarbons forming CO<sub>2</sub> and H<sub>2</sub>O. Furthermore, a significant amount of O (ads) remains on the surface after the co-reactant half-cycle. The figure was adapted from Mackus et al.<sup>23</sup>

reached when all the hydrocarbons have been removed from the Pt surface and O (ads) has been replenished.<sup>12,23</sup>

In this work, the surface chemistry of Pt ALD will be studied in more detail with vibrational broadband sum-frequency generation (BB-SFG) spectroscopy. BB-SFG spectroscopy is a nonlinear optical technique with sub-monolayer sensitivity and inherent surface selectivity. Surface groups can be identified and the (relative) density of surface groups can be determined *in-situ* during the ALD process. As such, BB-SFG spectroscopy was used to study the surface chemistry during ALD of Al<sub>2</sub>O<sub>3</sub> as discussed in this Thesis. For Pt ALD, the CH stretch region of the IR spectrum will be probed with BB-SFG spectroscopy during the ALD process. Both the reaction kinetics during the precursor half-cycle and the influence of temperature on the surface chemistry will be studied.

## 8.2 Sum-frequency generation

In the nonlinear optical process of sum-frequency generation (SFG), two light beams – with photon energy  $\hbar\omega_1$  and  $\hbar\omega_2$  – simultaneously interact with mat-

ter such as surface groups or the bulk of a material. This interaction induces a polarization  $\vec{P}(\omega_1 + \omega_2)$  in the matter which generates a new beam with a photon energy  $\hbar\omega_{sfg} = \hbar(\omega_1 + \omega_2)$ .<sup>24</sup> The relation between the polarization of the material  $\vec{P}$  and the strength of the electric field of the two driving beams  $\vec{E}_1$  and  $\vec{E}_2$  is given by,

$$\vec{P}(\omega_{sfg}) = \epsilon_0 \bar{\chi}^{(2)}(\omega_1, \omega_2) : \vec{E}_1, \vec{E}_2$$

with the  $\bar{\chi}^{(2)}$  tensor describing the second order susceptibility of the material which is a function of both  $\omega_1$  and  $\omega_2$ . From symmetry arguments it can be shown that the  $\bar{\chi}^{(2)}$  tensor has to be zero in the bulk of a centrosymmetric material. In these centrosymmetric materials, no SFG signal is generated.<sup>24</sup> On the other hand, the lower symmetry at a surface or an interface implies that the SFG process can occur there.<sup>24</sup> This makes SFG spectroscopy inherently surface selective for a centrosymmetric material such as *c*-Si and most amorphous materials.

In the case of *vibrational* SFG spectroscopy, the transitions between vibrational modes of e.g. surface groups are probed. Typical vibrational transitions have an energy matching photons in the mid-IR part of the spectrum, dictating the choice of photon energy for one of the two beams. For the other beam, visible light ( $\sim 800$  nm) is typically chosen and consequently the resulting SFG photons are also situated in the visible part of the spectrum.

In *broadband* vibrational sum-frequency generation (BB-SFG), a broadband mid-IR pulse of femtosecond duration is mixed with a spectrally narrow visible pulse (typically picosecond). This effectively probes a region ( $\sim 200\text{cm}^{-1}$ ) of the IR spectrum at once without having to change the central wavelength of the mid-IR laser. The vibrational information is now contained in the spectral shape of the visible SFG signal. The SFG response at a photon energy of  $\hbar\omega_{sfg}$  can be generated by multiple combinations of photon energy  $\hbar\omega_1$  and  $\hbar\omega_2$  contained in the driving beams. The response at  $\hbar\omega_{sfg}$  is now given by,

$$\vec{P}(\omega_{sfg}) = \epsilon_0 \int_0^\infty d\omega' \bar{\chi}^{(2)}(\omega', \omega_{sfg} - \omega') : \vec{E}(\omega'), \vec{E}(\omega_{sfg} - \omega'). \quad (8.5)$$

This equation can be simplified if the spectral width of visible beams is narrow compared to the IR beam and the resonances in  $\bar{\chi}$ . The integral can be dropped and the spectral response of the visible beam can be neglected, i.e.  $I_{vis}(\omega) = I_{vis}$ . The intensity  $I(\omega_{sfg})$  of the detected SFG signal can now be written as,

$$I(\omega_{sfg}) \propto |\vec{P}|^2 = |\epsilon_0 \bar{\chi}^{(2)}(\omega_{vis}, \omega_{sfg} - \omega_{vis})|^2 I_{vis} I_{ir}(\omega_{sfg} - \omega_{vis}). \quad (8.6)$$

This means that both the spectral shape of  $\bar{\chi}^{(2)}$  and that of the IR beam  $I_{ir}$  determine the shape of the final BB-SFG spectrum.

Equation (8.6) can be used to model the BB-SFG spectra as will be illustrated in Fig. 8.2. The second-order susceptibility can have non-resonant and

resonant contributions. A non-resonant contribution has an amplitude and phase that do not vary (strongly) with wavelength (see Fig. 8.2 (a)) and can be represented as a complex number. Conversely, a resonant contribution has an amplitude which peaks at a resonant frequency  $\omega_{res}$  (see Fig. 8.2 (a)) and its phase increases by  $\pi$  rad over the resonance (now shown). The spectral shape of a resonant contribution in the SFG spectra can be described by,

$$\bar{\chi}_{res}^{(2)}(\omega) = \frac{\rho A \exp(i\phi)}{\omega - \omega_{res} + i\Gamma} \quad (8.7)$$

with  $\rho$  the density of the surface group associated with the resonance,  $A$  the cross section of the contribution (roughly equal to the absorption cross section multiplied with the Raman cross section<sup>24,25</sup>),  $\phi$  the phase factor of the resonance, and  $\Gamma$  the spectral broadening of the resonance. The tensorial nature of  $\bar{\chi}^{(2)}$  was omitted for brevity. Note that the phase of the resonant signal is not equal to the phase factor  $\phi$ , but given by  $\phi - \arg(\omega - \omega_{res} + i\Gamma)$ . Figure 8.2 (a) shows an example of the spectral shape  $\bar{\chi}$  of both a resonant and a non-resonant contribution. The shape of the mid-IR beam  $I_{ir}$  is a property of the laser system and a typical shape can be seen in Fig. 8.2 (b). In the case that both a resonant and a non-resonant contribution are present, the combined response is a *coherent* (phase related) superposition of the two contribution multiplied with the spectral shape of the IR beam  $I_{ir}(\omega_{ir})$ . Therefore, the difference in phase between the two contributions influences the superposition. Two cases are illustrated in Fig. 8.2 showing the *in-phase* superposition (phase difference  $\phi \sim 0$ ) in panel (c) and the *out-of-phase* superposition (phase difference  $\phi \sim \pi$ ) in panel (d). These cases illustrate how the phase difference between the two contributions can significantly influence the shape of the BB-SFG spectra and such differences will actually be observed in the results presented in this work.

The measured BB-SFG spectra have to be deconvoluted by fitting a model to the data in order to quantify the relative surface coverage  $\rho$  of the surface groups. The spectra were modeled using the approach describe above, where the total response was given by  $\bar{\chi}^{(2)}(\omega) = \bar{\chi}_{NR}^{(2)} + \bar{\chi}_{res}^{(2)}(\omega)$ , with  $\bar{\chi}_{NR}^{(2)}$  a real number. The shape of the mid-IR beam was determined by fitting a spectrum that contained only a non-resonant contribution, e.g. a clean surface. The central position, broadening, and phase of the resonant contribution were determined from a spectrum with a strong resonant component and there parameters were fixed in subsequent fits. Then, the remaining spectra were fitted using a least-squares algorithm varying the amplitude of the non-resonant and resonant contributions.

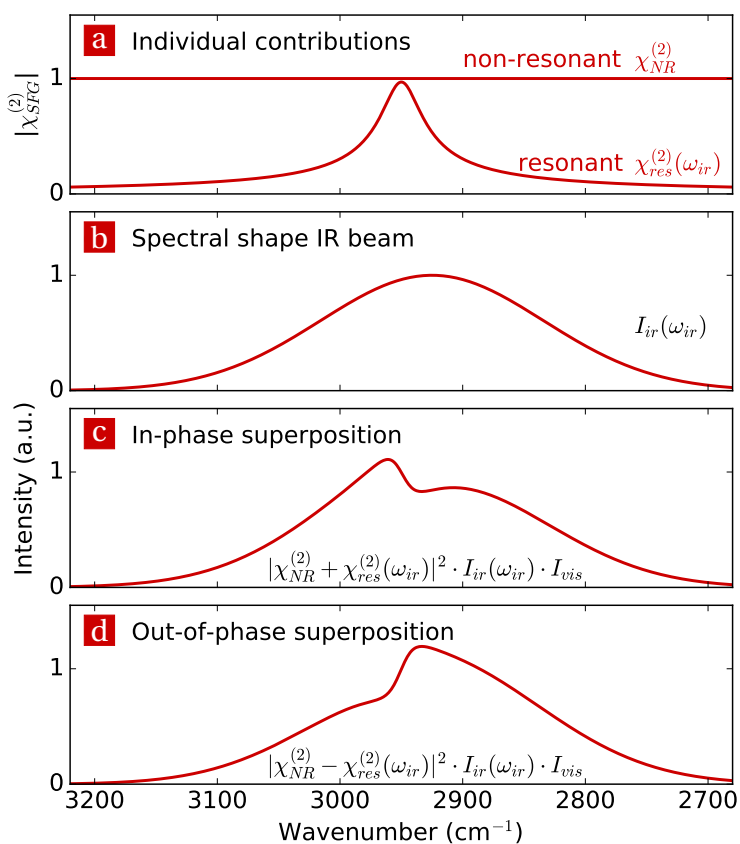


**Figure 8.2:** The shape of the BB-SFG response is affected by: **(a)** the spectral shape of the resonant contribution and a non-resonant contribution. **(b)** The spectral shape of the mid-IR beam used in the BB-SFG experiments. **(c)** The resulting BB-SFG response of an in-phase superposition of a resonant and a non-resonant contribution. **(d)** The same for a out-of-phase superposition.



## 8.3 Experimental details

### Experimental setup

All experiments were performed in a home built ALD chamber. The ALD chamber was equipped with two turbo-molecular pump (*Pfeiffer TMU 261P*) reaching a base pressure below  $1 \cdot 10^{-6}$  mbar. The MeCpPtMe<sub>3</sub> precursor (*Sigma-Aldrich* 98% purity) was vapor drawn (precursor temperature 70 °C, line temperature 80 °C). The flow of O<sub>2</sub>(g) gas was regulated by a needle valve and both precursor and co-reactant were dosed using ALD valves (*Swagelok 34C-A-GDFG-1KT*) driven by a computer controlled electronic relay (*National Instruments 9481*). For most experiments the relay is activated for 20 ms, which opened the ALD valve for the same duration. In some experiments, the relay was activated for 6 ms to admit just a small amount of precursor into the ALD chamber. If the relay is activated for a duration approaching the relay release and bounce time (better than 5 ms and 3 ms respectively), the exact pulse duration is no longer well defined. During the ALD cycles the chamber was continuously pumped, with a pressure varying between base pressure and  $\sim 1 \cdot 10^{-3}$  mbar (during the O<sub>2</sub>(g) pulse). The reactor walls were heated to 80 °C and the Si substrate was heated radiatively with a Boralectric heating element (*GE Advanced Ceramics ACSF0073 HTR1002*). A thermocouple (*Thermocoax 2ABAc05/1m/TI/FIM.K*) was glued to the back side of the sample with thermal paste (*RS 186-3600*). The sample temperature itself was computer controlled by modulating the power dissipation in the heating element with the measured temperature as input. This method of temperature control ensures a high accuracy (within 10 °C) which is important as temperature has a significant effect on the Pt ALD process.<sup>12,26</sup> The substrate was situated such that it can be studied with both *in-situ* spectroscopic ellipsometry (SE) and *in-situ* BB-SFG spectroscopy. For the *in-situ* SE measurements a *J. A. Woollam Co. M2000U* was used with a NIR extension (0.75-5.0 eV).

The BB-SFG setup was home built and consisted of a 90 fs solid-state laser system (*Spectra-Physics*) to generate the visible 795 nm beam and the tunable mid-IR beam operating around 3  $\mu$ m. The BB-SFG signal was detected with a liquid nitrogen cooled back-thinned CCD camera (*Princeton Instruments Spec-10*). For the Pt surfaces, *p*-polarized visible and mid-IR light was used to drive the SFG process. The *p*-polarized component of the SFG light was selected for detection using a polarizer (*Thorlabs GL10A*). Using the upper case letter *P* for the SFG light, this is denoted as the *Ppp* polarization combination (i.e. going from high to low photon energy). The *Ppp* polarization combination is the only combination allowed on the Pt surface due to the conductive nature of the film. For the SiO<sub>2</sub> surface the *Ssp* polarization combination was used since it is known to yield the strongest signals for e.g. CH<sub>3</sub> groups.<sup>27</sup> A more detailed description of the experimental setup is given in our earlier work.<sup>28</sup>

## Sample preparation

For both the BB-SFG and the SE experiments, two surfaces were studied: a Pt surface of a closed Pt film and a SiO<sub>2</sub> surface. Because of differences in the analysis techniques, slightly different samples were required.

For the SE measurements, the substrate consisted of a 2 inch Si(100) wafer. For the experiments on the SiO<sub>2</sub> surface, a 350 nm SiO<sub>2</sub> film was grown on top of the substrate by plasma-enhanced chemical vapor deposition (PE-CVD). This specific thickness was chosen for the best optical contrast for the SE measurement. For the experiments on the Pt surface, a second sample was prepared with the same procedure after which a ~ 30 nm Pt film was deposited on top of the SiO<sub>2</sub> film.

For the BB-SFG experiments, the substrate also consisted of a 2 inch Si(100) wafer. For the experiments on the SiO<sub>2</sub> surface, a ~ 90 nm SiO<sub>2</sub> film was grown on top of the substrate with PE-CVD. This specific SiO<sub>2</sub> thickness yields the strongest SFG signals for experiments on a Si substrate. For the experiments on the Pt surface, the SiO<sub>2</sub> layer was omitted and a thick Pt film was directly grown on top of the Si substrate. No optical enhancement of the SFG signal could be gained by adding a SiO<sub>2</sub> layer.

## 8.4 Results and discussion

### Characterization of the ALD process with in-situ spectroscopic ellipsometry

The Pt ALD process at 250 °C was characterized using *in-situ* SE. Figure 8.3 shows the thickness of the Pt film as a function of the number of ALD cycles for two different starting surfaces: a SiO<sub>2</sub> and Pt surface. Immediate growth was observed on the Pt surface with a growth-per-cycle (GPC) of ~ 0.6 Å, in line with the GPC reported in literature.<sup>26</sup> The growth on the SiO<sub>2</sub> surface showed a nucleation delay of ~ 100 ALD cycles after which steady-state growth was observed, again in line with what is reported for this ALD process in the literature.<sup>15</sup>

The influence of the precursor and co-reactant exposure on the GPC was investigated for steady-state growth on a thick Pt film. Saturation of the GPC was observed for a precursor exposure > 10 ms (see inset Fig. 8.3) and a co-reactant exposure > 20 ms (not shown). A pump down step of 45 s was performed after the precursor half-cycle and a pump down step of 30 s was used for the co-reactant half-cycle. The relatively long pump down steps were used to mimic the conditions under which the BB-SFG spectra would be collected. For this ALD process, typically a pump down or purge step in the order of 5 seconds is sufficient for either half-cycle.<sup>12,15,23,26</sup>

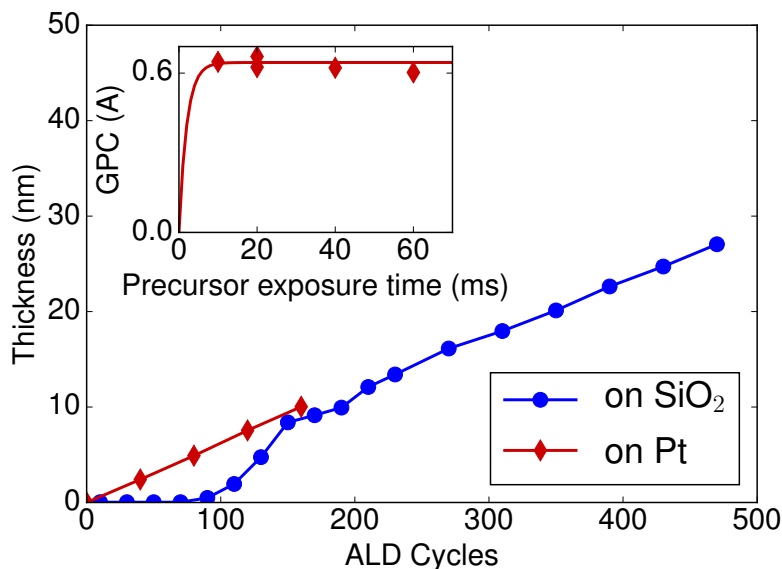


**Figure 8.3:** Thickness of the Pt film as a function of the number of ALD cycles measured with *in-situ* SE for ALD performed at 250 °C for two different starting surfaces: Pt and SiO<sub>2</sub>. The inset shows the saturation of the GPC of the precursor half-cycle for steady-state growth.

### BB-SFG spectra per half-cycle on Pt

The C-H stretch region was probed with BB-SFG spectroscopy during the steady-state growth of Pt ALD at 250 °C on a thick Pt film. Before recording the spectra, 5 Pt ALD cycles were performed to ensure steady state growth. Subsequently, the precursor was dosed, the reactor pumped down, and a BB-SFG spectrum was recorded. The same procedure was used for the co-reactant half-cycle. Figure 8.4 shows the BB-SFG spectra of the C-H stretch region recorded after the precursor and co-reactant half-cycle. The BB-SFG spectrum recorded after the O<sub>2</sub> half-cycle shows a single broad feature. The shape of this feature is typical for a non-resonant contribution probed with BB-SFG spectroscopy and its shape is related to the spectral shape of the mid-IR beam used in the experiment. To some extent, all metals have a non-resonant response. Therefore, this non-resonant contribution was assigned to the (thick) Pt film itself.<sup>24</sup> In the BB-SFG spectrum recorded after the precursor half-cycle, a large increase in the non-resonant contribution was observed. Moreover, a “dip” appeared in the spectrum. The overall shape is characteristic for the out-of-phase superposition of a resonant contribution and a non-resonant contribution (see also Fig. 8.2). The spectrum recorded after the precursor half-cycle was fitted and the spectral position of the resonant feature

was found to be  $2950\text{ cm}^{-1}$ . This is in agreement with the position reported for the C-H stretch mode of both the  $-\text{CH}_3$  groups of the MeCp ligand and  $\text{CH}_3(\text{ads})$  groups on a Pt surface.<sup>29,30</sup> Because the C-H stretch mode of both types of  $\text{CH}_3$  groups overlaps, it was not possible to differentiate between the two. From this point on, both these groups will be referred to as  $\text{CH}_3(\text{ads})$ . The H in the cyclopentadienyl ring ( $\text{C}_5\text{H}_4$ ) gives rise to a C-H stretch resonance which is situated at higher wavenumbers. Comparing the gas-phase IR spectra of cyclopentane, cyclopentene, and cyclopentadiene – see also supporting information – clearly shows that the C-H stretch mode of the  $\text{CH}_1$  groups is situated around  $\sim 3100\text{ cm}^{-1}$  (not observed).<sup>16,29</sup> The increase in the non-resonant contribution in Fig. 8.4 was assigned to C=C bonds deposited on the surface during the precursor half-cycle which will be justified in the next section.

From the spectra in Fig. 8.4 the following conclusions about the surface chemistry of the Pt ALD process at  $250\text{ }^\circ\text{C}$  can be drawn: Not all precursor ligands undergo dehydrogenation on the surface and a significant amount of  $\text{CH}_3$  groups remain on the surface as either  $-\text{CH}_3$  groups attached to the Pt surface or attached to the Cp ring. During the precursor half-cycle both the  $\text{CH}_3(\text{ads})$  groups and the C=C groups appear on the surface and these groups are removed in the subsequent co-reactant half-cycle.

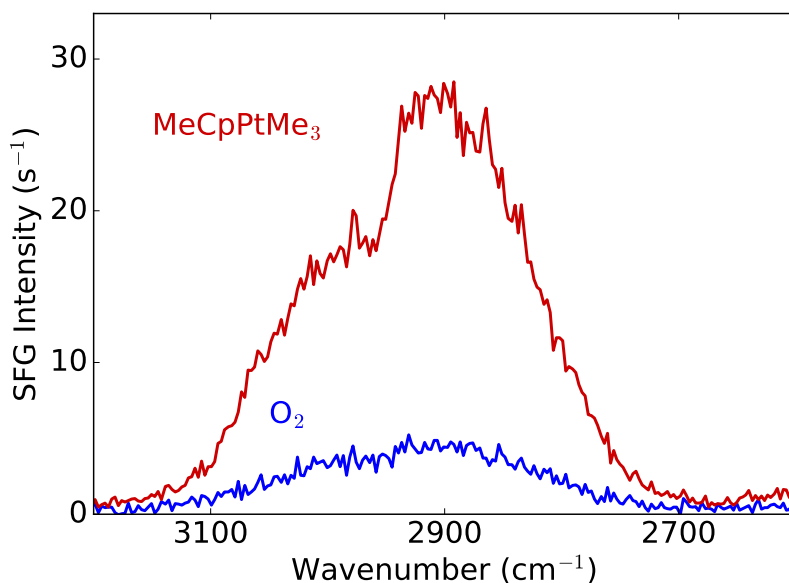


**Figure 8.4:** BB-SFG spectra of the C-H stretch region recorded at the end of the precursor ( $\text{MeCpPtMe}_3$ ) and co-reactant ( $\text{O}_2$ ) half-cycles during ALD at  $250^\circ\text{C}$ . Dosing the precursor resulted in an increase in the broad, i.e. “non-resonant”, feature with a out-of-phase resonant feature at  $2950\text{ cm}^{-1}$  superimposed on it.

## Interpretation of the non-resonant signals

Two different types of non-resonant signals were encountered: the non-resonant signal of a clean Pt surface after the co-reactant half-cycle and the *change* in this signal after the precursor half-cycle. The interpretation of the non-resonant signal after the co-reactant half-cycle was straightforward and the signal was attributed to the Pt metal itself. The cause of the change in the amplitude of the non-resonant contribution between the precursor and co-reactant half-cycle was less apparent and needs clarification. This change cannot be related to a change in the amount of Pt. The amount of Pt probed by BB-SFG is not changing since only the top part of the film was probed. Nor would it explain the decrease in the non-resonant signal after the co-reactant half-cycle since Pt is only added and not removed. The most likely causes of this change in the strength of the non-resonant contribution are: (1) A change in the Pt surface itself such as oxidation and reduction. (2) A precursor ligand or fragment which is added to and removed from the surface every ALD cycle. To test if the effect is solely caused by the Pt surface (cause (1)), the same ALD process was performed on a SiO<sub>2</sub> surface. Unlike the Pt film, the SiO<sub>2</sub> cannot be oxidized by O<sub>2</sub>(g) and it is unlikely that it is reduced by the precursor. It is also less likely that the precursor ligands, such as the Cp ring, will undergo structural changes due to the adsorption on the SiO<sub>2</sub> surface. Figure 8.5 shows BB-SFG spectra recorded before and after the SiO<sub>2</sub> surface was exposed to the precursor. Similar to the observations on the Pt surface, dosing the precursor on the SiO<sub>2</sub> surface resulted in an increase in the non-resonant contribution. Because the changing component of the non-resonant contribution was observed for both the Pt and the SiO<sub>2</sub> surface, it is not unique to the Pt surface and has to be related to (a part of) the precursor itself. Moreover, instead of the dip observed on the Pt surface a shoulder appeared at the same position. The shoulder on the SiO<sub>2</sub> surface was caused by the same resonant contribution assigned to CH<sub>3</sub>(ads) which caused the dip in the spectrum recorded on the Pt surface. The difference between the two cases is that on the Pt surface the two contributions are out-of-phase whereas on the SiO<sub>2</sub> surface they are in-phase. The observation of the same resonant signal on both the Pt surface and the SiO<sub>2</sub> surface is additional proof for its assignment to the CH<sub>3</sub>(ads) groups. It is unlikely that either the CH<sub>3</sub> or the MeCp ligand are altered upon chemisorption on the SiO<sub>2</sub> surface.

The methylcyclopentadienyl (C<sub>5</sub>H<sub>4</sub>CH<sub>3</sub><sup>-</sup>) ligand of the precursor warrants further investigation. The MeCp ligand might be the cause of the change in the non-resonant signal. The MeCp ligand or its fragments are deposited on the Pt surface in the precursor half-cycle and removed in the co-reactant half-cycle; in line with the appearance and disappearance of the non-resonant contribution on both the Pt and the SiO<sub>2</sub> surface. To test if the change in the non-resonant signal is caused by the MeCp ligand in the precursor, the state of the surface resulting from the adsorption of the MeCp ligand after precursor chemisorption has to be mimicked. Ideally, one would dose the MeCp ligand onto the Pt and the SiO<sub>2</sub> surfaces. However, the neutral form of the ligand

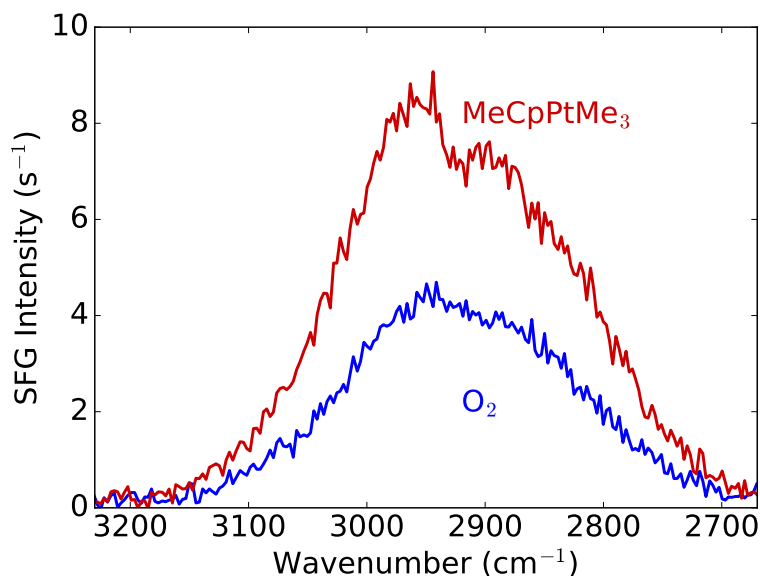


**Figure 8.5:** BB-SFG spectra of a  $\text{SiO}_2$  surface at  $80^\circ\text{C}$  before and after exposure to the Pt precursor using the Ssp polarization combination. The increase of the “non-resonant” contribution (broad feature) and the appearance of the “resonant” feature (shoulder) occur due to precursor exposure.

methylcyclopentadiene ( $\text{C}_5\text{H}_5\text{CH}_3$ ) was not suitable for this purpose since it only exists as a dimer. On the other hand, 1-methylcyclopentene ( $\text{C}_5\text{H}_7\text{CH}_3$ ) is stable in the gas-phase and is still quite similar to the methylcyclopentadienyl ligand (it has 3 additional H atoms resulting in only 1 instead of 2  $\text{C}=\text{C}$  bonds). Furthermore, it adsorbs onto the  $\text{SiO}_2$  and the Pt surface at all temperatures relevant for this work.<sup>31</sup> From this point on, the methylcyclopentene molecule will be referred to as “ $\text{Me}-\text{C}_5\text{H}_7$ ” to differentiate it from the MeCp ligand of the precursor. The  $\text{Me}-\text{C}_5\text{H}_7$  molecule was dosed onto two surfaces: a Pt surface and a  $\text{SiO}_2$  surface both at  $80^\circ\text{C}$ . Figure 8.6 shows the BB-SFG spectra recorded before and after the two surfaces were exposed to the  $\text{Me}-\text{C}_5\text{H}_7$  molecule. On both surfaces, an increase in the non-resonant contribution was observed after exposing the surface to the  $\text{Me}-\text{C}_5\text{H}_7$  molecule. At the same time, the dip / shoulder related to the  $\text{CH}_3(\text{ads})$  groups appeared on both surfaces. Again, the resonant contribution is in-phase with the non-resonant contribution on the  $\text{SiO}_2$  surface and out-of-phase on the Pt surface, mirroring the modeled spectra shown in Fig. 8.2. The similarity of the results for both the  $\text{MeCpPtMe}_3$  precursor and the  $\text{Me}-\text{C}_5\text{H}_7$  molecule on both surfaces strongly suggests that the cause of the changing non-resonant background is due to the MeCp ligand of the precursor. The MeCp ligand consists of two parts: the

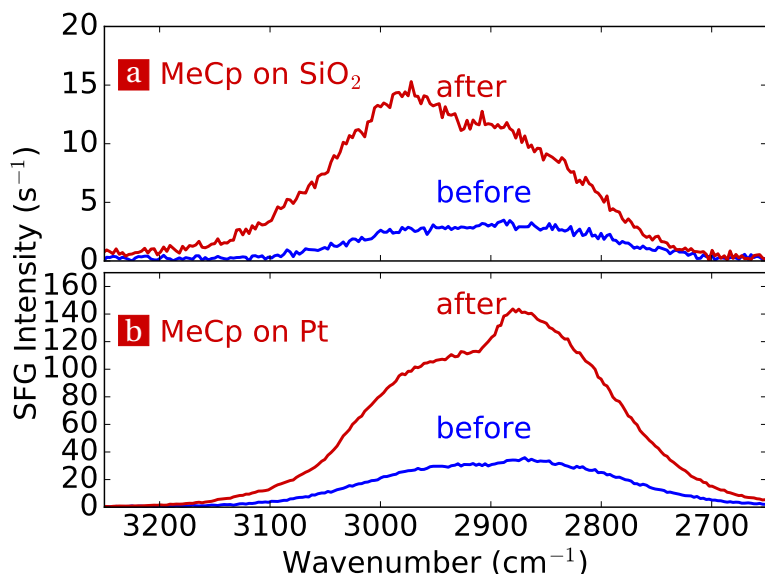


**Figure 8.6:** A comparison of the BB-SFG spectra probing the C-H stretch region on a  $\text{SiO}_2$  and a Pt substrate at  $80^\circ\text{C}$  exposed to  $\text{Me}-\text{C}_5\text{H}_7$ . Both spectra are very similar to those obtained with the Pt precursor,  $\text{MeCpPtMe}_3$ , on both Pt and  $\text{SiO}_2$  as can be seen in Fig. 8.4 and Fig. 8.5.

$\text{CH}_3$  group and the Cp ring. It is not expected that the  $\text{CH}_3$  groups (present in both the precursor and  $\text{Me}-\text{C}_5\text{H}_7$  molecule) are the cause of the change of the non-resonant contribution. Such an effect was not observed in, for example, thermal ALD of  $\text{Al}_2\text{O}_3$  using  $\text{Al}(\text{CH}_3)_3$  and  $\text{H}_2\text{O}$ .<sup>32</sup> This leaves the Cp ring as the likely origin of the change in the non-resonant contribution. On the  $\text{SiO}_2$  surface it is quite likely that the Cp ring remains unchanged after adsorption. However, on the Pt surface the Cp ring might undergo structural changes due to the catalytic nature of the Pt. From the similarity in the shape, position, or amplitude between the spectra no conclusions can be drawn about the state of the ring because it concerns a non-resonant contribution. Whether the ring has undergone ring-opening or not, in both cases unsaturated carbon-carbon bonds are present that are known for their large non-linear response.<sup>24,33</sup> This has led us to assign the changing part of the non-resonant contribution to  $\text{C}=\text{C}$  bonds present in the  $\text{MeCpPtMe}_3$  precursor and the  $\text{Me}-\text{C}_5\text{H}_7$  molecule. Hence, the changing non-resonant contribution could be seen as an indication that groups with  $\text{C}=\text{C}$  bonds are present on the surface, not necessarily in the form of Cp.

An additional check was performed using the  $\text{Me}-\text{C}_5\text{H}_7$  molecule to confirm the non-resonant nature of  $\text{C}=\text{C}$  contribution. If the broad feature is a

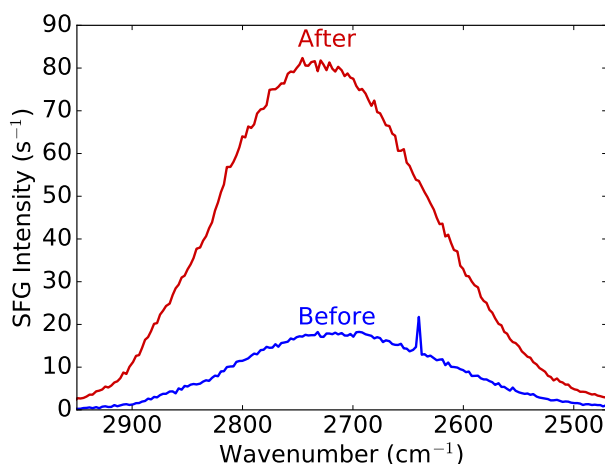


**Figure 8.7:** BB-SFG response of the Pt surface before and after Me-C<sub>5</sub>H<sub>7</sub> exposure in a part of the spectrum in which no “resonant” contributions are expected. Exposing the Pt surface to Me-C<sub>5</sub>H<sub>7</sub> also results in a significant increase in the amplitude of the “non-resonant” SFG signal in this part of the IR spectrum. This demonstrates that the “non-resonant” contribution is spectrally broad and spans at least from 3100 cm<sup>-1</sup> till 2650 cm<sup>-1</sup>. Note that the spectral shape reflects the spectral shape of the driving mid-IR beam which is also typical for a “non-resonant” contribution.

true non-resonant contribution the same response should be observed over a wide spectral range. Figure 8.7 shows the BB-SFG response around 2700 cm<sup>-1</sup> with spectra recorded before and after exposing the Pt surface to the Me-C<sub>5</sub>H<sub>7</sub> molecule. Apart from the resonant CH<sub>3</sub>(ads) contribution, the same behavior was observed in this part of the spectrum as was observed in the C-H stretch region: An increase in the non-resonant contribution was evident after dosing the Me-C<sub>5</sub>H<sub>7</sub> molecule on the Pt surface. This means that the non-resonant contribution is present from <2650 cm<sup>-1</sup> to >3100 cm<sup>-1</sup>.

### Surface termination as a function of temperature

The surface termination after the precursor half-cycle was studied with BB-SFG spectroscopy for temperatures ranging between 80 °C and 300 °C. For each temperature, the Pt surface was cleaned at high temperature (~ 300 °C) with a long O<sub>2</sub>(g) exposure. Then the sample was allowed to cool down to the appropriate temperature, exposed to precursor, and a BB-SFG spectrum was recorded. Figure 8.8 shows the BB-SFG spectra recorded after the precursor half-cycle at the different temperatures. All of the spectra show the typical shape indicative of precursor absorption with the coherent superposition of a resonant signal related to the CH<sub>3</sub>(ads) groups and the non-resonant signal related to the C=C groups. The strength of the CH<sub>3</sub>(ads) signal gradually



decreases with temperature, while the C=C signal remains relatively constant. Figure 8.9 shows the relative CH<sub>3</sub>(ads) and C=C coverage as a function of temperature obtained from the fit to the spectra in Fig. 8.8. From 80 °C up to 300 °C a monotonic decrease in CH<sub>3</sub>(ads) coverage was observed while the C=C coverage was fairly constant.

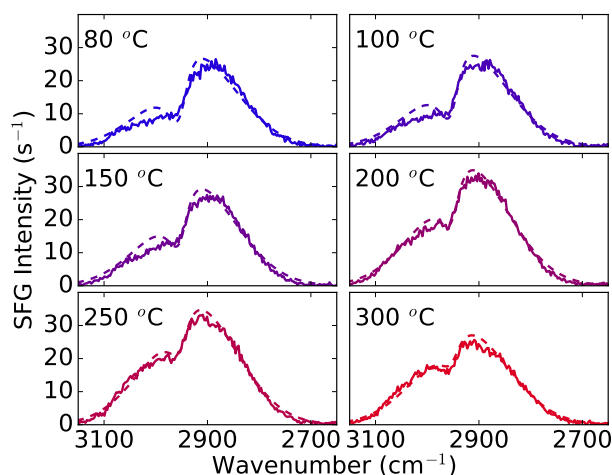


**Figure 8.8:** BB-SFG spectra obtained after precursor dose on a thick Pt film for a substrate temperature ranging from 80 °C up to 300 °C. The dashed lines are the fits to the data.

Figure 8.8 and Fig. 8.9 show that the MeCpPtMe<sub>3</sub> precursor adsorbs on the surface at temperatures ranging from 80 °C up to 300 °C. Therefore, precursor absorption is not the limiting step at low temperatures. This is in line with the observation that the related plasma ALD process for Pt, using the same precursor, has been demonstrated to work at temperatures as low as room temperature.<sup>11</sup> The decreasing CH<sub>3</sub>(ads) coverage with increasing temperature, observed in Fig. 8.9, might suggest a more efficient dehydrogenation of CH<sub>3</sub>(ads) at higher temperatures. This observation is in line with the trend reported in surface science for the dehydrogenation of CH<sub>3</sub> adsorbed on Pt(111) and Pt(110) into CH<sub>1</sub>.<sup>34-36</sup>

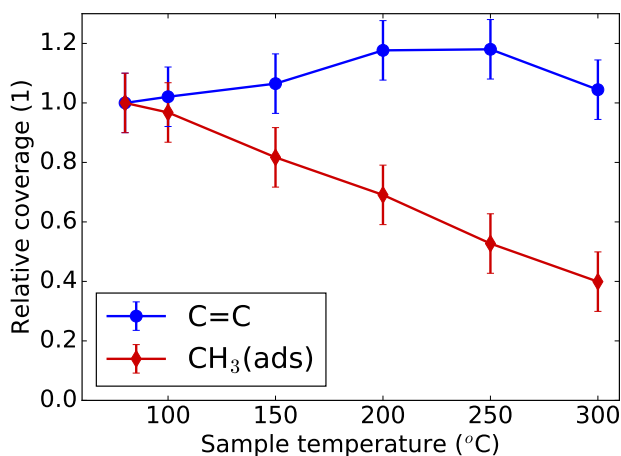


**Figure 8.9:** The trend in the relative coverage of the CH<sub>3</sub>(ads) (either bonded to Pt or to the Cp ring) and C=C groups with temperature. This data was obtained from a fit of the BB-SFG spectra in Fig. 8.8 and normalized to the coverage at the lowest temperature.

### Reaction kinetics during the precursor half-cycle

The reaction kinetics of the precursor half-cycle of ALD at 250 °C was studied to reveal is the surface chemistry changes during the precursor adsorption. The Pt surface was prepared by performing five ALD cycles to ensure steady-state growth. After the O<sub>2</sub>(g) half-cycle of the fifth ALD cycle, a BB-SFG spectrum was recorded. To study the reaction kinetics, instead of dosing one longer precursor exposure, multiple short exposures were performed. The SE measurements showed that a single ~ 10 ms precursor exposure was sufficient for saturation. Therefore, using the standard ≥ 10 ms pulses did not yield enough insight into the reaction kinetics. By activating the electronic relay which was driving the ALD valve for 6 ms, a small amount of precursor was allowed to enter the ALD chamber. This was estimated to be equivalent to a ~1 ms exposure judging from the number of pulses needed to reach saturation. After 11 of these “short” exposures, two 20 ms exposures were performed. The first of the 20 ms exposures was intended to ensure saturation. The second 20 ms exposure should confirm saturation and provide an indication of measurement uncertainty. After each precursor exposure, a BB-SFG spectrum was collected, resulting in the spectra shown in Fig. 8.10. Quantifying the relative CH<sub>3</sub>(ads) and C=C coverage by fitting the spectra in Fig. 8.10 resulted in Fig. 8.11. Both the CH<sub>3</sub>(ads) and the C=C coverage increased gradually with precursor exposure. Comparing the C=C coverage after the first 11 exposures with the coverage of the two long exposures did indeed confirm saturation. The CH<sub>3</sub>(ads) coverage did not yet reach saturation after the 11 short expo-

sure. It is peculiar that the two contributions show a difference in saturation behavior and this points towards a complex reaction mechanism.

The trends in the  $\text{CH}_3(\text{ads})$  and  $\text{C}=\text{C}$  coverage, shown in Fig. 8.11, were modeled assuming first-order reaction kinetics although this is obviously an oversimplification. Both data sets were fitted with a single exponential function  $(1 - \exp(-t/\tau))$ , shown as the solid lines in Fig. 8.11. The time constants obtained from this fit were  $\tau = 4$  ms for the  $\text{C}=\text{C}$  contribution and  $\tau = 13$  ms to the  $\text{CH}_3(\text{ads})$  contribution. Because the exposure time for the first 11 data points has a large uncertainty, the absolute value of these time constants is not reliable. However, the ratio of the time constants is not affected by this effect and the  $\text{C}=\text{C}$  contribution reached saturation roughly  $\sim 3$  times faster than the  $\text{CH}_3(\text{ads})$  contribution.

As stated, describing the reactions as first-order is an oversimplification. The reaction kinetics of the Pt ALD process are very likely more complex. Not only are there multiple competing reaction paths (see Eq. (8.2), Eq. (8.3), and Eq. (8.4)), it is also already known that the most prominent reaction path changes during the precursor half-cycle since more  $\text{CO}_2$  is formed at the beginning of the half-cycle due to the depletion of O adsorbed on the surface. On top of that, the build up of the hydrocarbon species including the  $\text{CH}_3(\text{ads})$  groups are very likely to change the chemistry near saturation.<sup>37,38</sup> These effects are probably for a large part responsible for the discrepancies between the modeled first-order reaction kinetics and the data. The peculiar observation that the  $\text{CH}_3(\text{ads})$  buildup is slower than the  $\text{C}=\text{C}$  buildup suggests that initially most of the precursor ligands undergo dehydrogenation or combustion and that these reaction paths are quenched near saturation. This would be in agreement with the quenched dehydrogenation on Pt(111) of e.g. cyclopentene at high surface coverages.<sup>37,38</sup>

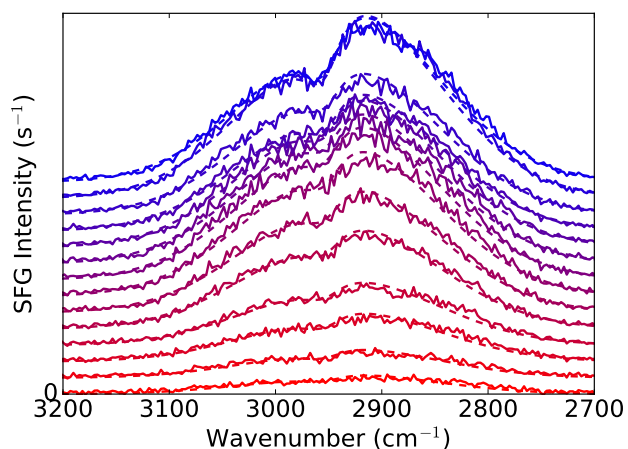


**Figure 8.10:** BB-SFG spectra of the C-H stretch region obtained for sequential precursor exposures revealing the reaction kinetics during ALD at 250 °C. Each spectrum has been offset for clarity, the dashed lines are fits to the data.

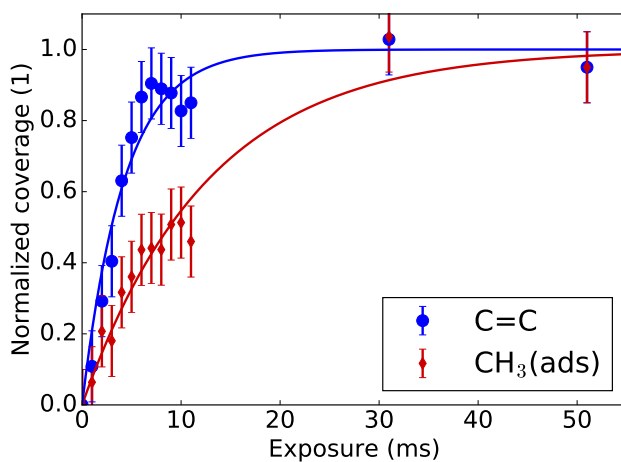


**Figure 8.11:** The trends in the relative coverage of the CH<sub>3</sub>(ads) (either bonded to Pt or to the Cp ring) and C=C groups obtained from fits in Fig. 8.10. The effective exposure time for the data points below 11 ms were estimated. The last two exposures had a duration of 20 ms. The solid lines are first-order reaction kinetics fitted to the data.

## 8.5 Discussion of the reaction mechanism

The insights obtained in this work lead to a new insights into the growth mechanism of Pt ALD using MeCpPtMe<sub>3</sub> as precursor and O<sub>2</sub> as co-reactant. This refined mechanism is shown graphically in Fig. 8.12.

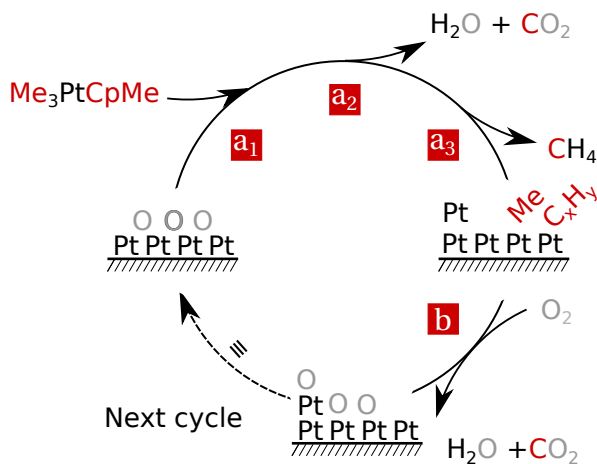


**Figure 8.12:** The key features of the reaction mechanism of Pt ALD using MeCpPtMe<sub>3</sub> and O<sub>2</sub>(g) as precursor and co-reactant, respectively. At the beginning of the Pt half-cycle, there is a significant amount of atomic O adsorb on the Pt surface. (a1) The MeCpPtMe<sub>3</sub> precursor adsorbs on this surface. (a2) Some of the ligands are combusted to CO<sub>2</sub>(g) and H<sub>2</sub>O(g) by the adsorbed atomic O. Other ligands either remain intact or dehydrogenate to form adsorbed C<sub>x</sub>H<sub>y</sub> and H. (a3) Some of the fragments recombine with adsorbed H on the surface to form CH<sub>4</sub>(g). In the co-reactant half-cycle, molecular O<sub>2</sub>(g) dissociates on the catalytic Pt surface and reacts with the remaining hydrocarbon groups forming CO<sub>2</sub>(g) and H<sub>2</sub>O(g). Furthermore, the surface is saturated with atomic O adsorbed on the surface.

In the precursor half-cycle, the MeCpPtMe<sub>3</sub> molecule absorbs onto the surface and might fragment. Some of the precursor ligands may undergo dehydrogenation. However, CH<sub>3</sub>(ads) groups were observed during and after the precursor half-cycle. Therefore it has become clear that not all precursor ligands undergo dehydrogenation and that CH<sub>3</sub> and C=C groups remain on the surface. The reaction kinetics of the CH<sub>3</sub>(ads) and C=C groups on the surface during the precursor half-cycle emphasize that the reaction mechanism is quite complex. Multiple reactions compete for the same hydrocarbon species on the surface and the balance between these reactions changes dur-

ing the precursor half-cycle. The relative coverage of the  $\text{CH}_3(\text{ads})$  groups decreases with increasing temperature, while the relative coverage of the  $\text{C}=\text{C}$  groups remains constant. This observation is in line with a more efficient dehydrogenation reported in the surface science literature for Pt(111) and Pt(110) at higher temperatures.

During the co-reactant half-cycle, molecular  $\text{O}_2(\text{g})$  gas is dissociated on the Pt surface. At low temperatures ( $< 200\text{ }^\circ\text{C}$ ) this dissociation does not occur when the carbonaceous layer is present, i.e. multiple cycles of ALD are not possible. Both the  $\text{CH}_3(\text{ads})$  and  $\text{C}=\text{C}$  groups are removed from the surface at sufficiently high temperatures. Absorbed O remains on the surface which is consumed in the subsequent precursor half-cycle.

## 8.6 Conclusion

The reaction mechanism of Pt ALD using  $\text{MeCpPtMe}_3$  and  $\text{O}_2(\text{g})$  gas was investigated with BB-SFG spectroscopy. Direct evidence for the presence of  $\text{CH}_3(\text{ads})$  on the surface after the precursor exposure was presented. This indicated that not all precursor ligands undergo dehydrogenation reactions. The precursor also induced a change in the non-resonant contribution of the BB-SFG signal which was investigated further. It was deduced that this change in the non-resonant signal originated from precursor fragments containing  $\text{C}=\text{C}$  bonds by a series of experiments exposing either a  $\text{SiO}_2$  or a Pt surface to the  $\text{MeCpPtMe}_3$  precursor or the  $\text{Me}-\text{C}_5\text{H}_7$  molecule. The reaction kinetics and the temperature dependence of the surface species during the precursor half-cycle were also studied with BB-SFG. This provided a more detailed picture of the reactions occurring during the precursor half-cycle and illustrated the complexity of this growth mechanism. Furthermore, this work demonstrates the viability of BB-SFG spectroscopy for studying the steady-state growth mechanism of the noble metal ALD processes.

## Acknowledgements

The authors would like to thank J.J.A. Zeebregts, J.J.L.M. Meulendijks, C.A.A. van Helvoirt, and C.O. van Bommel for their skillful technical support. This work was supported by the Dutch Technology Foundation STW and the Netherlands Organization for scientific Research (NWO, VICI Program on “Nanomanufacturing.”).

## 8.A Appendix

## Trend in the CH stretch modes of Cp molecules

Different species of Cp rings exist which are hydrogenated in various degrees which influences the spectral response of these molecules in the mid-IR part of the spectrum. Here, we will focus on the CH stretching modes of these molecules. The spectral response of the fully hydrogenated Cp ring cyclopentane ( $C_5H_{10}$ ) which has only  $CH_2$  groups, only shows the  $CH_2$  stretch modes. For this Cp ring, all stretch modes are below  $3000\text{ cm}^{-1}$ . For Cp rings which have double bonds and therefore are hydrogenated to a lesser degree, also  $CH_1$  groups are part of the ring. Because of the more rigid backbonding of these  $CH_1$  groups the CH stretch mode shifts to above  $3000\text{ cm}^{-1}$ . This is illustrated in Fig. 8.13 which shows the gas-phase absorbance in the C-H stretch region for a series of Cp rings. The feature above  $3000\text{ cm}^{-1}$  only appears for Cp rings which are not fully hydrogenated. The ratio between the intensity of the  $CH_2$  modes below  $3000\text{ cm}^{-1}$  and  $CH_1$  modes above  $3000\text{ cm}^{-1}$  increases going from cyclopentadiene ( $C_5H_6$ ) going to cyclopentane ( $C_5H_{10}$ ). For comparison 1-methylcyclopentene ( $CH_3-C_5H_7$ ) is also included in the figure. The Pt precursor  $MeCpPtMe_3$  has a Cp ring with 4 hydrogen atoms and a  $CH_3$  group attached to it. Hence, it will show similarities to cyclopentadiene and 1-methylcyclopentene.

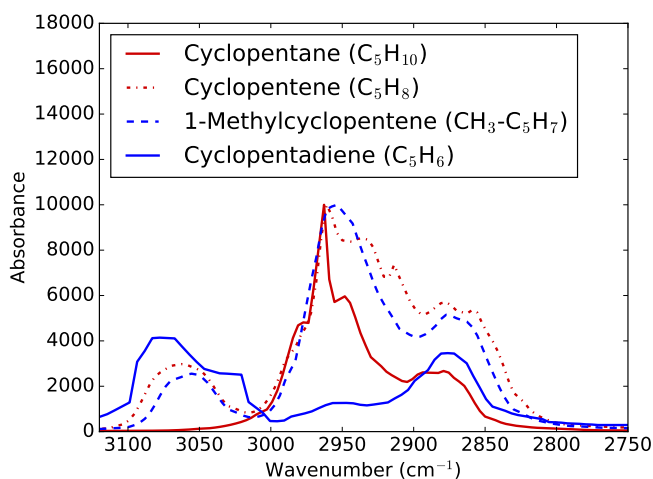


**Figure 8.13:** Gas phase absorbance spectra of the CH stretch region for 3 different Cp rings with a varying number of H atoms and a Cp ring with a methyl groups. For the molecule with only  $CH_2$  groups, the  $CH_1$  stretch mode at  $3060\text{ cm}^{-1}$  is absent. All other molecules have 1 or more  $CH_1$  groups and show this mode. Data taken from NIST.<sup>29</sup>

## Bibliography

- [1] Albert, Lewis, Schauer, Sotzing, Stitzel, Vaid, and Walt. Cross-reactive chemical sensor arrays. *Chemical Reviews*, 2000. doi:[10.1021/cr980102w](https://doi.org/10.1021/cr980102w).
- [2] Xue, Chen, Ma, Xing, Chen, Wang, and Wang. One-step synthesis and gas-sensing characteristics of uniformly loaded Pt@SnO<sub>2</sub> nanorods. *Journal of Physical Chemistry C*, 2010. doi:[10.1021/jp908343r](https://doi.org/10.1021/jp908343r).
- [3] Comstock, Christensen, Elam, Pellin, and Hersam. Tuning the composition and nanostructure of Pt/Ir films via anodized aluminum oxide templated atomic layer deposition. *Advanced Functional Materials*, 2010. doi:[10.1002/adfm.201000389](https://doi.org/10.1002/adfm.201000389).
- [4] Enterkin, Setthapun, Elam, Christensen, Rabu, Marks, Stair, Poepelmeier, and Marshall. Propane Oxidation over Pt/SrTiO<sub>3</sub> Nanocuboids. *ACS Catalysis*, 2011. doi:[10.1021/cs200092c](https://doi.org/10.1021/cs200092c).
- [5] Mackus, Weber, Thissen, Garcia-Alonso, Vervuurt, Assali, Bol, Verheijen, and Kessels. Atomic layer deposition of Pd and Pt nanoparticles for catalysis: on the mechanisms of nanoparticle formation. *Nanotechnology*, 2016. doi:[10.1088/0957-4484/27/3/034001](https://doi.org/10.1088/0957-4484/27/3/034001).
- [6] Vervuurt, Sharma, Jiao, Kessels, and Bol. Area-selective atomic layer deposition of platinum using photosensitive polyimide. *Nanotechnology*, 2016. doi:[10.1088/0957-4484/27/40/405302](https://doi.org/10.1088/0957-4484/27/40/405302).
- [7] George. Atomic layer deposition: an overview. *Chemical reviews*, 2010. doi:[10.1021/cr900056b](https://doi.org/10.1021/cr900056b).
- [8] Mackus, Verheijen, Leick, Bol, and Kessels. Influence of Oxygen Exposure on the Nucleation of Platinum Atomic Layer Deposition: Consequences for Film Growth, Nanopatterning, and Nanoparticle Synthesis. *Chemistry of Materials*, 2013. doi:[10.1021/cm400562u](https://doi.org/10.1021/cm400562u).
- [9] Dendooven, Ramachandran, Devloo-Casier, Rampelberg, Filez, Poelman, Marin, Fonda, and Detavernier. Low-temperature atomic layer deposition of platinum using (methylcyclopentadienyl)trimethylplatinum and ozone. *Journal of Physical Chemistry C*, 2013. doi:[10.1021/jp403455a](https://doi.org/10.1021/jp403455a).
- [10] Hamalainen, Munnik, Ritala, and Leskela. Atomic Layer Deposition of Platinum Oxide and Metallic Platinum Thin Films from Pt(acac)<sub>2</sub> and Ozone. *Chemistry of Materials*, 2008. doi:[10.1021/cm801187t](https://doi.org/10.1021/cm801187t).
- [11] Mackus, Garcia-Alonso, Knoops, Bol, and Kessels. Room-Temperature Atomic Layer Deposition of Platinum. *Chemistry of Materials*, 2013. doi:[10.1021/cm400274n](https://doi.org/10.1021/cm400274n).
- [12] Erkens, Mackus, Knoops, Smits, van de Ven, Roozeboom, and Kessels. Mass Spectrometry Study of the Temperature Dependence of Pt Film Growth by Atomic Layer Deposition. *ECS Journal of Solid State Science and Technology*, 2012. doi:[10.1149/2.006206jss](https://doi.org/10.1149/2.006206jss).
- [13] Aaltonen, Ritala, Tung, Chi, Arstila, Meinander, and Markku. Atomic layer deposition of noble metals: Exploration of the low limit of the deposition temperature. *Journal of Materials Research*, 2011. doi:[10.1557/JMR.2004.0426](https://doi.org/10.1557/JMR.2004.0426).



- [14] Aaltonen, Rahtu, Ritala, and Leskelaa. Reaction Mechanism Studies on Atomic Layer Deposition of Ruthenium and Platinum. *Electrochemical and Solid-State Letters*, 2003. doi:[10.1149/1.1595312](https://doi.org/10.1149/1.1595312).
- [15] Aaltonen, Ritala, Sajavaara, Keinonen, and Leskela. Atomic Layer Deposition of Platinum Thin Films. *Chemistry of Materials*, 2003. doi:[10.1021/cm021333t](https://doi.org/10.1021/cm021333t).
- [16] Kessels, Knoops, Dielissen, Mackus, and van de Sanden. Surface reactions during atomic layer deposition of Pt derived from gas phase infrared spectroscopy. *Applied Physics Letters*, 2009. doi:[10.1063/1.3176946](https://doi.org/10.1063/1.3176946).
- [17] Hiratani, Nabatame, Matsui, Imagawa, and Kimura. Platinum Film Growth by Chemical Vapor Deposition Based on Autocatalytic Oxidative Decomposition. *Journal of The Electrochemical Society*, 2001. doi:[10.1149/1.1381389](https://doi.org/10.1149/1.1381389).
- [18] Matsushima, Almy, and White. The reactivity and auger chemical shift of oxygen adsorbed on platinum. *Surface Science*, 1977. doi:[10.1016/0039-6028\(77\)90372-7](https://doi.org/10.1016/0039-6028(77)90372-7).
- [19] Campbell, Ertl, Kuipers, and Segner. A molecular beam study of the adsorption and desorption of oxygen from a Pt(111) surface. *Surface Science*, 1981. doi:[10.1016/0039-6028\(81\)90622-1](https://doi.org/10.1016/0039-6028(81)90622-1).
- [20] Gland, Fisher, and Kollin. The hydrogen-oxygen reaction over the Pt(111) surface: Transient titration of adsorbed oxygen with hydrogen. *Journal of Catalysis*, 1982. doi:[10.1016/0021-9517\(82\)90167-1](https://doi.org/10.1016/0021-9517(82)90167-1).
- [21] Christensen and Elam. Atomic layer deposition of Ir-Pt alloy films. *Chemistry of Materials*, 2010. doi:[10.1021/cm9031978](https://doi.org/10.1021/cm9031978).
- [22] Geyer, Methaapanon, Shong, Pianetta, and Bent. In Vacuo Photoemission Studies of Platinum Atomic Layer Deposition Using Synchrotron Radiation. *The Journal of Physical Chemistry Letters*, 2013. doi:[10.1021/jz301475z](https://doi.org/10.1021/jz301475z).
- [23] Mackus, Leick, Baker, and Kessels. Catalytic Combustion and Dehydrogenation Reactions during Atomic Layer Deposition of Platinum. *Chemistry of Materials*, 2012. doi:[10.1021/cm203812v](https://doi.org/10.1021/cm203812v).
- [24] Boyd. *Nonlinear optics*. Elsevier Science Publishing Co Inc, second edition, 1992.
- [25] Voges, Al-Abadleh, Musorrafiti, Bertin, Nguyen, and Geiger. Carboxylic Acid- and Ester-Functionalized Siloxane Scaffolds on Glass Studied by Broadband Sum Frequency Generation. *The Journal of Physical Chemistry B*, 2004. doi:[10.1021/jp046564x](https://doi.org/10.1021/jp046564x).
- [26] Knoops, Mackus, Donders, van de Sanden, Notten, and Kessels. Remote Plasma ALD of Platinum and Platinum Oxide Films. *Electrochemical and Solid-State Letters*, 2009. doi:[10.1149/1.3125876](https://doi.org/10.1149/1.3125876).
- [27] Chen, Shen, and Somorjai. Studies of polymer surfaces by sum frequency generation vibrational spectroscopy. *Annual review of physical chemistry*, 2002. doi:[10.1146/annurev.physchem.53.091801.115126](https://doi.org/10.1146/annurev.physchem.53.091801.115126).
- [28] Vandalon and Kessels. Chapter 5 of this thesis.
- [29] NIST. *NIST Chemistry Webbook*. NIST standard Reference Database Number 69, 2016.

- [30] Fan and Trenary. Symmetry and the Surface Infrared Selection Rule for the Determination of the Structure of Molecules on Metal-Surfaces. *Langmuir*, 1994. doi:[10.1021/la00022a044](https://doi.org/10.1021/la00022a044).
- [31] Nomura and Shima. Adsorption of hydrocarbons and formation of carbocations over zeolites studied by IR spectroscopy. *Journal of the Japan Petroleum Institute*, 2008. doi:[10.1627/jpi.51.274](https://doi.org/10.1627/jpi.51.274).
- [32] Vandalon and Kessels. What is limiting low-temperature atomic layer deposition of  $\text{Al}_2\text{O}_3$ ? A vibrational sum-frequency generation study. *Applied Physics Letters*, 2016. doi:[10.1063/1.4939654](https://doi.org/10.1063/1.4939654).
- [33] Bosshard, Bosch, Liakatas, Jager, and Gunter. Second-Order Nonlinear Optical Organic Materials: Recent Developments. In Hergert and Wriedt, editors, *Nonlinear optical effects and materials*. Springer Berlin Heidelberg, Berlin, Heidelberg, 2000. doi:[10.1007/978-3-540-49713-4\\_3](https://doi.org/10.1007/978-3-540-49713-4_3).
- [34] Fairbrother, Peng, Viswanathan, Stair, Trenary, and Fan. Carbon-carbon coupling of methyl groups on Pt(111). *Surface Science*, 1993. doi:[10.1016/0039-6028\(93\)90900-5](https://doi.org/10.1016/0039-6028(93)90900-5).
- [35] Fuhrmann, Kinne, Whelan, Zhu, Denecke, and Steinruck. Vibrationally resolved in situ XPS study of activated adsorption of methane on Pt(111). *Chemical Physics Letters*, 2004. doi:[10.1016/j.cplett.2004.04.030](https://doi.org/10.1016/j.cplett.2004.04.030).
- [36] Watson, Titmuss, and King. Surface products of the dissociative adsorption of methane on Pt(100)-(1x2). *Surface Science*, 2002. doi:[10.1016/S0039-6028\(01\)01678-8](https://doi.org/10.1016/S0039-6028(01)01678-8).
- [37] Campbell, Campbell, Dalton, Henn, Rodriguez, and Seimanides. Probing ensemble effects in surface reactions. 1. Site-size requirements for the dehydrogenation of cyclic hydrocarbons on platinum(111) revealed by bismuth site blocking. *The Journal of Physical Chemistry*, 1989. doi:[10.1021/j100339a056](https://doi.org/10.1021/j100339a056).
- [38] Henn, Dalton, and Campbell. Probing ensemble effects in surface reactions. 4. Cyclopentene adsorption on clean and bismuth-covered platinum(111). *The Journal of Physical Chemistry*, 1989. doi:[10.1021/j100339a059](https://doi.org/10.1021/j100339a059).



## 9.1 Conclusion

The work described in this dissertation focused on the growth mechanism of atomic-layer deposition (ALD) of ultrathin films. The main goal was to gain a fundamental understanding of ALD by studying the surface chemistry using BB-SFG spectroscopy. As part of this work, an *ex-situ* and an *in-situ* BB-SFG setup were designed and built. This design was documented in this dissertation and it has led to the identification of several practical considerations which should be kept in mind when using BB-SFG spectroscopy to study the surface chemistry during ALD.

The prototypical process of ALD of  $\text{Al}_2\text{O}_3$  was studied with BB-SFG spectroscopy. The  $-\text{CH}_3$  and  $-\text{OH}$  groups, ruling the surface chemistry of  $\text{Al}_2\text{O}_3$  ALD, could be measured with sub-monolayer sensitivity. The growth mechanism and surface chemistry of the steady-state growth of  $\text{Al}_2\text{O}_3$  ALD has already been studied extensively. However, several questions remained which were addressed in this work resulting in the following insights:

- The initial sticking probabilities  $S_0^{TMA}$  for TMA and  $S_0^{H_2O}$  for  $\text{H}_2\text{O}$  were determined. For TMA, a  $S_0^{TMA} = 4 \cdot 10^{-3}$  was found that was independent of temperature but for  $\text{H}_2\text{O}$  the initial sticking probability ranged from  $S_0^{H_2O} = 2 \cdot 10^{-5}$  at  $100^\circ\text{C}$  to  $S_0^{H_2O} = 4 \cdot 10^{-4}$  at  $300^\circ\text{C}$ .
- The  $-\text{CH}_3$  coverage after the TMA half-cycle ranged from  $6 \cdot 10^{14} \text{ cm}^{-2}$  at  $100^\circ\text{C}$  and decreased to  $4 \cdot 10^{14} \text{ cm}^{-2}$  at  $400^\circ\text{C}$ .
- The decrease in the GPC at low temperatures was shown to be caused by *persistent*  $-\text{CH}_3$  groups present on the surface. It was found that at low temperatures,  $\text{H}_2\text{O}$  is no longer reactive enough to remove all  $-\text{CH}_3$  groups in each cycle, resulting in the so far overlooked *persistent*  $-\text{CH}_3$  groups.

Several other fundamental aspects of the growth mechanism of  $\text{Al}_2\text{O}_3$  ALD were investigated as well, including topics such as: the kinetics of the ALD reactions, the self-limiting nature of the precursor half-cycle, and the bonding of the precursor to the surface.

The changes in the surface chemistry during the initial growth of  $\text{Al}_2\text{O}_3$  ALD on  $\text{SiO}_2$  and H terminated Si(111) were investigated on a half-cycle basis.

The subtle differences that were found in the surface chemistry reflected the commonly observed differences in the initial growth of  $\text{Al}_2\text{O}_3$  ALD on these ubiquitous starting surfaces. The key results were:

- TMA shows a reduced reactivity in the first precursor half-cycle on the  $\text{SiO}_2$  starting surface. All subsequent half-cycles show behavior similar to steady-state growth.
- The sticking probability for TMA during the first ALD cycle is a factor of 4 lower on  $\text{SiO}_2$  and a factor of 2 lower on H terminated Si(111) than during steady-state growth.

The steady-state growth of Pt ALD was also studied with BB-SFG spectroscopy. So far, the surface chemistry of this prototypical ALD process has not been studied directly and the exact nature of the hydrocarbon surface groups was not known. Key achievements include:

- Direct experimental evidence was found for the presence of  $-\text{CH}_3$  groups on the surface after the precursor half-cycle.
- The temperature trend in the  $-\text{CH}_3$  coverage after the precursor half-cycle and the reaction kinetics during the precursor half-cycle point to dehydrogenation of the hydrocarbon groups, confirming a hypothesis posed in earlier works.

To summarize, these findings demonstrate the unique flexibility and capability of BB-SFG spectroscopy as an analysis technique for the surface chemistry during ALD. It is excellently suited for initial growth studies and for following the reaction kinetics and can be used on a wide range of substrates. Especially qualitative and quantitative studies during initial growth might prove fruitful for novel development such as area selective ALD and ALD of ternary or doped materials. Moreover, the concept of *persistent* surface groups during ALD probably applies to other (more complex) ALD processes. As a matter of fact, several surprisingly complex mechanisms were encountered in these prototypical ALD processes. This indicates that ALD processes, which are often sketched and thought of as a single elementary reactions per half-cycle, are often oversimplified. In most cases, more complex mechanisms are at play.

## 9.2 Outlook

Although there are many issues that could be tackled with BB-SFG spectroscopy in the field of ALD, a topic which stands out is the surface chemistry during the initial growth. By definition, the surface chemistry changes from cycle-to-cycle during initial growth and this problem can only be tackled with a handful of analysis techniques. At the same time, initial growth becomes more relevant due to several trends including further reduction of layer thickness, area selective ALD, and ALD of more complex materials, including 2D materials.

What is lacking so far in most *in-situ* IR based analysis techniques (including BB-SFG spectroscopy) is sub-monolayer sensitivity at low wavenumbers (100 - 1000  $\text{cm}^{-1}$ ). Stretch modes of a bond consisting of a heavy atom with a light atom, such as the  $-\text{CH}_3$  and Si-H groups investigated in this work, provide relatively little information about the backbonding of those groups. This also holds to a certain degree for bending modes of the same groups. The bonds most interesting for mechanistic studies are those *between* “heavy” atoms such as Si, O, C, Al, Pt. Probing the vibrational modes of these bonds would yield a wealth of information on which species are present on the surface and how these species are bonded. However, the vibrational modes of such bonds are situated at low wavenumbers and hard or even impossible to measure. At the moment, these experiments are not possible due to the lack of laser systems covering this wavelength. However, through the progression of laser technology and the innovation in the field of non-linear optical crystals, generation of strong tunable broadband far infrared pulses should become (commercially) available in the (near) future.



## Sum-Frequency Generation Study of the Surface Chemistry During Atomic Layer Deposition

Atomic-layer deposition (ALD) is a *state-of-the-art* technique for the synthesis of ultrathin films. A key selling point of ALD is its unique capability to deposit highly uniform and conformal films with sub-nanometer thickness control. As such, ALD is an enabling step in the fabrication of nano-electronic components in devices such as logic and memory chips. In the process of ALD, material is deposited by a sequence of two or more self-limiting surface reactions. These self-limiting surface reactions rule the growth during ALD and lend the process many of its unique properties. A fundamental understanding of the growth mechanism of ALD is needed to keep up with the ever increasing requirements from industry. Therefore, *in-situ* analysis techniques capable of monitoring the surface chemistry during ALD are vital.

In this dissertation, the surface chemistry of ALD was studied by broadband sum-frequency generation (BB-SFG) spectroscopy. BB-SFG spectroscopy originates from the field of surface science and probes the vibrational transitions of surface groups. It is uniquely suited to monitor the surface chemistry due to its inherent surface selectivity and sub-monolayer sensitivity. In this work, BB-SFG spectroscopy was used to study the surface chemistry during ALD for the first time. A BB-SFG spectroscopy setup was designed and built. Several limitations and practical considerations were identified during this process. For example, the BB-SFG signals obtained from the surface groups during the *in-situ* studies were extremely weak. The weak BB-SFG signal led to the fundamental problem that the non-resonant contribution from the silicon substrate, normally negligible, was dominating the spectral response. This was mitigated by exploiting two phenomena: Firstly, the BB-SFG signals could be enhanced using an optical cavity. Secondly, this non-resonant signal could be suppressed, due to its short decay time, by carefully timing the probing pulses.

Subsequently, the surface chemistry of the prototypical processes of ALD of  $\text{Al}_2\text{O}_3$  and ALD of Pt were studied with BB-SFG spectroscopy. The well understood steady-state growth mechanism of  $\text{Al}_2\text{O}_3$  ALD, using  $\text{Al}(\text{CH}_3)_3$  as



precursor and H<sub>2</sub>O as co-reactant, served as a starting point for assessing the capabilities of BB-SFG spectroscopy. The –CH<sub>3</sub> and –OH surface groups ruling the surface chemistry of this process could be monitored during ALD with sub-monolayer sensitivity. Although many details of this ALD process have been studied, several open questions could still be addressed with BB-SFG spectroscopy. For example, the fundamental mechanism responsible for the reduced growth at low temperatures was not yet fully understood. In this work it was found that at low temperatures some of the –CH<sub>3</sub> groups are no longer reactive towards H<sub>2</sub>O, i.e. these groups are *persistent*. These *persistent* –CH<sub>3</sub> groups limit the precursor uptake and therefore the growth. The presence of *persistent* groups under certain conditions is expected to be more general. This was illustrated by others who, as a result of this work, showed that *persistent* groups also play a key role in ALD of zinc-tin-oxide. Moreover, for the Al<sub>2</sub>O<sub>3</sub> ALD process, several other fundamental aspects were addressed such as the temperature dependence of the absolute –CH<sub>3</sub> coverage, the reaction kinetics, and the sticking probabilities of the precursor and co-reactant.

Next, the surface chemistry during initial growth of ALD of Al<sub>2</sub>O<sub>3</sub> was studied on a SiO<sub>2</sub> and a H terminated Si(111) starting surface. The reactivity of the initial TMA half-cycle on the SiO<sub>2</sub> surface was found to be a factor of 4 lower than during steady state growth. On the other hand, all subsequent half-cycles showed behavior similar to that during steady-state growth. On the H terminated Si(111) surface the reactivity of TMA was found to be a factor of 2 lower than during steady-state growth. These subtle differences are in agreement with the commonly observed trends of virtually immediate growth on these two starting surfaces.

The ALD process of Pt, using MeCpPtMe<sub>3</sub> as a precursor and O<sub>2</sub> as a co-reactant, is seen as a model system for noble-metal ALD. The growth of noble metals by ALD in general is not completely understood and several questions about the underlying reaction mechanism remain. For the Pt ALD process, for example, the species of the hydrocarbon present on the Pt surface was unclear. With BB-SFG spectroscopy, direct evidence was found for the presence of –CH<sub>3</sub> groups on the Pt surface during ALD. Furthermore, evidence was found for dehydrogenation of the hydrocarbon groups on the catalytic Pt surface. This confirmed a hypothesis made in earlier work based upon an analysis of the gas-phase reaction products and the trends reported in the surface science literature pertaining to dehydrogenation of hydrocarbon species on Pt.

In conclusion, several new detailed insights into the growth mechanism of ALD were obtained with BB-SFG spectroscopy. The *inherent* surface selectivity of BB-SFG spectroscopy proved to be very valuable in this work and directly led to the observation of the *persistent* –CH<sub>3</sub> groups. It was also demonstrated that a range of ALD chemistries on substantially different substrates can be studied. As such, this work can contribute to the adoption of nonlinear vibrational spectroscopy as a more widely used analysis technique in the field of ALD. Furthermore, the new insight presented in this work will stimulate a discussion about some nuances and hidden complexities of film growth by ALD.

# Contributions of the author

The author has designed and performed all experiments, analyzed the data and wrote all parts of the dissertation.



# Acknowledgments

By its very nature, a PhD project is a trial and a test of character on many different levels. This specific project tested especially my perseverance and patience. Precisely because of these challenges the result is ever more rewarding: I will probably never forget the day that I obtained the first spectrum related to ALD. However, such a project would not be possible without the help and support of the people around me whom I would like to thank here.

First of all, I would like to express my gratitude to my direct supervisor and promotor Erwin. You gave me the freedom and trust needed to complete this project. The uncertainty that comes with building a new diagnostic setup during a PhD project probably also weighed on you. Questions such as “Will we get it to work?” arose in me but I never had the feeling that you doubted a successful outcome. Moreover, you allowed me to dedicate myself to the sole task of getting the setup to work by limiting external distractions. At the same time, I learned a lot from you about performing research and how to report on it. The standard you expect from your students (and yourself as is clear from your work) helped me to improve myself in many different aspects. Moreover, I really admire your unceasing strive for perfection and attention to detail while at the same time keeping the big picture in mind.

All staff members of the PMP group have had their contribution to my project but I would like to thank two of them in particular. Richard, I would like to thank you for being my co-promotor. Each time we spoke you were able to ask exactly the right questions to point me into a new direction. Moreover, I would like to thank Ageeth for giving me the time to finish my thesis; I really appreciate that. The project would not have been possible without the technical support of Janneke, Bernadette, Caspar, Cristian, Jeroen Joris, Ries, and the secretarial and administrative support of Jeanne and Lianne

Next I would like to thank my office mates. At the start of my PhD project I shared an office with İlker and Roy in N-Laag. All of us were focused on our work and as a result the office was mostly quiet (nice!) but we always found time to catch up in the morning. After our move away from N-Laag, the number of people in the office increased to 8 (the TNO building) and later to 12 (the new and very fancy Flux building). In TNO I really enjoyed the conversations with Bart Klarenaar about lasers and the good discussions with Harm about ALD, life, politics, and more recently Nano. Florian, I enjoyed our

---

after-hours conversations and I was honored to act as paronymph on your defense. I would also like to thank you for importing excellent local beers and showing us the Oktoberfest the German way! The Colorado 4 also have to be mentioned (although technically René was in a different office). Bart Macco, René, Bas, and Nick Thissen, we always had fun whether it was at a conference or just during the coffee break.

The contact with colleagues in PMP (present and past) made my stay all the more pleasant. Roger, we shared the pleasure (and sometimes misery) of maintaining the femtosecond laser system for quite a while and, apart from that, our interests are quite similar. I always enjoyed working with you and our personalities are complementary: When I come up with a make-shift solution nowadays, I often catch myself thinking “Roger would not approve of this”. This then motivates me to find an improved and less make-shift solution. Akhil, I really enjoy collaborating with you. Your cautious approach in both experiments and interpretation of data is commendable. Apart from that, we always seem to have a subject to talk about ranging from the differences between The Netherlands and India to more every day issues. Adrie, we went to some very nice conferences together and we seem to have a similar preparation style for traveling (do you need to prepare for that?). I would also like to mention some former PMP members by name. Nick Terlinden for supervising my MSc project and showing me nonlinear optics. Jan-Willem, your careful and meticulous interpretation of the optical response of graphene (and the related experiments) are still an inspiration for me. There are many more PMPeople I would like to thank but I cannot mention all of you here by name; nevertheless you have my gratitude.

During my PhD project I was also a member of the “Vereniging van Eindhovenense Natuurkundig Ingenieurs” (VENI) board. Our board meetings were always very enjoyable and it was a pleasure to be part of this organization. I would like to especially mention Paul Janssen here as I was inspired by (the layout of) his PhD thesis which I adopted to some degree in this work.

Last but certainly not least I would like to thank my family and friends outside the PMP group. Job, despite that we are both quite busy we always have something to talk about. Moreover, you always have time when it is really needed. Ingrid, thank you for the nice times at the “Côte de Vleuten” and hosting Lodewijk on a daily basis. I would also like to thank “De Hageveld groep” for their warm welcome years ago; it is a very special group and I always felt at ease. For this I am grateful to all of you! My mother Christel and my partner Claire I cannot thank adequately. Christel, thank you for an excellent upbringing and support over the years; I would not have been the person I am today without your guidance. I have you to thank for my levelheadedness, perseverance, and moral compass. Claire, the support during the last years were essential. When I was down you tried to lift my spirits a bit and reminded me to enjoy the nice things in life; for that I will always be grateful.

Vincent Vandalon  
Vleuten, March 2017

# Curriculum vitae

Vincent Vandalon was born in Geleen, the Netherlands, on June 15, 1983. After successfully obtaining his VWO diploma from the Stedelijke Scholengemeenschap in Roermond, he studied Applied Physics at the Eindhoven University of Technology (TU/e). Apart from his passion for physics, his interest in computer science resulted in, among other ventures, a project at the department of Mathematics and Computer Science. In this project, he built an application visualizing the real-time execution of computer code. Moreover, four months were spent at the Colorado School of Mines (CSM), Golden, Colorado (USA), investigating the growth mechanism of plasma-assisted ALD of  $\text{Al}_2\text{O}_3$  with ATR-FTIR absorption spectroscopy. After this internship, he started his graduation project in the Plasma and Materials Processing (PMP) group at the Applied Physics department of the TU/e. In 2011 he graduated on his work encompassing the characterization of the  $\text{SiO}_2/\text{Si}$  and  $\text{Al}_2\text{O}_3/\text{Si}$  interface with phase-sensitive second-harmonic generation (SHG) spectroscopy. Ensuing, Vincent started with his PhD research in the PMP group where he studied the surface chemistry during ALD with the nonlinear optical technique of broadband sum-frequency generation (BB-SFG) spectroscopy. His work introduced this analysis technique into the field of ALD and highlighted its key merits. For this research, he received the best student presentation award on the 15<sup>th</sup> International Conference on Atomic Layer Deposition in 2015 held at Portland, Oregon (USA).